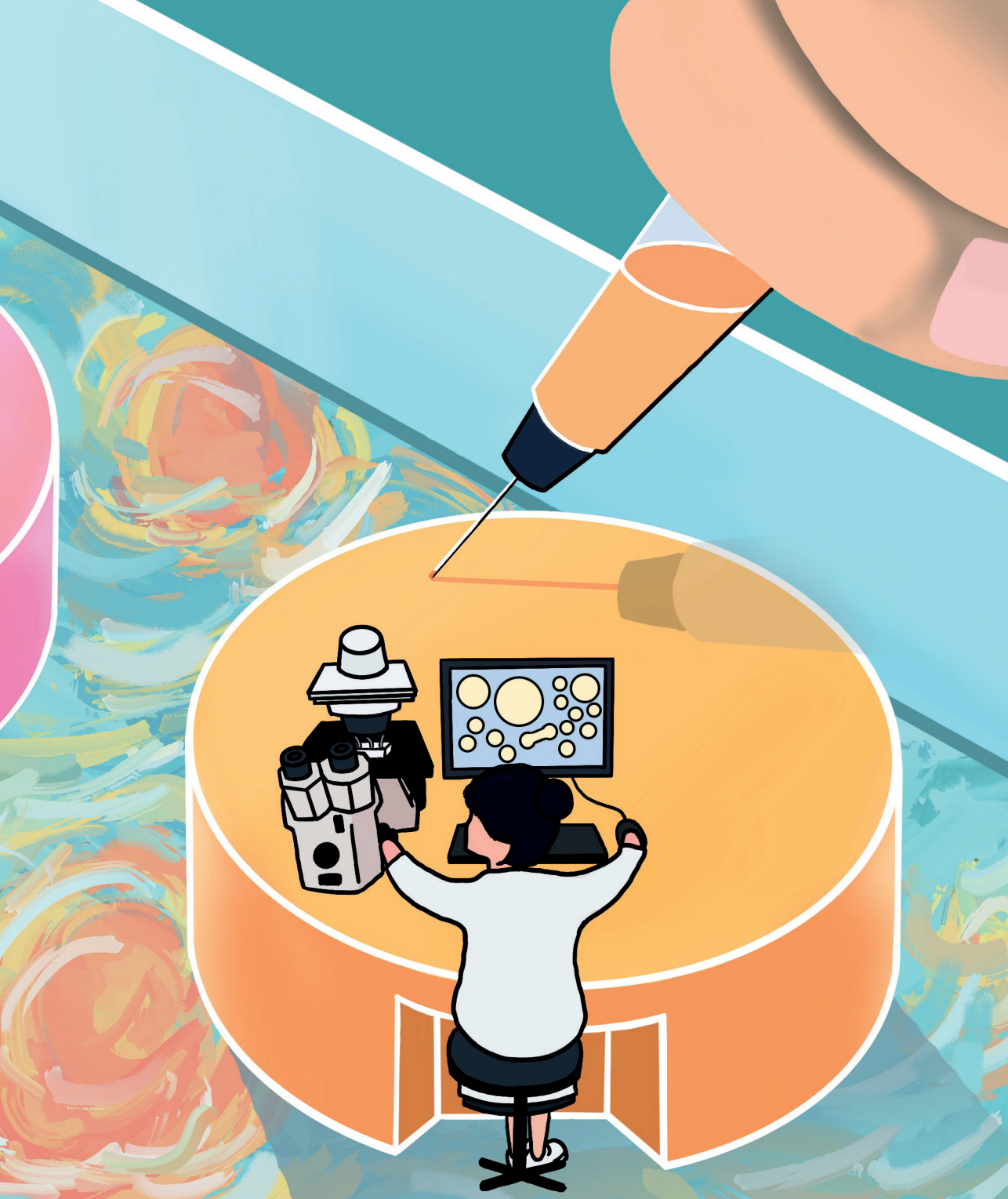

Microfluidic analysis of dynamic processes occurring during bubble formation and stabilisation

Boxin Deng

Propositions

1. Bubble coalescence at short time scales determines long-term foam stability. (this thesis)
2. Counterintuitively, higher emulsifier concentrations lead to unstable bubble formation, and more stable foam. (this thesis)
3. Miniaturization leads to bigger set-ups, and up-sets.
4. Precision experimentation is an undervalued part of science.
5. Peer pressure leads to motivation.
6. The pandemic increases the effort to stay in one's bubble.

Propositions belonging to the thesis, entitled

Microfluidic analysis of dynamic processes occurring during bubble formation and stabilisation

Boxin Deng

Wageningen, 25 November 2022

Microfluidic analysis of dynamic processes occurring during bubble formation and stabilisation

Boxin Deng

Thesis committee

Promotor

Prof. Dr C.G.P.H. Schroën

Personal chair at the Laboratory of Food Process Engineering

Wageningen University & Research

Co-promotor

Dr J. De Ruiter

Assistant professor at the Laboratory of Food Process Engineering

Wageningen University & Research

Other members

Prof. Dr J.H.B. Sprakel, Wageningen University & Research

Prof. Dr R.G.H. Lammertink, University of Twente, Enschede

Dr M. Marsiglia, IEP Energies nouvelles, Rueil-Malmaison, France

Dr M. Habibi, Wageningen University & Research

This research was conducted under the auspices of the Graduate School VLAG

(Advanced studies in Food Technology, Agrobiotechnology, Nutrition and Health Science)

Microfluidic analysis of dynamic processes occurring during bubble formation and stabilisation

Boxin Deng

Thesis

submitted in fulfilment of the requirements for the degree of doctor

at Wageningen University

by the authority of the rector Magnificus,

Prof. Dr. A.P.J. Mol,

in the presence of the

Thesis Committee appointed by the Academic Board

to be defended in public

on Friday 25 November 2022

at 4 p.m. in the Omnia Auditorium.

Boxin Deng

Microfluidic analysis of dynamic processes occurring during bubble formation and stabilisation

248 Pages

PhD thesis, Wageningen University, Wageningen, the Netherlands (2022)

With references, with summary in English

ISBN: 978-94-6447-395-7

DOI: https://doi.org/10.18174/576596

Contents

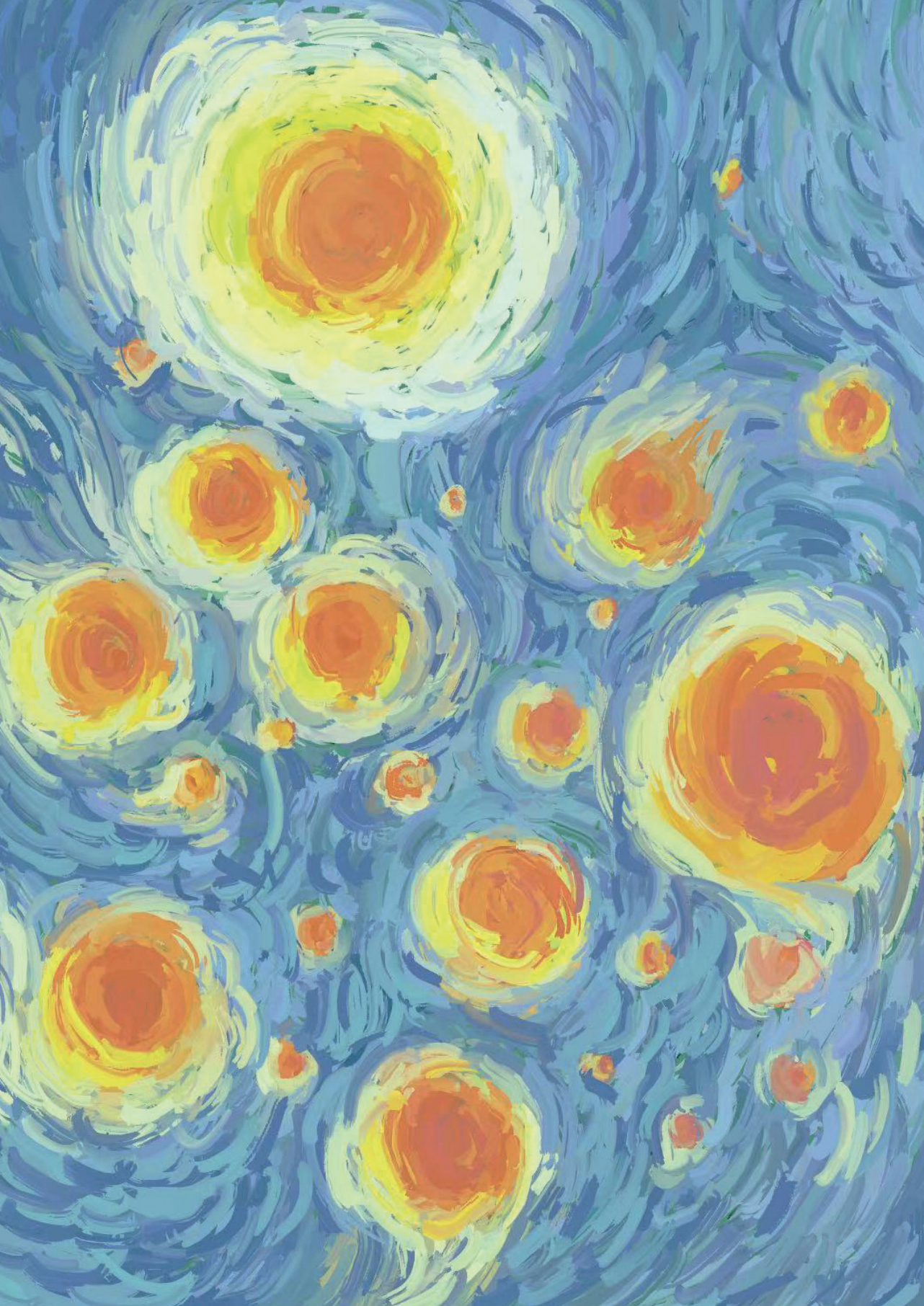

CHAPTER 1

Introduction and thesis outline

1.1 Foam

Foams are a common form of products in food, pharma and cosmetics. They contain bubbles dispersed in a liquid or solid phase. In food foams, the bubble size varies, typically, between 20 and 200 μm [1]. In general, these bubbles are subject to various destabilisation mechanisms such as coalescence (i.e., merging of bubbles) and disproportionation (i.e., coarsening by gas transfer from small bubbles to larger ones). To prevent coalescence, these small bubbles need to be covered with emulsifiers, which are mostly proteins in food foams. In practice, an excess amount of emulsifier is used to make sure these bubbles are sufficiently covered. In comparison to the amount of emulsifier needed for monolayer surface coverage (the minimum amount for interface stabilisation), the amount used in practice is much higher. To mitigate foam coarsening, either the diffusivity of the gas phase needs to be reduced (low temperature), the matrix would need to be solidified (as is the case in baked goods), or monodisperse bubbles can be used.

Up till now, due to the inaccessibility of the production lines for local analysis, and the very fast bubble formation process, the roles of emulsifier adsorption are mainly assessed and optimised using product properties such as foamability (i.e., the amount of air that can be dispersed into a solution) and foam stability (i.e., the variation in foam volume with time), which necessarily can only be measured at much longer time scales as that of bubble formation. In this thesis, we introduce new microfluidic techniques that allow highly reproducible bubble formation within very short time scales, which can be observed through high-speed imaging in combination with microscopy, unlike the situation in large-scale production lines where high overrun limits the visualisation of individual bubbles. We use these microfluidic techniques to study dynamic adsorption and its roles in bubble formation and stabilisation at relevant time scales.

1.2 Foam stabilisation

The foam consists of two (semi-)immiscible phases and is thermodynamically unstable. During foaming, an incredible amount of surface area is created that leads to an increase in the Gibbs free energy (ΔG) according to equation 1.1, which is a driving force for destabilisation.

$$\Delta G = \gamma \cdot \Delta A \qquad 1.1$$

Here ΔG is the surface free energy of the foam (N·m), γ the surface tension (N/m) and ΔA the net interfacial area created (m^2). Some processes lower ΔG, e.g., emulsifier adsorption lowers the surface tension (γ), and bubble coalescence reduces the interfacial area (ΔA).

Foams are destabilised through creaming (i.e., liquid drainage), disproportionation (i.e., coarsening), and coalescence during or after production (see the sketch in Figure 1.1). Coalescence is most relevant at short time scales (**this thesis**) and is driven by the tendency to minimise the Gibbs free energy. It takes place during or immediately after bubble formation upon bubble-bubble interactions (i.e., collisions) when the bubble surface is not yet fully covered with emulsifiers. When two bubbles approach, the liquid film between them will thin out until a certain thickness, and rupture when the thinning time is shorter than the contact time. The thinning rate (m/s) can be described through equation 1.2.

$$V_{thinning} = \frac{2h^3}{3\eta_c r^2}\Delta P \qquad 1.2$$

where h is the thickness (m) of the liquid film, ΔP the pressure difference (Pa) between the capillary hydrostatic pressure and the disjoining pressure, η_c the continuous phase viscosity (kg/(m·s)), and r the bubble radius (m).

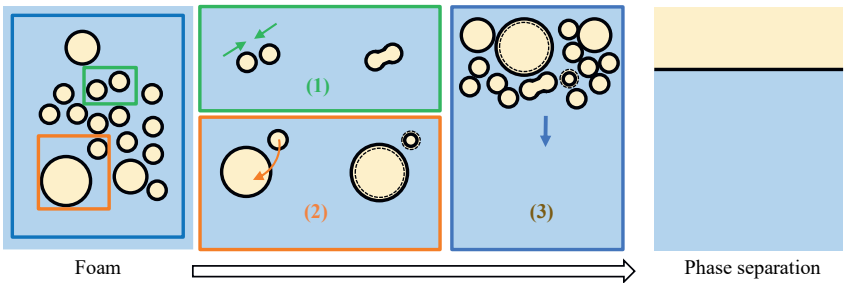

Figure 1.1. *Schematic illustration of foam destabilisation processes. From left to right: original foam, (1) coalescence, (2) disproportionation, (3) creaming, and completely destabilised 'foam' (i.e., phase separation). Note, if foam is exposed to the open atmosphere, processes (1) and (2) will occur between a huge 'bubble' (the atmosphere) and small bubbles [1]. For (2) and (3), dashed circles represent the original bubble sizes; solid circles represent their intermediate state during disproportionation. Gas phase: yellow; liquid phase: blue; interface: black line. Not to scale.*

Amongst others, coalescence is influenced by the continuous phase *viscosity*, which slows down the film thinning process (and more emulsifiers adsorb at the bubble surface if diffusion is not slowed down too much) [2,3], the approach *velocity* of the bubbles, which may shorten the contact time in a collision event and thus reduce coalescence [4], and emulsifier adsorption,

which leads to lowered surface tension and thus lowered ΔG (equation 1.1). The emulsifier adsorption rate varies with emulsifier type and concentration (**Chapter 7**).

Foam destabilisation processes take place simultaneously and do not exclude each other. Coalescence occurs at the microscale, and creaming and disproportionation proceed at the macroscale. Creaming implies that air bubbles migrate upwards, and simultaneously, the liquid phase among bubbles drains out. The creaming process is driven by a difference in density between dispersed and continuous phases; the creaming velocity (m/s) of a single bubble is defined in equation 1.3. Accordingly, foams with small bubbles and a high continuous phase viscosity are more stable against creaming [5]. Disproportion is driven by a difference in Laplace pressures (equation 1.4); as small bubbles have higher Laplace pressure, the gas phase has higher solubility and tends to diffuse to nearby larger bubbles. Hence, foams consisting of *monodisperse*, and large bubbles are relatively less affected by disproportionation [6]. Compared to emulsions, foams cream faster [6] and are more prone to disproportionation [1], due to the extremely low density of gas and its higher water solubility compared to oil (for oil in water emulsions).

$$V_{creaming} = \frac{2gr^2(\rho_d - \rho_c)}{9\eta_c} \qquad 1.3$$

$$\Delta P = \frac{2\gamma}{r} \qquad 1.4$$

where g is the gravitational constant, and ρ_d and ρ_c the densities (kg/m^3) of the dispersed and continuous phases, respectively.

1.3 Emulsifier adsorption

Emulsifiers are small amphiphilic molecules (i.e., so-called low-molecular weight surfactants, with **SDS** relevant in this thesis) and polymers, which are mostly proteins (**whey protein isolate mostly in this thesis**) for food foams. Emulsifier adsorption can be followed by surface tension measurement in time. Typically, low-molecular weight surfactants are more efficient in lowering the surface tension than proteins and do so at a higher rate. The maximum reduction in surface tension is about 30-40 mN/m for low-molecular weight surfactants, and about 15-20 mN/m for proteins, with the difference related to their specific physiochemical properties [3].

Emulsifier adsorption to the interface proceeds via a series of steps (Figure 1.2) [7]: (1) emulsifiers diffuse or convect from the bulk phase to the sub-interface layer, which is an 'imaginary' layer of solution adjacent to the interface, (2) emulsifiers diffuse through this sub-interface layer, (3) emulsifiers adhere to the interface, and for proteins, (4) conformational rearrangement starts upon adsorption [8]. There are two characteristic time scales playing a role: the diffusion time (t_d) and the kinetic adsorption time (t_k). The former time scale dominates step (2) and the latter time scale describes the balance between adsorption and desorption of emulsifiers at the interface (3). If $t_d > t_k$, through step (3) emulsifiers are assumed to adsorb at the interface immediately under diffusion-controlled conditions [9]; on the other hand, if $t_d < t_k$, the concentration gradient between bulk and the sub-interface layer can be ignored, and kinetic adsorption of emulsifiers at the interface is the rate-limiting factor [10].

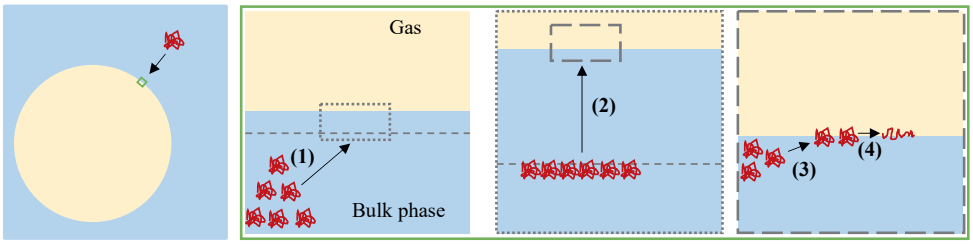

Figure 1.2. *Schematic illustration of emulsifier adsorption at a small section of bubble surface: (1) diffusion or convection from the bulk phase to the sub-interface (dashed line), (2) diffusion to the actual interface, (3) kinetic adsorption and desorption at the interface, and (4) specifically for proteins, conformational rearrangements and molecular interactions may take place. Highly schematic and not to scale.*

Emulsifier adsorption and the resulting lowered surface tension play an important role in bubble formation and stabilisation (e.g., in suppressing coalescence upon bubble-bubble interactions). The level of influence highly depends on the importance of t_d or t_k relative to bubble formation time. For example, it has been suggested that to eliminate the influence of interfacial tension on the initial size of droplets (without coalescence), the droplet formation time should be at least three folds higher than the characteristic time scale (t_d in this case) of mass transfer of low-molecular weight surfactants like SDS [11]. In another microfluidic study, for a range of C_{12}TAB concentrations (i.e., 0.1, 0.5 and 1 time the critical micelle concentration), t_d is always shorter than the droplet formation time, and as a result, droplet formation and the droplet properties are governed by equilibrium interfacial tension [12].

The relative magnitude of t_d and t_k is influenced by multiple factors, like the emulsifier properties (e.g., *bulk concentration*), the curvature (e.g., *bubble radius*), and the interfacial (e.g., *surface concentration*) and liquid phase properties (e.g., *viscosity* and *velocity*) [9,10,13]. Convective flow around bubbles leads to a boundary layer (of which the thickness inversely scales with the *Péclet* number), through which step (2) occurs by diffusion [11], and emulsifier mass transfer (step (1)) is enhanced by the convective flow for *Péclet* number above 1.

To complicate matters even more, the bubble formation time is sensitively dependent on the foaming techniques and process conditions; in practice, typical time scales for foaming processes are in the order of 1-10 ms [14], and in some systems, even shorter time scales have been reported, like < 0.3 ms for bubble formation at an orifice [15]. During foam production, an interplay between the time scales for emulsifier mass transfer and bubble formation will most probably play a role, leading to dynamic situations, e.g., co-existence of bubble formation and coalescence (**Chapter 3**). To control this interplay, it is important to understand emulsifier adsorption at relevant time scales (**Chapters 5, 6, 7**).

1.4 Microfluidics

Microfluidic technology has grown rapidly for the investigation of monodisperse droplet formation [16], even under process conditions close to those encountered during large-scale production of emulsions [17]. Microfluidic devices have been up-scaled and utilised as generators of monodisperse droplets [18–21]. Besides, precisely-designed microfluidic devices have been used as model systems to understand e.g., membrane emulsification [22]. Moreover, they have found applications as analytical tools to study sub-processes happening during the formation of individual droplets, for instance, the kinetics of emulsifier adsorption in relation to dynamic interfacial tension [11,23,24], and droplet coalescence [25–27].

A central theme for creating droplets and bubbles in microfluidics is the crucial role of confinement by the micrometre or millimetre-sized channels. The confinement dominates the deformation and breakup of the fluid interface during droplet and bubble formation [28]. Based on the characteristics of the device geometry and the droplet formation mechanisms, microfluidics can be categorized into two groups: *shear-based* and *spontaneous* devices. In shear-based devices such as T-junction [16,29–32] and flow-focusing [12,33–36], the flow of both dispersed and continuous phases need to be carefully manipulated to control e.g., droplet size and droplet formation frequency. Four regimes of droplet formation can be distinguished at

increasing *continuous phase* flow rate (or capillary number): squeezing, dripping, jetting, and parallel flow (where no droplet formation occurs). For instance, in the dripping regime, droplet formation is driven by a force balance between the viscous force exerted by the continuous phase and the interfacial tension force that varies with the type and concentration of emulsifiers [37]. In spontaneous devices, the 'dripping-jetting' transition is also observed, yet, at a higher *dispersed phase* flow rate (or capillary number). In these devices, typically, droplet formation is driven by a sudden decrease in Laplace pressure from that of a highly-curved meniscus, which is constricted in the channel, to that of a less-curved droplet, which grows in a collection channel (without confinement) [38]. Contrary to shear-based devices, the continuous phase flow is mainly used to transport droplets downstream [39–42].

Each type of device has pros and cons. In general, the shear-based devices are more flexible in tuning the droplet size, and more often developed as analytical tools for the measurement of e.g., dynamic interfacial tension; the spontaneous devices are less influenced by perturbations in pressures and flows during emulsification, and more promising for up-scaling [43]. Most microfluidic investigations have been carried out for droplets, and rarely for bubbles, and it is often assumed that the findings done for droplets will be translatable to bubbles (**Chapter 2**). Yet, given the compressibility and the extremely low gas phase viscosity that amongst others is expected to lead to higher surface expansion rates, extra effects can be expected to play a role. That is why we have made bubbles the core of this thesis: microfluidic techniques are used to characterise the formation, focusing on the sub-processes, and stabilisation of monodisperse bubbles at (sub)millisecond time scales.

1.4.1 (Partitioned) EDGE devices

EDGE devices are not that sensitive to pressure fluctuations and possess the unique feature of forming multiple droplets simultaneously [44]. The regular EDGE device has to some extent been up-scaled for making droplets via parallelisation [18] and proved to be robust in use. Besides, the regular EDGE device has been used to make bubbles stabilised with proteins [45]. Regular EDGE is the prototype of the partitioned-EDGE device which has parallel partitions, or pores, and we expect that the partitioned-EDGE device can be up-scaled (relatively) easily for making monodisperse emulsions and foams, and will show enhanced performance as was the case for individual units of partitioned-EDGE compared to regular EDGE [42].

A special feature of the partitioned-EDGE device in comparison to other devices is that droplet formation shows two pressure regimes (115-1000 mbar and 1400-2100 mbar, in the presence of 0.5% wt. SDS), and within each pressure regime, droplets are monodisperse and the droplet size is independent of the applied pressure, which allows the production of two distinct-sized emulsions (e.g., the droplet diameters are 9 and 28 µm, respectively; Figure 1.3) [42]. In the first pressure regime, a wider range of applied pressures is obtained with narrower pores (see **Chapter 6**, explained for bubble formation). The second pressure regime occurs through physical interactions between droplets growing at adjacent pores [46]; for which pore spacing (i.e., the distance between the centre of two pores) is an essential design parameter. Indeed, the second pressure regime occurs at a pore width of 5 µm, while it was not observed at a pore width of 40 µm. We expect that this will allow investigation of both bubble formation and bubble stabilisation at very short time scales, as discussed further in section 1.4.3 (see also **Chapters 3** and **4**)

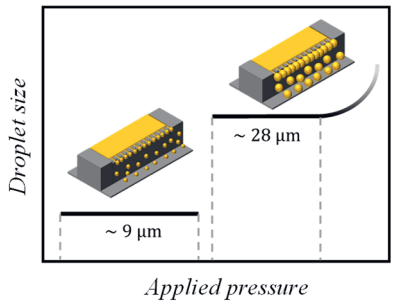

Figure 1.3. *Droplet size versus applied pressure, obtained for pore with 5 µm. Adapted from Şahin and Schroën (2015) [42].*

Given the layout of partitioned-EDGE, it is also expected that details of individual bubble and droplet formation at the pore can be elucidated. Mi and co-workers (2019) [47] used a terrace-based microchannel to study bubble formation, and divided one bubble formation cycle into 2D-expansion on the terrace and 3D-expansion in an unconfined chamber (Figure 1.4A). As part of 3D-expansion, the necking process of the gaseous thread can be further sub-divided into neck narrowing (a few milliseconds) and quick pinch-off. It was found that using a higher continuous phase viscosity leads to a longer necking time and thus a larger bubble size. In another work, Mittal and co-authors (2014)[48] used a straight-through microchannel to make droplets (Figure 1.4B). They defined two time scales for droplet formation (tens of milliseconds) and necking (a few milliseconds), and found that above a

certain dispersed phase pressure, the necking time and thus the droplet size, scales with the continuous phase viscosity.

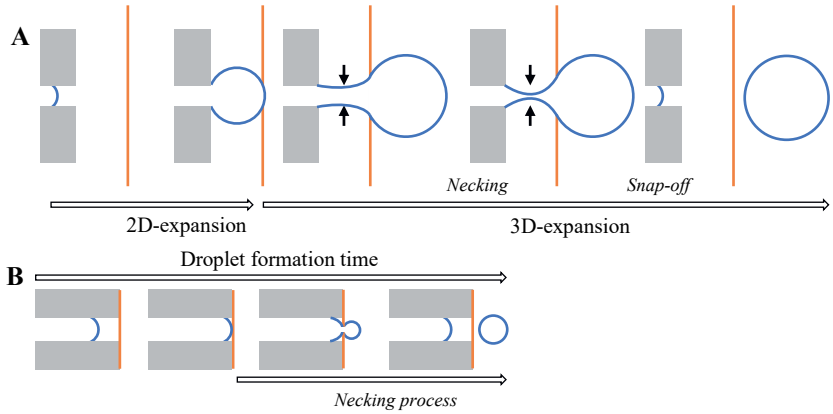

Figure 1.4. *Illustration of bubble formation in a terrace-base microchannel (A) and droplet formation in a straight-through microchannel (B). The orange line marks the sudden increase in channel height.*

From the above, it is clear that microfluidic platforms can be instrumental in gaining a deeper understanding of the formation of individual bubbles by investigating the sub-processes. In **Chapters 3-4** and **6-7**, microfluidics will be used to study bubble formation and stabilisation. An integral part of these investigations is the dynamic surface tension at work during these processes, to which we dedicated a separate chapter (**Chapter 5**).

1.4.2 Dynamic interfacial tension

In literature, microfluidic tensiometry has been proposed for the measurement of dynamic interfacial tension at short time scales. T-junction, Y-junction, and co-axial devices have been used. Up till now, microfluidic tensiometry has been developed based on three distinct measurement principles. First, the dynamic interfacial tension can be measured based on off-line analysis of droplet properties such as the *shape* and *size*. The deformation in droplet shape represents the time-evolving droplet rheology [23,49,50], and the size is determined by a force balance between viscous force and interfacial tension force during droplet formation in the dripping regime [37,51–53]. Second, the dynamic interfacial tension can be measured based on a force balance between interfacial tension force and an externally-applied pressure drop during droplet formation in the transition [54] or squeezing regimes [55]. Lastly, the dynamic interfacial tension can be derived from the Young-Laplace equation [56], and the measurement principle relies on tracking the movement of an interface, which moves (towards a position where the radius of curvature is smaller) to maintain a constant Laplace pressure, which

equals to a pre-set value. Again, compared to droplet surfaces, bubble surfaces have received less attention; the aforementioned principles can be extended to bubble surfaces to some extent, for example, the dynamic surface tension measurement carried out based on bubble deformation [49,57]. In **Chapter 5**, a microfluidic tensiometry is proposed to measure dynamic surface and interfacial tension for bubble and droplet surfaces, respectively, in the same device; the measurement relies on a different principle, and makes use of the special features of the partitioned-EDGE device.

1.4.3 Coalescence

Microfluidic techniques have been used to study coalescence. The typical approach is to de-couple droplet formation from coalescence; for example, monodisperse droplets are formed at a T-junction, and then transported one by one through a channel of various lengths, after which meet in a wider chamber [4,25–27,58]. Emulsifier adsorption can be manipulated by varying the length of the channel that stretches the time for emulsifier adsorption, and the emulsifiers (e.g., the type and concentration). For example, Muijlwijk and co-authors [27] varied the length of the channel and thus the adsorption time (11-173 ms), and observed droplet stabilisation at lower emulsifier concentration when a longer adsorption time was used. The first results were also obtained for bubbles; bubble stabilisation requires a considerably higher emulsifier concentration compared to droplet stabilisation.

With the aforementioned devices, adsorption times are imposed to be in the order of tens of milliseconds, while in practice these times would be much shorter leading to the use of an excess amount of emulsifier for emulsification [59], and even higher concentrations to stabilise foam. In **Chapter 6**, we target much shorter time scales as demonstrated in the literature, making use of the unique design of partitioned-EDGE that allows for the generation of bubbles (and droplets) in very close proximity. In this case, the bubble formation time sets the time available for emulsifier adsorption, and this allows bubble formation and coalescence to be studied at (sub)millisecond time scales.

1.5 Research outline and thesis chapters

The objective of this thesis is to understand emulsifier adsorption and its crucial roles in bubble formation and stabilisation at relevant time scales. We mainly study the adsorption dynamics of two classic emulsifiers: whey protein isolate as the ‘model’ emulsifier for food products (in **Chapters 3, 4, 6, 8**), and SDS as the ‘standard’ emulsifier widely studied in the

literature (in **Chapters 5** and **7**). Microfluidic techniques are used to understand emulsifier adsorption, by characterising various dynamic processes occurring during bubble formation and stabilisation. The content per chapter is described next, and a graphical abstract that brings all chapters of the thesis together is shown in Figure 1.5.

Chapter 2 provides a review of existing literature about the application of microfluidics in the production and analysis of (food) foams. We found that although microfluidics have been widely used to produce and characterise droplets, bubbles have been rarely studied. Compared with droplets, bubbles are formed faster, which implies that the formation and coalescence of bubbles need to be characterised at shorter time scales, imposing additional requirements on the microfluidics' design and the use of 'higher' speed cameras. In addition, gas compressibility makes working with bubbles more challenging.

In **Chapter 3**, we use the partitioned-EDGE device to study bubble formation as function of applied pressure. Bubble formation shows two pressure regimes, and emulsifier adsorption plays distinctly different roles in these two pressure regimes. In the low-pressure regime, also called the 'dynamic regime', emulsifier adsorption plays a role in the initiation of bubble formation; in the high-pressure regime, also called the 'static regime', bubble formation does not require prior adsorption of emulsifiers, but emulsifier adsorption is responsible for the finite extent of bubble coalescence. Using partitioned-EDGE devices, we can define two consecutive sub-processes (i.e., pore filling and necking) during one bubble formation cycle, with the bubble formation time as low as tens of microseconds.

To generalise more insights on bubble formation at (sub)millisecond time scales, in **Chapter 4**, we study the effects of process conditions on bubble formation and thus bubble properties, by monitoring the two consecutive sub-processes described earlier. This allows us to link process conditions to e.g., bubble formation frequency and bubble size. Special attention is given to protein concentration and continuous phase viscosity.

In **Chapter 5**, relying on the role of emulsifier adsorption in the low-pressure regime, we use the partitioned-EDGE device as a microfluidic tensiometry ('EDGE tensiometer'). It can be used for both droplet and bubble surfaces, and we successfully demonstrate that the EDGE tensiometer can evaluate the full range of dynamic interfacial tensions between that of the empty and the saturated interfaces. In the presence of SDS, the dynamic interfacial tension can be measured at time scales down to 1 ms and 0.1 ms for droplet and bubble surfaces,

respectively. This method is used to link results obtained with conventional pendant drop tensiometers to other microfluidic techniques.

In **Chapter 6**, relying on the role of emulsifier adsorption in the high-pressure regime, we use the partitioned-EDGE device to study instant coalescence. The process conditions are varied; in the experiments, we systematically analyse the size of initial and coalesced bubbles; in a semi-empirical model, we relate the extent of bubble coalescence to the bubble formation time. This method allows us to study bubble coalescence at short time scales, which are determined intrinsically by the device geometries and dynamics of bubble formation.

In **Chapter 7,** we study the roles of dynamic adsorption of SDS in bubble formation and stabilisation and compare this with other emulsifiers, particularly proteins such as whey protein isolate (in Chapter 6), β-lactoglobulin, and bovine serum albumin. SDS and protein adsorption takes place at essentially distinct time scales. At time scales down to 10 μs, the effectivity of the various emulsifiers in suppressing bubble coalescence is measured, which shows the importance of dynamic surface tension in interface stabilisation.

In **Chapter 8**, we leave the highly-defined world of microfluidic systems, and instead study bubble formation and stabilisation in a cross-flow membrane foaming system, which holds additional challenges. For example, a wide distribution of pore size and special flow profiles are present. Still, we can define windows of operation in which rather monodisperse bubbles can be formed.

Finally, in **Chapter 9**, we provide a general discussion of the main findings from this thesis. We attempt to link the findings obtained in very well-defined microfluidic systems to processes happening under conditions as they would encounter in larger-scale equipment, and amongst others show the first results obtained with a microfluidic micro-membrane with various pore sizes and report on pore activation and cross-talk between pores.

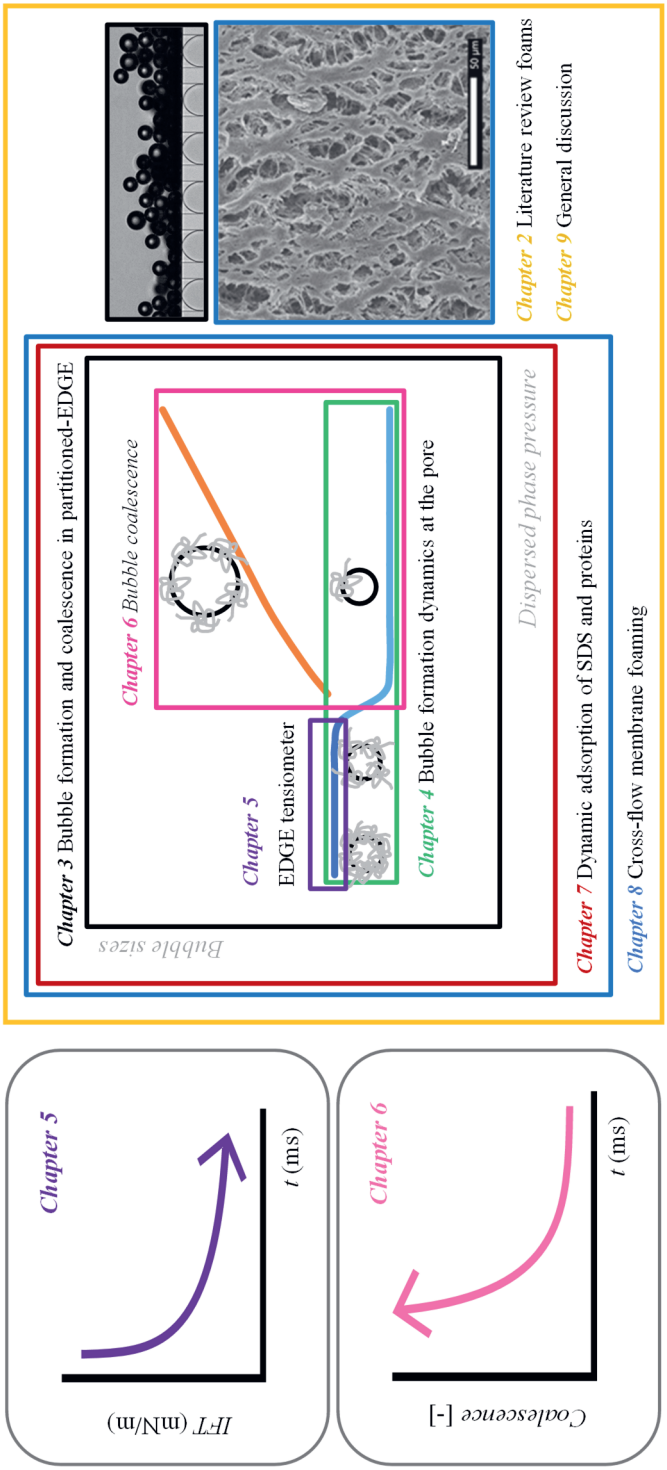

Figure 1.5. *Graphical outline of the thesis content and chapter division*

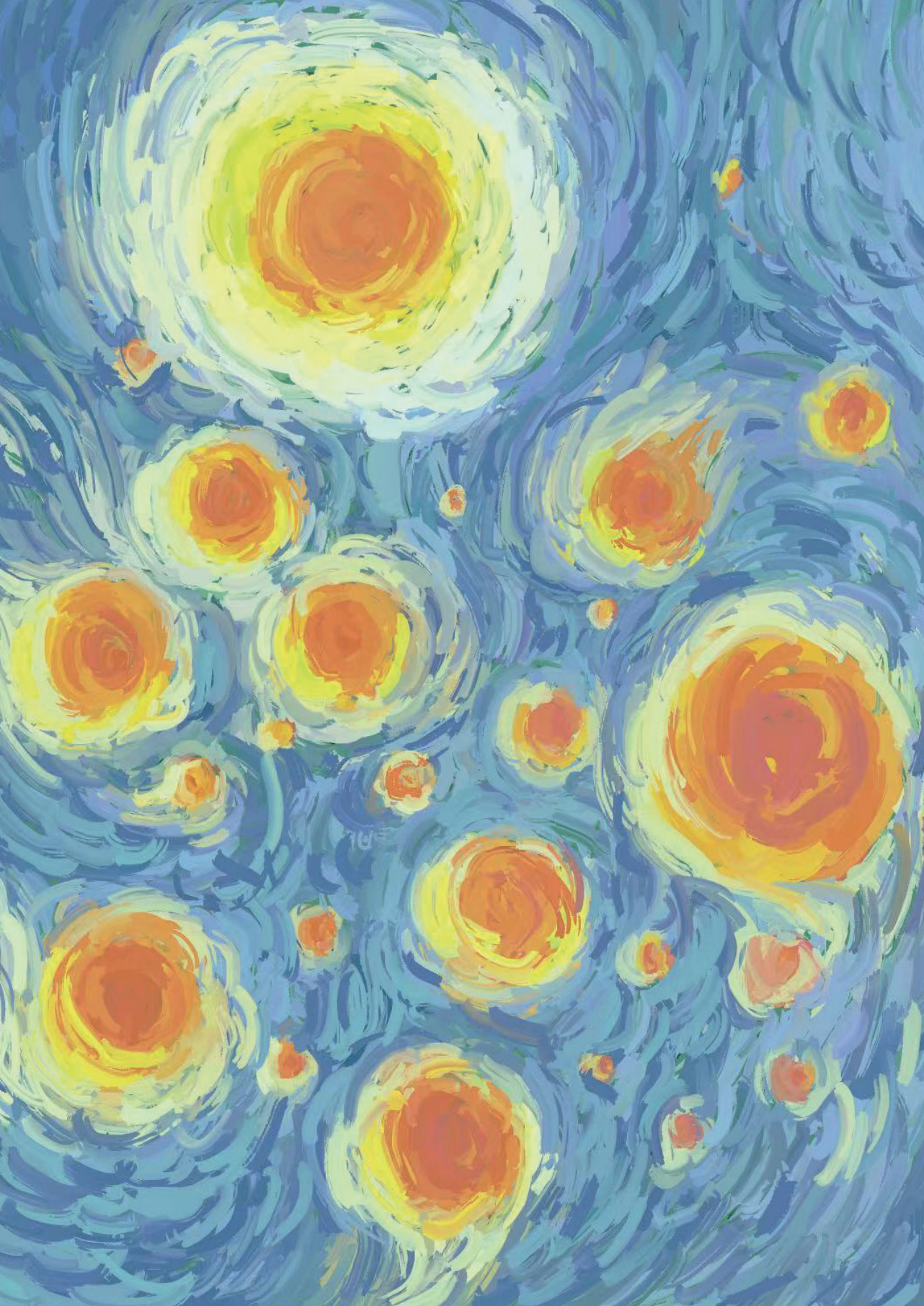

CHAPTER II 2

Application of microfluidics in the production and analysis of food foams

This chapter has been published as Deng, B., De Ruiter, J., Schroën, K. Application of microfluidics in the production and analysis of food foams. *Foods*, **2019**, 8(10), 476.

2.1. Abstract

Emulsifiers play a key role in the stabilisation of foam bubbles. In food foams, biopolymers such as proteins are contributing to long-term stability through several effects such as increasing bulk viscosity and the formation of viscoelastic interfaces. Recent studies have identified promising new stabilisers for (food) foams and emulsions, for instance, biological particles derived from water-soluble or water-insoluble proteins, (modified) starch as well as chitin. Microfluidic platforms could provide a valuable tool to study foam formation on the single-bubble level, yielding mechanistic insights into the formation and stabilisation (as well as destabilisation) of foams stabilised by these new stabilisers. Yet, the recent developments in microfluidic technology have mainly focused on emulsions rather than foams. Microfluidic devices have been up-scaled (to some extent) for large-scale emulsion production, and also designed as investigative tools to monitor interfaces at (sub)millisecond time scale. In this review, we summarise the current state of the art in droplet microfluidics (and, where available, bubble microfluidics), and provide a perspective on the applications for (food) foams. Microfluidic investigations into foam formation and stability are expected to aid in the optimisation of stabiliser selection and production conditions for food foams, as well as provide a platform for (large-scale) production of monodisperse foams.

2.2. Introduction

Foam is a colloidal system consisting of a high-volume fraction of the gas phase and a liquid (or solid) phase. It is made by mixing or injecting gas bubbles into the liquid (that later may be solidified). Emulsifiers, if any, in the foaming system are used for stabilising the newly created gas-water interface by decreasing the surface tension (γ), and modifying the interfacial viscoelasticity as well as the repulsive interaction forces between bubbles. However, foams are thermodynamically unstable. The principles of stability have extensively been described by Walstra (1989) [60]. The main destabilisation mechanisms of foam are disproportionation (also termed Oswald ripening), drainage, and coalescence, which are illustrated in Figure 2.1. These mechanisms occur simultaneously and act synergistically. Disproportionation is the most predominant and fast process. It is a result of the pressure difference between bubbles, due to the Laplace pressure $\Delta P = \frac{2\gamma}{R}$ in each bubble. Since the gas in the small bubbles (small radius R) has a higher pressure than that in large bubbles, it tends to diffuse through the liquid phase towards large bubbles. The average bubble size increases with time, with large bubbles growing at the expense of small ones. As a result, polydisperse foams are more prone to coarsening and subsequent destabilisation. Disproportionation is especially pronounced in foams due to the high solubility of a gas in water – in contrast, the effect is much smaller for emulsions, which consist of liquid droplets dispersed in another immiscible liquid phase (the solubility of e.g., triglyceride is very low in water). During foam drainage, water leaks out of the foam due to gravity (g: gravitational acceleration) based on the large density difference between the gas phase (ρ_{gas}) and water phase (ρ_{water}), and the bubbles rise. Their rising velocity scales with R^2, demonstrating the enhancement of drainage by disproportionation. Furthermore, due to the drainage process, the liquid film between bubbles becomes thinner, which initiates the coalescence of bubbles.

In the food industry, foaming is used to make less dense, airy food products, and thus modify their appearance and texture. Bubble stabilisation is crucial for this, and occurs in typical examples of liquid food foams: whipped tops, cappuccino, ice-cream, etc. In these products, proteins (typical dairy proteins) are mostly used as emulsifiers. Synergistic stabilisation effects between proteins and other ingredients were also reported, such as for milk foam for cappuccino that is stabilised by proteins and polysaccharides [61]. Traditional foaming operation is carried out by rotor-stator mixing, turbulent mixing, and steam injection. These

techniques use energy inefficiently, and the size distribution of generated bubbles is highly polydisperse, which is one of the underlying reasons for food foam instability (by disproportionation) as mentioned above [62].

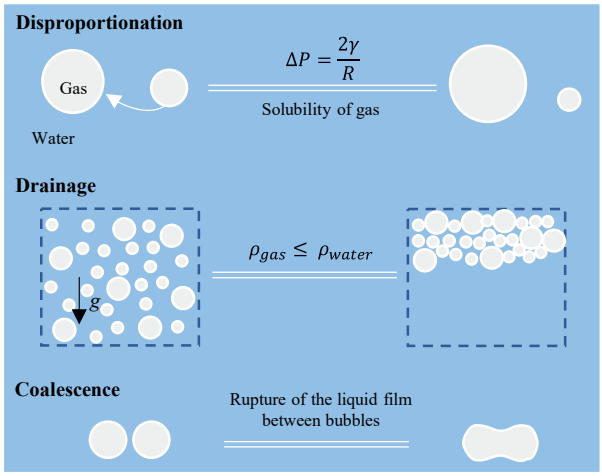

***Figure 2.1**. Illustration of the three main destabilisation mechanisms of foams, from top to bottom: disproportionation, drainage, and coalescence.*

To retard food foam destabilisation, the creation of monodisperse foams is a way to go, although this is difficult with conventional foaming techniques. Another way is to prevent coalescence or restrict bubbles rise, for example by absorbing stabilisers to the air-water interface or constructing a network in the continuous phase, respectively. Recently, colloidal particles have been introduced as novel stabilisers that can perform both of these stabilising functions. The resulting dispersions are termed Pickering foam (or Pickering emulsion), for a review see Lam et al. (2014) [63]. For food applications, a variety of food-grade (biobased) particles are studied, such as particles derived from proteins and (or) starch [64,65], and fat crystals [66]. These particles can absorb to the air-water interface where they may increase the steric barriers between bubbles, as well as increase the interfacial viscoelasticity, and (or) form a network in the continuous phase and increase its viscosity [63]. The deposition of particles and the exact stabilisation mechanisms still need to be detailed.

From the above, it is clear that although food foams are made at large-scale, understanding of the underlying mechanisms could still be improved, and for that microfluidic technology could provide valuable tools to study 'traditional' foams, as well as Pickering foams. The main topics that need to be addressed are bubble formation, interface stabilisation by emulsifiers or particles, and destabilisation processes in foams. It is expected that if these

aspects are understood this will lead to better use of ingredients, and thus a design of food foams based on first principles.

In the last decades, food research has benefited from a large number of developments in the field of microfluidic technology, in particular for applications in emulsions. Microfluidic droplet formation units are known to produce very small and uniform droplets at low energy consumption albeit the relatively low throughput limits their applicability. To overcome this restriction up-scaling has been attempted; achievements and associated challenges are discussed in a review by Schroën and colleagues [43]. Besides, microfluidic devices have also been developed as analytical tools to aid in the characterisation of emulsions [27,67,68], for example, to measure dynamic interfacial tension in the droplet formation process and to predict the emulsion coalescence stability. For further information, we recommend a review by Gunes (2018) [69] dedicated to studies using microfluidics and complex interfaces as present in foods.

Extensive studies using microfluidic devices have been performed in liquid-liquid systems (emulsions). Yet, the literature on gas-liquid systems (foams) remains comparatively scarce, not to mention literature related to food foams with complex (mixtures of) stabilisers. This is likely related to bubble formation being a much faster process than droplet formation, which is due to the low viscosity of the dispersed phase. It thus requires extremely short observation time scales, in particular when small micrometre-sized bubbles are needed. Based on the findings obtained from emulsions, microfluidic devices are expectedly highly suited to produce monodisperse (food) foams and to study foam formation as well as stabilisation. In this review, we will focus on reported contributions in the microfluidic field specifically dedicated to foams (where available), and also interpret methods and insights from emulsion studies and relate them to what can be expected for foams taking into account the fast dynamics at (sub)millisecond time scales. We will round off by describing how microfluidic devices can be used to produce monodisperse food foams at high throughput.

2.3. Microfluidic devices

Various microfluidic devices have been introduced for the formation of monodisperse foams, and they use either a shear force or spontaneous snap-off for bubble formation. The typical shear-based geometries include T-junction (Figure 2.2A) [16,70–72], flow-focusing (Figure 2.2B) [33,35,73–75], and co-flowing devices (Figure 2.2C) [76]. On the other hand, devices that use

spontaneous snap-off are microchannels (e.g., terrace-based microchannel, which is a so-called 2.5D geometry; Figure 2.2D) [41,77] and Edge-based Droplet GEneration (EDGE; Figure 2.2E, also termed STEP) devices [45].

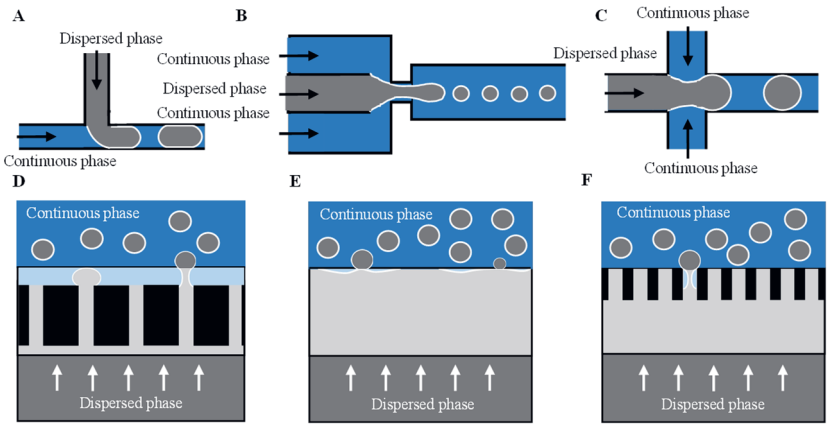

Figure 2.2. *Schematic layout of microfluidic devices: A. T-junction, B. flow-focusing, and C. co-flowing device; (D) terrace-based microchannel (MC); (E) EDGE, and (F) partitioned-EDGE droplet formation unit. Please note that in the top three devices channels have the same depth, while in the bottom three, a height difference is needed to allow spontaneous droplet formation to take place. Deep channels (of all the designs) and shallow areas (in the bottom three designs) are indicated as dark grey and light grey, respectively. The continuous phase (water phase) has a blue colour and shows as dark blue when flowing in the deep channel, and as light blue when in the shallow areas. The gas has no colour in this figure. The white outline indicates the gas-water interface. These schematics are not drawn to scale.*

In shear-based devices (also termed active devices), droplet formation is controlled by an external force: the shear stress exerted by the continuous phase flow. In spontaneous droplet formation devices (also termed passive devices), droplet breakup is induced by the minimization of surface energy through a combined effect of specific geometry and surface tension. Both types of microfluidic devices have their pros and cons. An extensive review that describes both types of microfluidic devices in great detail, and also includes membrane emulsification is by Vladisavljevic and co-workers (2012) [78]. Perspectives towards spontaneous emulsification devices for food production have been covered by Maan et al. (2011) [44], who also gave a comparison between spontaneous and shear-based devices [79].

2.4. Bubble and droplet formation

In the bubble (and droplet) formation process, various forces are involved to create and stabilise the gas-liquid (and liquid-liquid) interface. The three main forces are the surface tension force, viscous force, and inertial force. One of the key contributions to quantitatively describing bubble (and droplet) formation is to define a set of dimensionless numbers that

capture the relative importance of one force over another; thereby defining various formation regimes. When the dimensionless number is around unity, both of its constituting forces influence bubble and droplet formation, whereas a single force dominates at either low or high dimensionless number values. The dimensionless numbers used in this review are defined and summarised in Table 2.1.

Table 2.1. *Summary of dimensionless numbers and their definitions.*

Name and symbol	Definition	
	Equation	**Ratio of forces**
Capillary number, Ca	$\frac{\mu v}{\gamma}$	$\frac{\textit{Viscous stress}}{\textit{Interfacial stress}}$
Weber number, We	$\frac{\rho v^2 L}{\gamma}$	$\frac{\textit{Inertial stress}}{\textit{Interfacial stress}}$
Reynolds number, Re	$\frac{\rho v L}{\mu}$	$\frac{\textit{Inertial stress}}{\textit{Viscous stress}}$
Ohnesorge number, Oh	$\frac{\mu}{\sqrt{\rho \gamma L}}$	$\frac{\textit{Viscous stress}}{\sqrt{\textit{Interfacial stress} \cdot \textit{inertial stress}}}$

Symbols: μ, viscosity (Pa·s); ρ, density (kg/m^3); v, velocity (m/s); γ, interfacial tension (J·m^2); L, characteristic length (m).

Dominating forces are different for the regimes of spontaneous and shear-based formation, and bubbles and droplets. Typically, the spontaneous formation of bubbles and droplets operates at relatively low dispersed and continuous phase velocities, leading to negligible effects of viscous stress (e.g., low Ca) and inertia force (e.g., low We). Surface tension is the dominating force in that case. In shear-based formation, the capillary number of the continuous phase, Ca_c, is increased through the continuous phase flow velocity – which introduces significant viscous stress during emulsification. Often shear-based formation is required for high-throughput emulsion or foam production, e.g., to sustain monodisperse droplet or bubble formation when the dispersed phase velocity is high. If the dispersed phase is a liquid (e.g., emulsification) its high velocity introduces viscous stresses in the neck of the droplet (increased Ca_d; low Re_d). In the case of gas (e.g., foaming), its velocity is even higher than for a liquid under the same applied pressure. This is expected to introduce inertial stresses in the neck of the bubble (increased We_d; high Re_d). To compare various situations, Table 2.1 is instrumental: the influence of a single process parameter can be derived through these dimensionless numbers, for instance, the influence of the continuous phase viscosity.

2.4.1. Shear-based systems

Microfluidic investigations of foam have been carried out mostly with shear-based systems using model components. To translate generated findings to food foams, the bubble size needs to be derived from device geometry and process parameters. Complex scaling relations based on geometrical characteristics have been suggested. In a T-junction (Figure 2.2A):

$R_{pinch} = w + w_{in} - \left(\frac{hw}{h+w} - \varepsilon\right) + \left(2\left(w_{in} - \left(\frac{hw}{h+w} - \varepsilon\right)\right)\left(w - \left(\frac{hw}{h+w} - \varepsilon\right)\right)\right)^{1/2}$. Here, w is the width of the main channel (filled with continuous phase and formed bubbles), w_{in} the width of the side channel (filled with the dispersed phase), h the channel height, and ε the rounded corner of the device. Essentially, this equation uses the radii of the receding interface of the bubble growing at the end of the squeezing process which is based on the blockage of the main channel by the dispersed phase to predict the volumetric size of bubbles (and droplets) [32]. The size of bubbles (and droplets) is proportional to the device geometry dimension. Alternatively, simpler relations have been suggested that revolve around a force balance [16], or around basic observations related to the gas-liquid flow rate ratio, $\frac{Q_{gas}}{Q_{liquid}}$ [74,75]. For example, also in the squeezing regime in a T-junction, based on the pressure drop across the forming bubble, Garstecki et al. (2006) [16] found $L = d\left(\frac{Q_{gas}}{Q_{liquid}}\right) + w$ to predict the length (L) of plug bubbles (and droplets). Here, d is the characteristic width of the neck of the gaseous thread, and w the width of is the main channel. In a flow-focusing device (Figure 2.2B), different scaling relations were found. Within the same formation regime as mentioned above, Fu et al. (2010) [75] scaled L with the gas-to-liquid flow rate ratio and liquid Reynolds number as $\frac{L}{W_c} = 1.40(\frac{Q_{gas}}{Q_{liquid}})^{1.10}\,\mathrm{Re}^{0.46}$ (in which W_c is the microchannel width), to further incorporate the effect of continuous phase viscosity on the size of slug bubbles. In the dripping regime the normalised bubble diameter (d_b) was described as $\frac{d_b}{D} = 1.1(\frac{Q_{gas}}{Q_{liquid}})^{0.4}$, in which D is the dimension of the formation orifice [80].

Each scaling relation is valid only for the channel geometry and flow conditions they were derived for. Translating these relations to systems that contain other components, or even to other devices is difficult (if not impossible) due to changes in the device geometry (or dimension) and wetting conditions, bubble formation mechanisms, etc. For example, the

bubble formation mechanism in T-junction is dependent on both the device geometry and the process conditions, and varies from dripping to transition, and eventually to jetting. For flow-focusing devices, five flow patterns (Figure 2.3) were observed as function of the capillary numbers Ca of both phases, and scaling relations for droplet size have been developed for the dripping and jetting regimes [81]. For more information on scaling relations, we recommend reviews by Tu and colleagues (2015) [82] and Drenckhan et al. (2015) [15]. They summarise different bubble formation mechanisms and related scaling relations, and, in the latter review, hydrodynamic forces that are involved during bubble formation.

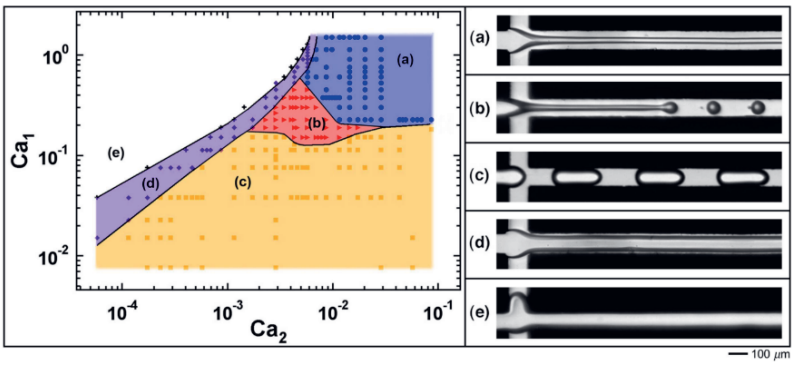

Figure 2.3. *Capillary number-based flow patterns in a flow-focusing microchannel. Ca_1 and Ca_2 are the capillary numbers of the dispersed and continuous phases, respectively. The five flow patterns are: (a) threading; (b) jetting; (c) dripping; (d) tubing; (e) and viscous displacement. Reprinted from Cubaud et al. (2008) [81], with permission of AIP publishing.*

Bubble and droplet formation in microfluidic devices have also been numerically modelled, to complement the experimental scaling laws. An example is the work by Dang et al. (2015) [83] using a Volume of Fluid (VOF) method and, secondly, a comparative method of coupled Level Set and VOF (CLSVOF). Numerical simulations yield valuable insights into the effects of changing device geometry and fluid properties, and can thus be used for engineering design studies to optimise foaming and emulsification processes. Accurate droplet size predictions are obtained particularly in the case of geometry-dominated droplet formation regimes. A more thorough understanding of the dynamic nature of the foaming and emulsification processes needs to be considered, which includes aspects such as wettability of the channel walls, moving contact lines, and dynamic surface tension due to adsorption of emulsifiers. Incorporating these aspects introduces new challenges and a separation of length scales that increase the computational complexity and cost. A range of numerical simulations and the associated challenges are reviewed in-depth by Wörner (2012) [84].

2.4.2. Spontaneous systems

Microchannel (MC) systems

Spontaneous droplet formation is not significantly influenced by the continuous phase flow, in contrast to the shear-based droplet formation discussed above [85]. In a grooved MC system (Figure 2.2D), Yasuno et al. (2004) [77] obtained foams with bubble size ranging from 33.6 to 51.1 μm and a coefficient of variation (CV) below 10%, and found that the bubble size was influenced by the continuous phase viscosity, yet independent of surface tension. Stoffel et al. (2012) [41] reported a two-stage bubble formation mechanism: the pressurized gas flows through a channel onto a shallow wide terrace, and then overflows into a deep channel (in which the continuous phase flow is present to carry away the generated bubbles). The radius of the curvature on the terrace gradually decreases, and when the critical radius is achieved a rapid pinch-off follows and a bubble is formed. The bubble size remains constant with increasing gas pressure in the so-called monodisperse regime, while as soon as the gas pressure exceeds a certain threshold (Figure 2.4), the size distribution becomes polydisperse. This transition to polydispersity has also extensively been reported for emulsions, and has been defined by a critical capillary number (of the dispersed phase), which indicates that the viscous force becomes dominant over surface tension force [86].

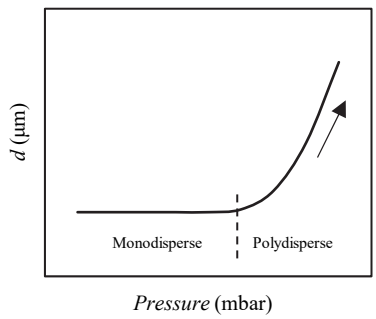

Figure 2.4. *Schematic diagram showing the effect of dispersed phase pressure on the bubble (droplet) size distribution.*

The viscosity ratio (ξ) between the dispersed and continuous phases is another important characteristic of MC systems. It has been extensively shown for emulsions that above a critical value of the viscosity ratio (ξ_{crit}), the droplet size (within the stable pressure range) is constant. At lower viscosity ratios, the droplet size distribution is still monodisperse, but the droplet size is larger than that at high viscosity ratio (Figure 2.5), which is linked to the slower inflow of the continuous phase onto the terrace due to higher viscous dissipation (see also

Figure 2.6) [45]. When the viscosity ratio is below a minimal value (ξ_{min}), the dispersed phase flows continuously from the terrace and droplet formation is impossible [40].

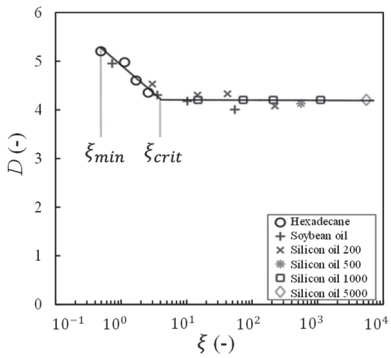

Figure 2.5. *The plot of the dimensionless droplet diameter (D) as function of the viscosity ratio (ξ) in terrace-based microchannels forming an oil-in-water emulsion. The viscosity of both phases is varied. Reprinted from van Dijke et al. (2010)* [40].

Given the much lower viscosity of air compared to oil (factor of 100), it was expected that bubble formation would not be possible with microchannel devices (based on Figure 2.5). However, monodisperse bubbles could be formed in a MC device [77], as well as in the EDGE devices that are discussed later [45]. This is likely due to the combination of low viscosity and compressibility of the gas phase (which is normally air), which induces a different formation behaviour compared with emulsification in the same system. On the other hand, possibly again due to its low viscosity, the volume of air that could be dispersed was found to be a lot higher than the volume of liquid for emulsions; the bubbles being significantly larger than the droplets, typically by a factor of 3-4.

For the underlying formation mechanism, spontaneous formation as a result of minimization of surface energy (as found for emulsions) is also expected to be the case for foams. Rayner et al. (2004) [87] have studied this mechanism for emulsion formation using a computational method (*Surface Evolver*), but to the best of our knowledge simulations for foam formation in microchannels have not been carried out yet. Also, the predictive scaling of bubble size and modelling attempts of the foaming systems still need to be performed, in contrast to the emulsification system.

Various geometries of microchannels have been developed, including straight-through and terrace-based types [78]. Geometry was identified to be a crucial factor determining droplet formation, in terms of both droplet size and operational stability. In the terrace-based MC

system, for example, on relatively short or wide terraces, droplets (or bubbles) are formed instantaneously when the disk-like bulb reaches the edge of the terrace. In contrast, on a relatively long or narrow terrace, the bulbs continue growing when first moving into the deep channel. As a result, the latter formation process is less stable and the final droplet (bubble) size is larger [41,88]. An overview of spontaneous droplet formation devices is discussed in a review by Vladisavljević et al. (2012) [78]. In addition, Computational Fluid Dynamic (CFD) simulations were also used to define constraints for these devices [86,89]. The simulation demonstrated the existence of a pressure gradient in the continuous phase on the terrace of the microchannel (Figure 2.6A). When this leads to reduced inflow of the continuous phase, larger albeit monodisperse droplets are formed. It was reported that the droplet diameter was typically 2.5-4 fold the height of the terrace in a grooved MC system [86]. Importantly, the aspect ratio between the long and short axis of the channel cross-section should be sufficiently large to support successful droplet formation in a straight-through MC system. Channels with near-circular or square cross-section instead have a continuous outflow of the dispersed phase. Numerical simulations have shown that the critical aspect ratio is 3-3.5 for channels with elliptical cross-section [89] and 2.6 for rectangular cross-section [90].

EDGE

The main difference of EDGE (Figure 2.2E) compared with microchannel devices is the much wider droplet formation plateau that connects the dispersed and continuous phases, and is capable of forming multiple droplets simultaneously. The plateaus are very shallow compared to the entry channel for the dispersed phase (Figure 2.6B). This means that the highest hydrodynamic resistance is in the droplet formation unit itself, which ensures a steady plateau filling and enhances pressure stability compared to microchannel designs.

Numerical simulations of EDGE show that steep pressure gradients occur around the droplet formation locations (Figure 2.6B), which can further explain the robustness of this system. As a result, the droplet size is constant over a relatively wide pressure range, and is 5.5-6.5 times the height of the plateau [92]. For foams, the first result shows that bubbles are at least 17 times the height of the EDGE plateau [19], or 3-4 times larger than droplets. It is important to realize that numerical simulations are very useful to predict trends, but do not cover all aspects that occur in practice. So far, they have been used to elucidate the effect of varying contact angles (which is a result of emulsifiers adsorption to the walls of the microfluidic devices) on the droplet size [93], or to predict the influence of different surface tensions [88].

However, the dynamic adsorption and redistribution behaviour of emulsifiers at the interface (leading to a temporally changing surface tension) is still challenging to incorporate in the simulations due to the small length and time scales involved.

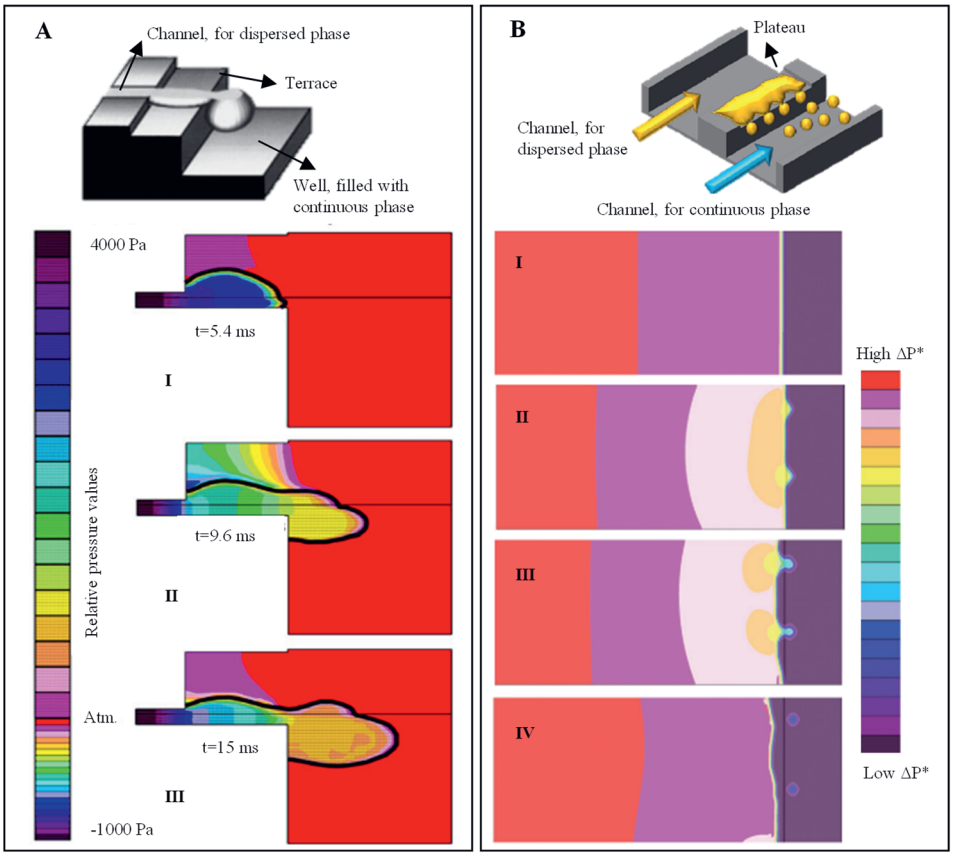

Figure 2.6. *In A, top: a forming droplet in the terrace-based MC system, adapted from Sugiura et al. (2002)* [86] *with permission from the American Chemical Society; bottom: half of the geometry of the MC system modelled to investigate the pressure gradient around the forming droplet at different time stages (I, II, and III) during emulsification, adapted from van Dijke et al. (2010)* [40]*. In B, top: droplet formation in an EDGE system, adapted from Sahin et al. (2016)* [91]*; bottom: droplet formation on the plateau modelled from continuous phase filling the plateau, till the droplets are detached (I through IV), used to investigate the pressure gradient around forming droplets (light blue); Adapted from van Dijke et al. (2010)* [92] *with permission from The Royal Society of Chemistry. In both systems, the pressure gradient near the droplet formation site becomes steeper with growing droplet size.*

2.4.3. Up-scaling microfluidics

To make the production of food foams using microfluidics feasible, its productivity would need to be enhanced. The typical route towards up-scaling is to operate several formation units in parallel, as has been demonstrated mostly for emulsions [18,21,94], and limitedly for foams [95]. However, the fabrication of such devices is currently far from trivial. An alternative

approach is to use membranes that can be produced readily at lower costs, yet are less well defined in terms of pore geometries. Here we only mention membranes as an option to be complete and limit ourselves to upscaling of microfluidic devices.

The main issue that needs to be addressed for parallelisation is the cross-talk between individual units. Cross-talk is known to significantly influence droplet detachment, in particular in parallelised shear-based devices. It is expected to be of even greater influence on bubble detachment, due to added complexity of compressibility and low viscosity of the gas phase [35,95,96] in comparison with emulsions. Shear conditions should be identical for all parallelised shear-based formation units to obtain monodisperse bubbles (or droplets). Thus, the units should be organised such that they do not shield others from the shear flow needed to detach bubbles, although this is difficult to realise.

The shear flow has smaller influence in spontaneous devices, since the bubble size is determined predominantly by the dispersed phase, and remains constant within a certain pressure range (typically hundreds of mbar). Still, for spontaneous droplet formation in microchannels, it has been reported that polydispersed droplets are formed as a result of relatively small pressure fluctuations [97]. The EDGE system is much less pressure sensitive and shows a wider pressure range in which monodispersed droplets are produced [45,85]. When introducing partitions on the main plateau (the so-called *partitioned*-EDGE, see Figure 2.2F), this leads to well-defined droplet formation locations while further increasing the pressure stability, and thus to a hundred fold increase in emulsion productivity [42]. We expect this to be a promising route towards large-scale production of monodisperse emulsions (foams).

Efforts are continually put into these spontaneous devices for in-depth study, for instance, a similar geometry which takes the advantages of both EDGE and MC systems (and buoyancy effects) was recently used by Opalski et al. (2019) [98] to study geometry effect on the throughput of monodisperse emulsion. The throughput of monodisperse emulsion in this geometry can be enhanced, and at the same time, a smaller increase in the volume of droplets was observed compared to a traditional MC system.

As mentioned previously, CFD can be used to simulate the droplet formation process at a single formation unit. Yet, there are much fewer simulations of multiple formation units that are working simultaneously. These larger-scale simulations would be an essential step to better understand how the parallelised droplet formation units work, including the relative

influencing aspects. For example, Hoang et al. (2014) [99] developed a bubble-splitting distributor that contains 8 parallelised channels (including 7 splitting distributors). Both their theoretical and experimental results indicate that the asymmetric flow due to fabrication inaccuracies and non-breaking bubbles leads to polydispersity, even if a bypass channel is used to better control the pressure.

2.4.4. Toward food grade emulsifiers

In most microfluidic investigations low molecular weight surfactants such as sodium dodecyl sulfate (SDS) [45,51,77] were used as surface active components; only limited food-grade emulsifiers such as Tween 20 [16,35] have been reported. Maybe even more importantly, in many studies the dynamic effects that these surface active components can create, such as lowering of interfacial tension at the time scales of droplets (bubbles) formation are often overlooked.

In food products, proteins together with other components (e.g., polysaccharides) are the stabilisers of choice and they have an even more complex way of stabilising interfaces. They have scarcely been used in combination with microfluidic devices. For example, Guell et al. (2017) [68] used a Y-junction to study the apparent interfacial tension of BSA and whey protein-stabilised emulsions, Muijlwijk et al. (2017) [27] studied the stability of protein-stabilised emulsions, and Dijke et al (2010) [45] used proteins for emulsification and foaming with EDGE devices.

The limited use of proteins is most probably because in fundamental sciences within which microfluidics have been extensively tested, model systems with well-defined characteristics are preferred. Proteins have high complexity and are known to induce wettability changes [91] which is an undesired side-effect. To prevent the binding of proteins to the microchannel walls, and thus wettability changes in time, the walls need some form of modification, which may be as simple as a pre-adsorbed protein layer. Furthermore, the knowledge available for low molecular weight surfactants (e.g., the adsorption dynamics to the interface) needs to be translated to protein adsorptions (see analytical tools section). As mentioned before, proteins show much more complex adsorption behaviour than well-studied low molecular weight surfactants, but luckily also for this microfluidic tools are available and have been used as described next.

2.5. Analytical tools

2.5.1. Critical parameters for foam formation and stability

Common emulsification methods such as stirred tanks, colloid mills, and high-pressure homogenizers, operate under a wide range of flow regimes. Three common flow regimes are the laminar viscous (LV) at low flow-Reynolds number, turbulent viscous (TV) and turbulent inertial (TI) [100]. Table 2.2 shows that in *all* flow regimes the resulting droplet size depends crucially on interfacial tension. Yet its actual value during droplet formation is very hard to determine, if at all. Only very recently, microfluidic platforms have been designed to measure dynamic interfacial tension for liquid-liquid systems under laminar flow conditions. The (sub)millisecond time scales that can be accessed in this way are not only relevant for emulsification within these microfluidic devices but also for large-scale operations, particularly those operating in the LV flow regime. Besides, a locally large velocity gradient and the convection mass transfer mechanism were also indicated in microchannels [101]. Turbulent flow can be induced in microchannels, for example by adjusting the roughness of the channel wall [102]. Laminar flow transfers to turbulent flow at a Reynolds number of approximately 2000, and it occurs earlier with a higher level of roughness. Foaming experiments at high Re may help to produce more insights into large-scale operations. We discuss the dynamic measurement of surface tension below.

For the production of stable foams, two time scales are relevant: one relates to the formation of bubbles during which they should be protected against coalescence, and the other to the life-time stability of the foam relating to gas transfer between bubbles. These time scales may be studied using microfluidic devices that were originally developed for emulsions. For example, a coalescence chamber has been suggested for early coalescence monitoring (see the section below), and a micro centrifuge can be used for the evaluation of stability under enhanced gravity. Although the latter does not completely represent the situation of ageing products under normal gravity, the experiments yield useful information about long-term stability within manageable experimental time scales.

Table 2.2. *Summary of equations for estimating expected mean droplet diameter, stresses exerted on droplets, and relative time scales in emulsification process under laminar and turbulent flow conditions* [100].

Flow Regime	Laminar-Viscous shear or elongational (LV)	Turbulent-Viscous shear forces (TV)	Turbulent-Inertial forces (TI)
Re – flow	< 1000	> approx. 2000	> approx. 2000
Re – droplet	< 1	< 1	> 1*
Mean Diameter ($d \approx$) #	$\frac{2\gamma \mathrm{We}_{cr}}{\eta_c G}$	$\frac{\gamma}{\sqrt{\varepsilon \eta_c}}$	$\left(\frac{\gamma^3}{\varepsilon^2 \rho_c}\right)^{1/5}$
External stress acting on droplets (σ)	$\eta_c G$	$\sqrt{\varepsilon \eta_c}$	$\sqrt[3]{\varepsilon^2 d^2 \rho_c}$
Droplet deformation time scale (τ_{DEF})	$\frac{\eta_d}{\eta_c G}$	$\frac{\eta_d}{\sqrt{\varepsilon\, \eta_c}}$	$\frac{\eta_d}{\sqrt[3]{\varepsilon^2 d^2 \rho_c}}$
Duration of disruptive stresses (τ_{DIS})	$\frac{1}{G}$	$\sqrt{\frac{\eta_c}{\varepsilon}}$	$\frac{1}{2}\left(\frac{\gamma^2 \rho_c}{\varepsilon^3}\right)^{1/5}$
Surfactant adsorption time scale (τ_{ADS})	$\frac{6\pi\Gamma}{d m_c G}$	$\frac{6\pi\Gamma}{d m_c}\sqrt{\frac{\eta_c}{\varepsilon}}$	$\frac{\Gamma}{m_c}\sqrt[3]{\frac{\rho_c}{d\,\varepsilon}}$
Droplet collision time scale (τ_{COL})	$\frac{\pi}{8G\phi}$	—	$\frac{1}{15\,\phi}\sqrt[3]{\frac{d^2 \rho_c}{\varepsilon}}$

Source: the data was adapted from Walstra, 1993 [103]*; Walstra and Smulders, 1998* [104]*; McClements, 2005* [5].

Symbols: Re, Reynolds number, either on the scale of the flow or the droplet [-]; d, droplet diameter (m); γ, interfacial tension ($J \cdot m^2$); We, Weber number [-]; η_c, viscosity ($Pa \cdot s$); G, velocity gradient (1/s); ε, power density ($J/(s \cdot m^3)$); ρ, density (kg/m^3); Γ, surface excess of surfactant (mol/m^2); m_c, surfactant concentration in the continuous phase (mol/m^3); Φ, volume fraction of the dispersed phase (m^3/m^3); σ, stress (Pa); τ, characteristic time (s); Subscripts: cr, critical value for droplet break-up; c, continuous phase; d, dispersed phase;

** For $d > \eta c^2/\gamma\rho$;*

 # Only if $\eta_d \gg \eta_c$.

2.5.2. Interfacial tension measurement

In the scaling relations (see Table 2.2, Rayner & Dejmek, 2015) [100] used to predict droplet (and bubble) sizes, the interfacial tension γ and the related surface coverage Γ of emulsifiers are important parameters. Both parameters are only scarcely reported. Moreover, typically the equilibrium interfacial tension of either the pure interface or that of an interface without emulsifiers is used, whereas in reality the interface will be partly covered and the actual interfacial tension is unknown since it changes dynamically. The typical time scales that are involved in bubble and droplet formation are in the (sub)millisecond range, and thus outside the reach of conventional measuring methods such as the droplet volume tensiometer.

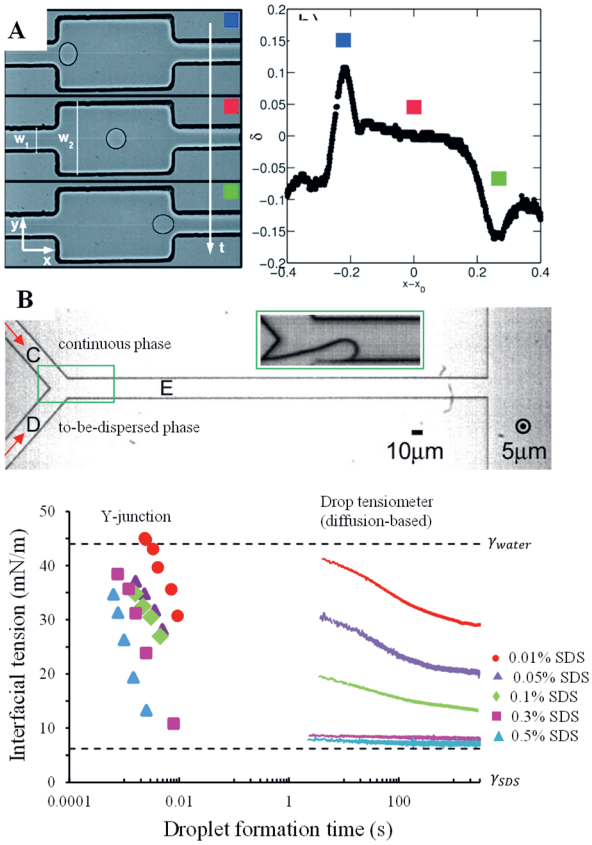

Figure 2.7. *A. Left: diagram of the expansion cell; right: the typical deformation (δ) of a droplet flowing in the expansion cell, reproduced from Brosseau et al. (2014)* [23] *with permission from The Royal Society of Chemistry. From the top (left) to the bottom (right), three important deformation points were indicated with different colour squares: the droplet just enters the expansion, the elongated droplet relaxes back to a sphere, and it enters the next constriction. B. Top: layout of a microfluidic Y-junction with an angle of 97° between channels C and D* [51]*, adapted with permission from the American Chemical Society; bottom: the dynamic interfacial tension for hexadecane-SDS solution of different concentrations, derived by using a Y-junction as function of droplet formation time. As a comparison, the interfacial tension obtained with a droplet volume tensiometer is given on the right. Reprinted from Muijlwijk et al. (2016)* [53]*, with permission from Elsevier.*

In microfluidic devices, droplet formation can take as short as 1 ms (for bubbles this is even faster), so they provide a platform to study emulsification, and expectedly also foaming, at the length and time scales that are relevant for current large-scale processes. Microfluidic tools have already been used for the characterisation of liquid-liquid emulsification systems. For example, Brosseau et al. (2014) [23] used a microfluidic flow-focusing device to derive the dynamic interfacial tension from the deformation of a droplet before and after passing through a geometrical constriction (the expansion cell shown in Figure 2.7A). Wang et al. (2009) [37] determined the dynamic interfacial tension during emulsification using a

microfluidic T-shaped device, and Steegmans et al. (2009) [51] using a Y-junction device (Figure 2.7B). Güell et al. (2017) [68] further extended to using proteins, and compared their findings with premix membrane emulsification based on a modified Ohnesorge number* (Oh*). A lot of information was generated in our group using the Y-junction with which, for instance, Muijlwijk et al. (2018) [105] carried out a comparative study on the dynamic adsorption behaviour of different types of emulsifiers including food-grade ones.

Figure 2.7B shows an illustrative example of dynamic interfacial tension values determined with the Y-junction for a hexadecane-SDS solution system. The top horizontal dashed line denotes the interfacial tension between hexadecane and pure water, and the bottom one indicates the equilibrium interfacial tension in the presence of SDS. On the left, curves are shown for very fast droplet formation in the microfluidic Y-junction, with interfacial tensions derived from a calibration curve. In doing this, we were able to distinguish the effects of varying emulsifier concentrations at specific droplet formation times. On the right, interfacial tension curves are shown generated with a droplet volume tensiometer that operates under diffusive conditions. It is immediately clear that the Y-junction can operate at much shorter time scales, which is due to enhanced mass transfer conditions. This is relevant for both microfluidics and other large-scale emulsification devices operating in the LV flow regime, while the drop volume tensiometer provides no access to these short time scales. To translate the technique to foams, it should be noted that bubble formation is even faster than droplet formation. Consequently, high-speed cameras are needed to record the fast bubble expansion.

2.5.3. Coalescence behaviour

In less dense, polydisperse foams, both the disproportionation and the drainage processes contribute to the thinning and rupture of films between neighbouring bubbles, and their subsequent coalescence (Figure 2.1). Using microfluidics, specifically the film dynamics and bubble coalescence can be studied in a so-called coalescence cell. Here, monodisperse bubbles are brought in close proximity to capture their initial coalescence stability. For gas-liquid systems, a microfluidic collision T-junction (Figure 2.8A) was designed by Yang et al. (2012) [106] to investigate the 1-on-1 coalescence stability of bubbles under confinement. Controllable coalescence in this case was realised for a range of continuous phase viscosities and flow rates of both phases. Fu et al. (2015) [107] employed a microfluidic expansion section (Figure 2.8B) to quantitatively study the coalescence mechanism of bubbles in non-Newtonian fluids. Depending on the flow rate of both phases, two different coalescence

mechanisms were found for the bubble trains: mechanism I, coalescence of two different bubbles; and mechanism II, recoalescence of two bubbles that broke apart from the same 'mother' bubble. For liquid-liquid systems, droplet fusion also has been investigated using microfluidic devices. Mazutis and colleagues [108,109] developed a device (Figure 2.8C) for chemical reactions and biological assays, in which droplets are used as micro-reactors, and the start and termination of a reaction can be precisely modulated by controlling the fusion of the droplets.

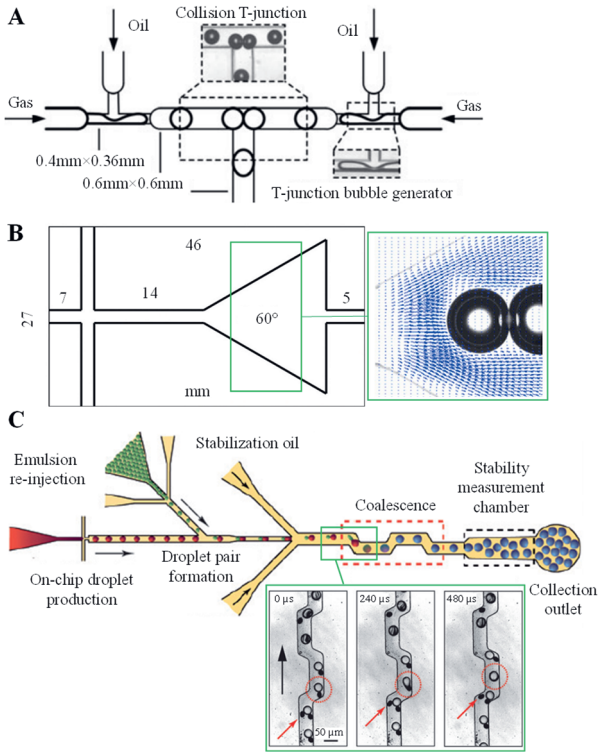

Figure 2.8. *A. Microfluidic system for 1-on-1 bubble interaction, reprinted from Yang et al. (2009)* [106]*. B. Microfluidic expansion device and the velocity field (obtained by micro Particle Image Velocimetry technique, micro-PIV) around the aligned bubbles, reprinted from Fu et al. (2015)* [107] *with permission from Elsevier. C. Droplet fusion device, consisting of a droplet generation junction, a coalescence channel and a detection unit, for the assessment of coalescence stability; reproduced from Mazutis et al. (2012)* [108] *with permission from The Royal Society of Chemistry.*

Away from rather isolated coalescence events (droplet pairs), multiple coalescence events were studied using a microfluidic coalescence chamber that was developed by Krebs et al. (2012) [110]. Basically, droplets are generated at a T-junction and allowed to interact in a wider channel. Using this device, for instance, the coalescence of SDS-stabilised droplets was monitored, the effects of flow velocity, oil viscosity (the dispersed phase), and oil volume

fraction on coalescence stability were investigated, and also enhanced interfacial mobility (Marangoni effect) [26] could be detailed.

Only very recently, Muijlwijk et al. (2017) [27] used this microfluidic coalescence chamber (Figure 2.9A) to study the stability of protein-stabilised foams and emulsions, and took the technique one step closer to application for food products. The device consists of a T-junction where the two phases meet and either bubbles (Figure 2.9B) or droplets (Figure 2.9C) are made, an adsorption channel (the meandering channel, in which emulsifiers can further adsorb to the interface), and a coalescence chamber. In this way, the time scales for adsorption and coalescence could be decoupled. Coalescence frequency was derived from analysing (image analysis) the droplet (bubble) size at the beginning and the end of the coalescence chamber (as illustrated in Figure 2.9A).

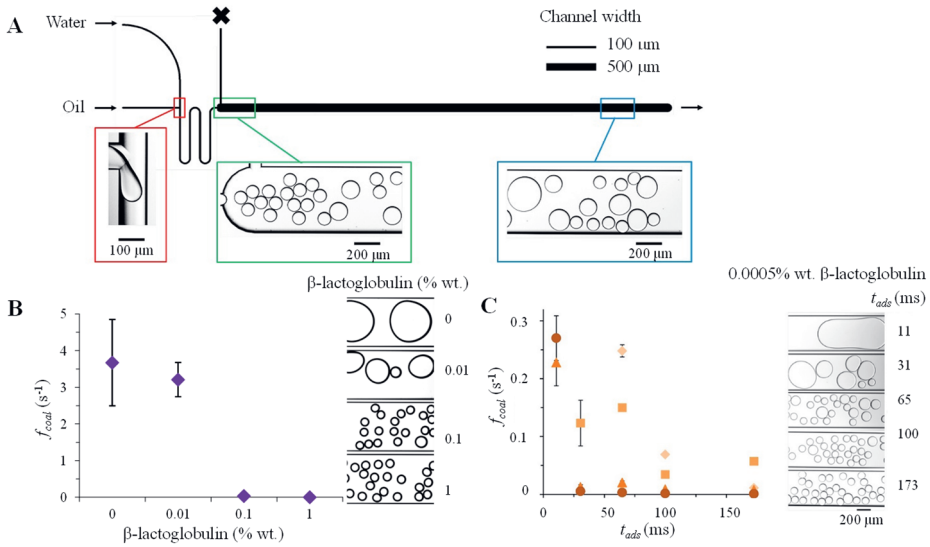

Figure 2.9. *A. Coalescence chamber, including a T-junction (red rectangle), a meandering adsorption channel, and a coalescence channel; Reprinted from Muijlwijk et al. (2017) [27], with permission from Elsevier. B. The coalescence frequency of bubbles as function of protein concentration, at 100 ms adsorption time; Reproduced from Muijlwijk (2017) [111]. C. The coalescence frequency of droplets as function of adsorption time (achieved by varying the length of the meandering channel) and % wt. β-lactoglobulin (0.005, 0.001, 0.05, 0.01, darker symbols correspond to higher concentrations); Reprinted from Muijlwijk et al. (2017) [27], with permission from Elsevier.*

Although considerably less data is available for bubbles, the experiments shown in the PhD thesis of Muijlwijk (2017) [111] are proof of the principle that the coalescence chamber is also suited to monitor foams. Bubbles were stabilised with β-lactoglobulin solutions of different concentrations, and a clear dependency of coalescence frequency on concentration was found

(Figure 2.9B). A minimum β-lactoglobulin concentration of 0.1% wt. was needed to keep the bubbles stable which is approximately 20 times the amount needed for emulsions studied in the same device (which is discussed later). When keeping in mind that the bubble formation process is a lot faster than droplet formation, it is not that surprising that the bubbles had comparatively lower protein coverage (see also Figure 2.7 for the effect of expansion rate), and thus lower stability than the much slower forming droplets.

Within investigations on emulsions, the layout of the coalescence chamber was varied, using different lengths of the meandering channel (Figure 2.9A), which allows for variation of adsorption time for emulsifiers prior to entering the coalescence chamber where the droplets interact. The coalescence frequency was a strong function of the β-lactoglobulin concentration, and besides, there was a clear effect of the adsorption time on it (Figure 2.9C). As expected, with the same protein concentration the longer the adsorption time the more stable the droplets were. In another investigation, even the oxidative state of the proteins was evaluated, and as was found in regular emulsions large differences in coalescence stability were noted [112].

2.5.4. Enhanced stability testing

Overall product stability and long-term effects are crucial for the shelf life of a food foam, but cannot be accessed by the coalescence chamber that operates at very short time scales after bubble formation. For polydisperse foams, the diffusion of gas from small to large bubbles (disproportionation) leads to coarsening [113]. This highlights the need for creating monodisperse foams. Although Xu et al. (2006) [71] reported that different types of emulsifiers can influence the interfacial viscoelasticity and thus potentially limit gas diffusion through e.g., protein-stabilised interfaces [77,114], it is not expected that this is a major influence due to the open nature of the protein layer.

A deeper understanding of the ageing mechanisms and the corresponding critical conditions are relevant for effective control over bubble destabilisation, and it is expected that microfluidics can contribute to this. The so-called micro centrifuge has been used for emulsion stability testing at high g-force (Figure 2.10) [115]. An emulsion is first created in a separate microfluidic device and transferred into a small container-like microfluidic chip that is mounted onto a rotating device. The chip is spun in front of a carefully synchronized high-speed camera. From the obtained images, the size of the droplets, their deformation, and also

coalescence behaviour could be derived. Under enhanced g-force conditions the (highly stable) droplets do deform greatly to a honeycomb structure, yet they do not coalesce (Figure 2.10). For less stable emulsions, extensive coalescence was observed that could even be related to the critical disjoining pressure [116].

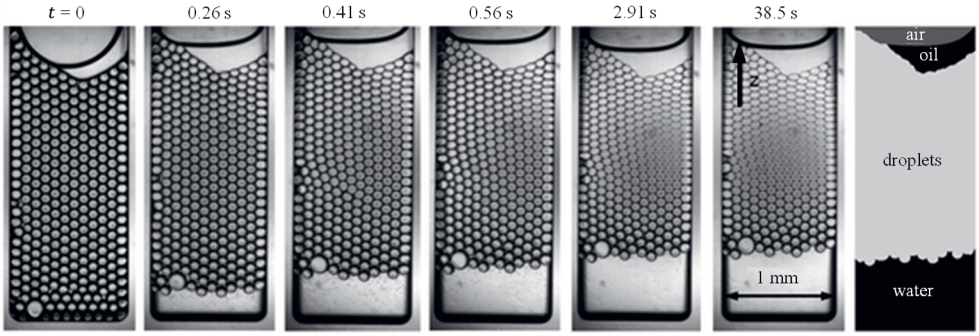

Figure 2.10. *Images obtained with the micro centrifuge in which a small container filled with droplets is spun around at high g-force. The emulsion used in this experiment is stabilised by 10 mM SDS, and droplets have a diameter of 97 µm. Through image analysis, the amount of separated oil, aqueous phase and droplets, as well as droplet size were determined (marked in the last image). Reproduced from Krebs et al. (2013) [115] with permission from The Royal Society of Chemistry.*

This analytical tools section indicates that many behaviours related to foam formation and stability can be investigated with microfluidic devices at relevant time scales. Although more research has been published for emulsions than foams, we believe that the developed devices can be easily extended to the study of bubbles. We foresee that this microfluidic toolbox could even be expected to become a good starting point for designing foam formulation using a bottom-up approach.

2.6. Toward practical application

Microstructures in novel foods (1-200 µm elements) [117] are in the range that can be made with microfluidic devices under very well-controlled conditions. Foams are in the upper part of this range (20 to 200 µm) [1], for instance, the air bubbles in ice cream normally are around 20-50 µm [118]. It is known that small bubbles with controlled size distribution can modify the texture and appearance of food products by reducing the influence of buoyancy and vertical stratification, leading to a creamier perception [119]. Through up-scaling of microfluidic devices, this can become a reality.

Disproportionation (which is caused by the polydispersity of bubbles) is the most important destabilisation mechanism in food foams, because of the challenge to control the size

distribution of bubbles produced with conventional foaming techniques. Accordingly, solidification is often used to improve the stability of aerated food products that in principle can be made in a rather monodisperse fashion by using microfluidic devices. The solidification method is, however, not relevant for all food foams, for instance, cappuccino foam [120]. Thus using microfluidic devices for monodisperse food foam production is highly promising. The monodisperse foams which are less prone to disproportionation can also help to improve the sensory properties of aerated products, for example, beer foams.

The use of microfluidics in food foam and emulsion preparation (and investigation) may also lead to better use of the starting materials (e.g., emulsifiers). For example, currently, an excess amount of emulsifiers is used in food production. Berton et al. (2011) [121] mentioned that during high-pressure homogenisation an excess of at least 30% of β-lactoglobulin was needed (compared to monolayer coverage) to protect the emulsions against coalescence within 46-72 hours. In the microfluidic system, this amount can be reduced through controlled production, leading to a higher fraction of adsorbed proteins. For example, Muijlwijk et al., (2017) [27] indicated that only 0.005% wt. β-lactoglobulin (which is close to the theoretical monolayer surface coverage) was sufficient for the emulsions to be stable in their experiment.

2.7. Conclusions - What's the future for microfluidics and food foam?

Following the demonstrated value of microfluidics in the formation of droplets (emulsions) and, to a limited extent, bubbles (foams), we foresee that this technique can have major contributions to the study and production of food foams. Here, we formulate four main potential applications:

1. **Dynamic adsorption of proteins and novel stabilisers to the air-water interface.** Since food foams are often stabilised by a mix of stabilisers, adsorption should be studied from the (sub)millisecond bubble formation time to the long-term redistribution of components within the foam. In particular, the short time scale requires microfluidic tools similar to those used to measure the interfacial tension of emulsion droplets – albeit at even shorter time scales. With current high-speed recording techniques these time scales can be easily accessed. This will allow us to unravel the adsorption mechanism of emulsifiers (proteins), and stabilisation mechanisms of novel stabilisers such as food-grade rigid or soft particles, and aid in the selection of suitable stabilisers for food foams.

2. **Microfluidic tools to study bubble disproportionation.** Disproportionation is the fastest destabilisation mechanism of foams – in contrast to emulsions where the dispersed phase has low solubility in the continuous phase. The development of a microfluidic tool to study disproportionation can yield insights into the disproportionation dynamics of well-defined, bi-disperse foams. In addition, it could be used to select stabilisers that limit gas dissolution, and formulate a maximum degree of polydispersity that still allows for homogeneous food foam for the duration of the product's shelf life.

3. **Turbulent flow regimes of foam formation in a microfluidic device.** It would be interesting to achieve turbulent conditions during foam formation in a microfluidic device (for example using wall roughness or agitating the flow). This would yield insights into the different formation and stabilisation mechanisms under the variety of flow conditions found in commercial foaming approaches.

4. **Upscaling of microfluidic platforms for high-throughput food foam production.** The key benefit of producing food foams in an up-scaled microfluidic platform is the bubble monodispersity that prevents disproportionation. At the same time, to assure this monodispersity, the bubble formation mechanism, stabilisation, and cross-talk between pores should be well-understood and tightly controlled. An interesting difference compared with emulsification is that bubble formation rates are extremely high, and should be balanced with timely adsorption of emulsifiers, or with another stabilising effect (e.g., using particles) to prevent early coalescence. Here, continuous phase flow and the gas-liquid buoyancy difference may aid in separating bubbles during their initial stabilisation.

To conclude, microfluidics can play a two-fold role in both understanding bubble formation and stabilisation (points 1 – 3), as well as the large-scale production of monodisperse foams (point 4). This bottom-up approach provides a promising route towards novel food foams with superior properties, such as well-defined bubble size, structure homogeneity, added functional ingredients, and an enhanced shelf life.

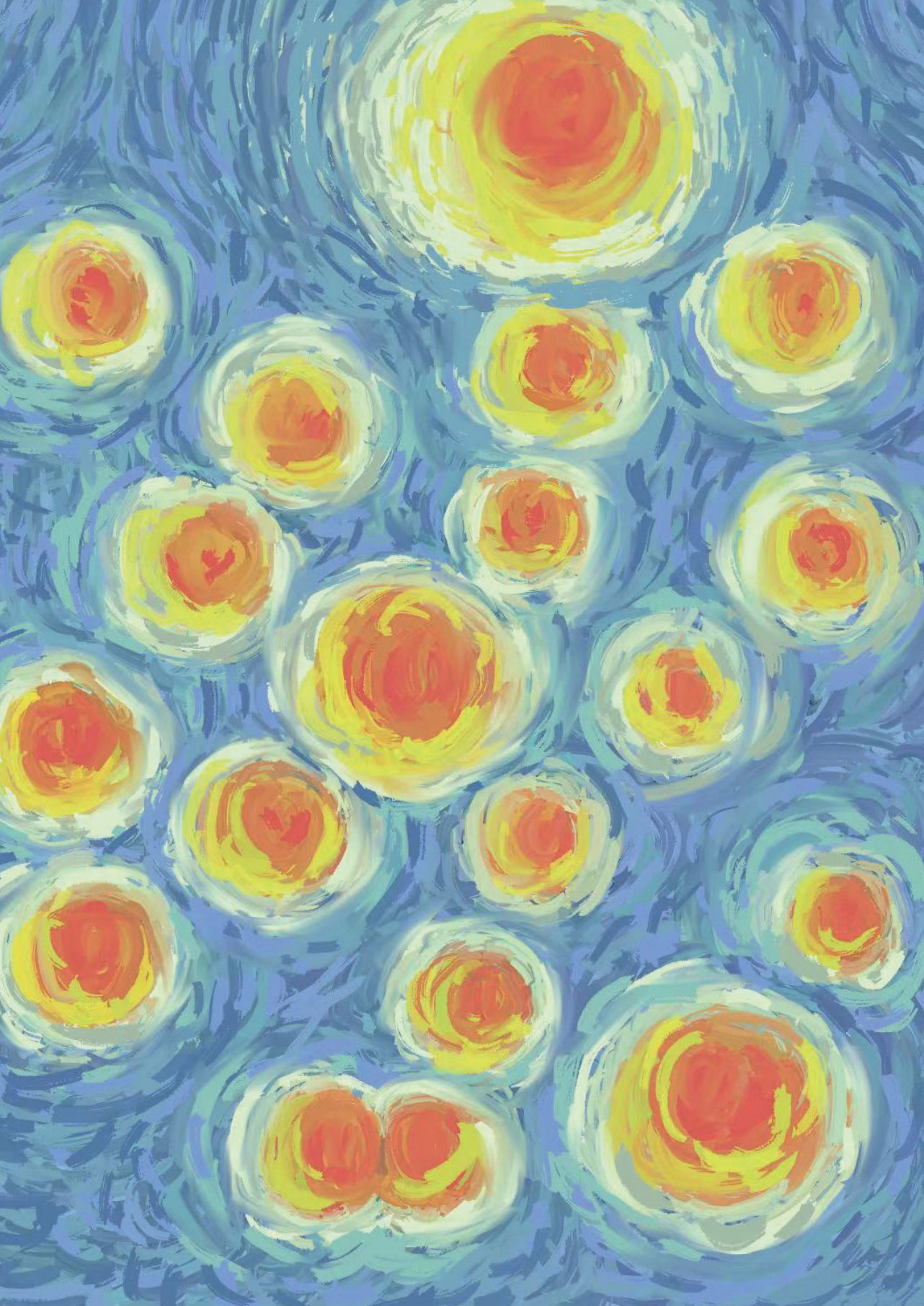

CHAPTER ‖ 3

Effects of dynamic adsorption on bubble formation and coalescence in partitioned-EDGE devices

This chapter has been published as Deng, B., Schroën, K. & De Ruiter, J., Effects of dynamic adsorption on bubble formation and coalescence in partitioned-EDGE devices. *Journal of Colloid and Interface Science*, **2021**, 602, 316-324.

3.1 Abstract

Hypothesis: Dynamic adsorption effects can play a crucial role in bubble formation and stabilisation. We hypothesize that microfluidic tools provide direct insights into these effects, and that the final bubble size depends on the intersection of time scales for bubble formation *versus* adsorption of proteins.

Experiments: We use a microfluidic device to study Laplace pressure-driven formation of bubbles that are stabilised by whey proteins. Bubble behaviour is studied as function of applied pressure imposed across the pores (P_d^*), and thus the bubble formation time (τ, ranging from µs to s), using high-speed recordings, quasi-static pressure arguments and a semi-empirical coalescence model.

Findings: We observe two distinct bubble formation regimes, delimited by the applied pressure required to initiate bubble formation in pure water, $P_d^* = 1400$ mbar. When $P_d^* <$ 1400 mbar, protein adsorption is a requisite to lower the surface tension and initialise bubble formation. Individual bubbles (fixed $d_0 \sim 25$ µm) are formed slowly with $\tau \gg 1$ ms. When P_d^* exceeds 1400 mbar, bubbles (fixed $d_0 \sim 16$ µm) experience no adsorption lag and thus are formed at steeply increasing frequency, with $\tau < 1$ ms. Interaction between these bubbles causes finite coalescence to a diameter d_{coal} that increases for lower τ. A minimum of 0.4 ms is needed to immediately stabilise individual bubbles. Our study provides a promising microfluidic tool to study bubble formation and coalescence dynamics simultaneously.

Graphical abstract

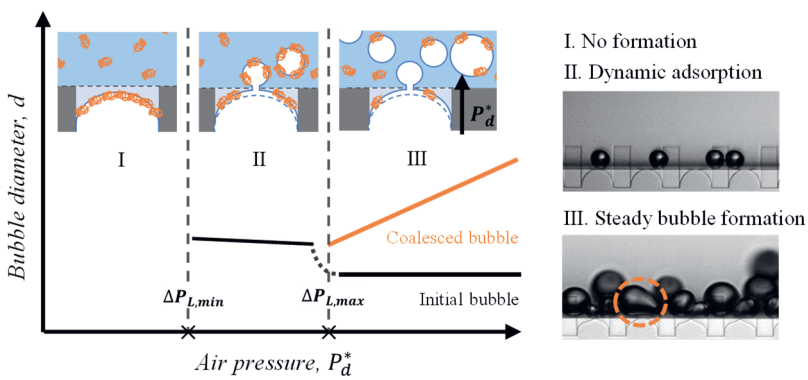

3.2 Introduction

Microfluidic devices are used to generate individual bubbles and droplets at microscale pores, which yields high monodispersity and tight control over volume and production frequency. Broadly, microfluidic geometries belong to the category of either shear-based or spontaneous devices. In shear-based devices such as flow-focusing [33–35,122] and T-junction [16,29,70,71], a bubble or droplet is sheared off from the -supplied thread (gas or liquid) by a contacting flow. This type of devices have high sensitivity to flow conditions (i.e., flow rate ratios), which, on one hand, allows to carefully tune the bubble size and the bubble formation frequency – though they are interrelated [33]. On the other hand, flow sensitivity poses a drawback in upscaling and steady operation of these devices – which is particularly challenging for bubble formation due to air compressibility [95]. To increase scalability, spontaneous devices with a sudden expansion in channel height (and thus being three-dimensional) have been developed [38,123]. In these devices, bubbles or droplets form spontaneously, not by shear but by a sudden decrease in Laplace pressure of the interface – from a confined, strongly-curved meniscus to a less-curved bubble or droplet. The continuous phase flow is then only needed for clearing the channel exit. As a result, spontaneous devices are capable of resisting fluctuations in flow, and thus show stable operation over a wider range of dispersed phase pressures or flow rates. These geometries are either straight-through microchannels with constant channel width [48,124], or also include a wider plateau or terrace to further manipulate droplet formation and the pressure stability. This plateau can be placed downstream of the channel just before the vertical step [20,41,77,85,86,88,125], or, inversely, the wider plateau can be partitioned into individual channels (pores) just before the vertical step, like in the so-called partitioned Edge-based Droplet GEneration (partitioned-EDGE) device [42].

So far, spontaneous devices have been mostly used for studying emulsification – droplet formation. Depending on the dispersed phase flow rate, droplets (or bubbles) are formed via a so-called 'dripping' or 'jetting' mechanism [48,86,126], or via two stable regimes [42] in which droplet formation in the second regime is dominated by droplet-droplet interactions [46]. Typically, as an individual droplet grows, the neck constricted within the channel contracts until finally the break-up is triggered. When the flux of dispersed phase out of the neck (forming the droplet) exceeds the supplying flux through the channel, the neck thins and breaks, and a droplet is formed [40,92]. Alternatively, when the neck shrinks to a width smaller than the channel's height, it thins following a Rayleigh-Plateau type instability and breaks [93].

In either of these cases, the inflow of the continuous phase towards the location of the neck is expected to stretch the neck and facilitate its break-up, thus playing a crucial role in droplet formation [127]. However, although the droplet formation mechanism has been extensively studied, and bubble formation shares many features with droplet formation, the dynamics of bubble formation is still under investigation and holds for example additional effects of air compressibility [126].

In spontaneous devices, interfacial tension provides the dominating force for the transformation of the constricted dispersed phase into droplets (or bubbles) [38]. The (few) studies of bubble formation in spontaneous devices are typically performed under conditions of constant, equilibrium surface tension [41,47,77], making use of very high loading of fast-adsorbing low-molecular weight surfactants like SDS or Tween 20, and relatively slow bubble formation. In this limiting case, the formed bubbles are either stable, or any coalescence after formation is simply neglected. However, in real foaming processes, the dynamic adsorption of surfactants to the interface is a crucial stage upon shear-induced fragmentation of bubbles [61] and has two important effects. First, adsorption of surfactants to a fresh interface lowers the surface tension which can influence both the initiation of bubble formation [45], and the bubble size [77]. Second, sufficient surface coverage prevents coalescence of bubbles [111,128] and thus slows down the increase of bubble size over time. In the production of food foams, whey proteins are commonly used as emulsifier. Compared to the above-mentioned low-molecular weight surfactants (e.g., SDS), protein adsorption slightly differs in interfacial behaviour. On one hand, once adsorbed at the interface, proteins undergo structural re-arrangement and thus form a viscoelastic interfacial film [68], providing protein-covered bubbles with a particularly high stability [61]. On the other hand, the adsorption of proteins is typically slower, even though it is accelerated due to enhanced mass transport in microchannels [27,53,68,129]. As concluded by Chen and co-authors [13], it is crucial to measure interfacial dynamics at relevant length and time scales. In the case of bubbles, bubble formation may happen at a micro- [41] or milli- [47,77] second time scale in spontaneous devices; an upper estimate of the time scale of whey protein-stabilisation has been given by Muijlwijk et. al (2017) [111]. They found that bubbles are stable against coalescence after allowing a (fixed) 100 milliseconds adsorption time in the presence of 1% wt. β-lactoglobulin, which is the major component of whey protein isolate. Thus, the time scales of bubble surface creation and protein adsorption possibly overlap. Dynamic adsorption effects are expected to play a

crucial role in bubble formation and stabilisation as mentioned above, yet they are not fully understood at relevant time scales.

In this work, we study bubble formation in a partitioned-EDGE device with whey proteins as the emulsifier. By varying the pressure difference across the pores between the dispersed and continuous phases, and thus the bubble formation frequency, we study a wide range of time scales of bubble formation. We observe the co-existence of bubble formation and finite bubble coalescence. Accordingly, we use a pressure analysis to explain the role of dynamic protein adsorption on the initiation of bubble formation, and use an empirical coalescence model to describe the successive bubble coalescence. We thus elucidate the role of dynamic adsorption of proteins within (sub)milliseconds using microfluidics.

3.3 Experimental

3.3.1 Microfluidic experiments

We studied the formation of air bubbles in aqueous (Milli-Q, Merck Millipore) solution of 5% wt. whey protein isolate (BiPro, 97.5% purity, Agropur, Canada), filtered with 0.22 µm PES filters (Merck, Germany). Bubbles are formed in a partitioned-EDGE microfluidic glass chip, which was previously designed in our group and produced using deep reactive ion etching technique by Micronit Microtechnologies B.V. (Enschede, the Netherlands). The design consists of relatively deep (H = 175 µm) dispersed (air) and continuous (aqueous) phase channels, connected by five shallow plateaus of 500 µm width (W), 200 µm length (L) and 1 µm height (h), as shown in Figure 3.1. The five plateaus operate more-or-less independently, with the first one being focused on in this study. The end of the plateau is partitioned into eight parallel pores of 40 µm width (w) and 20 µm length (l). The distance between the centres of two pores is 60 µm. The pores have the same height as the shallow plateau (h = 1 µm). The extreme shallowness of the plateau (and pores) is a key feature influencing the operation of the device, *via* both high Laplace pressure $\Delta P_L \sim \gamma/h$ (where γ is the surface tension between air and continuous phases) of the meniscus in the pore, and high hydrodynamic flow resistance $\mathcal{R} \sim 1/h^3$. Here, the hydrodynamic flow resistance of the pore itself can be calculated by $\mathcal{R} = \frac{12\eta l}{h^3 w\left[1\text{-}0.630\frac{h}{w}\right]}$, with η the viscosity of air and l, h, w the geometrical dimensions as mentioned above [130]. When this equation is used to calculate the hydrodynamic flow resistance of the shallow plateau, the geometrical dimensions used are W, L and h. The total hydrodynamic flow resistance of a single pore ($\mathcal{R}_{pore}$) is approximated by the resistance of the pore given above plus that of the entry path in front of it: a section of the shallow plateau with width $W/8$ and length L - l. This effective resistance is $\mathcal{R}_{pore} \approx 7\cdot10^{14}$ kg/(m^4·s) and has a significant contribution from the entry path on the plateau since that is relatively long. The considerable pore resistance enables complete filling of the entry plateau, and thus ensures a high pressure stability of the pores against pressure fluctuations during the foaming process [42].

In our experiment, both the air and the continuous phases were pressure-driven, using a digital pressure controller (± 2 mbar) operated by Smart Interface Software (Elveflow®, France). To avoid invasion of the shallow plateau and pores by the continuous phase before measurement we always first pressurised the air phase such that it continuously flows through

the pores. Then, we pressurised the air and the continuous phases to values P_d and P_c above ambient P_0, respectively. It is important to realise that the pressure applied to the air phase, P_d, decays exclusively over the high-resistance shallow region; while the pressure applied to the continuous phase, P_c, decays approximately linearly over the collection channel (neglecting viscosity variations due to the presence of bubbles) and reaches a value $P_c/2$ at the location of the shallow plateau positioned half-way through the channel. To understand bubble formation on a single-pore level, throughout our experiments we considered the pressure difference $P_d^* = P_d - P_c/2$ which drives air flow through the shallow pores, as shown in Figure 3.1.

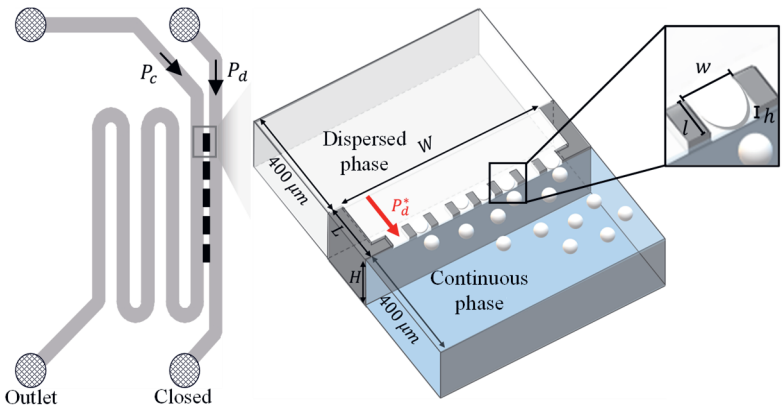

Figure 3.1. *Schematic illustration of the partitioned-EDGE microfluidic device: chip, plateau and pore. Chip (left): during the experiment the outlet of the dispersed phase channel is closed, and the air phase is forced to flow through the shallow plateau and pores under P_d^* (shown as a red arrow). Plateau (middle) and pore (right): bubbles are formed from the pores' exit. The white colour represents the air phase and the blue colour represents the continuous phase. The characteristic dimensions are explained in the text; schematics are not drawn to scale.*

While studying the effect of P_d^*, we aim to keep the continuous phase velocity (v_c) constant to avoid effects related to shear differences. For practical purposes we need to operate within two distinct shear regimes with a transition at 1400 mbar. For $P_d^* < 1400$ mbar, we set the velocity at $v_c = 0.20$ m/s. For $P_d^* \geq 1400$ mbar we set the velocity at $v_c = 1.03$ m/s. The higher velocity is needed to limit the extent of bubble crowding, which allows quantitative analysis of bubble formation up to $P_d^* \sim 2000$ mbar. We have verified (Figure A3.5) that this small variation in shear does not critically influence bubble behaviour. In the high-pressure regime, the flow rates of the two phases are interrelated, so we perform a series of calibration curves (Figure A3.1) to set these velocity conditions. We further test P_d^* up to 2800 mbar using qualitative observations.

3.3.2 Image analysis

Bubble dynamics were observed using a microscope (Axiovert 200 MAT, Carl Zeiss B.V., the Netherlands) equipped with a high-speed camera (FASTCAM SA-Z, Photron Limited, Japan). For each experimental condition (P_d, P_c), we recorded two in-line videos: one at a frame rate of 100,000 frames per second and with a resolution of 0.973 µm per pixel for measuring bubble size; and the other one at 700,000 frames per second and with a resolution of 0.973 or 0.402 µm per pixel for extracting formation dynamics of single bubbles such as the development of their diameter in time and the relevant time scales. We used a custom-written script in Matlab R2018b or Image J to extract the average diameters of bubbles that are formed at the pores (d_0; an average of up to 30 bubbles) or through coalescence (d_{coal}; an average of up to 50 bubbles), after their size has stabilised (i.e., their size stays unchanged before they are flowing out of the field of view). They correspond to volumes denoted as V_0 and V_{coal}, respectively. The size resolution is better than 1 µm. The bubble size distribution is expressed by the coefficient of variation (CV), which is defined as CV (%) = $(\sigma/d) \cdot 100$ (in which σ is the standard deviation and d the number-averaged bubble diameter). For the initial bubbles (d_0), the CV provides a measurement, within an individual experiment, of the deviation of monodispersity that is expected under perfect conditions (identical pores and applied pressures, no flow interactions). In addition, we performed a duplicate experiment to demonstrate good reproducibility of d_0 across experiments (Figure A3.2). The first video also yields the formation frequency f_0 of bubbles with diameter d_0 and the effective formation frequency of coalesced, stabilised bubbles $f_{coal} = f_0 V_0/V_{coal}$. The f_0 is determined by counting formed bubbles within a set period of time. The duplicate results in Figure A3.2 show good reproducibility across experiments.

3.4 Results and discussions

3.4.1 Observations of bubble formation and coalescence

The pores start generating relatively small bubbles when the applied pressure P_d^* reaches 1100 mbar. With increasing P_d^* more and more bubbles are formed (Figure 3.2A, snapshots 1-2), until bubble formation suddenly becomes more chaotic, producing both small and large bubbles at around and above 1400 mbar (snapshots 3-6). Visualisation at high frame rate allows us to distinguish two different bubble formation mechanisms, which typically occur at similar time scales. Small bubbles (with an averaged diameter d_0) snap-off from the meniscus in the pores; larger equilibrated bubbles (with an averaged diameter d_{coal}) are subsequently formed by coalescence in the collection channel – yet relatively close to the pore exits. Coalescence occurs primarily amongst successive bubbles from the same pore, while neighbouring pores are spaced sufficiently to prevent neighbouring bubble interactions.

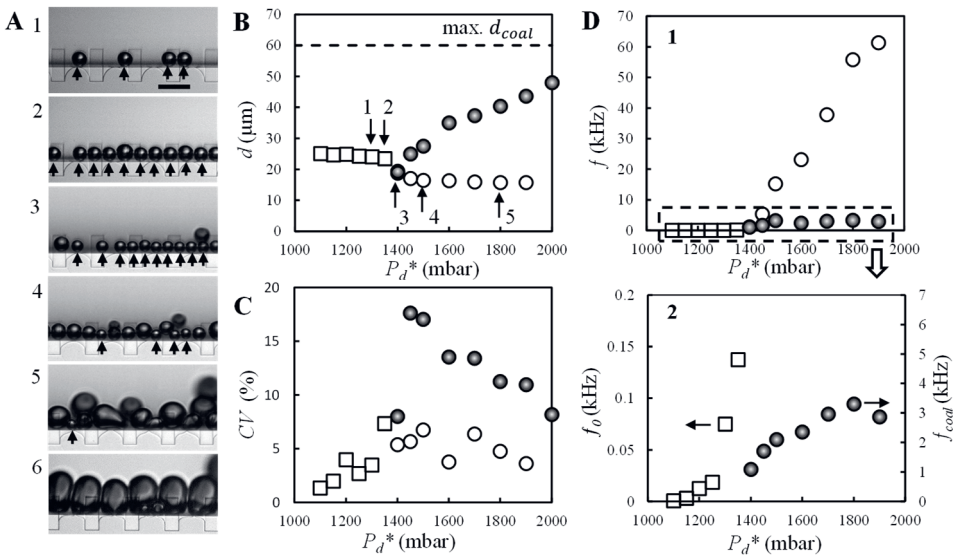

Figure 3.2. *Bubble observations as function of P_d^*. A. Snapshots of bubble formation behaviour. Arrows indicate the bubbles formed directly at the pores (d_0). Snapshots 1 – 6 were recorded at 1300, 1350, 1400, 1500, 1800, and 2800 mbar. In snapshots 1 – 4, all bubbles have detached from the pores; while in snapshots 5 – 6 some bubbles are still connected via a neck to their corresponding meniscus. Scale bar is 50 µm. B. Bubble diameters d_0 and d_{coal}. Numbers refer to snapshots in A. Around 2400 mbar d_{coal} converges to 60 µm (dashed line). C. Coefficient of variation, which measures the span of the bubble size distribution shown in B. D. Bubble formation frequencies f_0 and f_{coal}. The upper panel (D1) shows the full range up to 70 kHz, while the lower panel (D2) zooms in on the lower frequencies. Bubble frequencies are shown per pore. In B and D. open symbols correspond to initial bubbles, and closed symbols correspond to coalesced, stabilised bubbles. The flow velocity v_c is indicated by symbols: 0.20 m/s (squares) and 1.03 m/s (circles) at low and high P_d^*. Duplicate results for both diameters and frequencies show good reproducibility (Figure A3.2).*

In Figures 3.2B and C we plot the bubble diameters d_0 and d_{coal}, as well as the corresponding CV as function of P_d^*. The bubble diameter d_0 (open symbols) has two distinct, more or less constant, values in two distinct pressure regimes, which is similar to what has been found during emulsification performed in a similar device [42]. The diameter d_0 is initially around 25 µm and slightly decreases with increasing P_d^*. Monodispersity is high with a CV typically below 5%. The formation frequency f_0 (Figure 3.2D) increases with P_d^*, yet remains relatively low, namely < 140 Hz. At around 1400 mbar bubble formation changes drastically: d_0 shows a step-wise decrease, and then levels off at approximately 16 µm when P_d^* is increased up to 1900 mbar. This likely originates from both the stronger shear flow and the enhanced continuous phase inflow, facilitating the neck shrinking process, as detailed in Figure A3.5. The corresponding formation frequency f_0 suddenly increases to kHz order and increases roughly linearly with P_d^*. The transition is accompanied by the coalescence of bubbles, which has not been observed for droplets in the equivalent process of microfluidic emulsification, which is typically 100-1000 times slower. The stabilised, coalesced bubble diameter d_{coal} (closed symbols) increases with P_d^*. The CV of d_{coal} peaks at 1450 mbar since limited coalescence leads to a bi-disperse distribution of bubbles – yet it remains well below 20%, and decreases again when more bubbles coalesce at higher P_d^*. The coalescence phenomenon obviously reduces the effective formation frequency of stabilised bubbles to f_{coal}. This frequency increases for only a small range of P_d^* and then levels off at ~3 kHz (Figure 3.2D2). We studied coalescence for an extended range of P_d^* up to 2800 mbar and found that d_{coal} levels off at around 60 µm (with a CV typically around 10%) when P_d^* reaches 2400 mbar (dashed line in Figure 3.2B). This diameter is identical to the pitch between pores, and indeed the coalesced bubbles are observed to be moved out of the range of newly formed bubbles as they are pushed away by their neighbours (Figure A3.3), due to the so-called 'squeezing' effect [46].

3.4.2 Dynamics of bubble formation at the pore

To understand the formation and coalescence behaviours outlined above, we focus on an individual pore and study the air flow in this pore, followed by the expansion of a bubble into the continuous phase channel. Accordingly, a single bubble formation process is divided into two stages: the (pore) 'filling' stage and the (bubble) 'necking' stage. In Figure 3.3, panel A shows the progression and shape of the meniscus in the two stages, while panel B includes

the bubble formed during the necking stage. The stages of pore filling and bubble growth can be described using a quasi-static approach as the momentum of the gas is negligible compared to the static force of surface tension (Figure A3.4) [15]. The Laplace pressure over the air-water interface is calculated by $\Delta P_L = \gamma\left(\frac{1}{R_1}+\frac{1}{R_2}\right)$, with radii of curvature R_1 and R_2. Figure 3.3C shows three scenarios of the air-water interface during bubble formation, and at these locations the radii of curvature and thus the Laplace pressure are different. First, there is a two-dimensional meniscus in the pore ($\Delta P_L|_{pore}$, 1: blue line). When the meniscus advances in the shallow pore, entering the pore filling stage, $\Delta P_L|_{pore} \approx 2\gamma\cos(\theta)/h$ with contact angle θ and the radius of curvature $h/(2\cos(\theta))$ since $h \ll w$. Second, the meniscus is pinned at the pore edge ($\Delta P_L|_{pore,\,max}$, 2: green line). This causes air to collect at the edge of the pore and the meniscus reaches its maximum Laplace pressure $\Delta P_L|_{pore,\,max} \approx \gamma[1+\cos(\theta)]/h$, with the contact angle between the meniscus and the bottom wall of the pore being zero [41]. Note that $\Delta P_L|_{pore,\,max}$ is only marginally larger than $\Delta P_L|_{pore}$ for small contact angle θ, which is the case here as the glass walls are wetted by the aqueous phase. Finally, the meniscus leaps over the edge and a three-dimensional bubble grows in the continuous phase channel ($\Delta P_L|_{bub}$, 3: orange line), entering the necking stage. Over time the bubble diameter $d(t)$ increases and leads to a steep decrease of Laplace pressure, $\Delta P_L|_{bub} \approx 4\gamma/d(t)$, which induces a pressure jump in the continuous phase driving its inflow from the continuous phase channel towards the narrow air thread or neck at the edge of the pore [131]. During the necking stage, bubble growth and contraction of the neck happen simultaneously until the neck width narrows to the order of the pore's height [126]. Owing to the shallow pore height, the neck will then collapse extremely fast and generate a bubble. At the same time, the meniscus relaxes and retracts back into the pore for a finite distance. And subsequently, the next filling stage starts to replenish the detached volume of air (last two snapshots in Figure 3.3A).

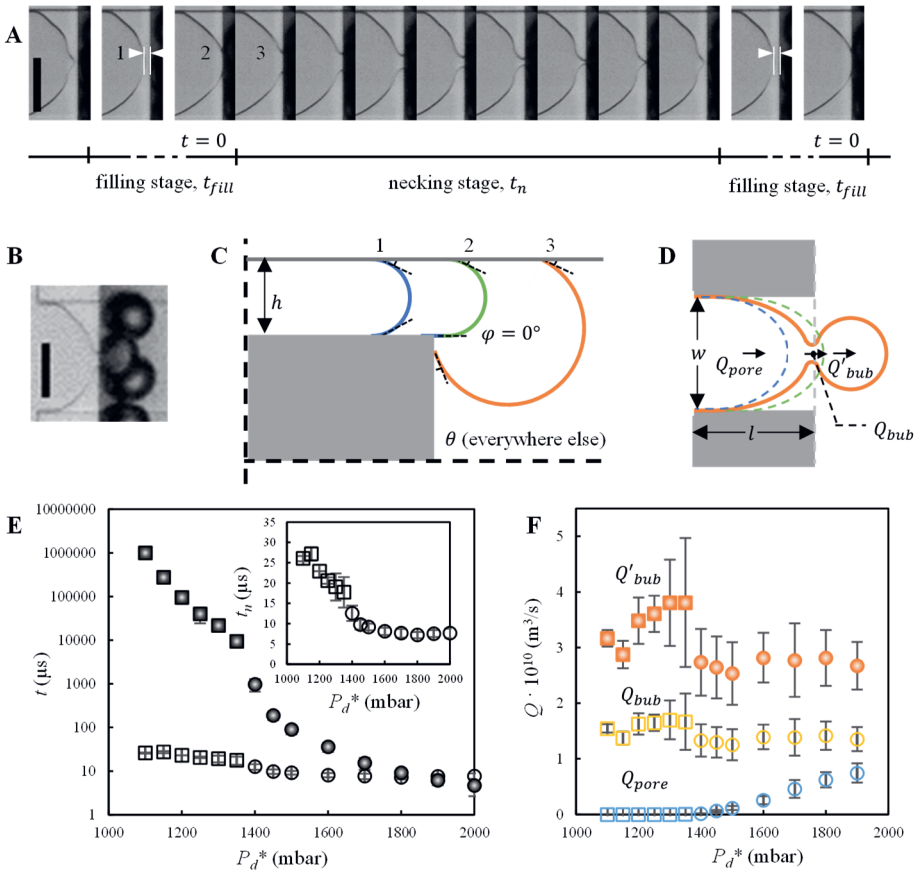

Figure 3.3. *Bubble dynamics at the pore. A. The meniscus behaviour during the filling and necking stages for $P_d^* = 1400$ mbar. Necking stage: dt = 1.43 µs between frames; only two representative frames are shown for the (much longer) filling stage. The scale bar is 20 µm. B. Snapshot of the necking process including growing bubble. The scale bar is 20 µm. C. Schematic illustration (side view) of the shape of the meniscus at three positions shown in A: 1 – meniscus inside the pore, 2 – meniscus pinning at the edge, 3 – expanding bubble (three-dimensional). θ is the contact angle between the meniscus and the pore walls; φ is the pinned angle. D. Schematic illustration (top view) of the air flow rates. E. Log-scale plot of the filling time (t_{fill}, closed symbols) and the necking time (t_n, open symbols) as function of P_d^*. Inset: t_n on a linear scale. The filling time is observed and averaged over multiple pores; for $P_d^* < 1400$ mbar the filling time is simply estimated by $1/f_0$, ignoring the negligible contribution of t_n. F. Air flow rates Q'_{bub} (orange, closed symbols), Q_{bub} (yellow, open symbols) and Q_{pore} (blue, open symbols) as function of P_d^*. In E and F, error bars (included for all data points) are not visible when they are smaller than the symbol. Different symbols represent different flow velocities: $v_c = 0.20$ m/s (squares) and 1.03 m/s (circles).*

The time scales for both stages are defined as the filling time t_{fill} and the necking time t_n (Figure 3.3A). The full time scale for one bubble formation is then $\tau = t_{fill} + t_n$. The filling time t_{fill} is infinitely long at low pressures, which corresponds to the absence of bubble formation. We can detect the first bubbles at 1100 mbar, when bubbles are formed at finite intervals of 1 second (which is the detection limit in our recordings). When P_d^* is increased

to 1400 mbar, the filling time steeply decreases over several orders of magnitude to ~1 ms (closed symbols in Figure 3.3E). It keeps decreasing to approximately 5 µs when P_d^* is increased to up to 2000 mbar. The necking time t_n also shows a decreasing trend, yet it is less steep: t_n first decreases from 25 to 14 µs when P_d^* is increased to 1400 mbar, and slowly converges to ~7 µs (open symbols in Figure 3.3E) at 1600 mbar, and then it remains constant. From 1900 mbar onwards the filling time t_{fill} is shorter than the necking time t_n. When t_{fill} is much shorter than t_n, this occasionally results in the formation of two necks from one pore as mentioned in Figure A3.3.

To understand the mechanism of bubble formation we use the quasi-static approach to quantify and compare the flow rates of air through the pore, and into the bubble. It has been argued that the surfactant coverage on an expanding bubble is homogenous [52], which allows to ignore Marangoni effects during the growth of the bubble (up to the final snap-off process). During the filling stage, the flow of air through the pore is driven by the pressure difference $P_d^* - \Delta P_L|_{pore}$. Since this pressure difference is at a maximum of 10% of the background pressure $P_c/2 + P_0$, compressibility effects can be neglected and the pore flow rate can be simply described by the Hagen-Poiseuille law: $Q_{pore} = \left(P_d^* - \Delta P_L|_{pore}\right)/\mathcal{R}_{pore}$, with $\mathcal{R}_{pore}$ the hydrodynamic flow resistance of the pore defined above. During the necking stage, two flows can be identified: pore flow and flow from the developing neck into the bubble. The pore flow rate is assumed to remain constant at Q_{pore} since both P_d^* and the Laplace pressure of the meniscus constricted within the pore ($\Delta P_L|_{pore} \sim 1/h$) remain unchanged. The flow into the bubble follows a steep Laplace pressure gradient $\Delta P_L|_{pore} - \Delta P_L|_{bub}$, accompanied by air expansion due to compressibility. Thus, we define two flow rates towards the bubble: Q_{bub} is the flow rate at the location, and local pressure of the neck, and Q'_{bub} is the (increased) flow rate into the growing bubble (Figure 3.3D). A bubble will be formed if the flow rate out of the neck region is higher than the flow rate into it: $Q_{bub} > Q_{pore}$ [93].

We analyse these flow rates starting from Q'_{bub} that can be measured directly from the growth rate of bubbles. Experiments at low P_d^* demonstrate that bubble volume increases linearly in time with a constant inflow Q'_{bub} until snap-off (Figure A3.6). The bubble has a single growth phase since the shallowness of the pore strongly limits volume addition from (i) the air ridge pinned at the edge of the pore (Figure 3.3C line 2) and (ii) the extremely fast break-up stage

(Figure A3.7). The growing bubble quickly reaches a curvature that is negligible compared to the pore's height, and thus the bubble volume increases linearly, driven by a constant Laplace pressure $\Delta P_L|_{pore}$ [20]. We can thus obtain Q'_{bub} from the ratio V_0/t_n, which is shown in Figure 3.3F (orange, closed symbols) for our full range of applied pressures P_d^*. The Q'_{bub} has a constant value at high applied pressures showing that the driving pressure $\Delta P_L|_{pore}$ is independent of P_d^*. At low applied pressures, Q'_{bub} is an increasing function of P_d^*, which is due to air expansion along the steep pressure gradient. We calculate the flow rate in the neck itself using the ideal gas law (Figure A3.8), to remove the effect of air expansion: $Q_{bub} = Q'_{bub}\frac{[P_c/2+P_0]}{[\Delta P_L|_{pore}+P_c/2+P_0]}$. Indeed, Figure 3.3F shows that Q_{bub} (yellow, open symbols) is constant not only for high, but also for low P_d^*. This separation into two distinct regimes will be addressed in the section below.

The pore flow rate Q_{pore} cannot be extracted directly from recorded videos, but we can calculate it from mass conservation throughout one bubble formation period. At the local (fixed) pressure of the neck we have $Q_{pore}\tau = Q_{bub}t_n$. Figure 3.3F shows the Q_{pore} values (blue, open symbols) derived based on the above-determined Q_{bub}, as well as time scales t_n and τ (Figure 3.3E). Q_{pore} increases with P_d^*, although it is nearly zero for P_d^* below 1400 mbar – in line with the steeply increasing filling time (Figure 3.3E), and again confirming the existence of two bubble formation regimes. We indeed find $Q_{bub} > Q_{pore}$ for all applied pressures up to 2000 mbar, confirming the criterion for bubble formation to take place. At even higher P_d^* (above 2400 mbar) the behaviour changes – we observe the formation of two neighbouring (and merging) necks from a single pore (Figure A3.3). This is in contrast to the catastrophic 'blow-up' behaviour demonstrated (for droplets) [48,86,126], which would involve the abrupt transition towards a continuous thread of air (or liquid) flowing out of the pore.

3.4.3 Two bubble formation regimes: The role of the dynamic adsorption

One question about bubble formation still remains: why do the pore flow rate (Figure 3.3F) and thus the bubble formation frequency (Figure 3.2D) decrease dramatically at applied pressures below 1400 mbar? The observed transition in bubble behaviour coincides with the pore Laplace pressure $\Delta P_L|_{pore} \approx 2\gamma\cos(\theta)/h \approx 1400 \pm 50$ mbar obtained for an air-water interface free of proteins (with γ_0 assumed to be 72.4 mN/m) and a low water contact angle

on the hydrophilic glass surface ($\theta \approx 15°$). Hence, for $P_d^* \geq 1400$ mbar, the pressure difference driving pore flow, $P_d^* - \Delta P_L|_{pore}$, is positive at all times. This leads to immediate air flow and short bubble formation time (τ) of approximately 10-1000 microseconds (Figure 3.3E). We call this the 'steady' regime: as a result of the fast pore dynamics, adsorption of whey proteins to the meniscus can be neglected and $\Delta P_L|_{pore}$ is virtually constant irrespective of applied pressures, namely 1400 mbar. Thus, on one hand, Q'_{bub} has a fixed value independent of P_d^* as the driving pressure for air flow into the bubble is constant; on the other hand, Q_{pore} increases linearly with $P_d^* - \Delta P_L|_{pore}$. Both are in line with our results shown in Figure 3.3F. The latter also allows us to extract the hydrodynamic flow resistance of the poyre $\mathcal{R}_{pore} = 6 \cdot 10^{14}$ kg/(m^4·s), which is in close agreement with the geometry-based estimation that we made earlier. The small deviation might be due to the fabrication accuracy of the geometry (e.g., with h being slightly larger than 1 µm). Finally, the constant bubble diameter d_0 in this steady regime (16 µm, see Figure 3.2B) is a result of constant Q'_{bub} and necking time. This decouples the bubble volume from the bubble frequency that can be tuned by varying P_d^*.

For $P_d^* < 1400$ mbar, pore filling and the subsequent necking process are inhibited when no protein adsorption takes place. Indeed, when we gradually decrease P_d^* an abrupt transition is observed at 1390 mbar when pure water is used as the continuous phase (Figure 3.4 inset 2). The air-water interface retracts from the pores and the shallow plateau (Figure 3.4 insets 1,2). However, when whey proteins are present in the continuous phase, bubble formation is initialised at a much lower pressure of $P_d^* = 1000$ mbar. Even though we cannot directly measure the (dynamic) surface tension of the meniscus, proteins must adsorb in order to gradually lower the surface tension and thus the Laplace pressure $\Delta P_L|_{pore}$. This induces a lag period in the filling time, required for $\Delta P_L|_{pore}$ to decrease below P_d^* [132]. Subsequently, the air phase starts flowing towards the edge of the pore, driven by a near-zero pressure difference; eventually, a bubble starts forming at the edge. The observed filling time thus strongly diverges with decreasing P_d^* in agreement with Figure 3.3E; at the same time, the calculated pore flow rate vanishes (Figure 3.3F). We call this the 'dynamic' regime. A similar steep decrease in bubble formation frequency with decreasing P_d^* is observed for experiments with varying protein concentrations (Figure 3.4). These protein solutions of 1-10% wt. have very similar quasi-equilibrium surface tension of ~49 mN/m (measured by pendant drop

tensiometry). However, a higher protein concentration allows for faster protein adsorption, so the bubble formation frequency is expected to increase with protein concentration – as can be confirmed in Figure 3.4. The apparent decrease of initialisation pressure with increasing protein concentration is a detection artefact since we are only able to detect the occurrence of bubbles down to a frequency of 1 bubble per second. In fact, based on the surface tension of 49 mN/m, the initialisation pressure would be approximately 950 mbar, which is consistent with our measurements and with the possible pinning effects at very low applied pressures.

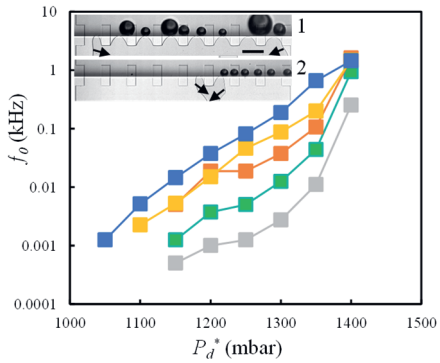

Figure 3.4. *Dynamic adsorption effects. Bubble formation frequency as function of P_d^* (up to 1400 mbar) for protein concentrations of 1 (■), 2.5 (■), 5 (■), 7.5 (■), and 10% wt. (■). Here, protein solutions have been adjusted to a constant viscosity of 2 mPa·s using glycerol, which has negligible effect on surface tension (< 2 mN/m for a maximum of 20% wt. glycerol). Duplicate experimental results for 10% wt. whey protein solution (as an example) show good overlap (Figure A3.2). Inset: bubble formation in absence of proteins. The markers 1 – 2 represent 1 – 1400 mbar and 2 – 1390 mbar, respectively, with pure water. The arrows indicate the retracting behaviour of the meniscus. (Note that bubbles will extensively coalesce due to the absence of proteins.) The scale bar is 50 µm.*

Irrespective of the extremely slow pore flow rate in the dynamic regime, the air flow into the bubble remains surprisingly fast since its driving pressure is $\Delta P_L|_{pore}$, which is just a few hundred mbar below the steady-regime value of 1400 mbar. Figure 3.3F shows that Q_{bub} is actually a bit higher before the transition at 1400 mbar, which may be explained by a change in the hydrodynamic flow resistance of the neck, which has different geometry in the two distinct regimes (Figure A3.5). Moreover, the minor differences in bubble growth rate across experimental conditions reinforce the idea that Marangoni flows have no significant effect on bubble expansion. On the other hand, the final thinning of the neck may locally cause heterogeneity of surface coverage and thus Marangoni flows that dictate necking time [28]. In our experiments, we observe that the combined effect of decreasing necking time and increasing Q'_{bub} yields a more-or-less constant bubble diameter d_0 in the dynamic regime (25 µm, see Figure 3.2B).

3.4.4 Bubble coalescence near the pore

The transition between the dynamic and steady regimes has direct implications for the coalescence stability of bubbles formed at the pores. Proteins may adsorb to the meniscus in the pore, and the bubble surface, either during its expansion or afterwards in the collection channel. Since the bubble surface expands significantly it is assumed that proteins previously adsorbed to the meniscus during the filling stage play only a minor role in terms of surface coverage. The amount of adsorption during bubble expansion is expected to be limited and to be very similar across all experimental conditions since both the expansion time (necking time in Figure 3.3E) and the bubble growth rate Q'_{bub} (Figure 3.3F) show only small variations. Across the experimental conditions, only for $P_d^* < 1400$ mbar bubbles are immediately stable against coalescence, while for $P_d^* \geq 1400$ mbar, bubbles coalesce to an extent that is strongly dependent on the bubble formation time τ. This demonstrates the intersection of time scales of bubble formation and protein adsorption, with a crucial time scale of 1 ms (Figure 3.5). For $\tau > 1$ ms (here obtained when $P_d^* < 1400$ mbar), the bubble surface can be stabilised with proteins, after this bubble has been released from the pore, well before the next bubble collides. On the other hand, for $P_d^* \geq 1400$ mbar, successive bubbles are formed within short time scales down to tens of microseconds. Even if proteins may adsorb to the bubble surface, the partial surface coverage is not sufficient at the time of interaction with successive bubbles. As a result, the bubbles coalesce, showing an increasing number of coalescence events $N = (V_{coal}/V_0)$ - 1 as function of increasing P_d^* when τ decreases below 1 ms (Figure 3.5). Eventually, the successive coalescence of bubbles stops when the growing bubble reaches stability, which is assumed to happen at near-monolayer surface coverage [133,134].

We have captured this conceptual understanding in a semi-empirical coalescence model (Appendix 3.6.9). It takes into account protein accumulation at the interface of both the expanding bubble (reaching coverage Γ_{exp} upon snap-off from the pore) and the growing bubble in the collection channel. This happens in a series of subsequent coalescence cycles, in which the newly formed bubble merges into the waiting, growing, bubble. The process ends when the surface coverage needed for stabilisation, Γ_{eq}, is obtained. The protein mass balance is derived in Appendix 3.6.9 and is formulated by $k^{2/3} = k\frac{\Gamma_{exp}}{\Gamma_{eq}} + \left(1 - \frac{\Gamma_{exp}}{\Gamma_{eq}}\right)\left(\frac{t_k}{t_1}\right)\left[\sum_{i=1}^{k-1} i^{2/3} + \frac{k^{2/3}}{2}\right]$. The number of bubbles that coalesce (k) is described by three

parameters, namely the independent variable t_k and the two fit parameters that are Γ_{exp}/Γ_{eq} and t_1. t_k is the time of a single coalescence cycle which is equivalent to the experimental bubble formation time τ; and t_1 is the minimum bubble formation time required to immediately stabilise a bubble and thus prevent any coalescence. Fitting the model to the experimental data yields $\Gamma_{exp}/\Gamma_{eq} = 0.26 \pm 0.03$ and $t_1 = 0.40 \pm 0.07$ ms. Our simple model captures the data well and yields a realistic stabilisation time which is close to the time scale required for bubble stabilisation in the steady regime (~1 ms). The model provides a framework for future refinement, in particular, the substitution of a rate equation for protein adsorption; and the dependency of stabilisation time on process conditions such as protein concentration and continuous phase viscosity. The latter are potential routes to control bubble coalescence and will be discussed in detail in future work.

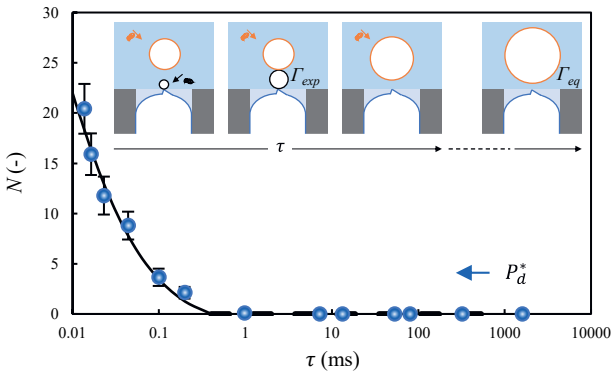

Figure 3.5. *Bubble coalescence. Number (N = k - 1) of coalescence events as function of bubble formation time (τ). From right to left, τ corresponds to P_d^* ranging from 1100 to 1900 mbar (indicated by an arrow). Inset: Schematics of protein adsorption during one bubble formation/coalescence cycle (the first three snapshots) and the end of a coalescence series. Protein adsorption to the interface of the expanding bubble and the coalesced, waiting bubble is indicated by black and orange arrows, respectively. Blue symbols: experimental data. Solid line: fit of our semi-empirical coalescence model (Appendix 3.6.9) to the data. Dashed line: the regime of non-coalescence for $\tau > t_1$.*

3.5 Conclusions

Time scales for emulsifier transport dynamics and adsorption are influenced by a variety of aspects such as the bulk concentration and diffusivity of the emulsifier, curvature of the interface, and presence of bulk convection [13]. As a result, it is nearly impossible to relate macroscopic interfacial tension measurements (performed in pendant drop tensiometer) to the stabilisation of bubbles and droplets formed at the microscale. Even though both observations are an effect of emulsifier adsorption, the transport dynamics are vastly different, from diffusion-dominated conditions for the first to much more dynamic conditions for the latter. Microfluidic techniques have tackled some of these issues, namely by measuring interfacial tension (for example, through deformation of droplets in contraction-expansion channels [23,50], droplet size resulting from well-defined shear conditions [37,53], or capillary-pressure based microtensiometry [135,136]) or studying coalescence upon droplet-droplet interactions [4,27,106,107,116] both at the microscale. However, these approaches still have limited time resolution and range. Three key characteristics of the partitioned-EDGE device used here are that we can directly study coalescence; we study it immediately after the formation of a fresh bubble surface; and we can vary bubble formation time (τ) over five orders of magnitude while keeping other aspects of the formation dynamics roughly constant (such as bubble size, bubble expansion rate and flow conditions in the collection channel). Our shortest bubble formation time is ~10 µs, which is significantly faster than other recent studies [41,47,126], and the longest bubble formation time is at a second time scale.

We demonstrate a rich bubble behaviour with the co-existence of bubble formation and coalescence at similar time scales. This is extremely relevant for large-scale foaming operations and is not incorporated in more traditional microfluidic studies that often exclude coalescence when studying the mechanism of bubble formation [41,47,77,95,126,137]. Distinct foaming regimes appear depending on the time scales of bubble formation and emulsifier adsorption. At low P_d^*, protein adsorption gradually lowers the surface tension and thus initiates bubble formation after a lag time (>> 1 ms). The resulting bubble formation frequency is relatively low, yet coalescence is prevented by timely creation of a stabilising protein layer. At high P_d^*, bubble formation does not suffer from this adsorption lag. The resulting formation frequency is high, and bubbles show finite coalescence as they interact before they are fully stabilised. The shortest formation time at which bubbles are still stable is between 0.2 and 1 ms, which can be determined with very high precision in this partitioned-

EDGE device, and is in line with the value predicted by our empirical coalescence model. The stabilisation time gives an estimate for the time scale of protein adsorption, which is governed by the enhanced mass transfer due to bulk convection and high protein concentration. Protein adsorption to the expanding bubble surface (in a time scale < 25 ms) will be limited, thus having limited effect on the growth dynamics (growth rate and shape) of the bubbles. Our next step is to further develop the current system as an analytic tool to quantify and predict bubble coalescence *via* device geometry, fluid and protein properties, and operation conditions.

3.6. Appendix

3.6.1. Calibration curves for the continuous phase flow rate

While studying the effect of applied pressure P_d^*, we keep the volumetric flow rate of the continuous phase, Q_c, constant to avoid any possible shear effects. We determined Q_c from the mass flow rate measured at the outlet of the device and the liquid density. For low P_d^* (< 1400 mbar) we use a target Q_c = 830 µl/min, leading to a velocity v_c = 0.20 m/s. For high P_d^* (≥ 1400 mbar) we need a higher flow rate to limit the extent of bubble crowding and coalescence. The flow rates of the two phases are interrelated at high P_d^*, we thus perform a series of calibration curves from which (P_d, P_c) couples are selected and then yield the intended P_d^* at a fixed Q_c (Figure A3.1). Our target here is Q_c = 4300 µl/min, leading to v_c = 1.03 m/s.

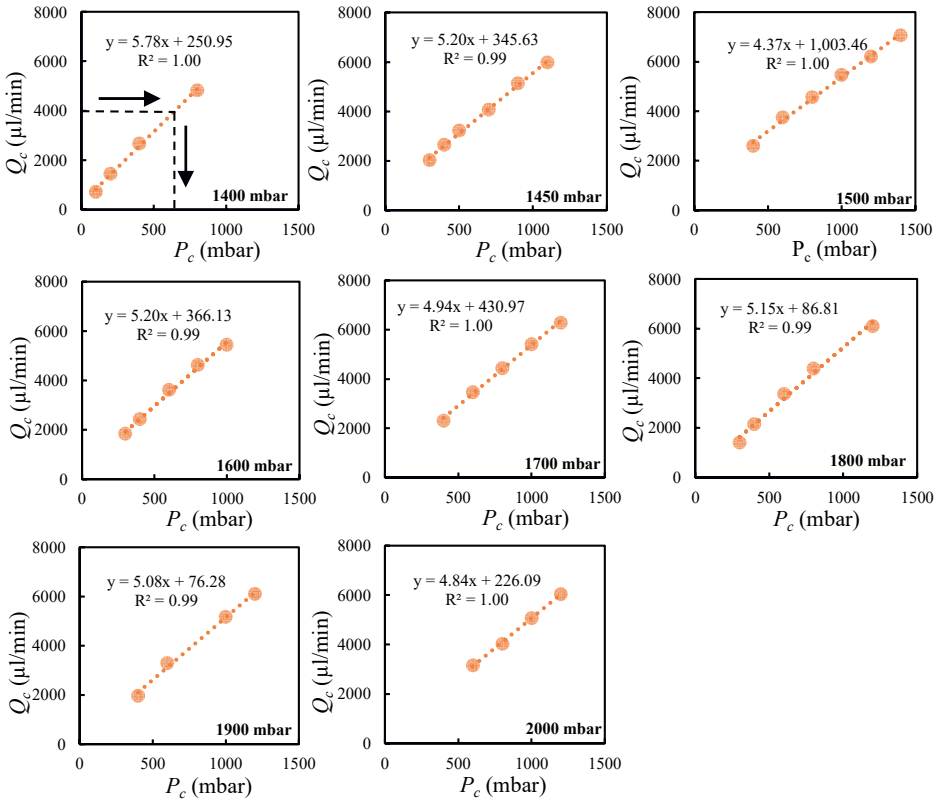

Figure A3.1. *Calibration curves performed to derive the required P_c for a constant continuous phase flow rate Q_c under different applied pressures P_d^*. The dashed line (and arrows) shown in the upper left panel indicate how we derive the required P_c for a target flow rate Q_c from a linear fit to the data.*

3.6.2. *Duplicate results of bubble sizes and the bubble formation frequencies*

Independent experiments are performed on bubble formation as function of applied pressure P_d^* (ranging from 1100 mbar to up to 2000 mbar), and the results are shown in Figure A3.2. Compared to the data shown in Figure 3.2B, as well as in Figure 3.2D and Figure 3.4 for 10% wt. whey protein solution (as an example), the bubble diameters and the bubble formation frequencies show good overlap. This proves the high reproducibility of our experiments and the validity of our results and findings.

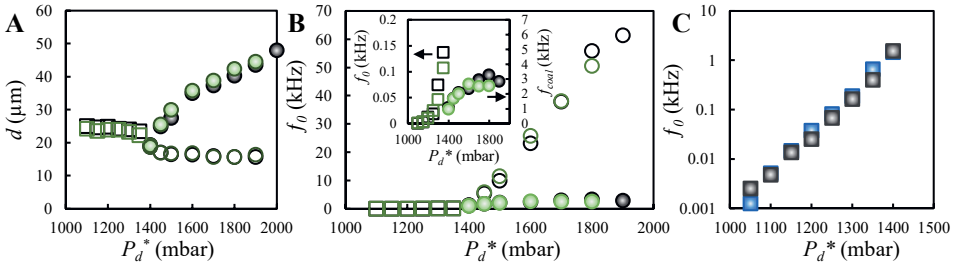

Figure A3.2. *Duplicate results for (A) bubble diameter (compare Figure 3.2B), (B) bubble formation frequency (compare Figure 3.2C), and (C) bubble formation frequency at pressures below 1400 mbar (10% wt. whey protein solution, compare Figure 3.4). Duplicate results are marked in green or blue in A-C. The flow velocity v_c is indicated by symbols: 0.20 m/s (squares) at low P_d^* and 1.03 m/s (circles) at high P_d^*. In A and B, open symbols correspond to initial bubbles.*

3.6.3. *Extension of Figures 3.2B and C for P_d^* up to 2800 mbar*

At high applied pressures (2200-2800 mbar) the bubble dynamics start to show different behaviours. The extension of the data set is represented by triangles in Figure A3.3. From 2200 mbar, the position of the neck that connects the bubble to the pore shifts away from the pore centre following the direction of continuous phase flow (downstream). Meanwhile, we occasionally observe two necks (and thus two bubbles) forming at the same pore, though these bubbles immediately coalesce. Note that at these applied pressures, we only measure coalesced bubbles since we cannot define any d_0 more. When P_d^* is increased to up to 2800 mbar, all eight pores are gradually activated to form two necks simultaneously (the inserted snapshot). The diameter d_{coal} increases with P_d^* until 2400 mbar, while after that it levels off at around 60 µm with a CV mostly below 10%. This diameter is identical to the pitch between pores, and indeed the coalesced bubbles are moved downstream along the pores due to the squeezing effect from their neighbours (Figure 3.2A, snapshot 6). Once the coalesced bubbles occupy the full pitch-width, a fresh small bubble will push the large bubble in front of it away from the pores and into the continuous phase channel. The formation frequency f_{coal} increases

for only a small range of P_d^* and then is more or less constant when P_d^* is between 1500 and 1900 mbar (Figure 3.2D, panel 2). Only when P_d^* is below 1500 mbar a portion of initial bubbles are stable and never coalesce, which means that f_{coal} is partly set by f_0 and increases weakly. For higher P_d^*, both f_0 (Figure 3.2D) and the number of coalescence events ($N+1$, see Figure 3.5) increases with P_d^*, and as a result, $f_{coal} = f_0/(N+1)$ is constant. Now, since the diameter d_{coal} levels off at $P_d^* \geq 2400$ mbar, the number of coalescence events will stabilise and consequently the formation frequency f_{coal} is expected to increase again along with the increase of f_0.

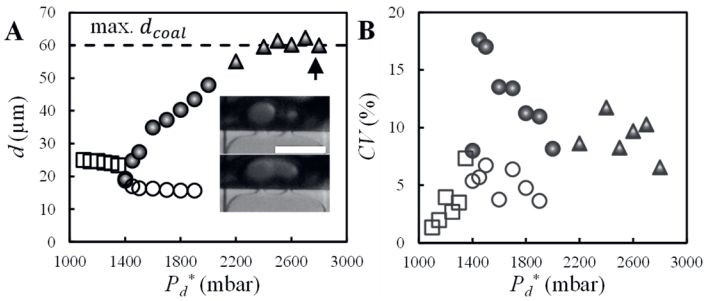

Figure A3.3. *A. Bubble diameters as function of applied pressure P_d^*. The inserted images are recorded at a frame rate of 700,000 fps and with a resolution of 0.402 µm per pixel; The scale bar is 20 µm. Around 2400 mbar the coalesced bubble diameter converges to a maximum value as indicated with the dashed line. B. The CV corresponding to bubble diameters shown in A as function of P_d^*. In A and B, the flow velocity v_c is indicated by symbols: 0.20 m/s (squares) at low P_d^* and 1.03 m/s (circles and triangles) at high P_d^*; open symbols correspond to initial bubbles.*

3.6.4. Quasi-static approach: dimensionless numbers

The growth of bubbles (and droplets) in microfluidics can be described by a quasi-static approach at small enough velocities of the gas (and liquid) phase, where its momentum must be negligible with respect to the dominating static force, surface tension [15]. The Weber number and Capillary number are thus calculated to verify whether the effects of fluid inertia and fluid viscosity are negligible, and confirm the validity of using the Young-Laplace equations.

The Weber number $\mathrm{We} = \frac{\rho v^2 L}{\gamma}$ describes the relative importance of inertia to surface tension forces.

The Capillary number $\mathrm{Ca} = \frac{\eta v}{\gamma}$ describes the relative importance of viscous forces to surface tension forces.

In which, L is the characteristic length scale (m), ρ the dispersed phase density (kg/m^3), v the dispersed phase flow velocity (m/s), η the dispersed phase viscosity (Pa·s) and γ the surface tension between air and continuous phases (N/m).

Referring to Figure 3.3F, we assume a 'worst-case' scenario of air flow rate $Q = 5 \cdot 10^{-10}$ m^3/s (which is much higher than all derived air flow rates) and then derive the air flow velocity through the cross-section of the pore, which equals to $v = 12.5$ m/s. With $L = 1 \cdot 10^{-6}$ m (the pore height), $\rho \sim 1.225$ kg/m^3 (at 20 °C), $\eta = 1.81 \cdot 10^{-5}$ Pa·s (at 20 °C), γ in the range of (4.9-7.9)$\cdot 10^{-2}$ N/m and $v = 12.5$ m/s, the two dimensionless numbers are calculated for the dispersed phase flow. We find that both Weber and Capillary numbers are of order 10^{-3}, showing that surface tension force dominates both fluid inertia and viscous forces.

3.6.5. Step-wise decrease of the bubble diameter d_0 at 1400 mbar

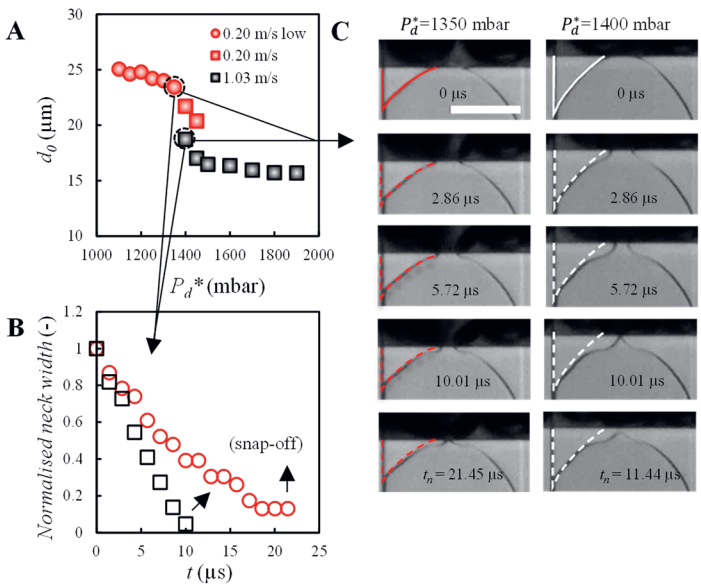

Figure A3.4. *A. Step-wise decrease of initial bubble diameter at P_d^* = 1400 mbar. B. Decrease of the normalised neck width in time for bubbles formed at P_d^* = 1350 mbar (○) and at the transition pressure (1400 mbar, □). C. Two image sequences for the two bubble formation processes shown in B. In B and C, the neck width over time is extracted from videos recorded at a frame rate of 700,000 fps and with a resolution of 0.402 µm per pixel. In B, the apparent neck width is normalised with the initial neck width (at t = 0 µs). The solid and dashed lines in C are drawn to indicate the variation in the meniscus' position and shape during bubble formation. The scale bar for the images is 20 µm.*

The step-wise decrease in d_0 at 1400 mbar has two contributions. The first is a small effect of shear since we increase v_c from 0.20 m/s at low P_d^* (red circles) to 1.03 m/s at high P_d^* (black squares). When v_c = 0.20 m/s is also used for high P_d^* (red squares; limited to two data

points due to crowding and extensive coalescence) the step-wise decrease in d_0 reduces – confirming the contribution of shear. The second contribution is the continuous phase inflow into the pore, which influences the dynamic evolution of the neck. In Figure A3.4B, it is shown that the shrinking process of the neck is faster at 1400 mbar, which is linked to a larger extent of continuous phase inflow as shown in Figure A3.4C. The area occupied by the continuous phase invading the pore is larger in that case. We will study the formation mechanism of the bubbles and the necking process for the whole range of applied pressures in future work.

3.6.6. The growth of the bubble volume over the necking time

Figure A3.5 shows the increase of bubble volume in time. The air flow rate into the bubble during the necking process, $Q'_{bub} = \partial V/\partial t$, can be derived from the slope of the plot. It is important to note that this way of deriving Q'_{bub} is only possible for low applied pressures, since if the growing bubble is surrounded by crowding bubbles it cannot be recognised in the image analysis software (custom-written Matlab script). In that case, we instead determine $Q'_{bub} = V_0/t_n$ which is underpinned by the observed linearity of bubble growth.

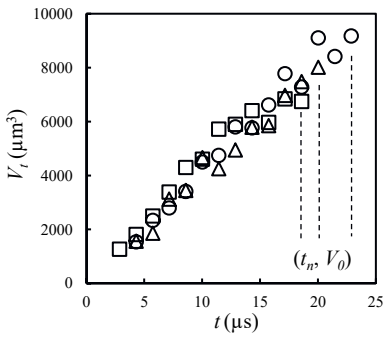

Figure A3.5. *Increase of bubble volume as function of necking time. The images used are recorded at a frame rate of 700,000 fps and with a resolution of 0.973 μm per pixel. $P_d^* = 1200$ (○), 1250 (Δ), and 1300 (□) mbar; the continuous phase velocity is 0.20 m/s. The dashed lines indicate the final V_0 and the corresponding necking time t_n.*

3.6.7. Theoretical calculation of the characteristic bubble diameter

During one bubble formation process, the bubble volume increases in three stages: the formation of a precursor which is a tiny bulb attached to the pore exit (Figure A3.6A; the necking process with linearly growing bubble volume (Figure A3.6B); and the final pinch-off of the neck (Figure A3.6C) [126].

Eggersdorfer et al. (2018) [93] studied the minimum droplet diameter obtained when a droplet is spontaneously forming at a pore. The break-up criterion is based on the total surface free energy after droplet breakup being lower than the free energy of the meniscus constrained in the pore. The minimum droplet diameter is given by $d_{min} = 3wh/[(w+h)\cos(\alpha)]$, which is determined only by the geometry of the pore (h and w) and the contact angle (α). In our case $d_{min} \approx 3$ µm (based on $w = 40$ µm, $h = 1$ µm and $\alpha \approx 15°$). Taking this as the equivalent diameter of the precursor shows that the volume $\sim d_{min}^3$ can be ignored compared to the final bubble volume $\sim d^3$.

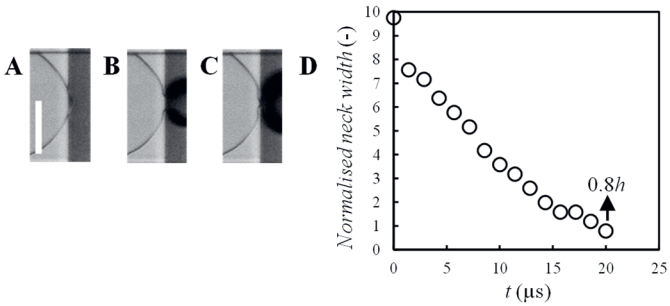

Figure A3.6. *The three stages during one bubble formation process: A. precursor formation, B. linear growth process, and C. final break-up process. These images were recorded at a frame rate of 700,000 fps and with a resolution of 0.402 µm/pixel at $P_d^* = 1150$ mbar ($v_c = 0.20$ m/s); The scale bar is 20 µm. D. Decrease of neck width in time for an example obtained at $P_d^* = 1350$ mbar; the neck width is normalised with the pore height h. The images used to extract the neck width are recorded at a frame rate of 700,000 fps with a resolution of 0.199 µm per pixel.*

Secondly, in Figure A3.6D ($P_d^* = 1350$ mbar), we normalise the neck width with the pore height h, and find that in the final stage of bubble growth the neck width is approximately ~0.8h. Since the pore height is the smallest dimension throughout (most of) the process, the flow resistance is expected to remain constant in time – which is in line with the linear growth observed in Figure A3.5. After reaching ~0.8h, the neck breaks up due to its instability and can do so very fast because it is very thin, so we can neglect additional volume increase. In conclusion, bubble growth can be described by the linear growth phase only.

3.6.8. Pressure-driven flow calculations and effect of air compressibility

The air flow rate Q'_{bub} is experimentally derived by the growth rate of the bubble, i.e., the ratio of V_0/t_n (Appendix 3.6.6). To calculate the flow rates through the neck (Q_{bub}) and in the pore (Q_{pore}) we use the principle of mass conservation (not volume), taking into account the air compressibility effect along the pressure gradients. Our simplified scenario is outlined by

a schematic illustration of the air flow rates and their corresponding driving pressures in Figure A3.7. From left to right: Q_{pore} is the air flow rate in the pore, which is constant in space and time (as explained below). Then, we assume a discrete pressure drop from the necking region (Laplace pressure of the meniscus in the pore) to the bubble (Laplace pressure of the bubble surface), yielding two points of measurement of air flow rates, which are Q_{bub} through the infinitely small neck, and Q'_{bub} into the bubble (as measured experimentally).

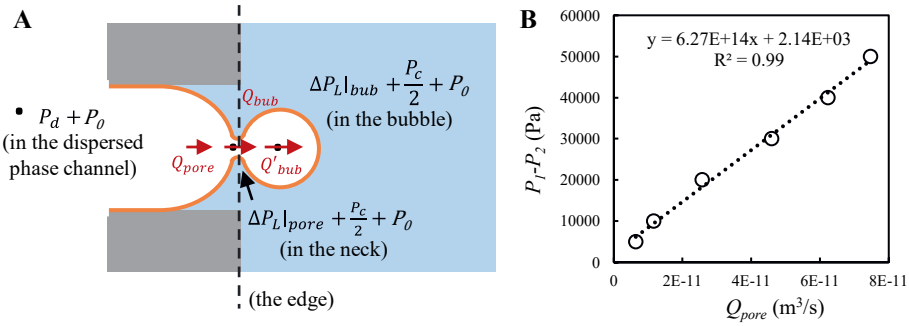

***Figure A3.7**. A. Schematic illustration of the pressures developed during one bubble formation process. B. The driving pressure over the pore versus the corresponding pore flow rate.*

The flow rate through the neck Q_{bub}

As shown in Figure A3.7A, for the air flow rate Q_{bub} the up (1) and down (2) stream pressures are defined as $P_1 = \Delta P_L|_{pore} + \frac{P_c}{2} + P_0$ being the air pressure in the pore (due to meniscus curvature in the pore) and $P_2 = \Delta P_L|_{pore} + \frac{P_c}{2} + P_0$ being the air pressure inside the growing bubble, respectively. Since the bubble diameter will soon reach a value $d \gg h$, the term $\Delta P_L|_{bub}$ can be neglected, and the pressure P_2 is re-written as the 'background' pressure $P_2 = \frac{P_c}{2} + P_0$. Due to the large ratio between pressure P_1 and P_2 the air will expand when flowing out of the shallow pore into the continuous phase channel. To take this into account we consider the conservation of mass (n) across the (assumed) discrete pressure drop. We link the local air flow rate Q_{bub} to Q'_{bub} using the ideal gas law, from which $PV = nRT$ is constant (V the volume, n the number of moles, R the gas constant, and T the temperature; we assume an isothermal process). We obtain $P_1 Q_{bub} = P_2 Q'_{bub}$ and thus $Q_{bub} = Q'_{bub} \frac{[P_c/2 + P_0]}{[\Delta P_L|_{pore} + P_c/2 + P_0]}$.

For $P_d^* \geq$ 1400 mbar, $\Delta P_L|_{pore}$ is assumed to stay constant at 1400 mbar since bubble formation is extremely fast and protein adsorption is considered to be negligible; and the pressure P_c is varied in the range of 650-910 mbar, aiming for the constant Q_c. For $P_d^* <$ 1400

mbar (and larger than the minimum required applied pressure), due to the adsorption of protein being slow, we assume that the Laplace pressure of the meniscus remains fixed at the applied pressure – i.e., once the meniscus starts moving no additional protein is adsorbed. Thus $\Delta P_L|_{pore}$ is assumed to be equal to P_d^*, the pressure P_c is kept constant at 100 mbar. The results of corrected air flow rate Q_{bub} is shown in Figure 3.3F in the manuscript.

The flow rate through the pore Q_{pore}

For the pore flow rate Q_{pore}, the driving pressure is equal to $P_1 = P_d + P_0$ being the absolute air pressure applied at the pore entrance minus $P_2 = \Delta P_L|_{pore} + \frac{P_c}{2} + P_0$. Both pressures are constant in time; for the latter, we assume that the Laplace pressure of the meniscus in the pore remains the same in the necking stage since the meniscus is still confined to the shallow height h. In the necking stage, locally there is no mass conservation of air flowing into and out of the neck, otherwise, it would not thin out. However, there should be overall mass conservation: all air molecules that flow through the pore during the total bubble formation time $\tau = t_{fill} + t_n$ are collected in a bubble that is formed in a (shorter) time t_n. Here we consider Q_{pore} at the neck location, thus the pressure is constant for both flow rates of Q_{pore} and Q_{bub}. We then use volume conservation and obtain $Q_{pore}\tau = Q_{bub}t_n$, in which Q_{bub} has been calculated as above, and τ and t_n are experimental results (Figure 3.3E). We calculate the pore flow rate $Q_{pore} = \frac{Q_{bub}t_n}{\tau}$ for our full range of applied pressures (P_d^* = 1100-1900 mbar), as shown in Figure 3.3F.

Lastly, we express the pore flow rate as function of applied pressure P_d^* to demonstrate that Q_{pore} is constant along the pressure gradient in the pore and to calculate the flow resistance $\mathcal{R}_{flow}$. To incorporate air compressibility we get $Q_{pore,\,in}P_2 = Q_{pore,\,R}\frac{P_1+P_2}{2}$, where the flow rate and pressure are taken at the pore entrance (left), i.e., $Q_{pore,\,in}$ and P_2, or as average values along the pore (right) [41]. $Q_{pore,R} = (P_1 - P_2)/\mathcal{R}_{flow}$ is the resistance-based flow rate described by the Hagen-Poiseuille law, and $(P_1 + P_2)/2$ is the pressure average. For the various P_d^* and P_c values mentioned above we get $Q_{pore,in} \approx Q_{pore,R}$ (with a factor 1.0-1.2), so in first approximation the air expansion is negligible, and Q_{pore} is constant along the pore. $\mathcal{R}_{flow}$ can

then be estimated following the Hagen-Poiseuille law from the slope of the plot as shown in Figure A3.7B.

3.6.9. Coalescence model

We provide a semi-empirical model to describe the number of coalescence events, based on a conceptual understanding of the stabilisation process as a series of events. From experiments, we know that the most likely coalescence route is that of successive bubbles from a single pore, so we consider a single pore here. We also observe that the air-water interface significantly expands during the bubble growth process ($d_0^2/hw_n \geq 10$), so any prior protein adsorption to the meniscus will be neglected in the model. The surface stabilisation process can then be modelled as a series of three separate events, see Figure A3.8. Proteins adsorb (I) to the surface of the rapidly expanding 'daughter' bubble that grows at the pore. In line with experiments, *immediately* after snap-off (II) the daughter bubble (with surface area A_1) coalesces into the 'mother' bubble in the collection channel. This increases the surface area of the mother bubble as $A_i = A_1 i^{2/3}$ (with i the number of the coalesce cycle) and also changes – typically decreases – its surface coverage. Thereafter, (III) proteins are adsorbed to the mother bubble, while the pore is refilled with air. Each subsequent daughter bubble thus coalesces after one bubble formation cycle (t_k) that is equal to the measured bubble formation time (τ). These events will be repeated until a total number (k) of daughter bubbles have coalesced into the mother bubble. The process will stop when the total adsorbed amount of protein is sufficient to reach the surface coverage needed for stabilisation (Γ_{eq}) of the surface area A_k.

The amount of protein adsorbed to the expanding daughter bubble (the black circle in Figure A3.8) is assumed to be independent of the length of the bubble formation cycle (which is controlled in the experiments by P_d^*). This is based on the observation that bubble formation dynamics remain relatively unaltered across our experimental conditions, including both the necking time t_n and the bubble growth rate Q'_{bub}. Thus, we ignore the adsorption dynamics in the event (I) and assume that when daughter bubbles reach their final surface area A_1, they reach a constant surface coverage Γ_{exp} (which possibly increases with protein concentration, but that is constant here, i.e., 5% wt. whey protein).

In contrast, the amount of protein adsorbed to the mother bubble in event (III) (orange circle in Figure A3.8) increases linearly with the duration of the bubble formation cycle $t_k = f(P_d^*)$,

which varies across experimental conditions, and with the surface area of the mother bubble A_i, which grows with each coalescence step. To a first approximation the amount of adsorbed protein m_p is *only* dependent on these two parameters, so $m_p = \bar{k}_{ads} t_k A_i$ with effective adsorption coefficient $\bar{k}_{ads}$ being independent of time and thus surface coverage. It should be noted that the latter is a strong simplification. The model could be refined by substituting a rate equation (based on an adsorption isotherm) in which the adsorption rate decreases with surface coverage. This increases the number of fitting parameters and would require larger data sets – so it is considered out of the scope of this paper. Here, we divide out $\bar{k}_{ads}$ by substituting the time scale to reach stabilisation of a single bubble (fit parameter t_1), and aim to demonstrate that our sequence of events captures the number of observed coalescence events.

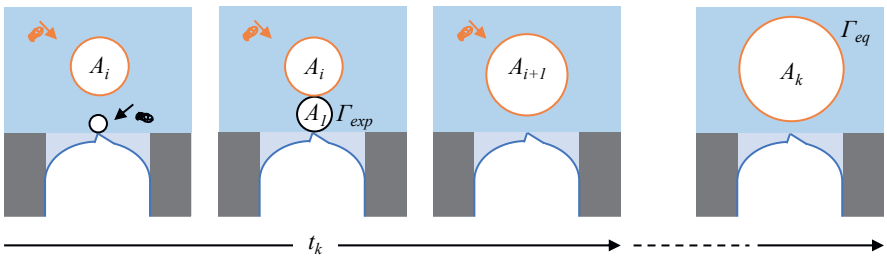

Figure A3.8. *Assumed coalescence scenario. The first three snapshots highlight one bubble formation circle, during which (I) proteins adsorb to the expanding daughter bubble (black), reaching a final surface coverage Γ_{exp}; (II) the daughter bubble coalesces into the mother bubble; (III) proteins adsorb to the mother bubble (orange). Protein adsorption is indicated by arrows. The process ends when after k steps the final bubble with surface area A_k is obtained.*

We write *a protein mass balance* for two cases. Equation A3.1 describes the stabilisation of a single bubble, where t_1 is the minimum bubble formation time needed to avoid coalescence (around 1 millisecond in the experiments). Equation A3.2 describes the stabilisation after coalescence of k bubbles, for bubble formation times $t_k < t_1$:

$$\Gamma_{eq} A_1 = \Gamma_{exp} A_1 + \bar{k}_{ads} t_1 A_1 \qquad \text{A3.1}$$

$$\Gamma_{eq} A_k = k \Gamma_{exp} A_1 + \bar{k}_{ads} \left[t_k \sum_{i=1}^{k-1} A_i + \frac{t_k A_k}{2} \right] \qquad \text{A3.2}$$

Note that in the final step the mother bubble may reach stability at any time between the last merging event and the next coalescence attempt, so the last merging event is counted as only half. We can eliminate the unknown adsorption coefficient $\bar{k}_{ads}$ from equation A3.2, using equation A3.1 and the relation $A_i = A_1 i^{2/3}$:

$$k^{2/3} = k\frac{\Gamma_{exp}}{\Gamma_{eq}} + \left(1 - \frac{\Gamma_{exp}}{\Gamma_{eq}}\right)\left(\frac{t_k}{t_1}\right)\left[\sum_{i=1}^{k-1} i^{2/3} + \frac{k^{2/3}}{2}\right] \quad \text{A3.3}$$

This equation can be fitted to the experimental data (t_k, k) with two fit parameters, namely the minimum bubble formation time to avoid any coalescence t_1 and the fraction of protein coverage obtained during the daughter bubble expansion process, Γ_{exp}/Γ_{eq}. The results of the coalescence model are displayed in Figure 3.5 in the main text, with fit parameters t_1 = 0.40 ± 0.07 ms and Γ_{exp}/Γ_{eq} = 0.26 ± 0.03. Our model (equation A3.3) captures the data well and yields a realistic stabilisation time that is very close to the lowest time scale required for bubble stabilisation observed in the experiment, namely 1 ms. At $t_k \lesssim 10$ ms the model does not apply to our experiment as neighbour interactions limit the extent of coalescence and/or bubbles may continuously grow from the pore ('blow-up') when the bubble formation time converges towards the necking time.

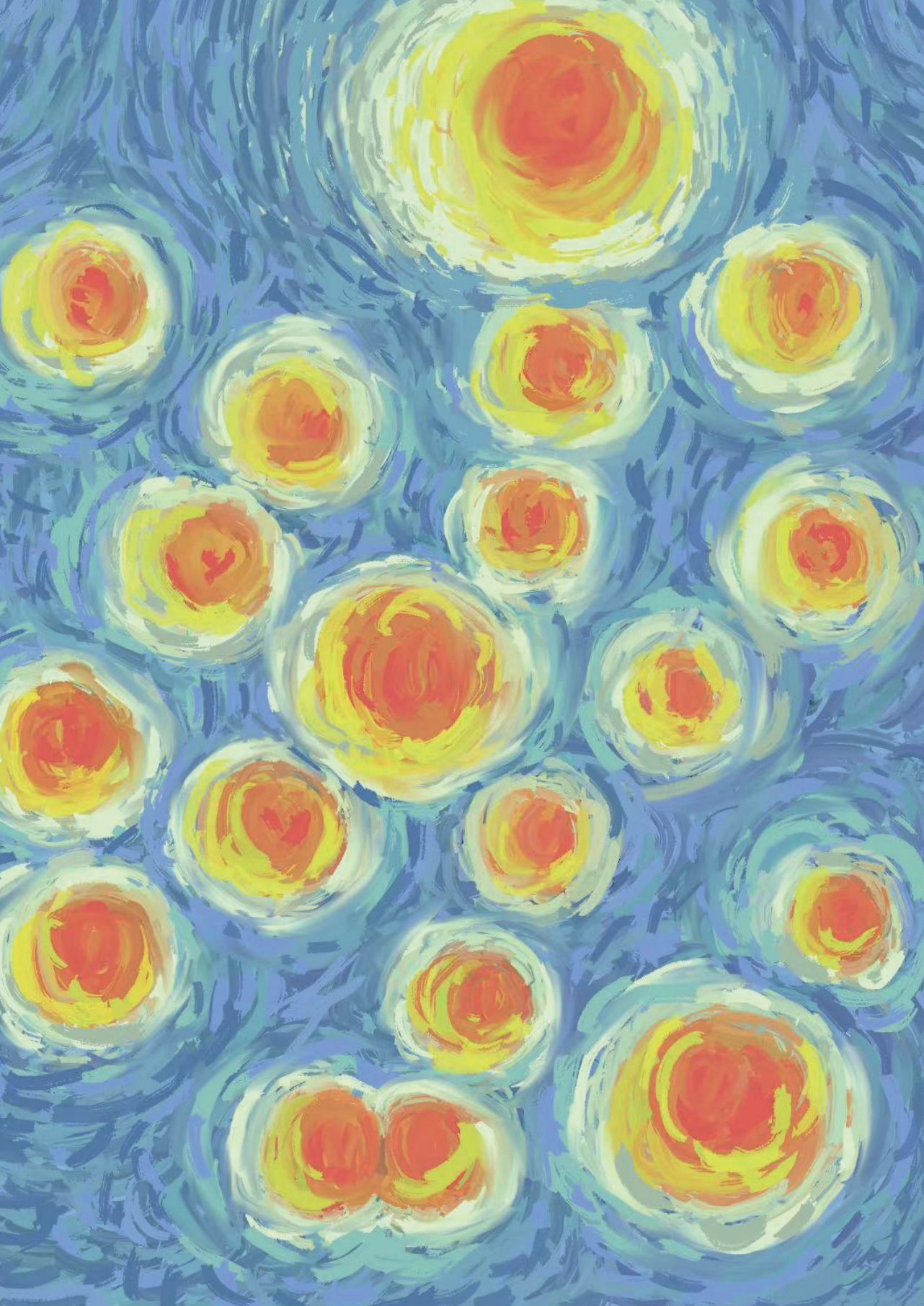

CHAPTER || 4

Dynamics of bubble formation in spontaneous microfluidic devices: Controlling dynamic adsorption via liquid phase properties

This chapter has been published as Deng, B., Schroën, K. & De Ruiter, J. Dynamics of bubble formation in spontaneous microfluidic devices: Controlling dynamic adsorption via liquid phase properties. *Journal of Colloid and Interface Science*, **2022**, 622, 218-227.

4.1. Abstract

Hypothesis: The interplay of interface evolution and emulsifier adsorption determines the formation and stabilisation of bubbles, and can be controlled by the liquid phase properties. *Experiments:* We studied bubble formation in an Edge-based Droplet GEneration (EDGE) microfluidic device at relevant length and time scale, allowing investigation of sub-events in a single bubble formation cycle. We vary the properties of the continuous phase that contains whey proteins and study a range of applied pressures (P_d^*).

Findings: The shallow pores highlight the crucial role of the Laplace pressure and dynamic adsorption of proteins to the meniscus. Bubble formation is divided into two regimes by the Laplace pressure of the bare meniscus inside the pore. At $P_d^* < 1400$ mbar, pre-adsorption of proteins is required to lower the Laplace pressure; the bubble formation frequency f_0 increases with increasing protein concentration and is hardly affected by velocity and viscosity. At $P_d^* \geq 1400$ mbar, bubble formation immediately occurs upon applying pressure, and f_0 mainly decreases with increasing viscosity. In both regimes, the initial bubble size d_0 mainly increases with the viscosity ($\sim\eta^{1/3}$). Bubble coalescence is only observed at $P_d^* \geq 1400$ mbar and can be effectively suppressed by raising protein concentration and viscosity within certain boundaries, yet ultimately this is at the cost of higher polydispersity of the bubbles. Our insights into the formation dynamics of *micrometre-sized* bubbles at time scales down to tens of microseconds can be used for effective control of bubble formation and stabilisation in practical applications.

Graphical abstract

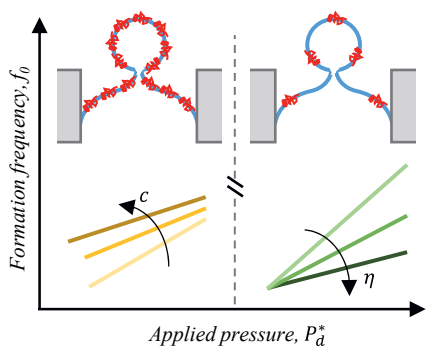

4.2. Introduction

Spontaneous emulsification can steadily produce monodisperse droplets and bubbles in parallelised devices [18,20,21,48,138–141], and recent research efforts focus on both optimising throughput *via* device geometry and understanding the on-site droplet (and bubble) formation mechanism. Typically, droplets (or bubbles) are formed at the exit of strongly confined pores that open into a much deeper collection channel. The formation is initiated above the breakthrough pressure – the Laplace pressure of the saturated meniscus constricted inside the pore, $\Delta P = \gamma(\frac{1}{R_1}+\frac{1}{R_2})$, where R_1 and R_2 are the radii of curvature of the meniscus, and γ its *equilibrium* interfacial (surface) tension [38,132,142]. A remarkable increase in the droplet size is observed upon increasing the dispersed phase flow rate [86,93], which is often reported as a transition from 'dripping' to 'jetting' regime [48]. The critical value of this flow rate, or the corresponding capillary number, increases with increasing pore height, pore length, the contact angle between the interface and the channel wall, and the inflow of the continuous phase [20,93,97,139,143]. In the dripping regime, droplet formation is dominated by interfacial tension, and the droplet size scales with the smallest dimension of the pore, showing very little dependency on dispersed phase flow rate [126,144]. In the jetting regime, viscous forces control droplet formation while the position of the neck moves more towards the edge of the pore; the neck adopts a quasi-static shape and remains open for a longer time. As a result, increasingly larger and ultimately polydisperse droplets are formed [86,90,126,145].

For practical applications, the dripping regime is most relevant because of the well-defined product that is formed. By increasing the dispersed phase flow rate, the formation frequency increases, while the bubble (or droplet) size remains roughly constant [39]. The bubble size increases with continuous phase viscosity as the formation dynamics are slowed down [41,47,77]. While most studies consider droplet formation at equilibrium interfacial tension, only a few studies consider the much faster bubble formation, and these studies are typically carried out at very high loading of fast-adsorbing low-molecular weight surfactants, like SDS and Tween 20 to avoid effects related to adsorption dynamics [41,47,126,146]. Yet, it has been shown that dynamic interfacial behaviour cannot be neglected when emulsifiers with slower adsorption dynamics (e.g., proteins) or low concentrations of fast-adsorbing low-molecular weight surfactants (e.g., SDS) are used during bubble formation [27,45,77,147] or droplet formation [12]; we have recently demonstrated [148] the roles of dynamic adsorption effects in both bubble formation and bubble stabilisation *versus* coalescence.

Using a (spontaneous) partitioned Edge-based Droplet GEneration (EDGE) device [148] with pores of 1 micrometre height, we found that the breakthrough pressure to initiate bubble formation in a whey protein solution is approximately 1100 mbar and that there is also a transition pressure of approximately 1400 mbar that delineates bubble formation into two regimes. Each of these two pressures is linked to a characteristic Laplace pressure of the meniscus (equation above) with the (lower) breakthrough pressure being the Laplace pressure of the *equilibrated* interface saturated with protein and the transition pressure being the Laplace pressure of the *bare* interface. This implies that for applied pressures above the Laplace pressure of the bare interface (high-pressure regime), bubble formation immediately starts without pre-adsorption of proteins. In contrast, in the low-pressure regime, protein adsorption at the meniscus is required to lower the surface tension and thus the Laplace pressure across the meniscus until it is below the applied pressure. In both cases, the constricted meniscus eventually forms a neck that feeds air to a bubble growing in the collection channel. Further protein adsorption may occur at this neck as well as at the growing and subsequently released bubble.

While bubble formation time is dominated – in the low-pressure regime – by adsorption of protein to the meniscus in the pore, and steeply decreases in the high-pressure regime, the stabilisation of the bubble surface is determined by adsorption of protein to the released bubble in the collection channel. In the low-pressure regime, the lag time for protein adsorption to the meniscus sets the bubble formation time that decreases from 1000 to 10 ms with applied pressure, while in the high-pressure regime the bubble formation time decreases further from 1 ms down to 0.01 ms. The bubble-bubble interaction between subsequent bubbles being formed at the same pore is set by this bubble formation time. On the other hand, the characteristic time scale for protein adsorption to the bubble itself is likely kinetically dominated [149] or showing mixed kinetic and diffusive behaviour – but in any case, is largely independent of applied pressure in the partitioned-EDGE device. As a result, when the bubble formation time drops below the characteristic time scale for protein adsorption, here determined to be around 0.4 ms, coalescence takes place upon bubble-bubble interaction. Accordingly, in the low-pressure regime with formation times larger than 10 ms, bubbles are inherently stabilised before bubble-bubble interaction, while in the high-pressure regime, bubbles may coalesce a few times before they are stable. The number of coalescence events depends on the applied pressure *via* the bubble formation time and its intersection with the

characteristic time scale for protein adsorption to the bubble. In summary, both bubble formation frequency and the extent of coalescence (if any) are determined by dynamic adsorption, and this is highly relevant for many multi-phase food systems (i.e., food foam or emulsion) that are stabilised by e.g., whey proteins.

Here, we study the effects of whey protein concentration, continuous phase velocity and continuous phase viscosity, on spontaneous bubble formation in a partitioned-EDGE device. Bubble formation shows two (low- and high-) pressure regimes, divided by the Laplace pressure of the bare meniscus inside the pore. At low pressures dynamic adsorption effects are dominant and bubble formation frequency increases with increasing protein concentration. In contrast, at high pressures bubble formation is independent of dynamic adsorption and is facilitated by continuous phase inflow; bubble formation frequency is now limited by the necking of the air thread and thus decreases with increasing viscosity of the continuous phase that constricts this neck. In both pressure regimes, the size of the formed bubbles increases with continuous phase viscosity – again due to its effect on the dynamics of necking of the air thread. The coalescence of these bubbles at high pressures can be controlled to a certain extent by raising protein concentration and continuous phase viscosity.

4.3. Experimental

4.3.1. Microfluidic experiments

In our microfluidic studies, air was used as the dispersed phase, and aqueous solutions of whey protein isolate (> 97.5% purity, BioPro, Agropur, Quebec, Canada) in MilliQ water (Merck Millipore) were used as the continuous phase. A range of protein concentrations (1-10% wt.) was tested, and the viscosity of all these solutions was adjusted to 2 mPa·s (at 20 °C) by adding a small amount of glycerol (99.5%, VWR International, Leuven, Belgium) that hardly influences the surface tension of the bulk liquid. In addition, using 2.5% wt. whey protein as a reference system, the continuous phase velocity and viscosity were investigated in the range of about 0.1-0.9 m/s and 2-6 mPa·s, respectively (at 20 °C). All solutions were filtered with 0.22 µm PES filters (Merck, Germany) before flowing into the microfluidic system.

We studied air bubble formation with the partitioned-EDGE glass chip as shown in Figure 4.1A. The chip was designed by our group and produced by Micronit Microtechnologies B.V. (Enschede, the Netherlands). The geometry consists of two deep channels with 400 µm width and 175 µm height, which are connected by five shallow plateaus of 200 µm length (perpendicular to the deep channels) and 500 µm width. During the experiments, we considered only the first plateau upstream in the dispersed phase channel (the inset in Figure 4.1A). This main plateau is further partitioned into eight parallel pores that each has a rectangular shape of 20 µm in length and 40 µm in width. The main plateau and the pores all have a height of h = 1 µm. The hydrodynamic flow resistance of the pore (or plateau) can be calculated by $\mathcal{R} = \frac{12\eta l}{h^3 w[1-0.630\frac{h}{w}]}$ [130], with η the viscosity, and l, w, h the geometrical dimensions for the pore (or L, W, h for the plateau).

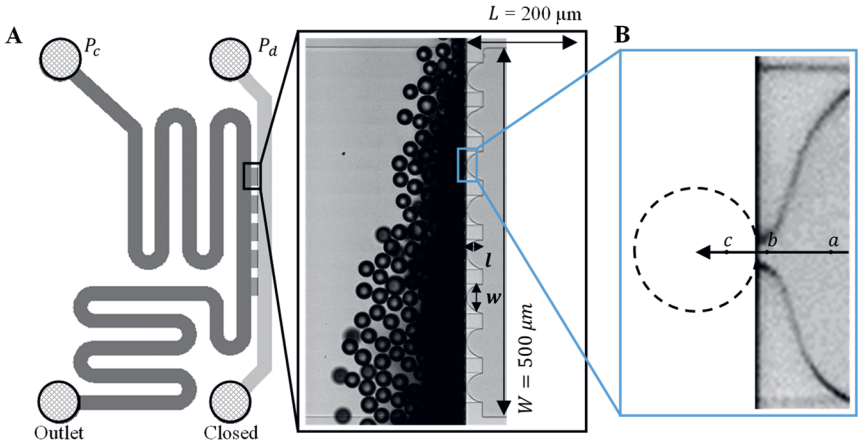

Figure 4.1. *Partitioned-EDGE device. A. Geometrical schematic of the partitioned-EDGE device. The inset is a microscopic image of the continuous phase side of the main plateau, which is active and forming bubbles. B. Illustration of air flow rates along the flow path during a single bubble formation cycle: Q_{pore} is the air flow rate inside the pore (location a), Q_{bub} is the local air flow rate through the neck located inside the pore (location b), and Q'_{bub} is the air flow rate into the growing bubble (location c). $Q'_{bub} > Q_{bub}$ due to air compressibility [148]; $Q'_{bub} \gg Q_{pore}$ within the studied pressure range. The dashed circle represents the growing bubble.*

The air and the continuous phases were controlled using a digital pressure controller via Smart Interface Software (Elveflow®, France) in such a way that an effective pressure difference $P_d^* = P_d - P_c/2$ is applied across the main plateau and the pores (with P_d and P_c the pressures applied externally to the air and the continuous phases, respectively). The applied pressure P_d^* was varied in the range of 1050-2000 mbar, with a transition pressure of 1400 mbar that divides bubble formation into two pressure regimes of 'low' and 'high' pressures [148]. While studying bubble formation as function of P_d^*, we kept the continuous phase velocity v_c constant in each pressure regime. The operation window was defined to enable both the observation and the quantitative analysis of bubble formation.

4.3.2. Image analysis

A high-speed recording system, including a microscope (Axiovert 200 MAT, Carl Zeiss B.V., the Netherlands) and a high-speed camera (FASTCAM SA-Z, Photron Limited, Japan), was used to observe and record bubble formation (and coalescence). For each experimental condition, we recorded two videos, one at 100,000 fps and the other one at 700,000 fps. The former video was used to measure the initial bubble size (d_0) and the coalesced bubble size (d_{coal}), which were averaged for up to 30 and 50 bubbles, respectively, using a custom-written script in Matlab R2018b; moreover, the formation frequency of the initial bubbles, f_0, was

obtained by counting the number of bubbles formed within a set period of time. From the latter recording we extracted the formation dynamics of individual bubbles at the pores. We evaluated two time scales (t_n and t_{fill}, which will be introduced later), and monitored the growth of the bubble in terms of its volume V_t and the thinning of the neck in terms of its width w_t. $w_t$was normalised as w_t/w_0, where w_0 is the initial neck width before thinning. Lastly, three air flow rates were defined as sketched in Figure 4.1B. Here we are mainly interested in the air flow rate into the growing bubble, Q'_{bub}, which can be directly measured from the slope of (V_t, t) plot, or it can be estimated from V_0/t_n under crowded conditions in which bubble growth in time cannot be followed. The air flow rates in the pore (Q_{pore}) and through the neck (Q_{bub}) can be calculated *via* mass conservation and ideal gas law [148], but they are only discussed qualitatively in this study.

4.4. Results and discussions

4.4.1. Bubble formation dynamics

Each bubble formation cycle can be divided into a pore filling stage and a bubble necking stage. The corresponding time scales are defined as the pore filling time (t_{fill}) and the bubble necking time (t_n) (Figure 4.2A). In the pore filling stage, the air phase flows inside the pore towards the edge. t_{fill} is strongly influenced by the applied pressure, P_d^*, and the hydrodynamic flow resistance of the pore ($\mathcal{R}$). The pore filling stage ends when the apex of the meniscus contacts the edge of the pore and forms a neck with a finite initial width (w_0). In the subsequent bubble necking stage, the air phase flows through this neck. A spherical bubble starts growing and the neck starts thinning out. When the neck width decreases to the order of the pore's height [126,127], the neck quickly breaks up within one microsecond and a bubble with volume $V_0 = \frac{\pi}{6} d_0^3$ is released into the collection channel. We observed that at low pressures the neck thins out very locally near the edge, and most of the meniscus remains static inside the pore; while at high pressures, the entire meniscus moves back and forth inside the pore and a longer neck is formed.

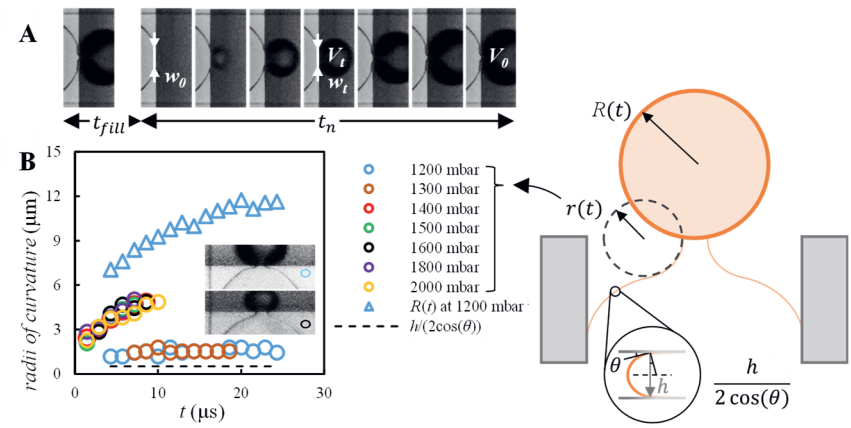

Figure 4.2. *Bubble formation at the pore. A. Snapshots of one bubble formation cycle at P_d^* = 1200 mbar. Necking stage: dt = 4.29 µs between presented frames. The bubble formation time is $t_{tot} = t_{fill} + t_n$. B. Left: Absolute radii of curvature as function of time. Inset: Comparison of neck shapes in the middle of one necking process ($t = t_n/2$). Up: low (1200 mbar); down: high (1600 mbar) pressure regime. Right: Schematic of these radii of curvature. Shown are the radius of curvature of (from top-to-bottom): the expanding bubble ($R(t) = d(t)/2$, where d(t) is the bubble diameter as function of time) and the neck, including in-plane radius (r(t)) and out-of-plane radius ($\frac{h}{2\cos(\theta)}$). The protein concentration is 2.5% wt. and the continuous phase viscosity is 2 mPa·s. v_c is constant at approximately 0.93 m/s.*

The dynamics of the neck – the shape and location of the meniscus – differ in the two bubble formation regimes (i.e., low and high applied pressures P_d^*) (inset in Figure 4.2B). The difference in necking dynamics can be captured by the geometric analysis of the three crucial curvatures (Figure 4.2 B, right). The radius of the positive out-of-plane curvature of the neck (inside the pore) is fixed by the pore's half height $\frac{h}{2\cos(\theta)}$, with θ the contact angle between the continuous phase and the channel wall (~15º to represent a hydrophilic channel surface). In addition, using the high-speed recordings (Table A4.1), we measured the radius of the growing bubble in the collection channel, $R(t)$, and that of the negative in-plane curvature of the neck inside the pore, $r(t)$, and plotted them as function of time for a series of P_d^* (Figure 4.2B left). From these radii of curvature, we can calculate the Laplace pressures $\Delta P = \gamma(\frac{1}{R_1}+\frac{1}{R_2})$ across the interface of either the bubble ($R_1 = R_2 = R(t)$) or the neck ($R_1 = \frac{h}{2\cos(\theta)}$ and $R_2 = -r(t)$), and follow their variations over time in the two pressure regimes. The growth rate of the bubble only shows minor dependency on the applied pressure (Figure A4.1), hence we show only a representative case of 1200 mbar in Figure 4.2B. While $R(t)$ grows towards its final radius upon release, R_0, the Laplace pressure of the bubble typically decreases only slightly from 100 mbar to 50 mbar, and these values are negligible compared to the Laplace pressure at the neck. For the neck, we consider the cases of low and high applied pressures. At low applied pressures (1200 and 1300 mbar in Figure 4.2B), the negative in-plane $r(t)$ is constant over time and is comparable in absolute value to that of the positive out-of-plane curvature, leading to a low Laplace pressure at the exit of the pore. This results in a large pressure drop inside the pore (on the plateau), which is strongly localised to the exit of the pore. In contrast, at high applied pressures, the absolute value of $r(t)$ increases over time and is substantially larger than $\frac{h}{2\cos(\theta)}$. Accordingly, the Laplace pressure decreases slightly along the pore and the largest pressure drop is located between the exit of the pore and the growing bubble. The difference between a strongly localised, constant pressure drop inside the pore (low applied pressures) and a pressure drop that shifts from the plateau into the continuous phase in time (high applied pressures) may be closely linked to the inflow of the continuous phase, which is driven by a reverse (inward) pressure gradient in the continuous phase. When the pressure drop is strongly localised near the pore's exit, the inflow of the continuous phase is negligible, while there is substantial inflow when the pressure drops more gradually and into the continuous phase.

To understand the effects of fluid properties on the formation frequency and the ultimate size of initial bubbles, we first evaluate their effects on each stage of a single bubble formation cycle.

Pore filling stage

The pore filling stage consists of an active period, which is preceded in the low-pressure regime by a static period. During this static period, protein adsorption is required to sufficiently lower the Laplace pressure across the meniscus inside the pore (ΔP_{pore}), until $\Delta P_{pore} \leq P_d^*$. During the subsequent active period, the air phase flows at a rate $Q_{pore}(t) = \Delta P_1(t)/\mathcal{R}$ towards the edge of the pore, with $\Delta P_1(t) = P_d^* - \Delta P_{pore}$ being the pressure drop along the pore and $\mathcal{R}$ the hydrodynamic flow resistance of the pore. In the low-pressure regime, the active period is much shorter than the static period, so its effect on the pore filling time (t_{fill}) can be ignored (Figure A4.2). The t_{fill} is determined by the lag time to adsorb the required proteins. In contrast, in the high-pressure regime with $\Delta P_1(t) > 0$, the active period (i.e., the pore flow process) takes place immediately, and the t_{fill} is determined by the applied pressure (P_d^*).

The pore filling time, t_{fill}, shows distinct characteristics in the two pressure regimes. At $P_d^* <$ 1400 mbar, t_{fill} decreases as P_d^* gradually increases to up to 1350 mbar (Figure 4.3A), since at a higher applied pressure an increasingly higher surface tension already allows for pore flow. With increasing protein concentration, a lower (quasi-) equilibrium surface tension can be obtained; moreover, protein adsorption is overall faster, which leads to a faster decrease in surface tension. Consequently, bubble formation is initiated at a lower P_d^* and the t_{fill} decreases with protein concentration (Figure 4.3B). As an illustration, bubble formation is initiated at 1150 and 1050 mbar, respectively, for 1 and 10% wt. whey protein; when P_d^* increases from 1150 to 1350 mbar, the t_{fill} decreases from 2000 to 90 ms for 1% wt. whey protein, while it decreases from 70 to 1.5 ms for 10% wt. whey protein. Lastly, at these low applied pressures t_{fill} is hardly (if at all) influenced by continuous phase velocity (Figure 4.3A) and viscosity (Figure 4.3C). The pore flow is insensitive to these continuous phase properties, which agrees with the earlier visual observation that the inflow of the continuous phase is negligible at low pressures.

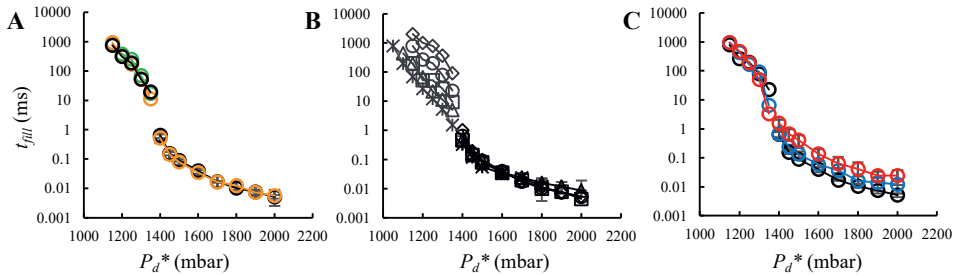

Figure 4.3. *Pore filling time as function of P_d^* for the effects of continuous phase velocity of 0.12 (○), 0.50 (○) and 0.93 (○) m/s (A), protein concentration of 1 (◊), 2.5 (○), 5 (□), 7.5 (Δ) and 10 (*) % wt. (B), and continuous phase viscosity of 2 (○), 4 (○) and 6 (○) mPa·s (C). In B, viscosity is adjusted using less than 20% glycerol, hence the effect of glycerol on surface tension is minor [47]. At P_d^* < 1400 mbar, we use the simple estimate $t_{fill} = 1/f_0$ neglecting the relatively short necking time. Unless stated otherwise, the protein concentration is 2.5% wt. and the continuous phase viscosity is 2 mPa·s; v_c is 0.12 m/s in the low-pressure regime and 0.93 m/s in the high-pressure regime.*

At $P_d^* \geq 1400$ mbar, t_{fill} decreases over two orders of magnitude, from ~0.6 to ~0.006 ms, as P_d^* is gradually increased to 2000 mbar (Figure 4.3A). The protein concentration now has negligible influence on t_{fill} (Figure 4.3B), except for a slightly shorter filling time observed in a protein-free system (0% wt., Figure A4.3). On one hand, this indicates that protein adsorption towards the meniscus (inside the pore) is negligible during these short times; on the other hand, any protein adsorption taking place on the channel walls possibly renders the glass surface more hydrophilic (leading to a lower contact angle) [91,150] and thus slightly increases the ΔP_{pore}. Hence, only in a completely protein-free system the higher contact angle results in a distinctly shorter t_{fill}. Considering the continuous phase properties, t_{fill} is again independent of velocity (Figure 4.3A). However, contrary to the observations at low applied pressures, t_{fill} increases by a factor of approximately 1.7 and 3.8 when the viscosity is increased from 2 to 4 and then 6 mPa·s (Figure 4.3C). This increase in t_{fill} is ascribed to the stronger inflow of the continuous phase during the bubble necking stage in this regime. During the subsequent pore filling stage, the continuous phase needs to be pushed out of the pore again, which provides an additional source of hydrodynamic flow resistance that increases with viscosity.

Bubble necking stage

At the end of the necking stage, the neck breaks up when its width vanishes ($w_t \approx 0$) and a bubble with volume V_0 is formed at the pore. At very low applied pressures up to 1200 mbar, monodisperse bubbles are formed at an increasing frequency with pressure. To understand

the obtained bubble volume, V_0, and the necking time, t_n, we first illustrate at 1200 mbar the effects of fluid properties on V_t (Figure 4.4A-C) and w_t/w_0 (Figure 4.4D-F). The V_t increases linearly and its slope $Q'_{bub} = \frac{\Delta V}{\Delta t}$ is independent of the effects of continuous phase velocity and viscosity (Figure 4.4A, C), while it slightly increases with the protein concentration (Figure 4.4B). While the bubble is growing, the neck width w_t/w_0 decreases linearly (Figure 4.4D), and the neck thinning rate (i.e., the slope $\frac{\Delta w}{\Delta t}$) decreases remarkably as the viscosity increases (Figure 4.4F), resulting in a significantly longer neck thinning process. In particular, the neck thinning rate is roughly inversely proportional to the viscosity – which follows from the linear increase of dissipation in the continuous phase (inflowed) with viscosity. Next to that, the air flow rate through the neck is not at all affected by this dissipation source and thus the bubble growth Q'_{bub} is independent of viscosity (Figure 4.4C); the bubble growth Q'_{bub} is also independent of the necking time as the crucial length scale for the hydrodynamic flow resistance is the constant pore height. Furthermore, the neck thinning rate slightly decreases as the protein concentration increases (Figure 4.4E), and this effect couples directly with a slight increase in the Q'_{bub} (Figure 4.4B). As the protein concentration is increased by a factor of 4 from 2.5 to 10% wt., Figure 4.3B shows that there is a large increase in t_{fill} (i.e., by a factor of approximately 10 at 1200 mbar); Figure 4.4H shows that the corresponding t_n is virtually constant. Hence, the above-mentioned coupling effects are considered to be minor and we assume that the bubble snaps off very quickly after the minimum required surface tension (for a given applied pressure) has been reached. This is likely the same for applied pressures $P_d^* \leq P_{tran}$, at which bubble formation is set by the applied pressure (i.e., by the dynamic adsorption of the emulsifier).

Both bubble volume expansion and neck thinning end at t_n – the necking time (Figure 4.4G-I). Across the full pressure range, t_n decreases and then levels off with P_d^* for protein concentrations below 5% wt. (Figure 4.4G). For $P_d^* \leq 1350$ mbar, t_n gradually decreases from ~25 to ~18 µs. Subsequently, t_n steeply decreases to ~13 µs at the transition pressure (1400 mbar) and then levels off at around 9 µs as P_d^* increases to 2000 mbar. Above the transition pressure of 1400 mbar, the markedly smaller t_n values are in line with the higher neck thinning rates (Figure A4.5) that result from a higher Laplace pressure locally at the neck and a stronger inflow of the continuous phase, which can squeeze the neck and further facilitate its breakup [127].

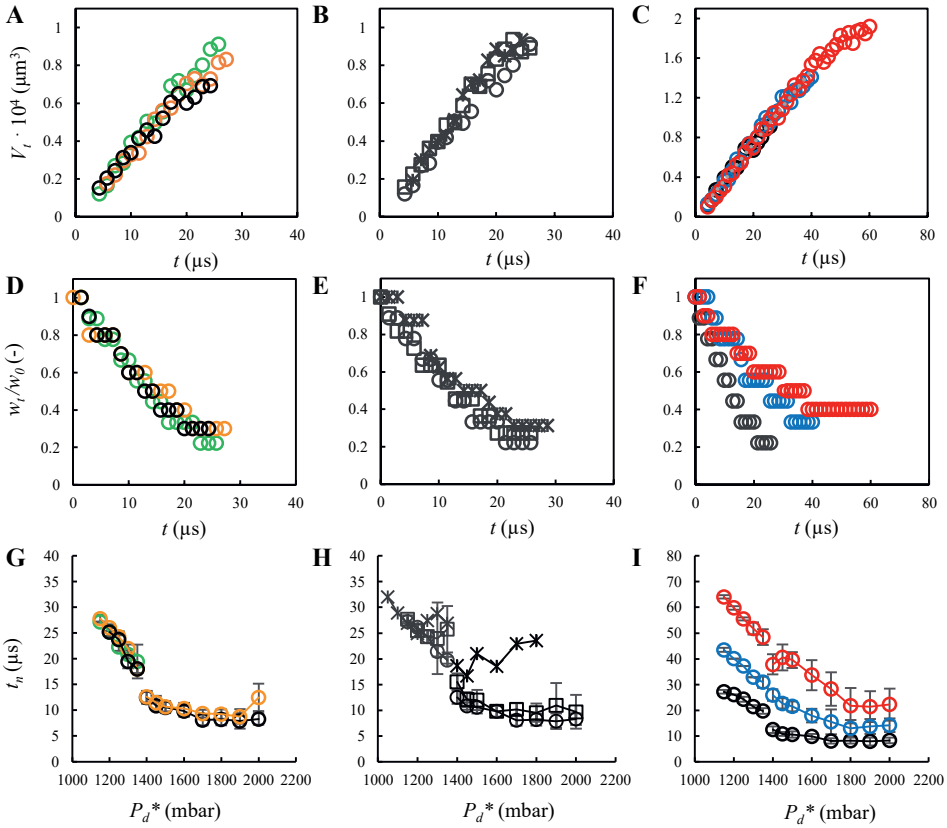

Figure 4.4. *Dynamics of bubble growth and necking. A–C. Bubble volume versus time at $P_d^* = 1200$ mbar for the effects of continuous phase velocity of 0.12 (○), 0.50 (○), and 0.93 (○) m/s (A), protein concentration of 2.5 (○), 5 (□), and 10 (*) % wt. (B), and viscosity of 2 (○), 4 (○), and 6 (○) mPa·s (C). D-F. Neck width versus time for the same fluid properties as in A-C. Note that the plateau phase observed in w_t/w_0 at the end of the necking process is ascribed to finite pixel resolution (Figure A4.4). G-I. Necking time as function of P_d^* for the same fluid properties as in A-C. In B, E, and H, only three protein concentrations are presented for higher visibility of the data points. Unless stated otherwise, the protein concentration is 2.5% wt. and the viscosity is 2 mPa·s; v_c is 0.12 m/s in the low-pressure regime and 0.93 m/s in the high-pressure regime.*

In terms of fluid properties, t_n is hardly affected by continuous phase velocity (Figure 4.4G), while there is a systematic influence of continuous phase viscosity (Figure 4.4I) and a surprisingly *non-monotonous* behaviour of t_n for different protein concentrations (Figure 4.4H). Firstly, as the continuous phase viscosity (η) increases from 2 to 4 and further to 6 mPa·s (by a factor of 2 and 3), t_n increases roughly by a factor of 2 and 3, so $t_n \sim \eta$ (Figure A4.6). Secondly, t_n shows distinct behaviours for higher protein concentrations (≥ 5% wt.). The typical behaviour is as follows (Figure 4.4H): in the low-pressure regime, t_n initially decreases with pressure, like the behaviour at lower protein concentrations. Yet, t_n starts increasing at a certain pressure that itself decreases with protein concentration (for example,

decreasing from 1350 mbar for 5% wt. to 1250 mbar for 10% wt.) (this is linked to amongst others the formation of polydisperse bubbles as will be elaborated on in the next section). Afterwards, t_n may decrease again as the pressure increases up to the pre-transition pressure of 1350 mbar. Accordingly, there is a local maximum in t_n in the low-pressure regime. In the high-pressure regime, t_n shows a similar behaviour: t_n first decreases with pressure and then increases for protein concentrations ≥ 7.5% wt. Again the transition point shifts to lower P_d^* for higher concentrations, yet, does not decrease again as found for the low-pressure regime.

In the high-pressure regime, t_n intersects with t_{fill} at P_{cross}, after which $t_{fill} < t_n$ (Figure 4.5A). At low protein concentrations, P_{cross} is approximately 1900 mbar and is not influenced by continuous phase velocity and viscosity. Yet, it decreases with increasing protein concentration (Figure 4.5B). For example, it shifts from 1900 mbar (for 2.5% wt. whey protein) to 1700 mbar for 10% wt. whey protein. Moreover, though it might be a coincidence, the P_{cross} equals the pressure at which t_n substantially increases as indicated above.

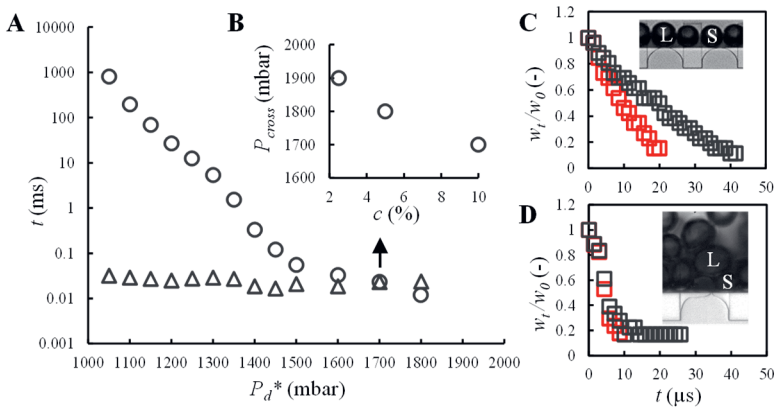

Figure 4.5. *A. Intersection of the two time scales obtained with 10% wt. whey protein: pore filling time (circles) and bubble necking time (triangles). B. Effects of protein concentration (c) on the intersection pressure (P_{cross}). C-D. Two distinct necking scenarios observed for 10% wt. whey protein at C – 1250 mbar and D – 1800 mbar. Insets: images show the resulting small (S) and large (L) bubbles. In the high-pressure regime, some large bubble formation is observed since 1500 mbar, yet only since 1700 mbar large bubbles account for more than half of the studied bubbles.*

At high protein concentrations, the sudden increase in t_n in both regimes results from the simultaneous formation of small and large bubbles directly at the pores. The occurrence of large bubbles appears seemingly random in terms of the instances and locations of formation. For 10% wt. whey protein, large bubbles start forming at 1250 mbar in the low-pressure regime, and then again systematically at 1700 mbar in the high-pressure regime. The t_n values

shown in Figure 4.4H are averaged for up to 30 bubbles, but we find distinctly different t_n values for either small or large bubbles. To illustrate this, we study the neck thinning process at two representative pressures (i.e., 1250 and 1800 mbar) with 10% wt. whey protein. The mechanisms causing the prolonged neck thinning are different in the two pressure regimes. At low pressure (1250 mbar in Figure 4.5C), the neck linearly thins out, and for the large bubbles, this happens at a lower neck thinning rate that results in a longer necking time. At high pressure (1800 mbar in Figure 4.5D), the neck initially has a fast neck thinning rate that is similar for both small and large bubbles, yet, after the neck narrows approximately to the order of the pore's height, for the large bubbles the extremely narrow neck remains open for an extended time, during which the neck might continue to thin out but at a much lower thinning rate. In this case, at the end of the prolonged neck thinning process, the neck is expected to break up due to a perturbation in local pressure conditions, or the growing bubble is simply cut off by the cross-flowing bubbles.

4.4.2. General discussion: Bubble size and formation frequency

The volume of the released bubble (Figure 4.6A-C) is the product of (constant) bubble growth rate and necking time, $V_0 = Q'_{bub} \cdot t_n$. The V_0 is linear in t_n, and the bubble size scales as $d_0 \sim t_n^{1/3}$. Thus, d_0 is as expected increasing when t_n increases, namely at low pressures (Figure 4.6A), as well as at high protein concentrations (Figure 4.6B) and high viscosities (Figure 4.6C). In terms of the 10% wt. whey protein experiments, Figure 4.6B indeed shows a local maximum in bubble size at low pressures. At high pressures, when t_n increases, large bubbles are also observed to form at the pores, yet a direct quantitative measurement of d_0 is limited by bubble crowdedness. Instead, we estimate the bubble size using $V_0 = Q'_{bub} \cdot t_n$, assuming that Q'_{bub} remains constant (which at least is the case for the lower pressures) and these estimates are shown for P_d^* up to 1900 mbar. In addition, corresponding to the mechanisms causing the prolonged neck thinning, at low pressure (1250 mbar in Figure A4.7), the bubbles are almost bi-dispersed; while at high pressure (1800 mbar in Figure A4.7), the bubbles are polydispersed. Furthermore, since t_n scales with the continuous phase viscosity (Figure 4.4I), we find $d_0 \sim \eta^{1/3}$ (Figure A4.6). This is in agreement with the $\frac{d}{d_{ref}} \approx (\frac{\eta}{\eta_{ref}})^{1/3}$ behaviour (where d_{ref} is the droplet diameter and η_{ref} the continuous phase viscosity used in a reference system) proposed for emulsification in a similar device [46]. Still, the most important message

here is that the monodispersity of the initial bubbles can be destroyed when an extremely high protein concentration or viscosity is used.

The bubble formation frequency, f_0, is the inverse of bubble formation time. At $P_d^* < 1400$ mbar with $t_{fill} \gg t_n$, the f_0 simplifies to $\sim 1/t_{fill}$ and increases with P_d^*. For a given P_d^* in the low-pressure range, the f_0 increases with the protein concentration (Figure 4.6E, panel 2) and is independent of the continuous phase properties (Figure 4.6D, F, panel 2). At $P_d^* \geq 1400$ mbar, the f_0 is equal to $1/(t_{fill} + t_n)$ and linearly increases as function of P_d^*, by approximately 50 times going from the transition pressure to the highest measured pressure of 1800 mbar (Figure 4.6D). Yet, for a given P_d^*, the f_0 here decreases as the protein concentration increases, which is opposite to the effect of protein concentration at low pressures; moreover, this distinct effect becomes stronger with increasing P_d^*. This is because at these high pressures, the t_{fill} is nearly independent of protein concentration (Figure 4.3B). The t_n is now of the same order of magnitude (as the t_{fill}), and does depend on protein concentration (Figure 4.4H). The extreme case is presented by 10% wt. whey protein, which shows an optimum in f_0 for intermediate P_d^* (e.g., 1700 mbar) and afterwards the f_0 even decreases due to the formation of large bubbles. Furthermore, at these high pressures the f_0 is again not affected by the continuous phase velocity (Figure 4.6D1), while it significantly decreases as the continuous phase viscosity increases (Figure 4.6F1). This decrease in f_0 with viscosity is ascribed to the inflow of the continuous phase that needs to be replaced by the next forming bubble, which ensures the effect of the viscosity on impeding the pore flow process.

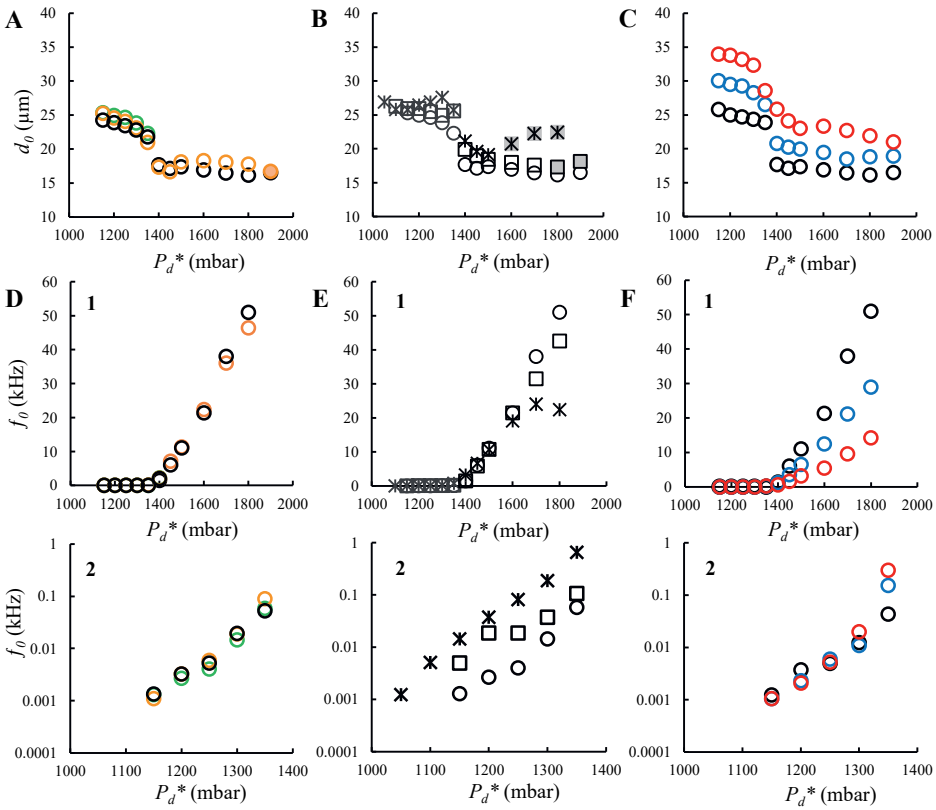

Figure 4.6. *Bubble properties. Bubble size and bubble formation frequency as function of P_d^* for the effects of continuous phase velocity of 0.12 (○), 0.50 (○) and 0.93 (○) m/s (A, D), protein concentration of 2.5 (○), 5 (□), and 10 (*) % wt. (B, E), and continuous phase viscosity of 2 (○), 4 (○) and 6 (○) mPa·s (C, F). In panel 1 (in D-F), the formation frequency is plotted across the full range of P_d^*; in panel 2, only the low pressures (< 1400 mbar) are shown. In B and E, only three protein concentrations are presented. In A and B, the estimates of d_0 for P_d^* up to 1900 mbar are shown with filled symbols.*

It is important to realise that bubble formation is extremely fast in the current device, and initial bubbles of size d_0 can further coalesce in the collection channel, forming a larger bubble size d_{coal} [148]. In general, coalescence is observed at any $P_d^* > 1400$ mbar; the extent of coalescence and thus d_{coal} decrease as the continuous phase velocity or protein concentration increases (Figure A4.8). For example, when 1% wt. whey protein is used, bubbles coalesce once they are in contact (i.e., infinite coalescence), which indicates that protein adsorption is too slow to stabilise the newly created bubbles. On the contrary, when 10% wt. whey protein is used, coalescence after bubble formation can be almost suppressed, albeit these bubbles are polydisperse at the time of formation. In addition, a high continuous phase viscosity can also be used to control coalescence, lowering the d_{coal} (Figure A4.8), yet at the expense of

lower bubble formation frequency (Figure 4.6F1). It is clear that the preparation of monodisperse bubbles requires a multi-faced approach. Next to that, these results indicate that in the partition-EDGE device, bubble formation and on-site coalescence can be studied simultaneously at a time scale down to tens of microseconds. We will discuss the bubble coalescence effects in more detail in future work.

The simultaneous increase in the initial bubble size (Figure 4.6B) and decrease in the bubble formation frequency (Figure 4.6E) for high pressures and high protein concentrations (e.g., at 1800 mbar for 10% wt. whey protein) show similarities with that observed above a critical dispersed phase flow rate during droplet formation in microchannel devices [39,86,97], in the so-called 'jetting' regime [48]; namely, the prolonged existence of a neck connects the continuously-growing bubble to the pore. The transition could be explained by the dynamic adsorption of proteins at high concentrations and the relative size of the two time scales ($t_{fill} < t_n$), which depends on the overall experimental conditions [148]. In the current research, for a relatively low protein concentration, the growth of larger bubbles at the pores could be suppressed up to high formation frequencies (although at the expense of a higher extent of bubble coalescence), which is at least partially due to the strong confinement provided by the extremely shallow pores in the partitioned-EDGE device.

Lastly, it is important to stress the crucial characteristic of the partitioned-EDGE device – its extreme shallowness that leads to the rich bubble formation behaviour (i.e., the two distinct bubble formation regimes) when used in combination with slow-adsorbing whey proteins. This introduces well-defined regimes of bubble formation that are delineated by the Laplace pressure of the saturated meniscus in the pore (i.e., the breakthrough pressure) and the Laplace pressure of the bare meniscus (i.e., the transition between low- and high- pressure regimes). This enriches the dripping regime by incorporating the effects of dynamic adsorption on bubble formation and stabilisation. It is good to mention that in literature, these two Laplace pressures are rarely discussed separately since they are small and similar in devices with larger dimensions and less prominent for droplets (that have lower interfacial tension). On the other hand, the extreme shallowness also ensures the air flow into the bubble, Q'_{bub}, to be mostly determined by the hydrodynamic flow resistance of the pore. Q'_{bub} is highly insensitive to potential perturbations in pressure and flow (which could otherwise translate into bubble size variation), and further ensures the pressure stability of the device, aiding the production of monodisperse bubbles. As an illustration, neighbouring pores

compete for the, limited, air flow in the low-pressure regime. Yet, except for periodic activation and deactivation of pores, this so-called cross-talking effect does not influence the properties of formed bubbles such as their size and size distribution. This proves the robustness of the partitioned-EDGE device compared to e.g., a parallelised flow-focusing device [95].

4.5. Conclusions

Compared with earlier microfluidic studies that use fast-adsorbing surfactants (e.g., SDS and Tween) to prevent droplet or bubble coalescence [41,47,48,77,126], the partitioned-EDGE device exhibits richer bubble behaviour over time scales that span five orders of magnitude (approximately *0.01-1000 ms*). This behaviour is due to the complementary effects of the key feature of the pore – the extreme shallowness and thus a high pore Laplace pressure –, and the use of slow-adsorbing whey protein. Bubble formation shows two regimes that are distinguished by the *dual* role of protein adsorption, divided by the minimum pressure required to initialise bubble formation in the protein-free system. *In the low-pressure regime*, bubble formation is initialised when adsorbed proteins decrease the Laplace pressure below the actual applied pressure, and accordingly, the bubble formation frequency increases with the applied pressure and the protein concentration. Due to the adsorption delay, bubble formation is relatively slow, allowing for additional protein adsorption to and thus stabilisation of the released bubbles. *In the high-pressure regime*, bubble formation occurs immediately upon applying pressure, essentially without protein adsorption taking place at the meniscus. As a result, the bubble formation frequency increases linearly with the applied pressure, and simultaneously, coalescence increases due to the shorter time available for further protein adsorption. Moreover, the frequency decreases with increasing protein concentration due to the formation of larger bubbles at the pore, and with viscosity, which is ascribed to the increased hydrodynamic flow resistance ($R \sim \eta$) of the continuous phase inflow. In our previous study performed in the same partitioned-EDGE device, we showed that monodisperse bubbles can be formed in both regimes [148]. Here that is proved to occur only at 'moderate' protein concentration (e.g., 5% wt. whey protein) and viscosity, and under these conditions, the initial bubble size mainly increases with the continuous phase viscosity, namely as $d_0 \sim t_n^{1/3} \sim \eta^{1/3}$. However, higher protein concentrations lead to a distinctly higher polydispersity of the initial (due to the formation of both small and large bubbles) and thus also of the final coalesced bubbles – which in first instance is counter intuitive. Lastly, we show here that the coalescence observed in the high-pressure regime, can be effectively suppressed by raising (to some extent) protein concentration and viscosity, to cover the created interface faster and to slow down the destabilisation of the film between bubbles.

The increase in bubble size (Figure 4.6B) due to the prolonged open neck (Figure 4.5D) may be very similar to the transition from dripping to jetting that has been observed under constant

interfacial tension [48,126,145]. The transition from dripping to jetting roughly coincides with the pressure P_{cross} at which pore filling time decreases below the bubble necking time. This means that parameters that influence either the pore filling process or the bubble necking process, such as the device dimension [20,97,139], the continuous phase inflow [143], the continuous phase viscosity (in this study), the emulsifier concentration (also in this study), and mostly the dispersed phase flow rate [48], ultimately play a role on the transition of dripping-jetting. For relatively low protein concentrations in this study, the dripping regime extends up to a very high formation frequency (tens of kHz); the jetting regime has not been observed but may be introduced at even higher pressures that we didn't study here.

Another key feature of the partitioned-EDGE design (i.e., spontaneous design) is that bubble formation is hardly dependent on shear conditions. This allowed us to study a wide range of bubble formation time scales (spanning five orders of magnitude) without changing the continuous phase flow conditions (that could, for example, influence mass transport rates). The available mass of protein for adsorption thus only depends on the chosen protein concentration and the rate of surface creation in time, and not also on continuous phase flow rate or possibly changing mass transfer rate of proteins [52]. Furthermore, the geometry of this pressure-based device allowed us to study bubble coalescence simultaneously with bubble formation at a time scale down to tens of microseconds since bubbles are released and are not immediately carried away by the flow. Compared with other microfluidic designs that decouple coalescence from the formation by accumulating monodisperse bubbles or droplets at a downstream location [4,106,107,111,116,151], the partitioned-EDGE device is believed to provide closer insights into the competing events of bubble (and droplet) formation and stabilisation versus coalescence at the industrially relevant (sub)millisecond time scales. In the current study, we demonstrated the appropriate pressure conditions and fluid properties that lead to the formation of monodisperse bubbles; our next step is to quantitatively study the corresponding bubble coalescence.

4.6. Appendix

4.6.1. Original images for data shown in Figure 4.2B

Table A4.1 shows the high-speed recordings used for extracting the in-plane, negative radii of curvature. We compare the thinning neck at three representative pressures: 1200 (representing the thinning neck at low pressures), 1400, and 1600 mbar (representing the thinning neck at high pressures). At high pressures, the meniscus moves back and forth inside the pore, in contrast to a more static meniscus observed at low pressures (e.g.,1200 mbar), and this is ascribed to a stronger inflow of the continuous phase (indicated by the blue arrows).

Table A4.1. *The raw images recorded with a pixel resolution of 0.402 µm/pixel.*

t (µs) \ P_d^* (mbar)	1200	1400	1600
0.00	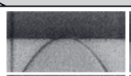	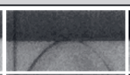	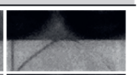
1.43	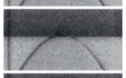	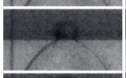	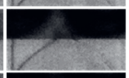
2.86	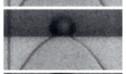	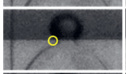	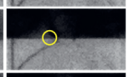
4.29	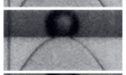	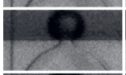	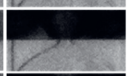
5.72	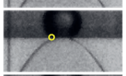	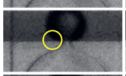	
7.15	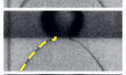	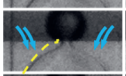	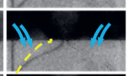
8.58	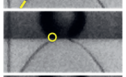	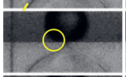	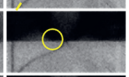
9.80	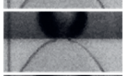	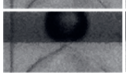	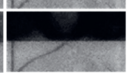
14.30	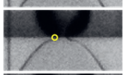		
18.59	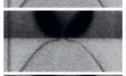		
22.88	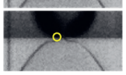		

4.6.2. The air flow rate into the bubble, Q'_{bub}

Figure A4.1 shows that the bubble volume linearly increases with time until the bubble eventually snaps off. Based on the experimentally-derived air flow rate Q'_{bub} (the slope of the plot), it is possible to derive the air flow rates Q_{bub} and Q_{pore} based on gas expansion (using the ideal gas law) and the principles of volume conservation, respectively [148], although

this is out of the scope of the current study. The main conclusion here is that the air flow rate Q'_{bub} is hardly influenced by the applied pressure.

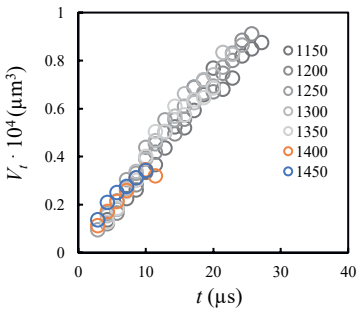

Figure A4.1. *The air flow rate into the growing bubble measured for 2.5% wt. whey protein with 2 mPa·s. Bubble sizes cannot be extracted as function of time for even higher pressures due to bubble crowdedness, which hampers the recognition of the bubble in our image analysis procedure.*

4.6.3. Geometry effect: the pore filling time at low pressures

At low pressures (up to 1400 mbar), the pore filling stage includes a static and an active period. To test whether the active period (i.e., the actual pore flow) contributes to the pore filling time or not, we test three device geometries, which vary in plateau length (L) while keeping the ratio of the pore to the main plateau length (l/L) constant at 20%. In addition, all the pores have 40 µm width and approximately 0.93 µm height. The hydrodynamic flow resistance of a single pore has a ratio of 1:2:4 for the devices with increasing L = 100, 200 and 400 µm. Figure A4.2 shows that the t_{fill} is independent of the hydrodynamic flow resistance of the pore, and thus is dominated by the static period that is determined by the dynamic adsorption of proteins.

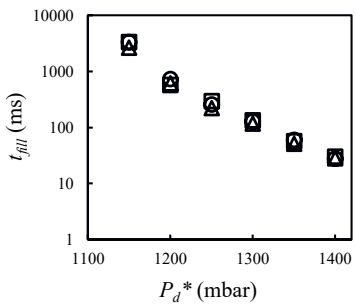

Figure A4.2. *The pore filling time estimated via $1/f_0$. The test was performed with 5% wt. whey protein (2 mPa·s) for devices with (l/L) 20/100 (□), 40/200 (○) and 80/400 (Δ).*

4.6.4. The t_{fill} obtained in a protein-free system

Figure A4.3 shows the filling time of a protein-free system, for pressures starting at 1400 mbar. The protein-free system is adjusted to have the same viscosity as the 2.5% wt. whey protein solution that is shown as a reference (2 mPa·s). The filling time of the protein-free system is slightly lower, in contrast to the constant filling time for all non-zero protein concentrations (1-10% wt., Figure 4.3B).

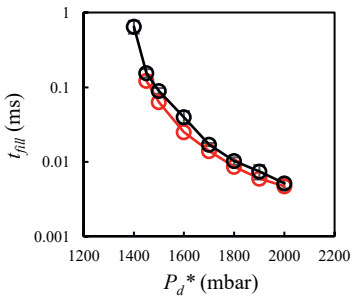

Figure A4.3. *The t_{fill} obtained in a protein-free system (0% wt., red circles). The data for 2.5% wt. whey protein (black circles) is plotted for comparison.*

4.6.5. Finite pixel resolution for small neck widths

Figure A4.4 shows a comparison of neck widths obtained either at our default pixel resolution (0.973 µm/pixel) or at a finer pixel resolution by increasing the magnification (i.e., 0.402 µm/pixel). The results indicate that the plateau observed while using the default settings is due to the limitation of our experimental resolution. It differs from that shown in Figure 4.5D, where the plateau appears due to a prolonged neck thinning process.

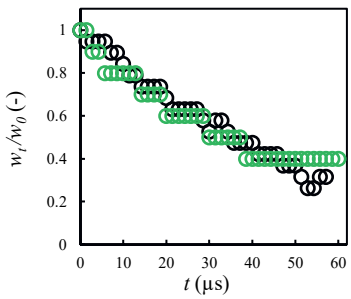

Figure A4.4. *The neck thinning process (at 1200 mbar) analysed with two pixel resolutions for2.5% wt. whey protein with 6 mPa·s. Symbols: green circles (0.973 µm/pixel) and black circles (0.402 µm/pixel).*

4.6.6. Neck thinning process at $P_d^* = 1600$ mbar

The neck thinning is much faster in the high-pressure regime than in the low-pressure regime. In Figure A4.5 we compare the neck thinning process at 1600 mbar with that at 1200 mbar

(filled symbols ●; representing selected data from Figure 4.4D-F). It is noted that the plateau observed in w_t/w_0 at the end of the neck thinning process is ascribed to finite pixel resolution, which is proven in Figure A4.4.

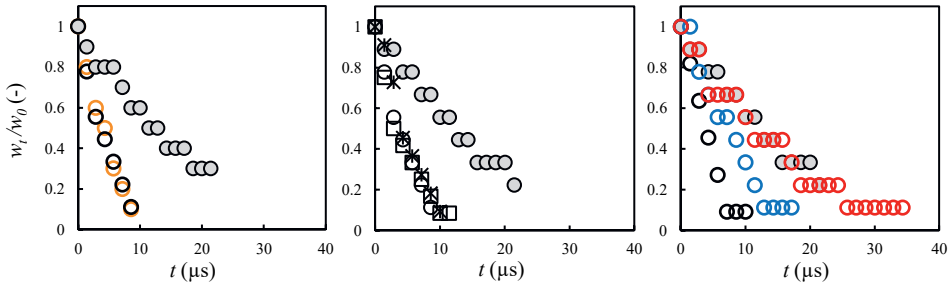

Figure A4.5. *The neck thinning process at 1600 mbar for the effects of continuous phase velocity of 0.50 (○) and 0.93 (○) m/s, protein concentration of 2.5 (○), 5 (□), and 10 (*) % wt., and continuous phase viscosity of 2 (○), 4 (○) and 6 (○) mPa·s. The neck thinning process at 1200 mbar is plotted for comparison (for one selected experimental condition: 2.5% wt. whey protein with 2 mPa·s at 0.93 m/s; ●).*

4.6.7. Scaling with the continuous phase viscosity η

We confirm that t_n scales with continuous phase viscosity, by plotting t_n/η in Figure A4.6A. Since the bubble volume is linear in t_n (from $V_0 = Q'_{bub} \cdot t_n$ with constant Q'_{bub}), the obtained V_0 also scales linearly with the continuous phase viscosity, and $d_0 \sim t_n^{1/3} \sim \eta^{1/3}$. We demonstrate the collapse of $d_0/\eta^{1/3}$ in Figure A4.6B.

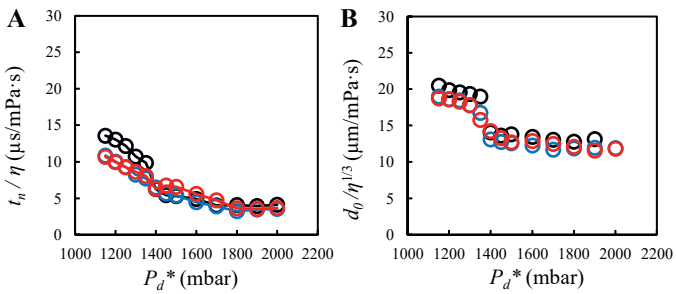

Figure A4.6. *Collapse for t_n/η and $d_0/\eta^{1/3}$. The data corresponds to that shown in Figure 4.4I and Figure 4.6C, respectively. Continue phase viscosity: 2 (○), 4 (○) and 6 (○) mPa·s.*

4.6.8. Bi-dispersed or discrete bubbles

With 10% wt. whey protein, the bubbles obtained at 1250 mbar are almost bi-disperse. Yet, those obtained at 1800 mbar are polydispersed, because bubble detachment is more sensitive to local conditions, such as local pressures and interactions between bubbles growing at neighbouring pores.

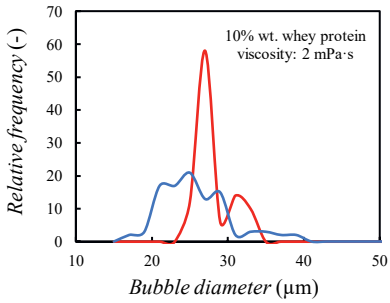

Figure A4.7. *Histogram plot (frequency plot) of bubble diameter for applied pressures of 1250 mbar (red line) and 1800 mbar (blue line).*

4.6.9. The coalesced bubble size

In the current study, the initial bubbles form and further coalesce at the pores in the high-pressure regime (with $P_d^* \geq 1400$ mbar). The extent of bubble coalescence can be tuned with P_d^* and the liquid phase properties that include protein concentration, as well as continuous phase velocity and viscosity. The extent of bubble coalescence and thus the d_{coal} decrease with the increasing continuous phase velocity and protein concentration. In addition, a high continuous phase viscosity can be used to tune bubble coalescence at the expanse of the bubble formation frequency. The d_0 (open circle) is shown for comparison.

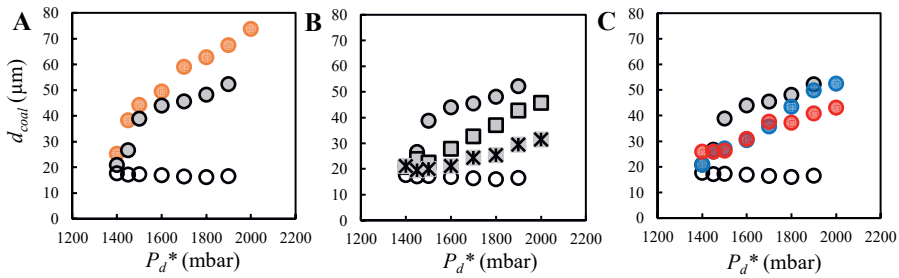

Figure A4.8. *The size of coalesced bubbles as function of P_d^* for the effects of continuous phase velocity of 0.50 (●) and 0.93 (●) m/s (A), protein concentration of 2.5 (●), 5 (■), and 10 (*) % wt., (B), and continuous phase viscosity of 2 (●), 4 (●) and 6 (●) mPa·s (C). Unless stated otherwise, the size of coalesced bubbles is collected under conditions of protein concentration 2.5% wt., viscosity 2 mPa·s, and v_c = 0.93 m/s in the high-pressure regime; under the same conditions, the size (○) of initial bubbles is shown for comparison.*

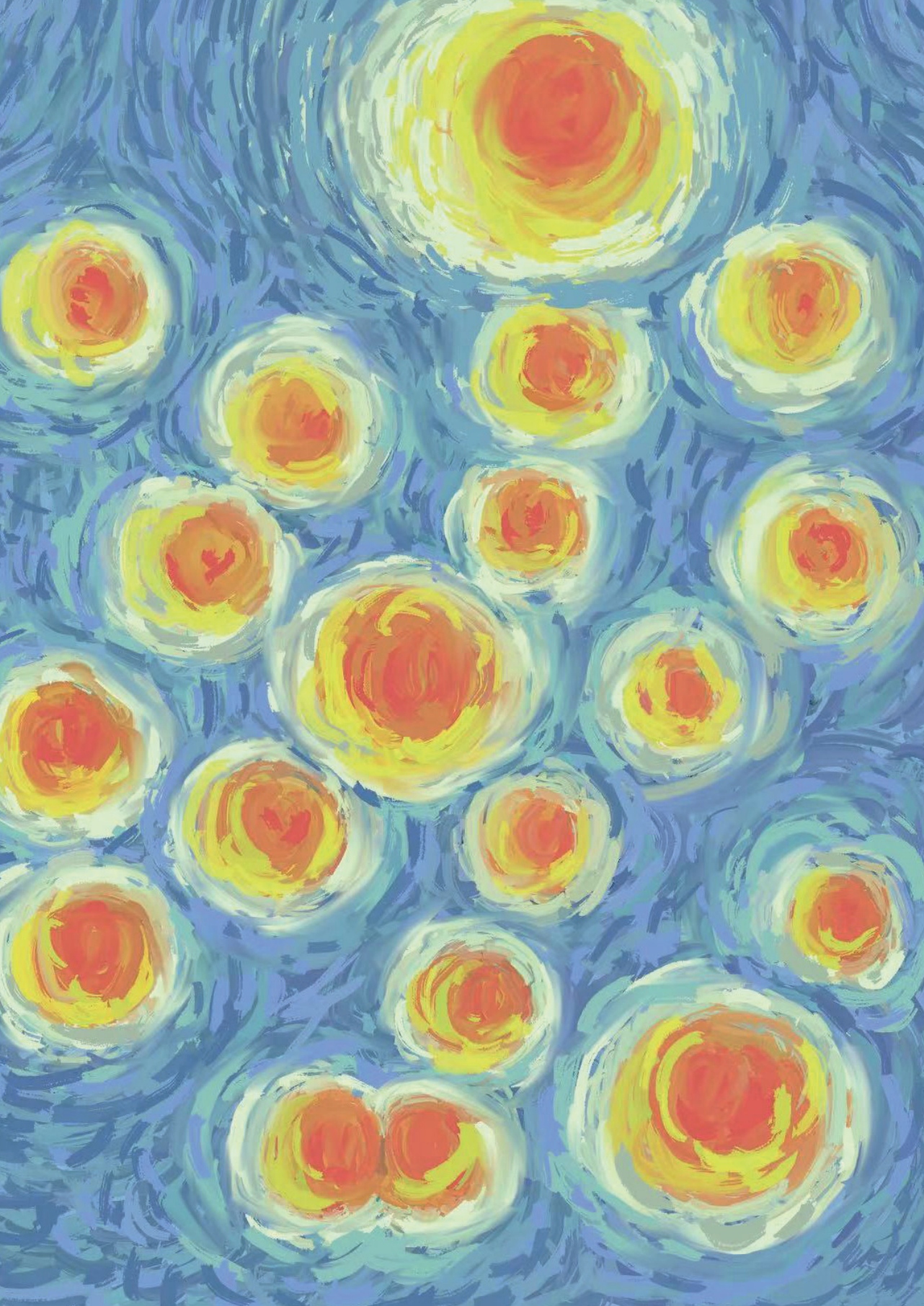

CHAPTER || 5

Capillary pressure-based measurement of dynamic interfacial tension in a spontaneous microfluidic sensor

This chapter has been published as Deng, B., Schroën, K., Steegmans, M., & De Ruiter, J. Capillary pressure-based measurement of dynamic interfacial tension in a spontaneous microfluidic sensor. *Lab on a Chip,* **2022**, 22, 3860-3868.

5.1. *Abstract*

The size of droplets and bubbles, and the properties of emulsions and foams strongly depend on dynamic interfacial tension (γ_d) – a parameter that is often inaccessible due to the very short time scales for droplet and bubble formation, and the inaccessibility of (e.g., food) production lines. To solve this challenge, we developed a microfluidic tensiometer that can measure γ_d by monitoring the formation time of both droplets and bubbles. Our tensiometer is a pressure-driven microfluidic device and operates based on the principle of a pressure balance: the formation of a droplet (or a bubble) is initialised when the Laplace pressure of the interface is decreased below the externally applied pressure, and this decrease is caused by a reduction in γ_d that can be calculated from the applied pressure and the Young-Laplace equation. The decay of γ_d due to emulsifier adsorption can be followed at the characteristic time scale, which is dependent on emulsifier type and concentration. For 0.05-1% wt. sodium dodecyl sulfate (SDS), we were able to measure γ_d at time scales down to *1 ms* and *0.1 ms* for droplet and bubble surfaces, respectively, at increasing applied pressures and SDS concentrations. Our tensiometer proves to be a *simple, robust* method that inherently allows access to nearly the full range of dynamic interfacial tension at relevant time scales.

Graphical abstract

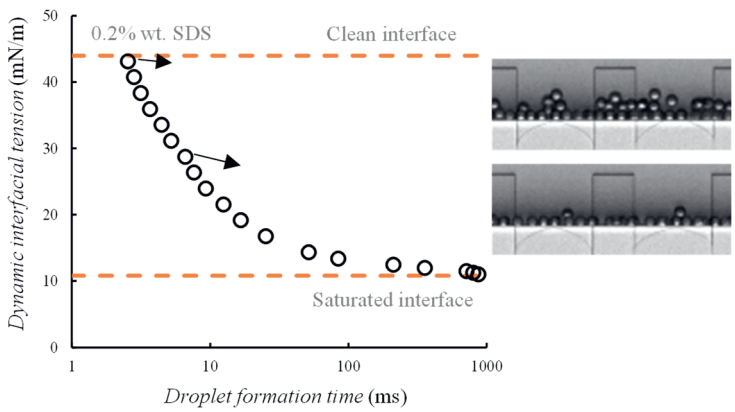

5.2. *Introduction*

Emulsions and foams are common forms of products in the food, cosmetics, and pharmaceutical industries and are dispersions of two (semi-)immiscible fluids that are stabilised by surface-active components (i.e., emulsifiers). Two competing processes occur during emulsification, namely droplet formation and coalescence, and both are influenced by emulsifier adsorption through the resulting *interfacial* tension and interfacial layer formation. The same applies to foaming, during which the dispersed fluid is a gas, thus forming bubbles, and the air-water tension is also referred to as *surface* tension.

Given the critical role of emulsifier adsorption, it is not surprising that often in emulsification and foaming research, an excess of emulsifier is used to dampen the effects of dynamic adsorption and induce a situation that is less affected by the dynamics of emulsifier adsorption and thus requires less tight control of the system [152]. In general, it is assumed that because of the high dosage the interfacial tension does not change throughout the process, and it is expected to be at its equilibrium value. Yet, real systems are often more complex with a wide variety of dispersed phase properties and the types of emulsifiers that may invalidate this assumption. For example, for slow-adsorbing whey protein isolate, we have demonstrated the role of dynamic adsorption (i.e., *dynamic surface tension*) on bubble formation and coalescence [148]. In addition, the interfacial tension controls macroscopic properties of emulsions and foams, such as their rheology and morphology. The measurement of the interfacial tension is thus both scientifically and practically important and must be assessed at the relevant time scales at which the dynamic interfacial tension decreases due to emulsifier adsorption. This characteristic time scale provides an indication of how fast the emulsion or foam will become stable.

The application of microfluidic technology has grown rapidly for the controllable production and the in-depth characterisation of emulsions and foams. Microfluidic tensiometers resting on manipulation of liquid-liquid or gas-liquid interfaces have been proposed for the measurement of dynamic interfacial tension – through so-called *microtensiometry*. With these methods, the dynamic interfacial tension can be measured at (sub)millisecond time scales, which agree with the formation time scales as would occur in industrial-scale emulsification processes. Typically 0.1-30 ms in high-pressure homogenisers and 0.1-100 s in colloid mills [153]. Mostly, shear-based T-junction, Y-junction and co-axial geometries are used to study dynamic interfacial tension based on offline analysis of droplet properties,

which are, typically, the *shape* representing the time-evolving deformability (i.e., droplet rheology) [23,49,50,57,154] or the *size* determined by a force balance between the interfacial tension force and the viscous drag force in the dripping regime of droplet formation [37,51–53,55,155,156]. The dynamic interfacial tension can be measured also during droplet formation in the transition or squeezing regime, based on a force balance between the interfacial tension force and the externally controllable pressure drop, which is called the 'pressure drop-based' measurement [54–56]. For all the above-mentioned scenarios, the dynamic interfacial tension is a result of emulsifier adsorption and linked to the size-dependent droplet formation time. A third measurement principle relies on monitoring the movement of an interface in a microfluidic channel or a microcapillary as driven by emulsifier adsorption, and the dynamic interfacial tension can be calculated from the Young-Laplace equation (i.e., capillary pressure). In this case, the dynamic interfacial tension can be linked to an emulsifier-dependent droplet formation time [132,157].

To widen the applicability of microfluidic tensiometers, it is crucial to improve their measurement accuracy and consolidate their measurement at (sub)millisecond time scales that are relevant to industrial processes. Though various measurement principles have been exploited, the aforementioned studies have been conducted either in shear-based devices that rely on very tight control of the flow fields and the physiochemical properties of the two phases (e.g., viscosity) to precisely control droplet formation (e.g., frequency and size) or in microcapillaries that require a highly accurate pressure sensor. In addition, complex theoretical models with fitting parameters through calibration curves are usually needed to describe the relationship between the droplet properties and the dynamic interfacial tension [158]. Moreover, the microfluidic tensiometers have been mainly characterised for droplet surfaces, yet, the characterisation for bubble surfaces has received less attention [57,156,157,159].

In this study, we introduced a spontaneous microfluidic tensiometer, which can be used for the measurement of dynamic interfacial tension in both droplet (i.e., o/w interface) and bubble (i.e., a/w interface) formation systems. This method has three strong points: First, the dynamic surface tension is directly calculated from the Young-Laplace equation, which avoids possible compressibility effects associated with bubble formation [154]. Second, the emulsifier-dependent time scales are determined from the formation frequency of droplets and bubbles, which is a fast and unambiguous analysis. Third, and most importantly, the measurements are independent of the formation processes of individual droplets and bubbles.

Thus, the method does not require tight control of continuous phase velocity and physiochemical properties of the two phases – only a tight control of the pressure drop across the meniscus in the pores, which sets the formation frequency and thus the time scale. To prove the robustness of our tensiometer, the results of dynamic interfacial tension versus emulsifier-dependent time scales were compared with those obtained by Muijlwijk et al. (2016) [53] with both a shear-based microfluidic tensiometer (Y-junction) and a macroscopic automatic drop tensiometer (ADT).

5.3. Experimental

5.3.1. Materials

Air and anhydrous hexadecane (> 99% purity, Sigma-Aldrich, USA) were used as the dispersed phase for bubble and droplet formation, respectively. Aqueous solutions of 0.05-1% wt. sodium dodecyl sulfate (SDS; > 99% purity, Sigma-Aldrich, USA) were prepared in ultrapure water (Milli-Q, Merck Millipore) and used as the continuous phase. For the microfluidic experiments, all aqueous solutions were filtered using 0.22 µm PES filters (Merck, Germany) before use.

5.3.2. Microchips and set-up

Custom-designed Edge-based Droplet GEneration microchips with partitioned plateaus (partitioned-EDGE) were produced by Micronit Microtechnologies B.V. (Enschede, the Netherlands). They were previously used to study droplet formation [42], as well as the formation and coalescence of bubbles [148]. In this study, the partitioned-EDGE microchip is further developed as a *sensor* for dynamic interfacial tension measurements, based on Laplace-pressure driven formation of droplets and bubbles in this device. The Young-Laplace pressure of a meniscus (ΔP_L) is defined in equation 5.1, where γ is the interfacial tension, R_1 and R_2 the principal radii of curvature, and θ the contact angle outside the meniscus (the walls of the device are wetted by the continuous phase).

$$\Delta P_{L,pore} = \gamma \left(\frac{1}{R_1} + \frac{1}{R_2} \right) \cos(\theta) \qquad 5.1$$

The partitioned-EDGE microchip consists of two deep channels, one straight channel for the dispersed phase and one meandering channel for the continuous phase (Figure 5.1A). The deep channels are connected in the parallel-running section by a shallow plateau of 200 µm length (L) and 500 µm width (W). The shallow plateau is further partitioned into eight identical parallel pores with 20 µm (or 40 µm) length (l); these pores have a rectangular cross-section with 40 µm width (w) and a very shallow height (h). The plateau and pores have h = 1 or 0.93 µm. Unless stated otherwise, a microchip with l = 20 µm and h = 1 µm was used for bubble formation and that with l = 40 µm and h = 0.93 µm was used for droplet formation. The layout of the shallow plateau and pores is shown in Figure 5.1B. A meniscus is formed in each pore, with R_1 and R_2 in equation 5.1 corresponding to the half-width (Figure 5.1C)

and half-height (Figure 5.1D) of the pore, respectively; equation 5.1 is further simplified as $\Delta P_{L,\,pore} = \frac{2\gamma}{h}\cos(\theta)$ due to $w \gg h$.

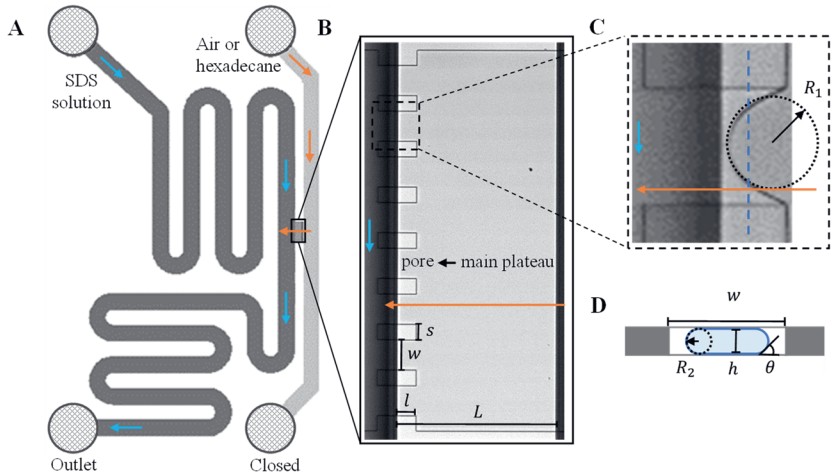

Figure 5.1. *A. Schematic illustration of the layout of the partitioned-EDGE device. B. A microscopy image of the main plateau and pores. C and D illustrate the two radii of curvature across the meniscus with C the top-view (microscopy) and D the head-on view of the pore (schematic, for the location indicated by a dashed blue line shown in C, not drawn to scale). In A-C, it is noted that the partition features extend into the continuous phase channel, yet at that side of the main plateau they do not interfere with droplet or bubble formation as their height (h) is much smaller than that of the deep channel; the flow of the continuous and dispersed phase is indicated by blue and orange arrows, respectively.*

The microchip was put in a chip holder (Fluidic Connect 4515, Micronit Microfluidics) and connected to the dispersed and continuous phases using PEEK tubing (0.75 mm, BGB®, Switzerland). The dispersed and continuous phases were pressurised at P_d and P_c using a digital pressure controller via Smart Interface Software (Elveflow®, France). The resulting effective pressure difference across the shallow region (main plateau with pores) is $P_d^* = P_d - P_c/2$ with $P_c/2$ representing the pressure half-way the meandering channel. When the outlet of the dispersed phase is closed, the dispersed phase flows onto the main plateau and into the pores, and forms droplets or bubbles in the continuous phase. When operating the sensor, P_d^* is varied while P_c is kept constant at 100 mbar to transfer the generated droplets or bubbles away from the pores, avoiding any effects related to variations in shear flow.

5.3.3. Data analysis

Videos and images were recorded with a high-speed camera (FASTCAM SA-Z, Photron Limited, Japan) connected to an inverted microscope (Axiovert 200 MAT, Carl Zeiss B.V., the Netherlands). In each experiment, two videos were recorded (at a frame rate of 100,000

fps and 700,000 fps, respectively) for the measurement of formation frequency (f_0) at each pore, and the analysis of time scales, in particular, pore filling time (t_{fill}) and neck thinning time (t_n) during bubble and droplet formation. Typically, f_0 was obtained by counting the number of bubbles or droplets formed at the pore within a set period of time, and $1/f_0 = t_{fill} + t_n$; the f_0 value was averaged over three independent recordings and thereafter the eight pores on the plateau. t_n was obtained by counting the number of frames taken by the neck thinning process, and t_{fill} represents the lag time between two subsequent neck thinning processes as will be discussed below.

5.4. Results and discussions

5.4.1. General formation behaviour of bubbles and droplets

Bubble formation

Bubble formation shows a low- and a high-pressure regime, delineated by the Laplace pressure for a emulsifier-free meniscus (i.e., the transition pressure, P_{tran}) [148]. This transition pressure P_{tran} is set by the characteristic dimension of the device (typically, h) and the surface tension of the two-phase system (γ_0) that is independent of the type and concentration of the emulsifier. For an a/w meniscus in a 1 μm pore, $P_{tran} \approx 1400$ mbar (point b in Figure 5.2A). Moreover, the low-pressure regime is bounded on the lower side by a breakthrough pressure (point a in Figure 5.2A) that corresponds to the Laplace pressure for a saturated meniscus and thus is dependent on the type and concentration of the emulsifier. For example, the breakthrough pressure significantly reduces from 1310 mbar for 0.05% wt. SDS to 800 mbar for 1% wt. SDS (Figure A5.2A). For whey protein isolate (WPI), the breakthrough pressure is much higher e.g., 1050 mbar for a high concentration of 10% wt. WPI [160] due to the higher equilibrium surface tension compared to that of SDS.

Furthermore, we zoomed in on bubble formation dynamics at the pore, and typically, a single bubble formation cycle can be separated into two stages, which are the pore filling stage and the subsequent bubble necking stage. The corresponding time scales are t_{fill} and t_n. In the low-pressure regime ($P_d^* < P_{tran}$), the pore filling stage further consists of two sub-processes: first, emulsifier adsorption to the *static* meniscus (inset in Figure 5.2B, location 1) and, second, pore flow. Dynamic adsorption is required to lower the surface tension and thus the Laplace pressure across the *static* meniscus, resulting in a lag period. When the Laplace pressure reaches the applied pressure (i.e., $\Delta P_{L,\,pore} = P_d^*$), the pore flow process and the subsequent bubble necking stage are initiated. Specifically, the (partially-) covered meniscus advances towards the edge of the pore (inset in Figure 5.2B, location 1→2), leaps over it, and forms a bulb that expands in volume while the neck that connects the bulb to the supplying pore shrinks during a time scale t_n (inset in Figure 5.2B, location 2→3). When the neck width decreases below the pore's height, the neck quickly snaps off and a bubble (with V_0) is released into the continuous phase. Simultaneously, the meniscus relaxes rapidly (which benefits from the small surface area of the meniscus constricted in the pore) and returns to an approximately half-circular shape in less than 10 µs (i.e., return to location 1). During one

bubble formation cycle, the location profile of the meniscus is 1 → 2 → 3 → 1. The pore filling time t_{fill} is typically much larger than the bubble necking time t_n, and t_{fill} markedly decreases with the applied pressure P_d^* (Figure 5.2A) since increasingly higher surface tension is sufficient to enable $\Delta P_{L,\,pore} = P_d^*$. Next to that, t_{fill} decreases as SDS concentration increases (Figure A5.2B).

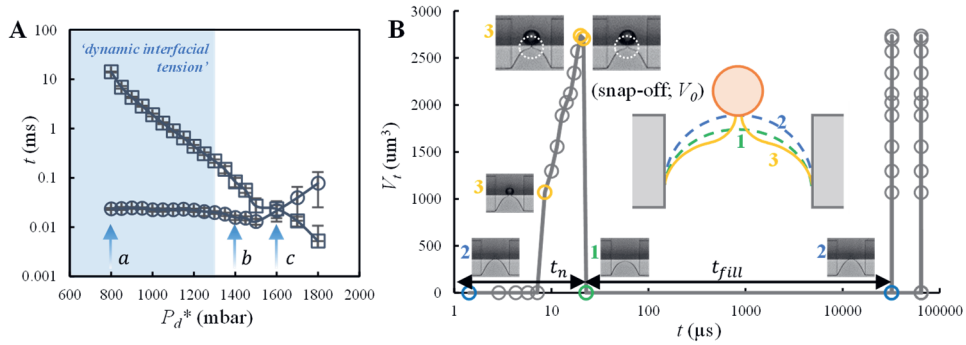

***Figure 5.2**. Bubble formation with 0.5% wt. SDS. A. The two time scales versus the applied pressure: pore filling time (□) and necking time (○). The range of interest of applied pressures for the measurement of dynamic interfacial tension is shaded with blue colour. The letters point to the breakthrough pressure (a), the transition pressure (b) and the pressure (i.e., the cross-over pressure) above which instability can be observed during bubble (or droplet) formation (c; will be discussed below). B. The temporal evolution of bubble volume for three bubble formation cycles at P_d^* = 800 mbar. Note that during the first cycle, the first few V_t data points of the growing bubble are missing (shown as zero) since the bulb is too small to be captured by the image analysis software. Inset: schematic of the shape of the meniscus during one bubble (or droplet) formation cycle: 1 – represents the moment when the meniscus starts moving; 1 → 2 – represents the pore filling process; 2 → 3 → 1 – represents the bubble necking process and the meniscus relaxation (upon bubble snap-off). Snapshots are shown; the numbers refer to those defined in the inset.*

In the high-pressure regime ($P_d^* \geq P_{tran}$), pore flow is instantaneously initiated upon applying pressure, since lowering the Laplace pressure of the meniscus, and thus emulsifier adsorption, is not required. Although this regime is interesting for the extremely fast bubble formation [148], and the rich behaviour of possible coalescence events and instabilities [160], it cannot be used for tensiometry due to the absence of necessary emulsifier adsorption to the meniscus.

Droplet formation

Two pressure regimes were previously reported for droplet formation in similar EDGE devices [42], namely based on variations in droplet size and the size distribution against applied pressure. It was found that in the low-pressure regime, monodisperse droplets with a coefficient of variation below 3% are formed; and the droplet size remains mostly constant with applied pressure. When the formation transits to the high-pressure regim7e, an increase is observed in both the mean droplet size and the size distribution [42]. In the current study, we

found that droplet formation shows a breakthrough pressure like bubble formation, and the breakthrough pressure also decreases as the SDS concentration increases. For example, it shifts from 600 to 155 mbar when the SDS concentration is increased from 0.05 to 1% wt. However, in contrast to bubble formation, we found that the transition pressure between the two regimes also decreases with the SDS concentration. For $c_{SDS} < 0.5\%$ wt. the transition pressure is still constant, and – similar to the case of bubble formation – set by the Laplace pressure for the pure hexadecane-water interface (i.e., 900 mbar). On the other hand, for $c_{SDS} \geq 0.5\%$ wt., the transition pressure decreases (far) below this Laplace pressure. Instead, the transition accompanied by an increase in droplet size and polydispersity occurs close to the cross-over pressure (P_{cross}) at which t_{fill} decreases below t_n – as illustrated for bubbles by point *c* in Figure 5.2A [160]. In this case for droplets, however, this cross-over pressure is smaller than the Laplace transition pressure ($c < b$). This observation is most likely due to the much slower formation of droplets, which is caused by the markedly higher viscosity of the hexadecane than the air phase (i.e., a factor of approximately 200).

To conclude, in the current study, we *only* focus on the low-pressure regime – irrespective of the nature of this transition –, to measure the dynamic interfacial tension as function of the emulsifier-dependent lag time. We have studied the formation of bubbles to measure dynamic surface tension at an *a/w* interface, and the formation of droplets to measure dynamic interfacial tension at an *o/w* interface. Our microfluidic tensiometer is termed after the microfluidic device – 'EDGE tensiometer'

5.4.2. 'EDGE tensiometer' for dynamic interfacial tension measurement

In this section, the results are discussed following the sequence: (1) the method definition, focusing on the measurement principles and the accuracy analysis of the EDGE tensiometer; 2) the method validation, comparing the dynamic interfacial tension decay versus the emulsifier-dependent time scales with known dynamics reported in the literature.

Measurement principles

In the low-pressure regime of the partitioned-EDGE device, the time scale of droplet or bubble formation is dominated by that for emulsifier adsorption to the meniscus in the pore. The applied pressure sets the 'final goal', namely the (dynamic) interfacial tension at which droplet or bubble formation starts. While the reached γ_d value is thus independent of the composition of the continuous phase, namely the type and concentration of emulsifier, it is

obtained via dynamic adsorption through a *lag time* τ that is emulsifier-dependent. τ can be well approximated by the droplet or bubble formation time $1/f_0$, with f_0 the formation frequency. In doing so we neglect the time scales for the pore flow (i.e., meniscus motion after adsorption) (Figure A5.1-1) and the neck thinning (Figure A5.1-2), which are both much smaller than the lag time. The dynamic interfacial tension, γ_d, at the moment that the pore flow is initiated, can be derived from the Laplace pressure of the meniscus constricted in the shallow pore, as discussed above, and expressed as equation 5.2:

$$\gamma_d = \frac{hP_d^*}{2\cos(\theta)} \qquad 5.2$$

The time-dependency of the dynamic interfacial tension is captured by varying the applied pressure P_d^* and measuring $\tau = 1/f_0$, for each pressure condition. In equation 5.2, the contact angle is prescribed as 15°. It is assumed that after the necking stage, during which the meniscus expands significantly and a droplet or a bubble is released, an essentially clean interface is created.

Measurement accuracy analysis

For accurately known channel height h, there are two variables in equation 5.2 that might influence the accuracy of the calculated γ_d values, which are the applied pressure P_d^* and the contact angle θ. First, the accuracy of the applied pressures, determined by the resolution of the pressure control system, is as low as 0.1 mbar in this study. Accordingly, the dynamic interfacial tension can be measured at a resolution of 0.005 mN/m. It is also important to realise that our applied pressures are not influenced by additional dynamics, for example, the equilibration of the interface as was reported for other pressure methods (e.g., a micropipette interfacial area-expansion method) [157]. Second, for a variation of 5° or 10° around a contact angle of 15°, the maximum variation in the dynamic interfacial tension is approximately 1.2 or 2.8 mN/m, respectively. This means the assumed contact angle represents a realistic hydrophilic glass surface, in both droplet and bubble systems [88,92]. To guarantee good measurement accuracy of γ_d, it is important to measure the contact angle for each experimental condition, and ideally use a system with low contact angle of the continuous phase as $\cos(\theta)$ is less sensitive to variations in θ when θ is closer to zero.

On the other hand, the accuracy of the determined adsorption time scale is set by the magnitude of time scales of pore flow and neck thinning that we neglect with respect to adsorption lag time. In the typical case of P_d^* far away from the transition pressure, the determined adsorption time scale is indeed exact. Yet, t_n becomes comparable to the adsorption lag time at applied pressures just below the transition pressure – when the dynamic interfacial tension approaches the equilibrium value of the pure interface. In this case, to improve the accuracy of the adsorption lag time τ, it should be approximated as t_{fill}, namely by subtracting the necking time from $1/f_0$. The reproducibility of the measurements is shown in Figure A5.3.

Method performance

Dynamic interfacial tension at the o/w interface

The dynamic interfacial tension, γ_d, is plotted against the droplet formation time for SDS concentrations in the range of 0.05-1% wt. Figure 5.3A clearly demonstrates that the number of droplets formed within a set period of time, and thus the droplet formation frequency, increases as the applied pressure increases. In Figure 5.3B, as the applied pressure decreases (following the direction of the arrow), a lower dynamic interfacial tension is required to push the Laplace pressure below the applied pressure ($\Delta P_{L,\,pore} \leq P_d^*$) and thus a longer lag time is needed for emulsifier adsorption to take place.

With the EDGE tensiometer we retrieve the well-known dynamics of SDS adsorption in the hexadecane-water (o/w) system. The γ_d values are between the interfacial tension for the bare (γ_0 = 44 mN/m) and that for the saturated hexadecane-water interface, with the latter depending on emulsifier concentrations. In the rapid fall region typically below 10 ms in Figure 5.3B, the adsorption rate increases with SDS concentration, and accordingly, the γ_d value at a fixed lag time decreases as the SDS concentration increases up to 1% wt. This is ascribed to the increased number density and fast disaggregation of SDS micelles [37,52,54], which results in an increasingly higher availability of SDS monomer as SDS concentration increases above c_{cmc}. After the initial decrease, γ_d converges to a plateau phase due to the fact that the interface gradually approaches saturation and the activation barrier for adsorption increases [9]. At the end of this plateau phase, an equilibrium interfacial tension (γ_{eq}) is assumed to be reached. Figure 5.3B shows that γ_{eq} decreases with the SDS concentration, and levels

off for SDS concentrations above 0.3% wt., which is just above the critical micelle concentration, c_{cmc} = 0.28% wt. This is in good agreement with literature, where a constant interfacial tension was obtained for SDS concentrations with $c/c_{cmc} > 1.4$ [37].

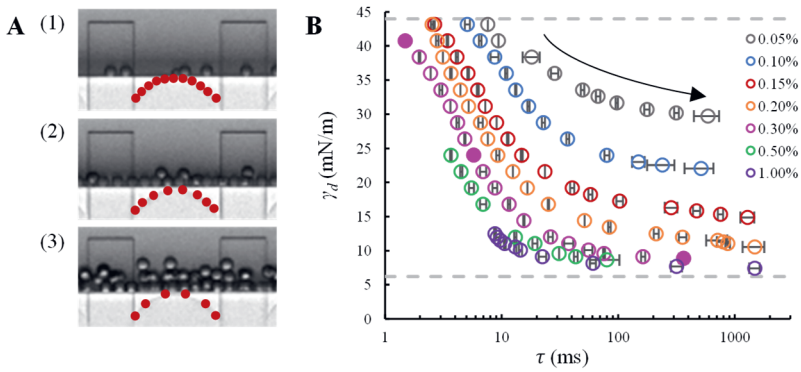

Figure 5.3. *A. Snapshots of droplet formation in the low-pressure regime at three increasing applied pressures: (1) 185 mbar, (2) 500 mbar, and (3) 900 mbar. In B, from right to left, the data from these snapshots are shown with filled circles, recorded in the presence of 0.3% wt. SDS (pink). The red dots on the meniscus schematically represent the relative amount of SDS molecules at the initiation of pore flow. B. Dynamic interfacial tension versus the lag time at the o/w interface for a series of SDS concentrations. The applied pressure decreases along each curve (top to bottom indicated by the arrow), with the initial and end pressures, namely the breakthrough and transition pressure, depending on the SDS concentrations. Dashed lines: (upper) interfacial tension for the bare interface and (lower) interfacial tension for the saturated interface with SDS concentration above c_{cmc}. Error bars (here and below) indicate the uncertainty in bubble formation time for repeated recordings; mostly, the error bars are smaller than the symbols.*

Dynamic surface tension at the a/w interface

The dynamic surface tension is plotted against the bubble formation time for the same range of SDS concentrations. Like the case of droplet formation, as the applied pressure decreases (indicated by the arrow), a longer lag time is needed for emulsifier adsorption to lower the γ_d and thus the Laplace pressure to lower values; at a fixed lag time, γ_d decreases as the SDS concentration increases (Figure 5.4A). We also retrieve the well-known dynamics of SDS for the air-water (a/w) system. The dynamic surface tension decreases from 72.4 mN/m for the bare air-water interface to the value for the saturated air-water interface, which varies for SDS concentrations below c_{cmc}. Yet, although γ_d tends to level off at low applied pressures for SDS concentrations above 0.3% wt., an obvious plateau phase is not (yet) observed.

The performance of the EDGE tensiometer is compared for the o/w and a/w interfaces. In doing so, a normalised interfacial tension (γ_n) was calculated using equation 5.3.

$$\gamma_n = \frac{\gamma_d - \gamma_{eq}}{\gamma_0 - \gamma_{eq}} \qquad 5.3$$

The normalised interfacial tension is plotted against time for two SDS concentrations. In line with literature [161], the γ_n values are lower for the o/w interface than the a/w interface, and their variation spans over a wider range of (normalised) tensions, especially on the low end due to the difference in pinning of the meniscus (Figure 5.4B). The minimum γ_d that can be measured depends on the minimum applied pressure that can keep the meniscus constricted in the pore, and still allow the pore flow and the subsequent droplet or bubble formation process to take place. In the droplet formation system, the applied pressure can be reduced very closely to the pressure that corresponds to the equilibrium interfacial tension of a saturated interface, and this allows us to monitor the long-time behaviour of γ_d entirely. However, in the bubble formation system, the meniscus retracts from the pore when the applied pressure reduces to a critical value, which increases significantly with decreasing SDS concentrations (below c_{cmc}). The pressure corresponding to the saturated interface then cannot be fully reached. This discrepancy is likely due to contact line pinning, or the lack thereof, which is a resisting force (against the retraction) that is proportional to the dispersed phase viscosity and thus 100 times lower for air than hexadecane [162].

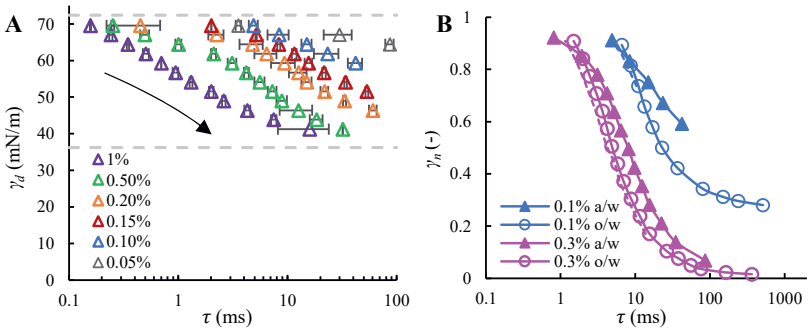

Figure 5.4. *A. Dynamic surface tension versus the adsorption lag time at a/w interface for a series of SDS concentrations (same as shown in Figure 5.3B). Dashed lines: (upper) interfacial tension for the bare interface and (lower) interfacial tension for the saturated interface with SDS concentration above c_{cmc}. B. Comparison of SDS adsorption towards a/w and o/w interfaces. Empty circles: o/w interface; filled triangles: a/w interface. The equilibrium interfacial tension values were concentration-specific for o/w and a/w interfaces, respectively, and taken from [53] and [71], respectively. In B, dashed lines for the o/w cases: corrected adsorption time after subtracting the necking time.*

On the high end of the monitored tensions, the much higher viscosity of the hexadecane phase leads to a slight overestimation of the time scale τ when using the approximation by $1/f_0$ since the necking process is relatively slow with this more viscous dispersed phase. This can be solved by an additional analysis step, namely by measuring and subtracting the necking time (dashed lines in Figure 5.4B). Lastly, in the droplet formation system, for high SDS

concentrations above c_{cmc} (i.e., 0.5 and 1% wt., shown in Figure 5.3B) a transition from monodisperse to polydisperse droplet formation is obtained earlier that inhibits measuring at applied pressures that approach the maximum γ_{eq} of the bare interface.

Method comparison

The EDGE tensiometer is compared with two other tensiometry techniques, namely the shear-based microfluidic Y-junction, in which dynamic interfacial tension is derived from droplet size that is determined by a force balance, and the conventional automatic drop tensiometer (ADT), in which dynamic interfacial tension is determined from the interface shape of a millimetric droplet subjected to gravitational and interfacial tension forces under quiescent conditions. The flow condition of the continuous phase and the location for emulsifier adsorption in these methods have been sketched in Figure 5.5A. The comparison is made based on four concentrations, which are 0.05, 0.1, 0.3 and 1% wt. SDS.

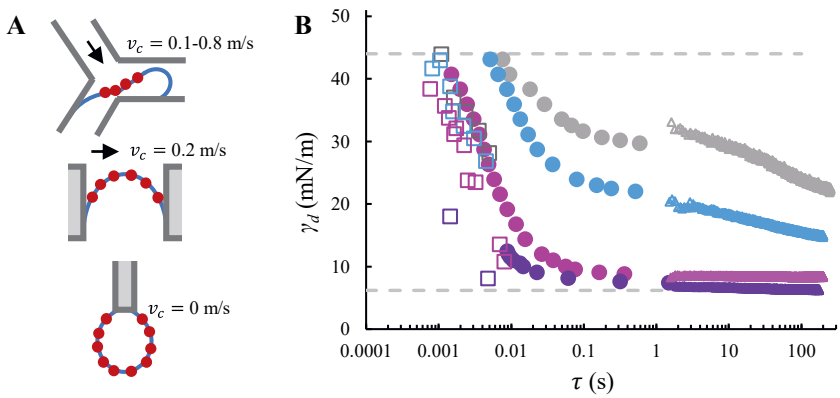

Figure 5.5. *Method comparison. A. Schematics of adsorption locations in Y-junction, EDGE tensiometer and ADT technique. The red dots represent SDS molecules. From top to bottom: the characteristic (i.e., smallest) dimension is tens of micrometers, one micrometer, and a few millimeters. The schematics are not drawn to scale. B. Dynamic interfacial tension versus time obtained with Y-junction (□□□□), EDGE tensiometer (●●●●), and ADT technique (△△△△). The comparison is illustrated with four SDS concentrations: 0.05 (grey), 0.1 (blue), 0.3 (pink) and 1 (purple) % wt. The data sets for Y-junction and ADT are adapted from Muijlwijk et al. (2016), with permission from Elsevier* [53].

Figure 5.5B clearly highlights that nearly the full range of the dynamic interfacial tension decay from γ_0 to γ_{eq} can be assessed in the EDGE tensiometer and Y-junction; moreover, the EDGE tensiometer allows the assessment of dynamic interfacial tension of a saturating interface (which corresponds to the plateau phase), which is beyond the range accessible by the Y-junction. In the EDGE tensiometer, the dynamic interfacial tension is measured at time scales that are inherently needed for emulsifier adsorption. In the Y-junction, the time scale

is determined by the force balance (i.e., which determines the droplet snap-off), and γ_d at higher time scales (> 10 ms) are inaccessible due to the limitation of the dripping regime. Using the ADT technique, the accessible time scale is simply the rate of data capture; and γ_d values at lower time scales are inaccessible as the concentration-dependent decrease of γ_d is much faster than the time required to refresh the interface, and the data capture is started, which is typically after 1 second (i.e., experimental resolution).

In terms of time scales, the EDGE tensiometer data overlaps with the extremities of the other two data sets. At the lower end of the time scales accessible with the EDGE tensiometer ($\tau <$ 10 ms), agreement is observed with the Y-junction data in terms of the decreasing trend in γ_d as function of time (Figure 5.5B). In the Y-junction, the obtained γ_d values are consistently lower than those obtained with the EDGE tensiometer at the same time scale. This is due to the continuous phase flow and the resulted (stronger) convective transfer of SDS towards the dilute interface [37,101]. At the upper end of the time scales accessible with the EDGE tensiometer ($\tau \sim 1$ s), the EDGE tensiometer data stitches together with the ADT data, for SDS concentrations in the range of 0.1-1% wt. In the presence of only the lowest concentration that is 0.05% wt. SDS, a lower γ_d is obtained with the EDGE tensiometer. This discrepancy suggests that emulsifier adsorption is likely dominated by distinct mass transfer mechanisms, depending on the emulsifier concentration used. When the emulsifier concentration is low (e.g., 0.05% wt.), the dynamic interfacial tension decay follows a diffusion-controlled mass transfer mechanism and the radius of the curved interface is a key parameter [135]. In the EDGE tensiometer, dynamic adsorption is enhanced since the mass transfer distance (i.e., the depletion depth) is shorter for a highly-curved interface (i.e., the meniscus is confined in a micrometre-sized pore) [50,163]. This results in a faster decay in the dynamic interfacial tension and thus a lower γ_d at $\tau \approx 1$ s, compared to the ADT data. On the other hand, when the emulsifier concentration is higher (i.e., > 0.1% wt. in this study), dynamic adsorption is enhanced by the bulk concentration and the kinetics of emulsifier adsorption at the interface plays an important role. We have calculated the characteristic time scales for mass transfer (Figure A5.4), and it is found that the adsorption time (at the interface) is longer than the diffusion time (from the bulk phase to the sub-interface), which is in line with literature [155]. This indicates that at these higher concentrations, emulsifier mass transfer is either mixed diffusion-kinetic controlled [164] or purely kinetic-controlled [55]. Besides, as the interface gradually approaches saturation (e.g., at $\tau \approx 1$ s), the adsorption barrier may also

slow down the adsorption of SDS monomers, which is also responsible for the transition from diffusion- to kinetic-controlled mass transfer mechanism [9]. For 0.1% wt., emulsifier mass transfer is likely mixed diffusion-kinetic controlled; γ_d continues to decrease at $\tau > 1$ s and reaches an equilibrium value that is lower than the γ_d values accessible with the EDGE tensiometer. This explains that γ_n does not reach zero for 0.1% wt. in Figure 5.4B.

The EDGE tensiometer stands out from the existing microfluidic tensiometers in multiple aspects. First, the EDGE tensiometer is simple and universal since no complex theoretical models or sophisticated calculations are needed. Second, the dynamic interfacial tension is linked to the adsorption lag time – which can be approximated as the droplet or bubble formation time in this device – which makes the method insensitive to produced droplet or bubble size and continuous phase properties (e.g., velocity and viscosity [160]). Third, the adsorption lag time inherently covers the full decrease of dynamic interfacial tension from γ_0 to γ_{eq}, as the low-pressure regime in this device is bounded by the Laplace pressures of the (nearly) empty and saturated interfaces. Fourth, both o/w and a/w interfaces can be characterised; in the latter case, the dynamic surface tension can be estimated without any correction for compressibility. Last but not least, the geometrical characteristics of the partitioned-EDGE device allow us to work with multiple tensiometers (i.e., multiple pores) at the same time: the time scale obtained from a single experiment is an averaged value (here, from eight parallel tensiometers) leading to a high accuracy and a high statistical efficiency.

5.5. Conclusions

In the *partitioned-EDGE device*, bubbles and droplets are formed in two pressure regimes [42,148]. The low-pressure regime is typically bounded by the Laplace pressures of the empty and saturated interfaces, and therefore suitable for tensiometry. To initiate the formation of bubbles and droplets, the Laplace pressure needs to be decreased below the applied pressure, and this is caused by a reduction in the dynamic interfacial tension due to emulsifier adsorption. The dynamic interfacial tension can be calculated from the Young-Laplace equation and linked to the adsorption lag time τ, which can be estimated from the – easily monitored – formation frequency.

We studied droplet and bubble formation in the presence of 0.05-1% wt. sodium dodecyl sulfate (SDS), and *for the first time* introduced a microfluidic tensiometer based on a *spontaneous* device – the 'EDGE tensiometer', where the continuous phase flow is only used for carrying the generated droplets and bubbles away from the sensor. In the EDGE tensiometer, τ is emulsifier-dependent (i.e., the type and concentration); emulsifier adsorption is enhanced due to the highly-curved interface and the high bulk concentration. It is found that τ varies in the range of *1-1500 ms* and *0.1-90 ms* in terms of droplet and bubble surfaces, respectively, with increasing applied pressures and SDS concentrations. This range of time scales intersects with that encountered in industrial scale high-pressure homogenizers (0.1-30 ms) [153], which implies that the EDGE tensiometer provides insights that not only help scientists understand the effect of dynamic adsorption on droplet and bubble formation (and coalescence), but also can be applied to design industrial processes in a more efficient way, for instance making better use of emulsifier materials.

5.6. Appendix

5.6.1. Crucial pre-conditions

The time for one bubble formation cycle (τ) can be estimated by $1/f_0$, which includes three consecutive contributions: (1) the time required for emulsifier adsorption; (2) the time during which the pore is filled (i.e., forward motion of the meniscus); (3) the necking time t_n during which the bubble grows and the neck contracts. Both (1) and (2) contributions are included in pore filling time, t_{fill}. For the interfacial tension analysis, the dynamic interfacial tension (γ_d) calculated using the Young-Laplace equation and applied pressure (P_d^*) should be expressed as function of only the time for emulsifier adsorption (i.e., the so-called *adsorption lag time,* τ), namely contribution (1). Below, we demonstrate that this adsorption lag time can be represented by the experimentally easily accessible bubble formation time $1/f_0$.

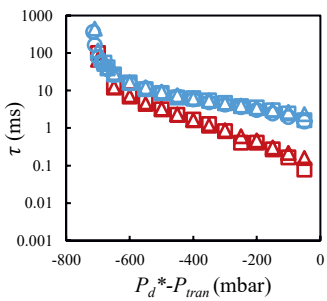

Figure A5.1-1. *The adsorption lag time ($\tau \approx 1/f_0$) as function of the normalised applied pressure (P_d^* - P_{tran}), measured in the presence of 1% wt. SDS (□Δ) in a bubble system and 0.3% wt. SDS (□○Δ) in a droplet system. The hydrodynamic flow resistance of the pore has a ratio of 1:2:4 in microchips with pore length/main plateau length equal to 20/100 (□), 40/200 (○), and 80/400 (Δ). The negative pressure values indicate that they are in the low-pressure regime, below the transition pressure. The normalised applied pressure (P_d^* - P_{tran}) is used to normalise the data sets obtained at different P_{tran} due to variations in the working system (droplet vs. bubble), namely 1400 mbar (red symbols) and 900 mbar (blue symbols).*

First, we evaluate the pore filling time. An important observation is that the pore filling time is hardly influenced by the hydrodynamic flow resistance of the pore, $\mathcal{R}_{pore}$. We have tested this in devices with varying plateau length to vary the hydrodynamic flow resistance, while keeping necking dynamics (t_n) constant. Figure A5.1-1 shows the results obtained for bubble (red symbols) and droplet (blue symbols) systems in the presence of SDS. The hydrodynamic flow resistance of the tested microchips has a ratio of 1:2:4, and if τ were dominated by the time to fill the pore (i.e., during pore flow), this would result in a time scale that is inversely proportional to $\mathcal{R}_{pore}$. However, all the data sets collapsed, which indicates that τ is dominated by adsorption lag time that is independent of pore length (please note that t_n can

be neglected here as $t_{fill} \gg t_n$ as will be discussed in Figure A5.1-2). Therefore, these results prove that t_{fill} is mostly determined by the characteristic time scale of dynamic adsorption (of the tested emulsifier), while it is hardly influenced by the actual pore flow process.

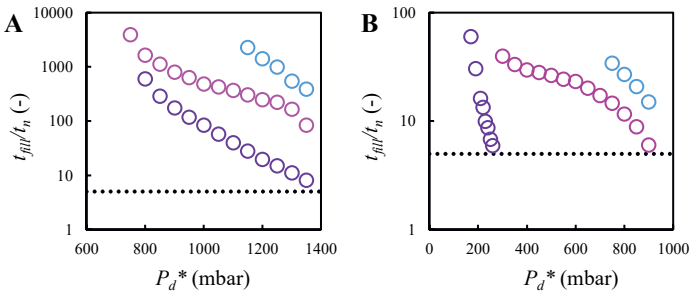

Figure A5.1-2. *The relative time scales t_{fill}/t_n in terms of bubble (A) and droplet (B) formation for the effects of SDS concentration: 0.1 (○), 0.3 (○) and 1 (○) % wt. The dashed line represents t_{fill}/t_n = 5.*

Second, we evaluate the necking time, and the results show that the pore filling time is much larger than the necking time $t_{fill} \gg t_n$ over most of our working range of applied pressures for both bubble and droplet systems. For bubble formation, $t_{fill} \gg t_n$ exists across the full range of applied pressures; only in the presence of 1% wt. SDS, which is the extreme concentration tested here, $t_{fill}/t_n \sim 5$ is observed at the pressure that is only slightly below the P_{tran} (Figure A5.1-2A). For droplet formation, $t_{fill}/t_n \sim 5$ is also only found at the pressure that is just below the transition pressure, illustrated in the presence of 0.3 and 1% wt. SDS (Figure A5.1-2B). $t_{fill} \gg t_n$ proves that τ can be estimated by $1/f_0$ (as shown in Figure A5.1-1).

5.6.2. The breakthrough pressure & the lag time

The breakthrough pressure corresponds to the Laplace pressure of the saturated meniscus. It decreases with increasing SDS concentration and levels off for SDS concentrations above c_{cmc}. In Figure A5.2A, the breakthrough pressure is plotted against SDS concentration for both bubble (a/w) and droplet (o/w) interfaces. In Figure A5.2B and C, the lag time is plotted against the applied pressure for two SDS concentrations. In general, as the applied pressure increases, the lag time decreases as increasingly higher dynamic interfacial tension is needed, requiring less emulsifier adsorption. For a given applied pressure (and thus a given dynamic interfacial tension), the lag time decreases as the SDS concentration increases due to faster SDS adsorption.

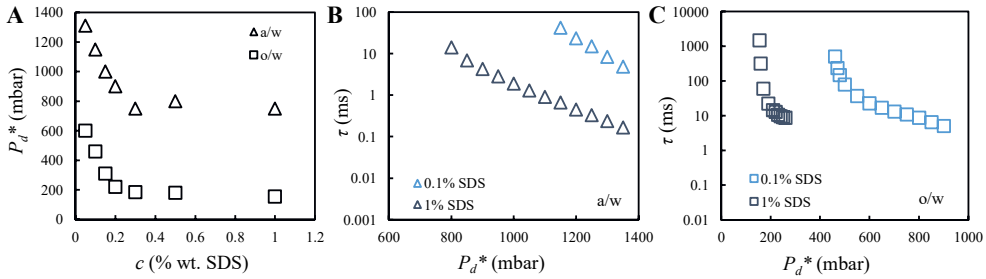

Figure A5.2. *A. The breakthrough pressure versus SDS concentration for bubble (a/w) and droplet (o/w) formation. The adsorption lag time as function of the applied pressure during the formation of bubble (B) and droplet (C). Two concentrations are shown for comparison, demonstrating the concentration effect on the lag time.*

5.6.3. The reproducibility of the γ_d measurement

The high working stability of the EDGE tensiometer is proved with three repeated experiments for droplet surface in the presence of 0.05% wt. SDS.

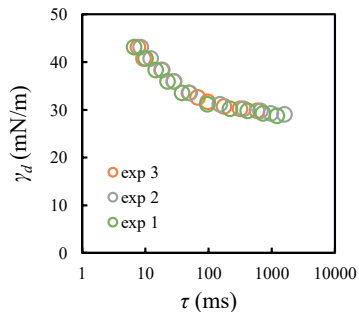

Figure A5.3. *Reproducibility tested with 0.05% wt. SDS for droplet surface.*

5.6.4. Comparison of the characteristic time scales

The relative magnitude of the two characteristic time scales determines the mass transfer mechanism of emulsifier molecules, namely the diffusion time (t_m) and the adsorption time (t_{ads}). In a stationary flow field, these two time scales can be estimated using the equations shown below. The diffusion coefficient (D) is assumed to be in the range $1\cdot10^{-10}$~$1\cdot10^{-9}$ m^2/s; the excess surface concentration (Γ_{eq}) is assumed to be $3.9\cdot10^{-7}$ mol/m^2; the adsorption rate constant (k_{ads}) is presumably in the range of 1000-2000 m^3/(mol·s), and the desorption rate constant (k_{des}) is assumed to be 500 1/s. The bulk SDS concentration (c) varies in the range of 0.01-1% wt. (i.e., 0.35-34.68 mol/m^3).

$t_m = \frac{h_p^2}{D}$ (with $h_p \approx \frac{\Gamma_{eq}}{c}$ the characteristic mass transfer distance of an emulsifier)

$$t_{ads} = \frac{1}{k_{ads}c + k_{des}}$$

According to the estimate shown in Figure A5.4, it is clear that 1) for 0.01-0.05% wt., the mass transfer is most likely diffusion-controlled; 2) for 0.1% wt., the mass transfer is likely mixed or purely kinetic controlled; for > 0.1% wt., the mass transfer is kinetic-controlled.

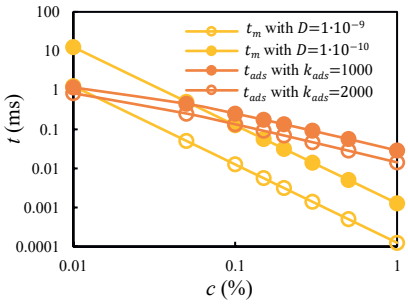

Figure A5.4. *The two characteristic time scales estimated for 0.05-1% wt. SDS.*

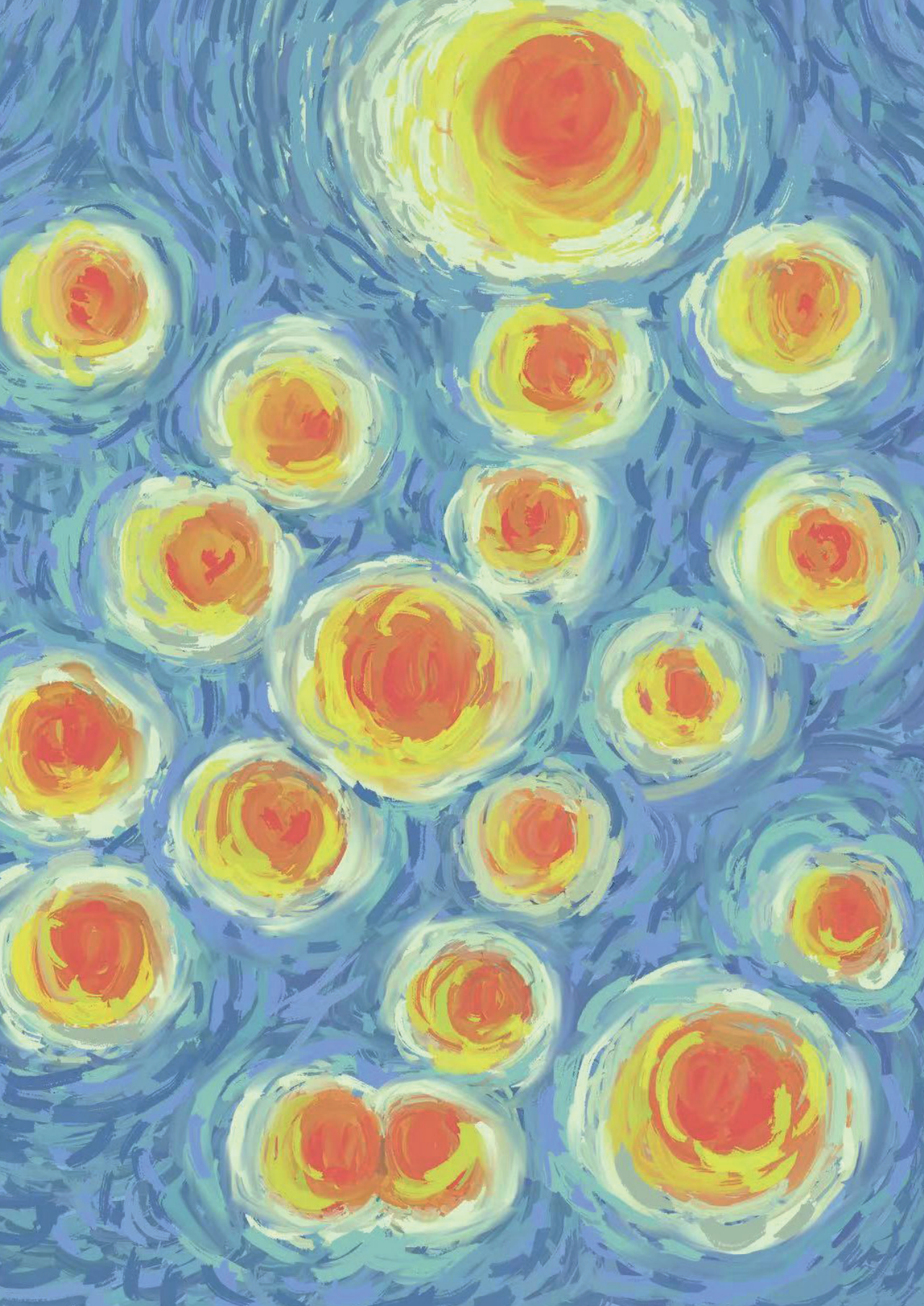

CHAPTER || 6

Onsite coalescence behaviour of whey protein-stabilised bubbles generated at parallel microscale pores: Role of pore geometry and liquid phase properties

This chapter has been submitted as Deng, B., Wijnen, D., Schroën, K. & De Ruiter, J., Onsite coalescence behaviour of whey protein-stabilised bubbles generated at parallel microscale pores: Role of pore geometry and liquid phase properties.

6.1 Abstract

In the formulation of (food) foams, an excess of protein is needed to prevent *instant* coalescence of bubbles from happening at (sub)millisecond time scales. However, protein adsorption and its influences on coalescence stability rarely have been investigated under such conditions of *short time scales* and *high protein concentrations*. In the current study, the coalescence stability of whey protein-stabilised bubbles was studied using a microfluidic device, for a wide range of process conditions, including bubble-forming pore geometries and liquid phase properties. The bubble formation time was varied via the applied pressure, and the corresponding extent of bubble coalescence was quantified via the analysis of bubble sizes obtained through high-speed recordings. The experimental results of bubble coalescence as function of bubble formation time, in the presence of various protein concentrations, were also captured in a semi-empirical model. The amount of proteins accumulating at the surface of coalescing bubbles can be derived from a mass balance, with protein adsorption towards the surface of coalescing bubbles assumed to follow a Langmuir isotherm. The model showed a good fit with the experimental results, and we found that as the protein concentration increases from 2.5 to 7.5% wt., in our device the minimum time required to stabilise bubbles decreases from 0.5 to 0.1 ms. From a practical perspective, our microfluidic device can be used as an efficient tool to capture, at *(sub)milliseconds,* the instant behaviour of bubble coalescence, providing closer insights for industrial-scale production of (food) foams that also takes place at these time scales.

Graphical abstract

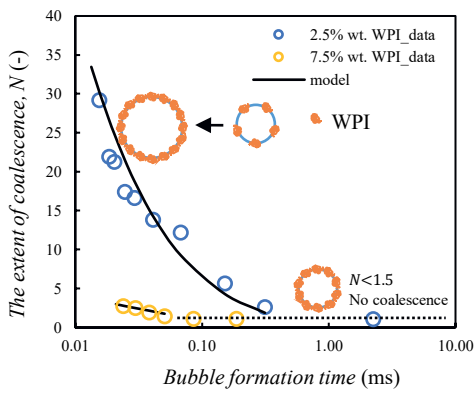

6.2 Introduction

Foams and emulsions are dispersions of two (semi-)immiscible phases. When producing a foam, the formation of a large number of bubbles results in a large increase in interfacial area (ΔA) and an increased deviation from thermodynamic equilibrium of the system – i.e., an increased Gibbs free energy ($G = \gamma \cdot \Delta A$) [5,158]. The coalescence of formed bubbles drives a reduction in interfacial area (ΔA), which minimises the Gibbs free energy. This can be – partially – suppressed by adding emulsifiers during foaming, which lowers the surface tension (γ) and thus slows down the increase in bubble size with time [128]. The final properties of a foam depend on the occurrence of bubble coalescence at the short time scales of foaming [15]; and represent a balance between bubble formation and bubble coalescence due to the finite time scale associated with emulsifier adsorption (e.g., proteins) [148].

Microfluidic platforms provide promising routes to study the coalescence stability of bubbles at short time scales. So far, a number of studies have been carried out with droplet coalescence as the sole focus, and typically, droplet coalescence is de-coupled from droplet formation. For example, monodisperse droplets are first formed at a T-junction, and subsequently, droplet coalescence is studied at a location downstream that allows interaction among droplets in a so-called coalescence chamber [4,25–27,58]. The extent of droplet coalescence can be tuned by manipulating the type and concentration of the emulsifier and the adsorption time, which is controlled by varying the length of the channel that connects the formation junction with the coalescence chamber, and that keeps the droplets spatially separated for some time. Studies have been performed to determine the critical time scale for emulsifier adsorption to stabilise an emulsion. As an illustration, with an adsorption time of 100 ms, 0.05% wt. β-lactoglobulin is needed for complete stabilisation of an emulsion [111]. However, unlike these model systems, practical emulsion systems are prone to *instant* coalescence, and the extent of droplet coalescence is dominated by the competition between emulsifier adsorption and droplet formation at time scales that are, typically, the droplet formation time (e.g., 0.1-30 ms in the high-pressure homogeniser [153]), which is much faster as currently described for microfluidic devices. For the production of a (food) foam, the bubble formation time can be even shorter (e.g., < 0.3 ms) [15]. To compensate for the fast dynamics of bubble formation and thus suppress bubble coalescence, a very high emulsifier concentration is typically used, especially when the selected emulsifier is a slow-adsorbing one (e.g., proteins). So far, *instant* coalescence of bubbles at very high protein concentrations has not yet been

well characterised. The microfluidic platforms as aforementioned are not suitable for this purpose since the adsorption channel and thus the adsorption time are not short enough for this purpose.

In this work, we studied the coalescence stability of whey protein-stabilised bubbles in a microfluidic device, where multiple bubble-forming pores are placed in close, well-defined proximity (i.e., partitioned-EDGE). Monodisperse, micrometre-sized bubbles are formed simultaneously and collide *instantly* at time scales down to tens of microseconds. We quantified bubble coalescence for different bubble-forming pore geometries, continuous phase viscosities and protein concentrations by investigating the interactions between bubbles that are growing at (or flowing away from) the pores. Moreover, we propose a semi-empirical model based on a mass balance of proteins accumulating at the surface of coalescing bubbles, and with this model, the extent of bubble coalescence as function of bubble formation time is described for various protein concentrations.

6.3 Experimental

6.3.1. Materials

Air bubbles were formed and stabilised in aqueous solutions (Merck Millipore) of whey protein isolate (> 97.5% purity, BioPro, Agropur, Quebec, Canada). The protein concentration (c) and the continuous phase viscosity (η) were varied in the range of 2.5-10% wt. (η = 2 mPa·s) and 1.4-10 mPa·s (c = 2.5% wt.), respectively. The viscosity of the continuous phase was adjusted with glycerol (99.5%, VWR International, Leuven, Belgium). The solutions were filtered with 0.22 µm PES filters (Merck, Germany) before use.

6.3.2. Microfluidic device

The partitioned-Edge-based Droplet GEneration (partitioned-EDGE) microchip (Figure 6.1) was designed in our group and fabricated by Micronit Microtechnologies B.V. (Enschede, the Netherlands). The design consists of two deep channels that are connected by a shallow plateau of length L and 500 µm width (W). The shallow plateau is further partitioned into identical pores with length l and width w, with partitions having width s; the pores are shorter than the plateau (i.e., $l = L/5$) – such that each pore is preceded (upstream) by a portion of the shallow plateau with length $L - l$. The shallow plateau and pores have the same height of h, and they are perpendicular to the direction of continuous phase flow. The hydrodynamic flow resistance ($\mathcal{R}$) of a channel with a rectangular cross-section (here the shallow plateau or pores) is given by $\mathcal{R} = \frac{12\eta l}{h^3 w[1-0.630\frac{h}{w}]}$, where η is the viscosity and l, h, w are the channel dimensions [130].

The hydrodynamic flow resistance of an individual flow path and the entire unit is defined as $\mathcal{R}_{pore}$ and $\mathcal{R}_{unit}$, respectively; $\mathcal{R}_{pore}$ represents the sum of the resistance of a pore and its portion of the preceding shallow plateau; $\mathcal{R}_{unit}$ is the resistance of the entire shallow plateau including all parallel pores. $\mathcal{R}_{pore}$ and $\mathcal{R}_{unit}$ are calculated for each device, as shown in Figure 6.1. The characteristics of the microchips are shown in Table 6.1.

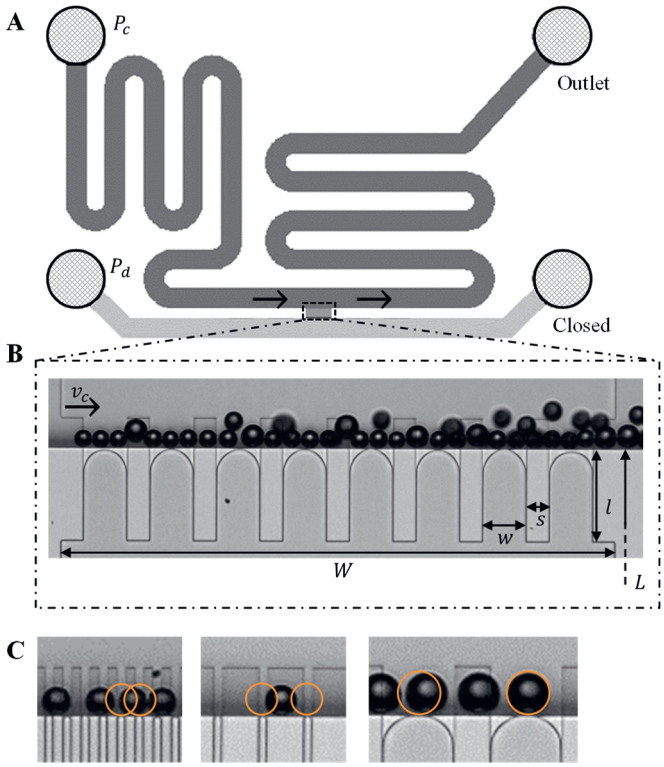

Figure 6.1. *A. Layout of the glass chip with a shallow plateau (inside the dashed box) bridging two deep channels. B. Photograph of the pore region on the continuous phase-side of the shallow plateau. See text for description of the geometrical parameters. C. Interactions between bubbles tuned by varying pore and partition width. In each snapshot, two neighbouring bubbles at the moment of snap-off are sketched with two orange circles.*

The air and continuous phases were pressurised using a digital controller (with an accuracy better than 0.1 mbar) via Smart Interface Software (Elveflow®, France). First, the air was pressurised at P_d and then the continuous phase at P_c. In an earlier study, we showed that the applied pressure across the shallow plateau and pores is given by $P_d^* = P_d - P_c/2$ [148]. Besides, we demonstrated that bubble formation can be divided into a low- and a high-pressure regime [160]; and the transition pressure (P_{tran}) between the two pressure regimes corresponds to the Laplace pressure of the pure air-water interface (i.e., meniscus in the pore) given by the Young-Laplace equation, $\Delta P_L = 2\gamma(\frac{1}{h}+\frac{1}{w})\cos(\theta)$. Here, γ is the surface tension, h and w the pore height and width, and θ the contact angle between the continuous phase and the channel wall. P_{tran} was calculated for each device and shown in Table 6.1. In the current study, bubble coalescence was studied as function of applied pressure in the high-pressure regime, and P_d^* was varied while keeping the continuous phase velocity (v_c) constant at approximately 1 m/s,

providing a constant flow field around bubbles. When necessary, the applied pressure was further normalised as (P_d^* - P_{tran}) to compare at equal steps in pressure concerning the start of the high-pressure regime. The standard condition for liquid phase properties was set to 5% wt. whey protein solution with a viscosity of 2 mPa·s.

Table 6.1. *Characteristics of the microchips.*

Number of pores [-]	Dimension [w - l/L; μm] $s = 20\ \mu m^*$	P_{tran} (mbar) [£]	P_{cross} (mbar) [$]	d_0 (μm) [§]
19 (50*)	5 – 40/200	1750	2050	11.7 (-)
16	10 – 40/200	1600	2050	12.0
12	20 – 40/200	1550	2050	15.2
8 (11*)	40 – 40/200	1500	1950	17.3 (-)
5	80 – 40/200	1500	1725	20.8
8	40 – 20/100	1500	1700	18.8
8	40 – 80/400 [#]	1500 or 1400	2200	16.8

** For pore widths of 5 and 40 µm, an additional partition width of s = 5 µm was studied to represent the distinct scenarios of bubble-bubble interactions at the pores. These designs contain a higher number of pores as indicated between brackets in the first column; the size of initial bubbles (d_0) in the high-pressure regime is not accessible in these devices (due to bubble crowdedness), yet, it is assumed to stay the same as that obtained for the standard partition width since we found that in the low-pressure regime d_0 is independent of the partition width.*

[#] For the dimension of 40-80/400, two microchips have been used, with h being either 0.93 or 1 µm, corresponding to a transition pressure of 1500 and 1400 mbar, respectively. The rest of the microchips all have h = 0.93 µm.

[£] Resolution of 50 mbar, in agreement with experimentally-imposed steps in applied pressure.

[$] P_{cross} was estimated for each device under the standard condition for liquid phase properties.

[§] The size of initial bubbles formed in the high-pressure regime; this is an average of accessible values. The d_0 as function of the applied pressure is shown in Figure A6.2.

6.3.3. Image analysis

The recording system combines an inverted microscope (Axiovert 200 MAT, Carl Zeiss B.V., the Netherlands) with a high-speed camera (FASTCAM SA-Z, Photron Limited, Japan). Videos were recorded at two distinct frame rates: 700,000 fps to extract time scales of bubble formation and 100,000 fps to extract bubble sizes. The typical time scales are the pore filling time (t_{fill}) and the bubble necking time (t_n), the sum of which makes up the time for one bubble formation (τ). The initial bubble size at the pore, d_0, was averaged for up to 50 bubbles; the coalesced bubble sizes d_{coal} and d_{mix} (as will be defined below) were averaged for up to

100 bubbles. A custom-written script in Matlab R2018b was used for the analysis of bubble sizes. The coefficient of variation (CV) was calculated to describe the bubble size distribution: CV (%) = $(\sigma/d) \cdot 100$, where σ is the standard deviation and d the number-averaged diameter).

6.4 Results and discussions

In partitioned-EDGE devices, dynamic adsorption dominates bubble formation in the low-pressure regime and stabilisation in the high-pressure regime (i.e., against bubble coalescence). At low pressures, bubbles can only be formed after the Laplace pressure of the meniscus has been sufficiently decreased through protein adsorption. This induces a lag time that dominates the bubble formation time (τ) and strongly decreases as the applied pressure increases. At applied pressures above P_{tran}, there is no lag time and the bubble formation time decreases linearly with the applied pressure – typically from a millisecond down to tens of microseconds –, and inversely with the hydrodynamic flow resistance of the flow path.

In Figures 6.2A and B, snapshots represent typical behaviours of bubble formation in the low- and high-pressure regimes; particularly, bubble formation co-exists with bubble coalescence in the high-pressure regime. To study bubble coalescence, the minimum applied pressure is equal to P_{tran}, and the maximum applied pressure is limited by the requirement to have monodisperse initial bubbles (blue shaded region in Figure 6.2C). At sufficiently low applied pressures, the initial bubbles remain monodisperse and the initial bubble size (d_0) is independent of the applied pressure (Figure 6.2C; empty circles and dashed line for those pressures at which d_0 is inaccessible due to bubble crowdedness). Above a critical applied pressure, bubbles are polydisperse due to the simultaneous formation of small and large (initial) bubbles, and d_0 increases with P_d^* (indicated by the obliquely upward dashed line). We have shown previously that this polydispersity coincides with a change in the dynamics of a single bubble formation cycle. Each bubble formation cycle can be divided into two stages: the pore filling stage and the subsequent bubble necking stage that leads to bubble snap-off. These stages have time scales of t_{fill} and t_n, respectively. t_{fill} is much larger in the low-pressure regime (than in the high-pressure regime), which proves the dominance of protein adsorption on bubble formation. In the low-pressure regime, t_{fill} decreases with P_d^* and is orders of magnitude larger than t_n (Figure 6.2C). Yet, in the high-pressure regime, because t_{fill} decreases drastically with P_d^* while t_n levels off, the two time scales eventually intersect at $P_d^* = P_{cross}$. It is at or above P_{cross} that polydispersity is introduced, depending on the device and liquid phase properties. P_{cross} is estimated for each device, shown in Table 6.1.

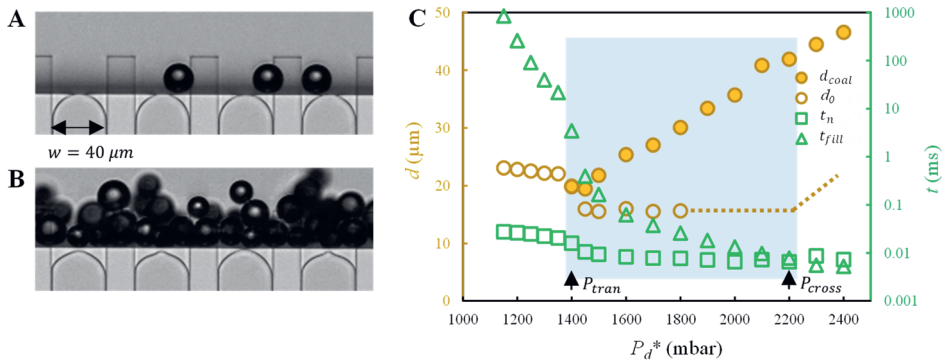

Figure 6.2. *A-B. Snapshots made during bubble formation at 1300 and 1500 mbar, respectively. C. Bubble sizes and time scales as function of applied pressure. Open circles are for the initial bubble size, closed circles are for the coalesced bubble size. The dashed line is drawn based on experimental observations; monodisperse bubbles are formed at applied pressures below P_{cross}, and both the bubble size and the polydispersity increase at applied pressures above P_{cross}. The monodispersed pressure range of interest for bubble coalescence is shaded with blue colour. The time scale on the right axis is plotted on logarithm scale and denotes both the necking time (squares) as well as the filling time (triangles). For results shown in A-C, the device has dimensions l/L = 40/200, w = 40 μm, and s = 20 μm.*

The partitioned-EDGE device has the capability to produce multiple bubbles simultaneously, and together with the aforementioned characteristics of bubble formation at well-defined locations, namely the pore exits, the partitioned-EDGE device provides a platform for the quantitative investigation of *instant* bubble coalescence. In the current study, bubble coalescence will be studied for the device and liquid phase properties. The device geometry (i.e., the bubble-forming pore geometry) will be investigated through the plateau length, and the width of the pore and partition. The liquid phase properties include the protein concentration and continuous phase viscosity.

6.4.1 What happens to the initial bubbles after formation?

Bubble formation at the pore

Coalescence will be evaluated with respect to the size of initial bubbles. While d_0 remains relatively constant within our interest range of applied pressures (Figure 6.2C and Figure A6.2), it does vary with the pore resistance, $\mathcal{R}_{pore}$ (Table 6.1). This is because the bubble volume is proportional to the air flow rate (Q'_{bub}) into the growing bubble $V_0 = Q'_{bub} \cdot t_n$ [160], and $Q'_{bub} = \Delta P_{Lap}/\mathcal{R}_{pore}$. The Laplace pressure ($\Delta P_{Lap}$) corresponds to the clean air-water interface as dynamic adsorption towards the meniscus can be neglected for the high frequency of bubble formation obtained in the high-pressure regime. Q'_{bub} decreases with increasing $\mathcal{R}_{pore}$, with $\mathcal{R}_{pore}$ depending on device geometry: it increases with increasing

plateau length (L) and with decreasing pore width (w) (and height), but it is independent of the partition width (s) (Figure A6.1). t_n is only slightly influenced by $\mathcal{R}_{pore}$ (Figure A6.3), and thus d_0 varies roughly as $\left(1/\mathcal{R}_{pore}\right)^{1/3}$ (Figure A6.2F).

The constant Q'_{bub} against applied pressure (for a fixed device geometry) is a special property of the partitioned-EDGE device. First, it ensures that bubble formation has high stability against fluctuations in the applied pressures, proven by the constant d_0 and the corresponding monodispersity (Figure A6.2 and Figure A6.4). Second, it sets a constant surface expansion rate, and thus a constant approach velocity of the growing bubble towards the bubbles that are sitting in front of the pores. This observation is relevant as the contact time in a collision event decreases as the approach velocity increases [4], and in the current study this contact time will remain constant across the full range of applied pressures.

Furthermore, we found that a higher pore resistance leads to a wider pressure window. Although P_{tran} shows a slight increase with decreasing pore width, P_{cross} increases more strongly with both decreasing pore width and increasing plateau length. As an illustration, P_{cross} is 1700 and 2200 mbar, for 40-20/100 and 40-80/400 devices (i.e., w - l/L), respectively, while P_{tran} is the same (Table 6.1). In a previous study, P_{cross} was observed to decrease with increasing protein concentration [160], which makes it even more important to choose a device geometry that supports an initially high P_{cross}. Additionally, to visualise both formation and coalescence of bubbles at the pores, the pores need to be sufficiently spaced. The 40-80/400 device is thus selected to investigate the roles of liquid phase properties on bubble coalescence and to minimise interaction between neighbouring pores. A maximum P_{cross} around 2200~2250 mbar is obtained for low protein concentrations and continuous phase viscosities, and it shifts to lower values for higher protein concentration (> 5% wt) and continuous phase viscosity (> 2 mPa·s) (Figure A6.5).

In terms of liquid phase properties, d_0 increases only marginally with increasing protein concentration (Figure A6.2D) and continuous phase viscosity that is below 2 mPa·s (Figure A6.2E). Yet, d_0 increases substantially for continuous phase viscosity above 2 mPa·s (Figure A6.2E). These changes in d_0 are directly related to changes in t_n (as $V_0 \sim t_n$) due to the liquid phase properties (Figure A6.3). Typically, the initial bubbles formed at applied pressures below P_{cross} are monodisperse with CV values below 5% (Figure A6.4), providing a simple

and robust system for the investigation of *instant* bubble coalescence as will be discussed in the next session.

Bubble coalescence upon onsite collision

Upon collision, the thin film that separates the two colliding bubbles drains out and ruptures; then, coalescence occurs, increasing in bubble size. As shown in Figure 6.2B, the bubble population includes both initial and coalesced bubbles. The probability of bubble coalescence largely depends on the confinement exerted by existing bubbles (in front of the pores). As the applied pressure increases, the *fraction* (f_{d_0}, %) of remaining initial bubbles decreases due to the increased bubble crowdedness and the limited time allowed for protein adsorption to take place, with the decline rate of f_{d_0} depending on protein concentration.

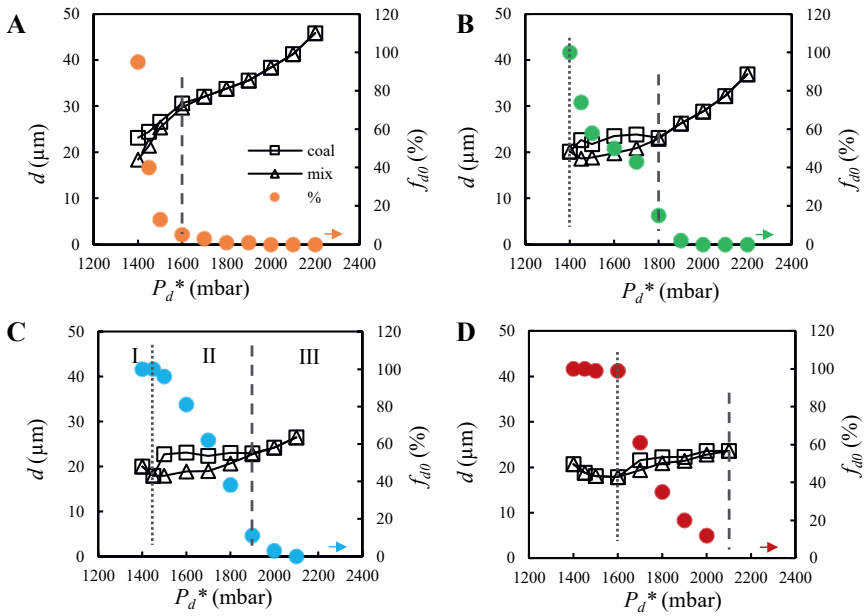

Figure 6.3. *The fraction of remaining initial bubbles and the bubble size as function of applied pressure for 3.5 (A), 5 (B), 7.5 (C) and 10 (D) % wt. whey protein. The viscosity is 2 mPa·s. The three sub-ranges of applied pressure are marked: a dotted line between sub-range I and II, and a dashed line between II and III. The coalesced bubble size has been calculated for only the coalesced bubbles (d_{coal}, squares) and the mixed bubble population (d_{mix}, triangles). These experiments were performed with the 40-80/400 device, and the transition pressure is 1400 mbar. Filled circles: the fraction, f_{d_0}, of initial bubbles out of 100 bubbles in the mixed bubble population (right axis).*

In Figures 6.3A-D, the size of coalesced bubbles calculated based on either the mixed bubble population (d_{mix}) or purely the coalesced bubbles (d_{coal}), excluding the initial ones, are plotted as function of applied pressure for a range of protein concentrations. Our interest range of

applied pressures can be divided into three sub-ranges (I-III) based on the observed difference between d_{mix} and d_{coal}. As illustrated for 7.5% wt. whey protein (Figure 6.3C), in subrange I ($1400 < P_d^* \leq 1450$ mbar), the initial bubbles are dominating (with $f_{d_0} \approx 100\%$) as bubble coalescence is almost suppressed; as a result, the d_{mix} and d_{coal} values overlap. In subrange II ($1450 < P_d^* \leq 1900$ mbar), bubbles that do and do not coalesce co-exist, leading to a gap between these two values. And lastly, in subrange III ($P_d^* > 1900$ mbar), most bubbles coalesce, thus the remaining initial bubbles ($f_{d_0} < 10\%$) hardly influence the estimation of d_{mix}, which overlaps again with the d_{coal} value.

Furthermore, as the protein concentration increases, sub-ranges I and III become wider and narrower, respectively. The two extreme cases are for 3.5 and 10% wt. whey protein. For 3.5% wt. whey protein, sub-range III extends over almost the full range of applied pressure and is preceded only by a sub-range II ending at approximately 1600 mbar. This is in line with the observation of extensive coalescence since 1450 mbar – more than half of the (mixed) bubbles have coalesced; from 1600 mbar onwards, less than 5% of the bubbles are of initial size (Figure 6.3A). On the other hand, for 10% wt. whey protein, sub-range I ends at 1600 mbar, and sub-range II extends all the way up to P_{cross} (Figure 6.3D). The take-away message is that with increasing applied pressure, an increasing fraction of initial bubbles is involved in coalescence. The gap (between d_{mix} and d_{coal}) observed in sub-range II indicates an underestimation of the size for coalesced bubbles when using the mixed bubble population. Yet, the underestimation is mostly *below* 15%, and for simplicity reasons the coalesced bubble size estimated from the mixed bubble population is used for further analysis.

The extent of bubble coalescence

The extent of coalescence is captured by the average number of coalescence events that a coalesced bubble has undergone. It is defined as $N = \frac{V_{coal}}{V_0} - 1$, where $V_0 = \frac{\pi}{6} d_0^3$ and $V_{coal} = \frac{\pi}{6} d_{coal}^3$ are the volumes of initial and coalesced bubbles. N is a good parameter to interpret the effects of device geometry and liquid phase properties, solely, on bubble coalescence, since their effects on the initial bubble size can be eliminated. In general, d_{coal} reflects an 'equilibrium' state of bubble formation and coalescence, and its value provides an impression on the properties of final products (Figure A6.6); while N highlights the *extent* of bubble coalescence, revealing stabilising activities at the interface (Figure 6.4). In the following

section, the number of coalescence events is plotted versus the bubble formation time (τ), rather than the applied pressure, since τ sets the time available for protein adsorption, and thus the interplay between bubble formation and protein adsorption. As a reference, bubbles with $N < 0.5$ are considered to be stable.

Device geometry: Bubble formation frequency and bubble-bubble interactions

Coalescence is studied as function of applied pressure for a range of plateau lengths, pore widths and partition widths. As expected, the coalesced bubble size increases with applied pressure (Figure A6.6), next to any geometrical effects. For the latter, d_{coal} increases with shorter plateau length (Figure A6.6A) and increases when the centre-to-centre distance between pores is smaller (i.e., small pore width (Figure A6.6B) or small partition width (Figure A6.6C)). Yet, for quantitative analysis, we need to correct for variations in d_0 (Table 6.1) and thus as indicated previously, study the number of coalescence events.

The number of coalescence events (N) is plotted against the bubble formation time, that is namely, the formation frequency of individual flow paths (i.e., pores). As shown in Figure 6.4A, N increases with decreasing bubble formation time, showing no dependency on changes in plateau length. Yet, N increases with reduced pore width (Figure 6.4B), as well as with reduced partition width (Figure 6.4C) when narrow pores are separated by narrow partitions (e.g., $w = s = 5$ µm). It is important to note that in the case of varied plateau length, all designs have eight pores, and thus a unit frequency of eight times the pore frequency. As a result, the level of crowding in front of the pores is the same for the same bubble formation time τ. Then, N is a direct function of τ (which collapses the original data that is a function of the applied pressure and the plateau length as shown in Figure A6.6A). On the other hand, the number of pores on the shallow plateau increases with reduced pore width and partition width in our designs (Figure A6.1). For a given τ, the unit frequency thus increases with reduced pore width, leading to a higher level of crowding. Moreover, for narrow pores (e.g., $w = 5$ μm), the unit frequency further increases with reduced partition width, which results in a higher level of crowding, and particularly, physical interactions between bubbles growing at neighbouring pores when $w + s < d_0$ (Figure 6.1C, left). This increasing number of collisions is responsible for the promoted bubble coalescence [25]. In conclusion, the device geometry can be varied to tune bubble coalescence, namely, through varying the bubble formation frequency, and/or the *interaction* between bubbles growing at adjacent pores and those flowing in the collection channel. Lastly, it is also worth mentioning that an increase

in $\mathcal{R}_{pore}$ (with reducing pore width) causes a lower surface expansion rate; this means a relatively longer contact time [4], and this might also contribute to the increased *N*.

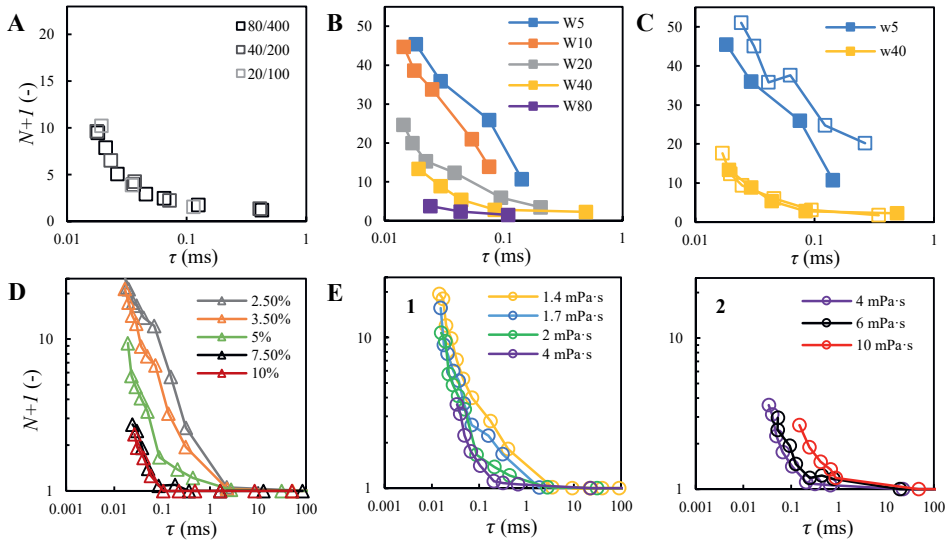

Figure 6.4. *The number of coalesced bubbles (N+1) as function of the bubble formation time. N+1 is plotted for the effects of plateau length (A), pore width (B), partition width (C), protein concentration (D), and continuous phase viscosity (E, panels 1 and 2). To plot the extent of bubble coalescence on a logarithm scale (in D-E), N+1 is used instead of N (number of coalescence events), where N+1 < 1.5 indicates the absence of coalescence. In A, w = 40 µm and s = 20 µm; in B, l/L = 40/200 and s = 20 µm; in C, l/L = 40/200, s = 20 µm (filled squares) and s = 5 µm (empty squares); in D-E, l/L = 80/400, w = 40 µm and s = 20 µm. In E, panel 1 shows low viscosity and panel 2 higher viscosity. Unless stated otherwise, the experiments were performed under standard conditions for the liquid phase: 5% wt. whey protein with a viscosity of 2 mPa·s.*

Liquid phase properties: Interface stabilisation

To prevent bubble coalescence, measures can be taken to either slow down drainage or stabilise the interface, by raising the continuous phase viscosity and protein concentration, respectively. As shown in Figure 6.4E and Figure A6.6E, coalescence (both *N* and d_{coal}, respectively) decreases as the continuous phase viscosity increases up to 4 mPa·s (Figure 6.4E, panel 1), and increases again as the continuous phase viscosity increases from 4 further to 10 mPa·s (Figure 6.4E, panel 2). In the former case, *N* is lowered by the lowered rate of film drainage [2,3]. In the latter case, *N* increases again with higher continuous phase viscosity, likely because the hydrodynamic force increases with continuous phase viscosity [15], thus promoting greater bubble deformation that increases the chance of coalescence upon bubble-bubble interactions. Increasing protein concentration reduces coalescence substantially as expected, but this effect levels off from 7.5% wt. onward (Figure 6.4D and Figure A6.6D). In the extreme case of 10% wt. whey protein, coalescence was observed only at $\tau < 0.1$ ms,

and N decreases marginally compared with 7.5% wt. whey protein, which indicates the limit to increasing protein concentration to foster protein adsorption and stabilisation of the interface.

6.4.2 How to model bubble coalescence?

The number of times that a bubble coalesces can be estimated using two key ingredients, namely (1) a simplified understanding of the stabilisation process by dividing it into a series of events regarding surface creation and protein adsorption, and (2) protein adsorption following a Langmuir isotherm. In the next section, we discuss both aspects and combine them into a semi-empirical model, which captures the role of dynamic adsorption in interface stabilisation and thus can be used to describe the experimentally obtained number of coalescence events versus bubble formation time ($N \sim \tau$).

Bubble stabilisation as a series of events

In the designs with sufficiently-spaced pores (here we use the 40-80/400 device design), coalescence events take place mainly between bubbles successively formed from a single pore, eliminating interactions between bubbles growing at neighbouring pores. The extent of coalescence is then mostly determined by the competitive processes of bubble formation and dynamic adsorption, which can be precisely tuned by varying the applied pressure and the protein concentration, respectively. We only consider protein adsorption to the spherical bubble surface. Any prior adsorption to the meniscus in the pore is considered irrelevant, since, bubbles can be formed without protein adsorption to the meniscus in the high-pressure regime, and the air-water interface expands significantly compared to the surface area of the meniscus during the bubble growth process ($d_0^2/hw_n \gg 10$).

The stabilisation of the bubble surface can be modelled as a repeated cycle of three separate events (I-III, see Figure 6.5), which has been discussed in our previous work [148] and will be recapitulated here. We refer to the bubble that is growing due to coalescence events as 'mother bubble' (with surface area A_i), and the individual bubbles that are formed at the pores and merge into this mother bubble as 'daughter' bubble(s) (with surface area A_1). While the daughter bubble is rapidly expanding, proteins adsorb (I) to the bubble surface and result in a (relatively low) surface coverage of Γ_{exp} at the moment of its snap-off. In line with experiments, (during or) *immediately* after snap-off from the pore (II) the daughter bubble coalesces into the mother bubble that is sitting in front of the pore in the collection channel.

The coalescence event increases the surface area of the mother bubble as $A_i = A_1 i^{2/3}$ (with i the number of the coalesced bubbles) and changes – typically decreases (Figure A6.7) – its surface coverage (expressed in mass per available surface area). Throughout each cycle, (III) proteins continuously adsorb to the surface of the mother bubble in the collection channel, yielding a net increase in surface coverage. These three events proceed repeatedly until a total number (k) of daughter bubbles have coalesced into forming the final mother bubble, which has surface area A_k and equilibrium surface coverage Γ_{eq}.

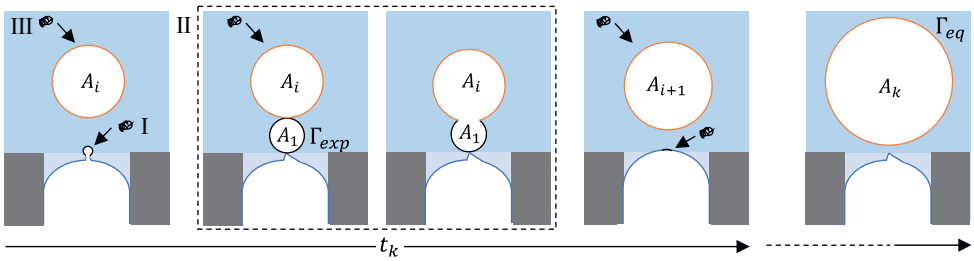

***Figure 6.5**. The assumed series of events regarding interface creation and protein adsorption. The first four snapshots highlight one cycle of coalescence, during which (I) proteins adsorb to the expanding daughter bubble (black), reaching a surface coverage Γ_{exp} upon the bubble's snap-off; (II) the daughter bubble merges into the mother bubble (dashed box); (III) proteins adsorb to the mother bubble (orange). Protein adsorption is indicated by arrows. After k cycles, coalescence ends with a final bubble with surface area A_k and equilibrium surface coverage Γ_{eq}. t_k is equal to the measured bubble formation time (τ).*

Protein adsorption

Protein adsorption to the mother bubble surface (event III in each cycle) is assumed to follow Langmuir-type adsorption, which is an isotherm that yields a reasonable approximation with few fitting parameters (Ockham's razor) [165]. At high bulk protein concentrations of c_0 = 25-75 kg/m^3 used in this work, the maximum equilibrium surface concentration (Γ_∞) is reached, which is then independent of the bulk protein concentration [166–169]. The change of surface coverage in time is given by [13]:

$$\Gamma(t) = \Gamma_\infty \left\{1 - \exp\left(-\frac{t}{\tau_{kin}}\right)\right\} \qquad \text{with} \qquad \tau_{kin} = \frac{1}{\beta c_0} \qquad 6.1$$

The kinetic time constant is dependent on bulk protein concentration, as well as adsorption (β) and desorption (α) rate constants, and its full description is $\tau_{kin} = \frac{1}{\alpha} \cdot \frac{1}{1+\kappa c_0}$, with $\kappa = \frac{\beta}{\alpha}$ the adsorption coefficient. For β-lactoglobulin the adsorption coefficient is approximately 27 m^3/kg [170], and thus for bulk protein concentrations of 25-75 kg/m^3, $\kappa c_0 \gg 1$ and the kinetic time constant can be approximated as shown in equation 6.1.

On the other hand, the rapid expansion of the daughter bubble induces strong local flows radially away from the expanding surface. In the same device, our experiments show that this bubble expansion rate hardly changes for different applied pressures and bulk protein concentrations – providing constant flow conditions. Hence, protein adsorption towards the expanding surface is assumed to scale with the displaced protein mass, which varies only with c_0. The adsorbed mass is then $\sim c_0\delta'^3$ with δ'^3 the, fixed, volume from which proteins are adsorbed) and distributes over the surface as $\Gamma_{exp}\pi d_0^2$, which leads to $\Gamma_{exp} \sim \delta c_0$ with δ a characteristic length scale ($\delta = \frac{\delta'^3}{\pi d_0^2}$).

A semi-empirical model

While the subsequent coalescence event (i) takes place, protein adsorption to the mother bubble follows equation 6.1. The mother bubble has accumulated a surface coverage over the course of all previous cycles of adsorption and coalescence, which introduces a starting point for the surface coverage of the mother bubble (Γ_{start}) (Figure A6.7)**.** In the i-th cycle, Γ_{start} is determined by the endpoint of adsorption to the mother bubble in the previous cycle (i-1), plus the protein adsorbed to the expanding daughter bubble (Γ_{exp}; an event I) that subsequently merged into this mother bubble and dilatated its surface area (event II), *i.e.*, $\Gamma_{start,i} = \frac{\Gamma_{i-1}A_{i-1}+\Gamma_{exp}A_1}{A_i}$. Therefore, we can write a mass balance ($A_i\Gamma_i$) for the protein mass accumulated at the surface of the mother bubble over the subsequent coalescence cycles 1, 2…i (right-hand side of equation 6.2). Coalescence stops after k cycles when the surface coverage reaches the value needed for stabilisation, Γ_{stab} ($<\Gamma_\infty$) and thus the accumulated mass upon stabilisation is $A_k\Gamma_{stab}$ (left-hand side of equation 6.2). Using $A_i/A_1 = i^{2/3}$, $\tau_{kin} = \frac{1}{\beta c_0}$ and $\Gamma_{exp} \sim \delta c_0$ from above we finally obtain the mass balance in equation 6.3:

$$A_k\Gamma_{stab} = A_i\Gamma_\infty\left\{1 - \left[1 - \frac{\Gamma_{i-1}A_{i-1}+\Gamma_{exp}A_1}{\Gamma_\infty A_i}\right] exp\left(-\frac{t_k}{\tau_{kin}}\right)\right\} \qquad (i = 1, 2\ldots k) \qquad 6.2$$

$$\frac{\Gamma_{stab}}{\Gamma_\infty}k^{2/3} = i^{2/3} - \left[i^{\frac{2}{3}} - \frac{\Gamma_{i-1}}{\Gamma_\infty}(i-1)^{\frac{2}{3}} - \frac{\delta}{\Gamma_\infty}c_0\right] exp\left(-t_k\beta c_0\right) \qquad (i = 1, 2\ldots k) \qquad 6.3$$

This mass balance has three fitting parameters (groups) that are independent of applied pressure and bulk protein concentration, namely $\frac{\Gamma_{stab}}{\Gamma_\infty}$ (dimensionless and between 0 and 1), $\frac{\delta}{\Gamma_\infty}$ (in m^3/kg), and β (in m^3/s/kg); and itself is an explicit function of the bulk protein

concentration c_0 and the bubble formation time t_k (and thus the applied pressure). Note that the maximum equilibrium surface concentration (Γ_∞) is unknown, and thus the first two fitting parameters are grouped. While fitting the model to the experimental data, equation 6.3 is iterated over i = 1, 2,… using that the term $\frac{\Gamma_{i-1}}{\Gamma_\infty}(i - 1)^{\frac{2}{3}}$ is the right-hand side in the previous iteration. The fitting parameters are optimised such that the sum of squared errors of all data points is minimised. The (relative) squared error is defined as $\left(k_{exp} - k_{mod}\right)^2/k_{exp}^2$, while the model k value for each data set is found using the equality in equation 6.3, obtained by subsequent linear interpolation between the two integer values bounding the solution. Only the experimental k values that are above 1.5 are fitted and used in the error minimisation as the relative uncertainties diverge when no coalescence ($k < 1.5$) takes place.

We can fit equation 6.3 simultaneously to the series of (k, t_k) data sets obtained for c_0 = 25-75 kg/m^3. In terms of experimental parameters, we fit the number of coalescence events $N = k - 1$ versus bubble formation time $\tau = t_k$. The key parameter resulting from the model is t_1 – the minimum time required to immediately stabilise the surface of daughter bubbles and thus inhibit coalescence, and it can be derived from the obtained fitting parameter$s$ by calculating stability for k = 1 in equation 6.4:

$$t_1 = -\frac{1}{\beta c_0} LN\left[\left(1 - \frac{\Gamma_{stab}}{\Gamma_\infty}\right) / \left(1 - \frac{\delta}{\Gamma_\infty} c_0\right)\right] \qquad 6.4$$

Fitting the model to the four experimental data sets simultaneously yields a realistic value for β = 46.8 m^3/(kg·s) and t_1 = 0.5-0.1 ms (Table A6.1) that decreases with increasing protein concentration up to 7.5% wt. The β value is in the same order of magnitude as other values reported in the literature, for example, 9.7 m^3/(kg·s) derived for 4% wt. β-lactoglobulin [171]. The fitted time scales agree well with our experimental data; as illustrated for the extreme case of high protein concentration (10% wt., see Figure 6.4D), bubbles are formed and fully stabilised at time scales down to 0.1 ms. These fitted time scales give an estimate for the time scales of protein adsorption, and the resulting stabilisation of a foam at increasing protein concentrations. In Figure 6.6, our semi-empirical model shows good agreement with the *instant* coalescence behaviour of bubbles formed at time scales varying in the range of 0.01-2.8 ms. It is worth mentioning that our system closely represents aspects of industrial-scale foaming, in terms of both time scales and process conditions, namely the high protein

concentration and the flow field, both of which enhance dynamic adsorption towards the surface of initial (daughter) and coalesced (mother) bubbles.

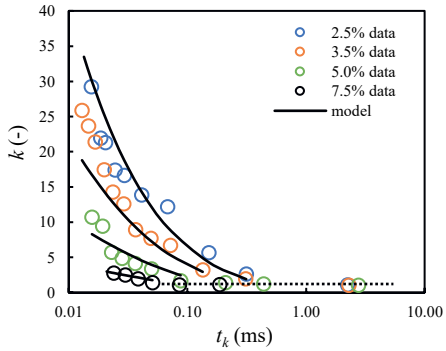

Figure 6.6. *A semi-logarithmic plot of the number of coalesced bubbles versus the bubble formation time for the comparison between experimental and model values. The experimental data was extracted from Figure 6.4D. The dashed line represents k < 1.5, for which bubbles are considered to be stable.*

6.5. Conclusions

In this work, the short-term coalescence stability of whey protein isolate-stabilised bubbles is investigated as function of bubble formation time, using experiments and a semi-empirical model. The bubble formation time is varied in the range of 0.01-2.8 ms, which also represents the interaction time as bubble collisions are studied immediately at the exit of the pores. The observed transition behaviour between stabilisation and coalescence demonstrates that the adsorption time is also within this range. The experimental results show that the extent of coalescence increases with decreasing bubble formation time and it can be further tuned through device geometry and liquid phase properties (within certain boundaries), by manipulating bubble-bubble interactions and interface stabilisation, respectively. Besides, our semi-empirical model captures the data well, and we can fit the model simultaneously to four experimental data sets obtained for different protein concentrations, while confirming the trends in coalescence. Most importantly, both experimental results and the model show that the minimum time required to obtain an *instantly*-stabilised foam decreases with increasing protein concentration; from the model, it decreases from 0.5 to 0.1 ms as the protein concentration increases from 2.5 to 7.5% wt.; from the experimental, at 10% wt. whey protein, 0.1 ms ensures an immediate stabilisation of monodisperse bubbles.

With this microfluidic device, we can study the *instant* coalescence of bubbles formed at time scales down to tens of microseconds. To control bubble coalescence, it is crucial to control the interplay between dynamics of bubble formation and protein adsorption at the relevant time scales. For industrial-scale production, where bubbles (and droplets) are typically formed in (sub)milliseconds, high protein concentrations are essentially needed to enhance mass transfer and thus stabilise the interfaces. On the other hand, a similar stabilisation effect can be achieved by simultaneously adjusting multiple liquid phase properties, for example, combing a moderate protein concentration with a moderate continuous phase viscosity (e.g., 5% wt. with 2 mPa·s). To conclude, our microfluidic device can be used as an analytical tool for bubble stabilisation. With this tool, we can study the stabilisation dynamics of bubbles under conditions that are relevant to large-scale production, such as enhanced mass transfer by strong flow fields and high concentration of emulsifiers, and do so at short time scales. Therefore, the microfluidic tool provides guidelines for controlling bubble stabilisation against instant coalescence in practical applications.

6.6. Appendix

6.6.1. The hydrodynamic flow resistance

In our microfluidic designs, the total width (W) of the shallow plateau is fixed. As the pore width (w) decreases, the number of pores on the shallow plateau increases; in particular, for narrow pores, it further increases with reducing partition width. For each design, the hydrodynamic flow resistance of the individual flow paths ($\mathcal{R}_{pore}$) and the entire unit ($\mathcal{R}_{unit}$) are calculated. Both of $\mathcal{R}_{pore}$ and $\mathcal{R}_{unit}$ decrease with increasing pore width; when the narrow pores are separated by narrow partitions, $\mathcal{R}_{unit}$ further decreases, while $\mathcal{R}_{pore}$ remains relatively constant. As the plateau length increases from 100 to 400 µm, $\mathcal{R}_{pore}$ increases at a ratio of 1:2:4.

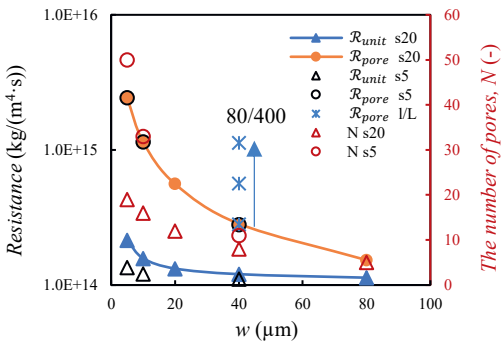

Figure A6.1. *The hydrodynamic flow resistance of the individual flow paths and the entire unit, and the number of pores in each design. For the first four data sets, l/L = 40/200; for the fifth data set (l/L series), s = 20 µm. On the second vertical axis, N represents the number of pores.*

6.6.2. The initial bubble size

The initial bubble size (d_0) is evaluated for the effects of 1) plateau length (l/L), 2) pore width (w), 3) partition width (s), as well as 4) protein concentration and 5) continuous phase viscosity, for bubbles formed in the high-pressure regime. On the upper end of the high-pressure regime, a quantitative measurement of the d_0 is impossible due to bubble crowdedness in front of the pores. Therefore, the d_0 is only shown for applied pressures at which initial bubble sizes can be accessed with the image analysis software (Figure A6.2). Note that for the effects of narrowed partition width, the initial bubbles are not accessible in the entire high-pressure regime because of bubble crowdedness in front of the pores and the fact that $w + s$ is close to d_0. Figure A6.2C, however, shows that the d_0 is independent of the partition width in the low-pressure regime, and we extrapolate this to the high-pressure

regime. This is assumed to hold since $V_0 = Q'_{bub} \cdot t_n$ and both Q'_{bub} ($\sim 1/\mathcal{R}_{pore}$) and t_n (as will be shown in Figure A6.3C) are independent of the partition width. In general, the initial bubble size is mainly influenced by the pore width (i.e., $\sim(1/\mathcal{R}_{pore})^{1/3}$, Figure A6.2F) and the continuous phase viscosity, through varied air flow rate into the bubble and bubble necking time, respectively.

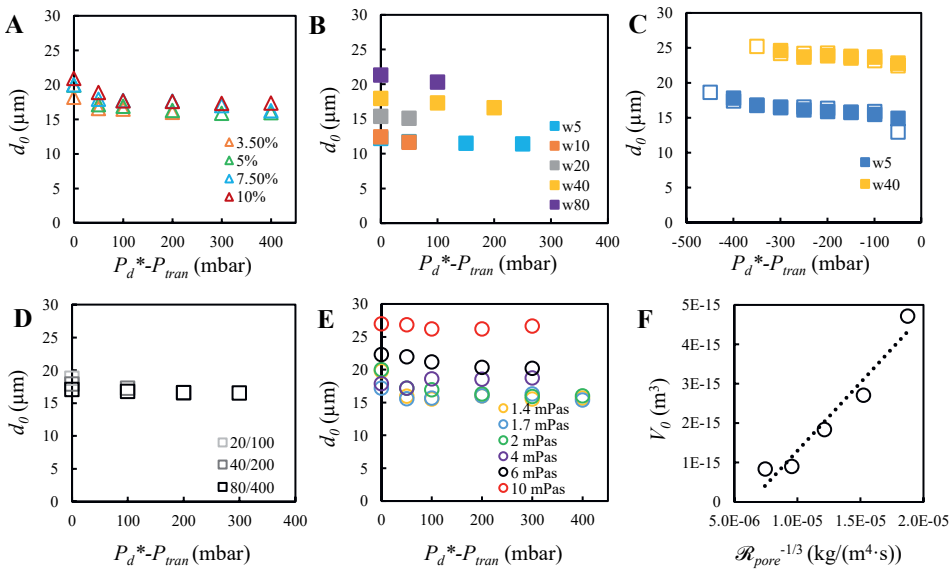

Figure A6.2. *The initial bubble size as function of applied pressure for the effects of plateau length (A), pore width (B), partition width (C), protein concentration (D) and continuous phase viscosity (E). The normalised applied pressures are used to correct for the transition pressure that varies with the pore width. In A, w = 40 µm and s = 20 µm; in B, l/L = 40/200 and s = 20 µm; in C, l/L = 40/200, s = 20 µm (filled square) and s = 5 µm (empty square); in D-E, l/L = 80/400, w = 40 µm and s = 20 µm. F. The volume of initial bubbles as function of* $(1/\mathcal{R}_{pore})^{1/3}$*. The size (and thus the volume) of initial bubbles and the* $\mathcal{R}_{pore}$ *are extracted from Table 6.1 in the manuscript and Figure A6.1 (specifically, for varied pore width), respectively.*

6.6.3. The bubble necking time

The bubble necking time (t_n) is plotted against applied pressure. Within our interest range of applied pressures, t_n typically slightly decreases and levels off as function of applied pressure. It is hardly influenced by variations in device geometry (i.e., plateau length, pore and partition width; Figure A6.3A-C). Next to that, t_n increases slightly with increasing protein concentration from 2.5 to 10% wt., and marginally with increasing continuous phase viscosity that is below 2 mPa·s. t_n increases substantially with the continuous phase viscosity that is increased further up to 10 mPa·s, due to the increased viscous dissipation of the continuous phase in the pore. The size of initial bubbles changes accordingly with t_n, and the description is referred to Appendix 6.6.2.

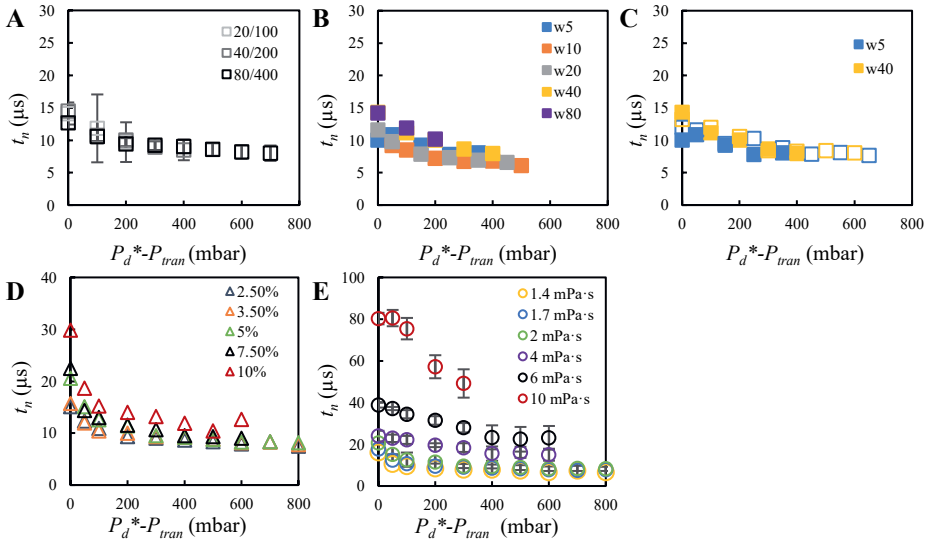

Figure A6.3. *The bubble necking time as function of applied pressure for the effects of plateau length (A), pore width (B), partition width (C), protein concentration (D) and continuous phase viscosity (E). In A, w = 40 µm and s = 20 µm; in B, l/L = 40/200 and s = 20 µm; in C, l/L = 40/200, s = 20 µm (filled square) and s = 5 µm (empty square); in D-E, l/L = 80/400, w = 40 µm and s = 20 µm.*

6.6.4. The coefficient of variation (CV) – monodispersity evaluation

The coefficient of variation (CV) for the initial (empty circles) and coalesced (filled circles) bubbles are calculated, for the effects of protein concentration and continuous phase viscosity. The initial bubbles are monodisperse with a CV mostly below 5%. The coalesced bubbles are polydisperse, yet, the CV is varying between 5 and 25%, depending on the applied pressures and the liquid phase properties, which are comparable to but still better than those obtained in commonly used foaming techniques [15]. The CV increases mainly due to bubble coalescence, and the co-existence of bubble formation and coalescence.

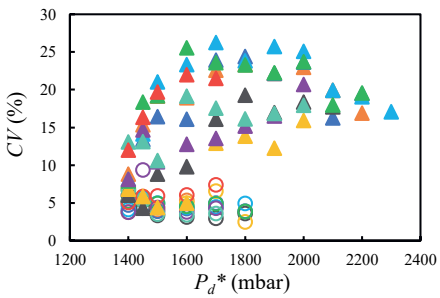

Figure A6.4. *The coefficient of variation (CV) evaluated for initial (empty circles) and coalesced (filled triangles) bubbles, for the effects of protein concentration of 3.5 (○▲), 5 (○▲), 7.5 (○▲) and 10 (○▲) % wt., and continuous phase viscosity of 1.4 (○▲), 1.7 (○▲), 4 (○▲), 6 (○▲) and 10 (○▲) mPa·s.*

6.6.5. *The cross-over pressure, P_{cross}*

P_{cross} decreases with increasing protein concentrations above 5% wt. and with increasing continuous phase viscosities above 2 mPa·s. This is because of the increased t_n (Figure A6.3D-E) shifts its intersection with the t_{fill} to lower applied pressures.

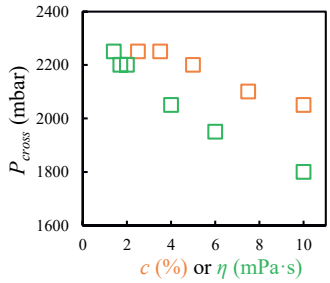

Figure A6.5. *The P_{cross} for various protein concentrations (c) and continuous phase viscosity (η).*

6.6.6. *The coalesced bubble size*

The coalesced bubble size is shown in Figure A6.6 for experimental conditions corresponding to the d_0 results (Figure A6.2). The description of these results is referred to the manuscript.

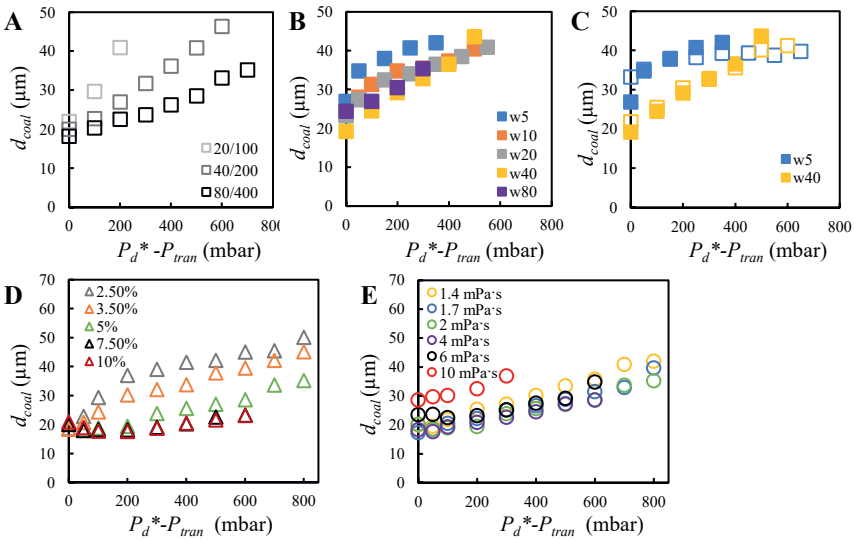

Figure A6.6. *The coalesced bubble size measured using the mixed bubble population for the effects of device geometry, including plateau length (A), pore width (B), partition width (C), and fluid properties, which are protein concentration (D) and continuous phase viscosity (E). In A, w = 40 µm and s = 20 µm; in B, l/L = 40/200 and s = 20 µm; in C, l/L = 40/200, s = 20 µm (filled square) and s = 5 µm (empty square); in D-E, l/L = 80/400, w = 40 µm and s = 20 µm.*

6.6.7. *The empirical model*

Subsequent adsorption cycles follow the rate equation in equation 6.1 shown in the manuscript (black curve, Figure A6.7), yet, are shifted towards a starting surface coverage that is set by all previous cycles. As an example, the first two cycles are shown below in Figure A6.7: the first cycle (orange line) starts at non-zero surface coverage due to the whey protein adsorbed previously to the expanding first daughter bubble (upward arrow). The second cycle (green line) starts at *decreased* surface coverage due to the merging of a new daughter bubble into the mother bubble. Although the merging leads to additional protein mass, it also leads to a strong surface dilatation that causes a net decrease in surface coverage (down and left arrows). These adsorption cycles continue until the surface coverage needed for stabilisation is reached, i.e., equation 6.3 in the main manuscript is fulfilled.

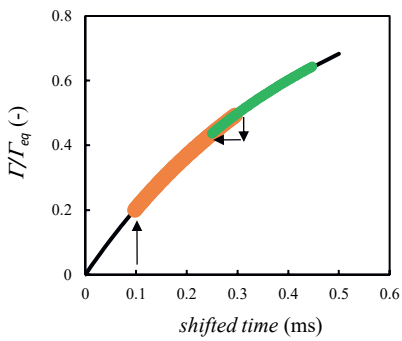

Figure A6.7. *Evolution of surface coverage in subsequent adsorption cycles. An example of the first two (1: orange, and 2: green lines) cycles are shown.*

Fitting the model simultaneously to a series of data sets, namely four data sets obtained for varied protein concentrations, we obtain an estimate for each fitting parameter, shown in Table A6.1.

The fit parameter β and the resulting time scale t_1 are discussed in the main text. Here we comment on the other two fitting parameters. First, the fitting results are largely independent of the prescribed $\frac{\Gamma_{stab}}{\Gamma_\infty}$ (which varies between 0 and 1). To reduce the number of fitting parameters we have used fixed $\frac{\Gamma_{stab}}{\Gamma_\infty} \approx 0.5$ based on values of ≈3.7 [170] and ≈1.6 mg/m^2 [172] for Γ_∞ and Γ_{stab}, respectively. Second, from the fit parameter $\frac{\delta}{\Gamma_\infty}$ we can estimate the 'swept' volume from which proteins are adsorbed, using the aforementioned value for Γ_∞, as well as

the known bubble size d_0. The size of this volume is (2.3 μm)^3, which is a realistic value given the bubble size.

Table A6.1. *The fitting parameters based on data sets obtained for c_0=25-75 kg/m^3.*

$\frac{\Gamma_{stab}}{\Gamma_\infty}$=0.5	Fitting parameters
$\frac{\delta}{\Gamma_\infty}$ (m^3/kg)	3.8·10^{-3}
β (m^3/s·kg)	46.8
t_1 (ms)	0.5-0.1
(derived from the other fit parameters)	

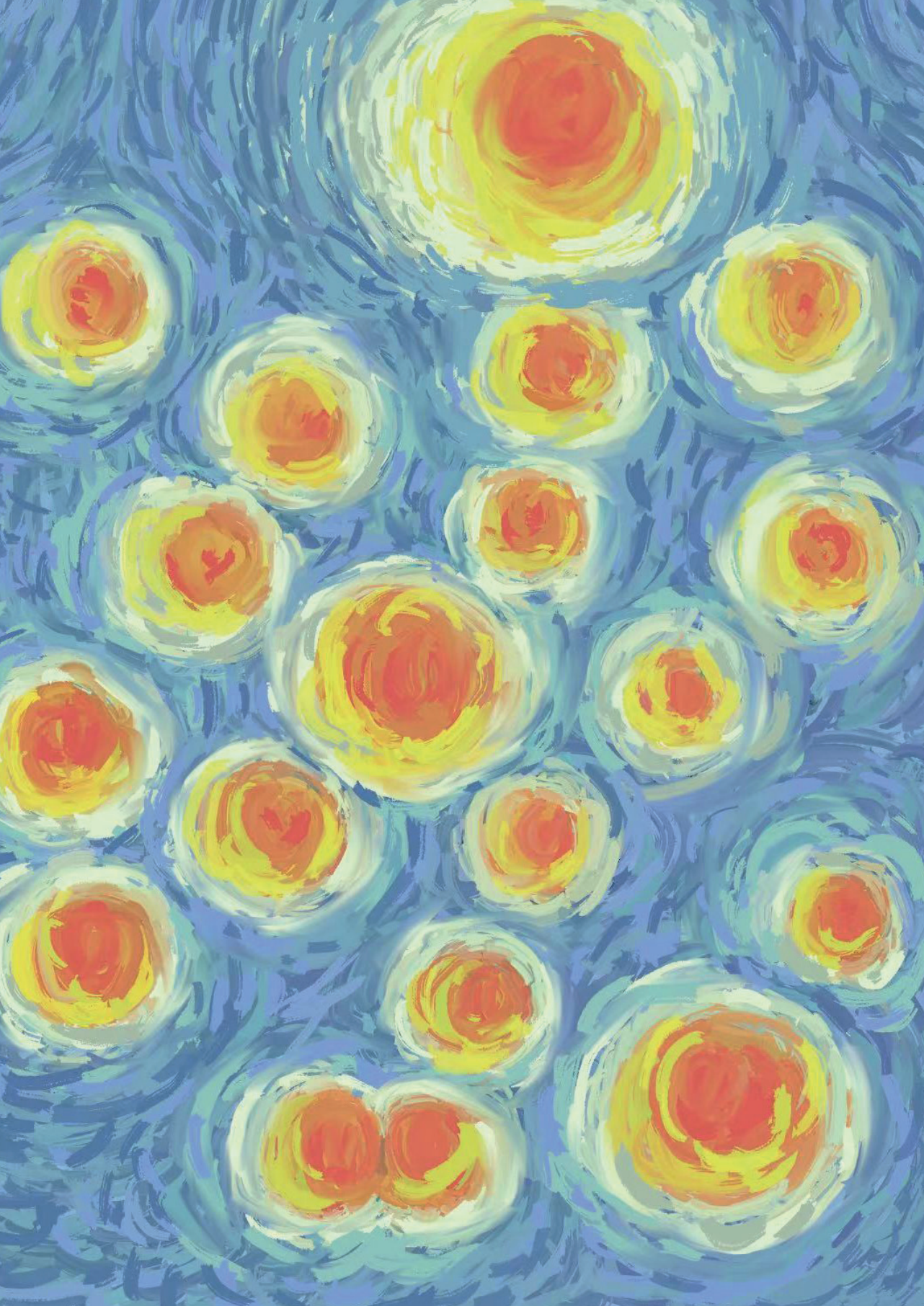

CHAPTER 7

A microfluidic study of bubble formation and coalescence tuned by dynamic adsorption of SDS and proteins

This chapter has been submitted as Deng, B., Schroën, K. & De Ruiter, J., A microfluidic study of bubble formation and coalescence tuned by dynamic adsorption of SDS and proteins.

7.1 Abstract

Hypothesis: Emulsifier adsorption at *short-term* time scales plays important roles in the formation and instant stabilisation (i.e., against coalescence) of bubbles during foaming. The properties of an emulsifier, such as the *type* and *concentration*, determine its interfacial behaviour and thus the aforementioned roles.

Experiment: The partitioned-EDGE device was used, in which emulsifier adsorption can be studied conveniently via monitoring the dynamic processes occurring during bubble formation and coalescence, and the resulting bubble properties in two pressure regimes (i.e., at low versus high pressures). We studied sodium dodecyl sulfate (SDS) for a range of concentrations (0.05-3% wt.), and multiple proteins, including 5% wt. whey protein isolate (WPI), β-lactoglobulin (β-lac), and bovine serum albumin (BSA).

Findings: As SDS concentration increases up to 3% wt., the bubble formation time decreases in the low-pressure regime due to the faster adsorption of SDS, and increases in the high-pressure regime due to the promoted 'dripping-jetting' transition; next to that, the neck thinning process slows down, leading to longer necking time (i.e., bubble growing time) and thus larger bubble size in both pressure regimes. Moreover, at time scales down to 10 µs, SDS is most efficient in suppressing *instant* bubble coalescence, followed by BSA, WPI, and finally, β-lac; these stabilising effects are related to the dynamic surface tension. We conclude that to explain the roles of emulsifier adsorption in a foam product, it is crucial to understand the emulsifier adsorption behaviour at both *short-term* (i.e., this work) *and long-term* time scales. The partitioned-EDGE device proves to be a *simple, quick* platform for the *short-term* investigation of emulsifier adsorption at the relevant time scales of bubble formation.

Graphical abstract

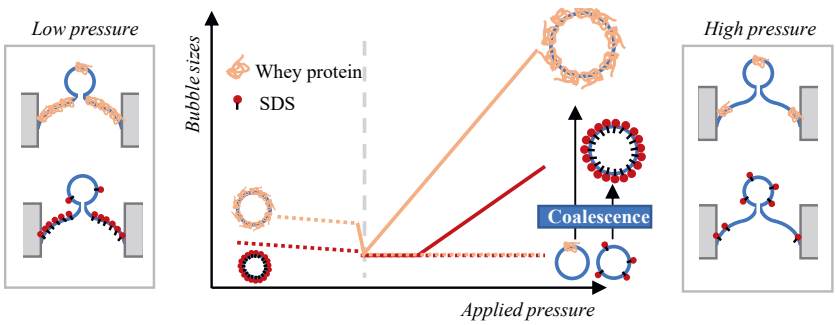

7.2 Introduction

Foams and emulsions are dispersions of two (semi-)immiscible phases that are typically stabilised with surface active components, i.e., emulsifiers. Emulsifier adsorption affects the interface in two ways, by lowering the interfacial tension and varying the interfacial rheological properties (e.g., viscous and elastic properties) [173,174]; at first, it promotes the formation of individual bubbles (and droplets) and determines their (initial) properties such as bubble formation frequency and size [148], and second, it hinders bubble coalescence and slows down the increase of bubble size with time [128]. Depending on the relative magnitude of time scales for bubble formation and emulsifier mass transfer, the surface tension typically varies with time, known as *dynamic surface tension* [175]. During large-scale foam production, emulsifier adsorption and the resulting dynamic surface tension decay occur at a similar time scale as that of bubble formation, i.e., (sub)millisecond [1]; bubble coalescence occurs if the bubble surface is not sufficiently covered. Typically, emulsifier properties like the *type* and *concentration* can be manipulated to tune bubble properties, and to do so, it is crucial to understand the emulsifier adsorption behaviour at time scales that are relevant to bubble formation and coalescence, although it is already good to point out that these time scales are very short, and thus difficult to assess.

Microfluidics has been explored widely in making uniform droplets and bubbles, and also in unravelling the dynamic processes occurring during the formation of droplets and bubbles, such as dynamic interfacial tension. Compared to conventional techniques – a drop tensiometer that characterises emulsifier adsorption through measurement of dynamic interfacial tension and interfacial rheology for the millimetre-sized interface at (slower than) second time scales [176,177], microfluidic measurements provide direct insights into the roles of emulsifier adsorption at the *relevant interfaces* (e.g., strongly curved), at the relevant *(sub)millisecond time scales*, and under the relevant *flow conditions* [13]. Emulsifier adsorption and the resulting dynamic interfacial tension [11,52,53,55,155], and droplet coalescence [25–27] are typically studied through direct analysis of droplet sizes on chip. Most microfluidic studies used fast-adsorbing low-molecular weight surfactants, like SDS (and Tween 20); for making droplets and bubbles, typically, a sufficiently high concentration is used, and an equilibrium interfacial tension is assumed to play a role [38,41,47,92,126]. In contrast, slow-adsorbing proteins are less studied [27,45,58,68,91,178]; in comparison to SDS, protein adsorption lowers the interfacial tension more slowly, and exhibits intermolecular interactions at the interface that endows the

interface with a viscoelasticity [129,179]. Both effects lead to the formation of larger droplets and bubbles [45,77]. In fact, in the presence of slow-adsorbing proteins or low concentration of fast-adsorbing surfactants [12,77,147,160], or even high concentration of fast-adsorbing surfactants, depending on the dispersion techniques and process conditions, dynamic interfacial behaviour crucially impacts the fast formation and stability of droplets and, especially, bubbles. Bubble formation is extremely fast due to the significantly lower gas viscosity, which enlarges the dynamic effects that are highly unexplored.

In this study, the partitioned Edge-based Droplet GEneration (partitioned-EDGE) device is used to form bubbles within two distinct pressure regimes, namely a low- and a high-pressure regime [148]. We study the effects of the type (i.e., SDS and proteins) and concentration of emulsifiers on the roles of emulsifier adsorption in the dynamics of bubble formation and stabilisation. In the low-pressure regime, the crucial parameters are the bubble formation time that reflects the *dynamic surface tension*, as well as the bubble necking time and the neck thinning rate, which are influenced by both dynamic surface tension and interfacial rheology; while in the high-pressure regime the crucial parameter is *the extent of bubble coalescence*, which is monitored via the analysis of bubble sizes.

7.3 Experimental

7.3.1 Materials

Air was used as the dispersed phase. Aqueous solutions (MilliQ, Merck Millipore) of emulsifiers were used as the continuous phase. The solutions used are 0.05, 0.1, 0.2, 0.5, 1 and 3% wt. sodium dodecyl sulfate (SDS; with > 99% purity, Sigma-Aldrich, USA), 1% wt. Tween 20 (with > 99% purity, Sigma-Aldrich, USA), and 5% wt. proteins, including whey protein isolate (WPI; with > 97.5% purity, BiPro, Agropur, Canada), β-lactoglobulin (β-lac; with > 95% purity, obtained by selective precipitation of commercial whey protein isolate), and bovine serum albumin (BSA; with ≥ 96% purity, Sigma-Aldrich, Germany). All solutions were filtered with 0.22 μm PES filters (Merck, Germany) before use in the experiments.

7.3.2 Partitioned-EDGE microfluidic chip

The custom-designed partitioned-EDGE microchips are made of borosilicate glass and produced by Micronit Microtechnologies B.V. (Enschede, the Netherlands). The geometry consists of two deep channels, with one straight channel for the dispersed phase and one meandering channel for the continuous phase (Figure 7.1A). The deep channels are connected by a shallow plateau (green box) of 200 μm length (L) and 500 μm width (W). The shallow plateau is further partitioned into eight identical parallel pores with 20 μm length (l) and 40 μm width (w) on the continuous phase side (Figure 7.1B). Unless stated otherwise, the main plateau and pores have 1 μm height (h). In the experiment, the chip was put in a chip holder (Fluidic Connect 4515, Micronit Microfluidics) and connected to the dispersed and continuous phases using PEEK tubing (0.75 mm, BGB®, Switzerland); with the outlet being closed, the pressurised dispersed phase flowed continuously onto the main plateau and pores, and finally into the continuous phase in the form of bubbles. Here, the partitioned-EDGE device was used to study bubble formation (Figure 7.1C) and coalescence (Figure 7.1D).

7.3.3 Microfluidic experiments

Both the air and continuous phases were pressurised using a digital pressure controller, which controls pressures at an accuracy below 0.1 mbar, via Smart Interface Software (Elveflow®, France). In the experiment, the air is firstly pressurised at P_d and then the continuous phase at P_c, resulting in a pressure difference across the main plateau and pores [148], namely the applied pressure $P_d^* = P_d - P_c/2$. While P_d^* is varied, the continuous phase velocity (v_c) is kept

constant in each pressure regime to avoid any effect of shear, namely approximately 0.1 m/s in the low-pressure regime and 1 m/s in the high-pressure regime. Lastly, it is worth to mention that in the experiments with SDS, the microchip was pre-treated with 5% wt. WPI (which would form a more hydrophilic layer, an approved method [91]) to avoid retraction of the meniscus at low SDS concentration and applied pressure.

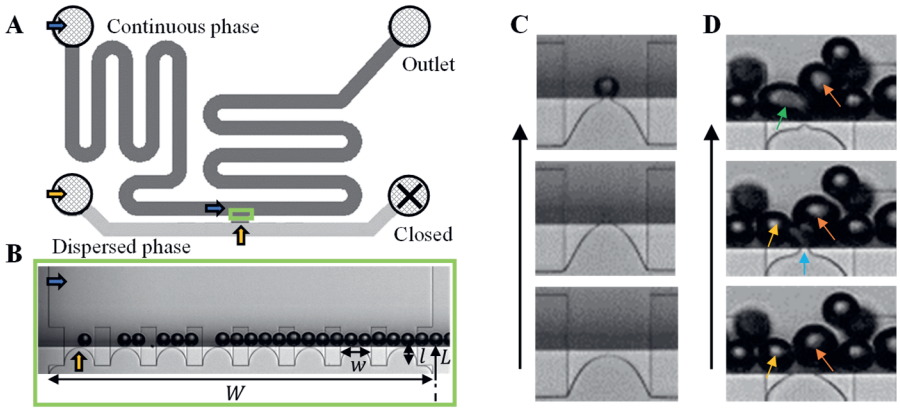

Figure 7.1. *The layout of the partitioned-EDGE device (A) and the pores on the continuous phase side of the shallow plateau (B). C. One bubble formation cycle. From bottom to top: the meniscus moves towards and leaps over the edge of the pore, leading to a growing bulb. D. Bubble formation and coalescence at the pore; coalescence of the two bubbles marked by ↗ and ↗ leads to the formation of the bubble marked by ↗. Bubbles are stabilised either immediately after formation or after coalescing a few times (↗). In C and D, the bottom-to-top arrows indicate time.*

7.3.4 Data analysis

Videos and images were recorded using a high-speed camera (FASTCAM SA-Z, Photron Limited, Japan) that is connected to the microscope (Axiovert 200 MAT, Carl Zeiss B.V., the Netherlands). In each experiment, two videos were recorded. One is recorded at a frame rate of 700,000 fps for the characterisation of time scales, including pore filling time (t_{fill}) and bubble necking time (t_n), with the bubble formation time (τ) being $\tau = t_{fill} + t_n$. The other video is recorded at a frame rate of 100,000 fps for the measurement of bubble sizes. A custom-written script in Matlab R2018b is used for the analysis of bubble sizes. The initial bubble size, d_0, is averaged for up to 50 bubbles; the coalesced bubble size, d_{coal}, is averaged for up to 100 bubbles. The coefficient of variation, CV (%) = $(\sigma/d) \cdot 100$ (with σ the standard deviation and d the number-averaged diameter) was used to describe the bubble size distribution.

7.4 Results and discussions

7.4.1 Background: Roles of dynamic adsorption in the partitioned-EDGE device

In an earlier study of bubble formation in the partitioned-EDGE device, whey protein was used as the emulsifier, and bubble formation shows a low- and a high-pressure regime, delineated by the Laplace pressure of the meniscus devoid of any emulsifier (P_{tran}) (Figure 7.2A) [148]. Besides, two other crucial pressures are the *breakthrough pressure* (P_{min}), which is the Laplace pressure of the meniscus saturated with emulsifiers and bounds the low-pressure regime on the lower end of the pressure range, and the *cross-over pressure* (P_{cross}) above which the pore filling time decreases below the bubble necking time. The transition and breakthrough pressures can be calculated using the Young-Laplace equation $\Delta P_L = \gamma\left(\frac{1}{R_1}+\frac{1}{R_2}\right)\cos(\theta)$, where R_1 and R_2 are the principal radii of curvature, γ the surface tension, and θ the contact angle between the channel wall and the continuous phase.

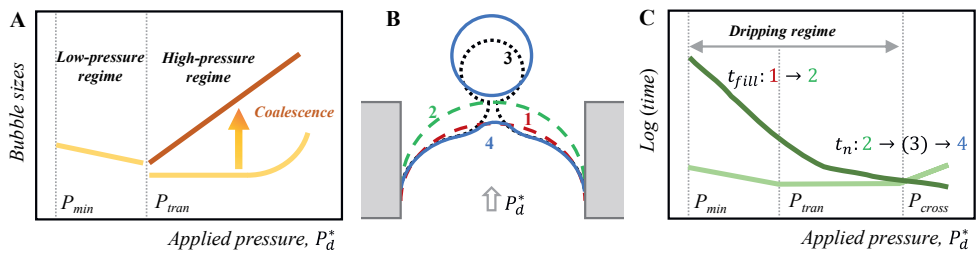

Figure 7.2. *Schematic illustration of bubble formation behaviours in the partitioned-EDGE device. A. Division of low- and high-pressure regimes, and the crucial pressures, in the presence of whey protein. B. One bubble formation cycle (1-4), with 2 and 4 representing the moment when the necking process is initiated and when the neck breaks up, respectively. C. The pore filling and necking time as function of the applied pressure. The trajectory of the meniscus in the pore during the pore filling and bubble necking stage are marked, referring to B.*

One bubble formation cycle is divided into two stages: the pore filling stage and bubble necking stage. In the low-pressure regime ($P_d^* < P_{tran}$), protein adsorption *at the meniscus* is required to lower its surface tension, and thus the Laplace pressure below the applied pressure. The pore filling stage consists of, first, the just-mentioned slow adsorption at a static meniscus (at position 1 in Figure 7.2B) and, second, the fast pore flow process that is initiated as soon as $\Delta P_L \leq P_d^*$; during the pore flow process, the meniscus moves forward in the pore until it reaches the edge of the pore (position 1 to 2, Figure 7.2B). The corresponding pore filling time (t_{fill}) is determined by the applied pressure and protein adsorption. Afterwards, in the bubble necking stage (t_n), the (partially-) covered meniscus leaps over the edge and

expands into a bulb outside the pore (position 2 to 3, Figure 7.2B), which grows in volume while the neck narrows and finally quickly snaps off at a neck width below the pore's height at t_n ($t_{fill} \gg t_n$) (indicated by shape 4 in Figure 7.2B). In the high-pressure regime with $P_d^* > P_{tran}$, the pore flow process immediately takes place, driven by a positive pressure drop P_d^* - P_{tran}; the t_{fill} decreases as function of the applied pressure and converges to t_n (Figure 7.2C). The neck width narrows faster in the high-pressure regime than in the low-pressure regime, resulting in shorter t_n, which was ascribed to the continuous phase inflow [160]. At pressures above P_{cross} where the pore filling time and necking time intersect, the 'dripping-jetting' transition can occur, marked with increased bubble size and polydispersity [160].

Bubble formation and thus bubble properties show distinct dependencies on *protein adsorption* in the two pressure regimes [148]. In the low-pressure regime, protein adsorption plays an important role in the initiation of bubble formation and thus the bubble formation frequency; next to that, protein adsorption at the meniscus influences the interfacial properties of the meniscus and thus the neck thinning process and t_n (and, as a result, d_0). The initial bubbles are formed at an extremely low frequency (typically below tens of bubbles per second) and stabilised before the occurrence of bubble-bubble interactions that may induce coalescence. In contrast, in the high-pressure regime, bubbles form and coalesce immediately (Figure 7.2A). The extent of bubble coalescence can be reduced by decreasing the bubble formation frequency (i.e., decreasing P_d^*) and stabilising the bubble surfaces (e.g., via increasing the protein concentration).

In the current work, *dynamic adsorption* is tuned by varying the type and concentration of emulsifiers. We focus on the formation and coalescence of bubbles stabilised with a standard low-molecular weight surfactant – SDS; besides, the results are qualitatively compared with those obtained for β-lac and BSA, as well as whey protein; the latter protein has been described in previous work [160]. This work allows us to highlight any emulsifier-related differences that occur during the highly dynamic processes that underlay foaming.

7.4.2 Bubble formation and coalescence: SDS concentration effects

The total bubble formation time

The bubble formation time (τ) is plotted as function of the applied pressure in Figure 7.3. In the low-pressure regime, $t_{fill} \gg t_n$ and thus $\tau \approx t_{fill}$. τ decreases monotonically as function of

the applied pressure since for increasing applied pressure an increasingly higher surface tension already initiates the pore flow, and thus shortens the lag time for SDS adsorption. In addition, τ decreases as SDS concentration increases up to 3% wt., due to faster adsorption and thus faster reduction in the surface tension. For SDS concentrations above the critical micelle concentration, which is approximately 0.20-0.28% wt. [38,52,54,55,157], mass transfer is enhanced due to the higher number density of SDS monomers resulting from fast disaggregation of SDS micelles [37,52,54]. In the high-pressure regime, τ eventually increases again with pressure, and this is a function of SDS concentration. For 0.05-0.1% wt. SDS, τ decreases as the applied pressure (P_d^*) is raised up to 1800 mbar, and afterwards increases slightly. For 0.2-0.5% wt. SDS, τ jumps from 0.02 ms to 0.1 ms at 1800 mbar, and then levels off. For 1-3% wt. SDS, the shortest τ is obtained at about 1500 mbar, and thereafter, τ slightly increases with P_d^* and levels off since 1800 mbar. It should be noted that in the high-pressure regime, t_{fill} still decreases with the applied pressure, showing no dependency on the SDS concentration (Figure A7.1). Thus, there is negligible SDS adsorption towards the meniscus during the pore filling stage, and the decrease of the pore filling time is exclusively attributed to the higher driving pressure. However, the bubble necking time (as discussed below) largely dominates the strongly shortened pore filling time, leading to the observed increase of overall bubble formation time around 1800 mbar in Figure 7.3.

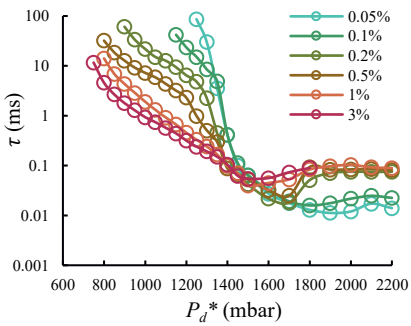

Figure 7.3. *The bubble formation time as function of the applied pressure for a range of SDS concentrations. The transition pressure is 1400 mbar.*

The bubble necking time

The influence of SDS concentration is also evaluated for the bubble necking time (t_n). t_n is a result of the neck thinning process, which is influenced by the interfacial properties of the meniscus. Across the full range of applied pressures, irrespective of the pressure regimes (i.e., P_{tran} = 1400 mbar), t_n varies in three sub-ranges (Figure 7.4A), divided as follows: I. the

plateau phase at $P_d^* \leq 1150$ mbar; II. bubble formation in the dripping regime for *all* SDS concentrations at $1150 \leq P_d^* \leq 1500$ mbar (the upper bound is given by the lowest P_{cross} for the used SDS concentrations, namely 1550 mbar for 3% wt.); and III the start of polydispersity at $P_d^* > 1500$ mbar. The sub-range I exists only for SDS concentrations above 0.2% wt.; t_n remains constant as function of P_d^* and increases with SDS concentration. We looked into the neck thinning process and observed that the neck thinning rate is independent of the applied pressure (Figure A7.2A), while it is lower as SDS concentration increases, which was also observed in previous study [180]. In sub-range II, t_n decreases as function of P_d^*, and this is a function of SDS concentration. For 0.05-0.2% wt. SDS, this is due to an overall faster necking process (Figure A7.2B), accelerated by the increasing dynamic surface tension of the neck region at increasing P_d^* [181]. For 0.5-3% wt. SDS, the neck thinning rate varies with time; there is a strong increase in the thinning rate with pressure at the beginning of the necking process, but within 5 μs all thinning rates again slow down to the low-pressure value (Figure A7.2C). The shift in thinning rate likely indicates a sudden decrease of the initially-higher surface tension of the neck region due to a fast replenishment of SDS monomers from the continuous phase in the pore, or a Marangoni flow along the expanding bubble surface towards the neck region [182]. Lastly, in sub-range III, t_n again increases significantly as function of P_d^* – which explains the increase in τ as shown in Figure 7.3. The increase of t_n starts at the applied pressure P_{cross}; the P_{cross} decreases from 1750 mbar for 0.05% wt. SDS to 1550 mbar for 3% wt. SDS. This is in line with the initiation of dripping-jetting transition at P_{cross} [160], which occurs earlier for lower interfacial tension [183].

The bubble size for initial and coalesced ones

Depending on the applied pressure and SDS concentration, initial bubbles of size d_0 may further coalesce, leading to enlarged bubbles of size d_{coal}. The bubble sizes shown in Figure 7.4B mostly have the size as bubbles were formed at low pressures, while coalescence is more prominent at high pressures, albeit which is strongly dependent on SDS concentration, as later explained in greater detail. In sub-range I (Figure 7.4B), d_0 increases almost linearly as function of P_d^*, which can be ascribed exclusively to an increase in the air flow rate into the growing bubble (Q'_{bub}), since the bubble volume ($V_0 = Q'_{bub} \cdot t_n$) is linear in both the air flow rate and the necking time that remains relatively constant (Figure 7.4A). In sub-range II up to 1350 mbar, d_0 decreases as function of P_d^* because of the strong decrease of t_n (Figure

7.4A) that dominates the continuous increase of Q'_{bub}. Typically, in the low-pressure regime (e.g., at $P_d^* \leq 1350$ mbar), initial bubbles are formed and stabilised before bubble-bubble interactions that may lead bubble coalescence to occur. The d_0 increases for SDS concentrations above 0.2% wt., in line with the changes in t_n.

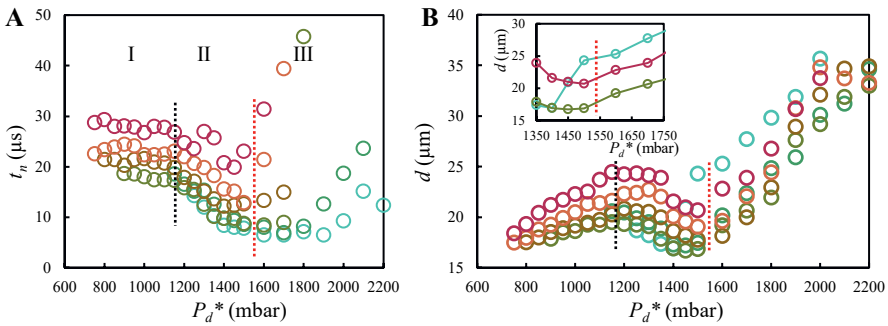

Figure 7.4. *A. Effects of SDS concentration on bubble necking time as function of applied pressure for 0.05 (○), 0.1 (○), 0.2 (○), 0.5 (○), 1 (○) and 3 (○)% wt. SDS. For ≥ 0.2% wt. SDS, t_n is analysed for applied pressures up to 1800 mbar, including a cross-over pressure for all SDS concentrations; axis y is shown up to 50 µs to visualise the effects of SDS concentration; at > 1800 mbar, t_{fill} is very short and t_n (which is approximately τ) levels off at a slightly higher value for increasing SDS concentrations. B. The corresponding bubble size as function of the applied pressure for the same range of SDS concentrations. Inset in B: to visualise the difference for 0.05, 0.2 and 3% wt. Dashed lines: the transition between I and II (black) or II and III (red).*

At the higher applied pressures of sub-range II, the bubble size shows distinct variations as function of P_d^* in the range of $1400 \leq P_d^* \leq 1500$ mbar for different SDS concentrations. Firstly, for $c = 0.05\%$ wt., bubble coalescence is observed since $P_d^* = 1450$ mbar, resulting in a marked increase in bubble size (inset of Figure 7.4B). Secondly, for $c > 0.2\%$ wt., d_0 continuously decreases as function of P_d^* till the end of sub-range II (and increases with SDS concentration). Thirdly, for $c = 0.1$-0.2% wt., bubble coalescence is likely partly suppressed; the bubble size remains constant at approximately 17 µm and is independent of the applied pressure and SDS concentration, which is likely because the few coalescence events balance out the decrease in d_0. In sub-range III, the bubble size shows an overall increasing trend with the applied pressure. The bubble size is influenced by multiple aspects, such as the initial bubble size, the extent of coalescence, and the dripping-jetting transition; as a result, the bubble size shows non-monotonous behaviour as function of SDS concentration, leading to polydispersity.

Typically, although the dripping-jetting transition occurs at lower applied pressures as the SDS concentration increases, the dripping regime is still wider, due to the larger impact of

increasing SDS concentration on the initialisation of bubble formation. Consequently, the dripping regime widens and shifts to lower applied pressures. In the low-pressure regime, bubbles are mostly monodisperse with CV around 5% (Figure A7.3); at higher applied pressures, bubbles become much more polydisperse due to the finite extent of bubble coalescence and most importantly, the formation of polydispersed, large bubbles upon dripping-jetting transition.

7.4.3 Comparison between SDS and proteins

Observation of bubble formation in the presence of SDS and WPI

The transition pressure (P_{tran}) is determined by the *device geometry and dimension*, the *type of interface* (e.g., gas-liquid or liquid-liquid), and also the *contact angle* between the continuous phase and the channel wall, while as above-discussed for SDS and in previous work for WPI [160], both the breakthrough pressure (P_{min}) and the cross-over pressure (P_{cross}) show dependency on the type and concentration of emulsifiers. As an illustration, at a constant transition pressure (i.e., 1400 mbar in this study), P_{cross} decreases from approximately 1750 to 1550 mbar as SDS concentration increases from 0.05 to 3% wt., and it decreases from 1900 to 1700 mbar as WPI concentration increases from 2.5 to 10% wt. The reduction in P_{cross} indicates that the 'dripping-jetting' transition occurs earlier at high concentrations of SDS and WPI; this implies that, maybe counter-intuitively, high emulsifier concentrations are detrimental for controllable high-frequency production of *monodisperse, small* bubbles, even though bubbles are stabilised against coalescence to a higher extent [160]. In practice, an 'optimal' concentration can be chosen such that bubbles are formed at a high frequency in the dripping regime, and are stabilised simultaneously and sufficiently.

For SDS and WPI, we observe fundamental differences during bubble formation at the pore. The neck thinning process, leading to snap-off of a bubble, can be accompanied by continuous phase inflow (into the pore), which is driven by a pressure drop along the pore and into the continuous phase. For WPI, this inflow was observed only in the high-pressure regime, characterised by the formation of *long necks* (comparing the top and the bottom rows of Figure 7.5B for WPI) and the *back-and-forth movements* of the meniscus (in the pore) during the consecutive cycles of bubble formation [160]. In the presence of SDS, the continuous phase inflow exists in both pressure regimes, as illustrated by a comparison of the necking behaviour between WPI and SDS in the low-pressure regime (Figure 7.5A) and the

similarities of the neck shape in both pressure regimes for SDS (Figure 7.5B). Moreover, in the presence of SDS, the continuous phase inflow can be visualised by system-specific 'tracking-particles' – satellite bubbles that are formed within a certain range of applied pressures (Figure 7.6, as will be discussed in the next section). The distinct interfacial behaviours of proteins and low-molecular weight surfactants are likely responsible for the aforementioned observations. For proteins, the surface tension starts to decrease only when the surface coverage exceeds 1 mg/m^2 of protein [134]. Next to that, according to Hinderink et al. (2021) [129], intermolecular interactions between protein molecules signifying an early stage interfacial network, are already present at time scales of 0.16-1 s. In the low-pressure regime of WPI, bubble formation is relatively slow and the bubble formation time is in the range of 0.01-1 s; therefore, an (early stage) interfacial network can be expected to modify the viscoelasticity of the meniscus, which becomes more viscous and less deformable. As a result, during the necking process, the meniscus experiences a higher resistance towards deformation, and is confined to the exit of the pore. The typical behaviour of WPI versus SDS is also seen for other emulsifiers (Figure 7.5A): with two other proteins (e.g., 5% wt. β-lac and BSA), we see long necks and the back-and-forth movements of the meniscus only in the high-pressure regime, while as also expected, with low-molecular weight surfactants (1% wt. SDS and Tween 20) we observe these characteristics in both pressure regimes.

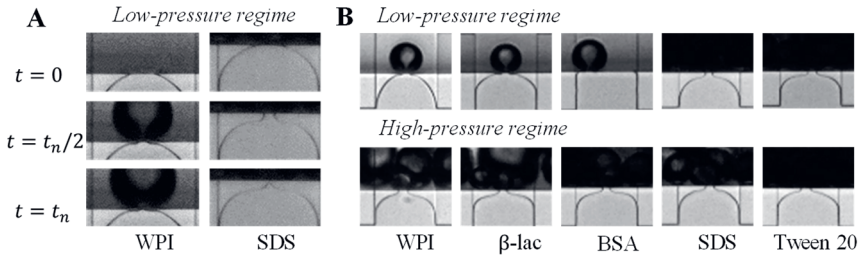

Figure 7.5. *A. Snapshots of the neck region in the middle of a necking process recorded at 1250 (up) and 1700 (bottom) mbar, respectively, for a range of emulsifiers. B. Detailed comparison of necking behaviour in the presence of WPI and SDS.*

Satellite bubbles

Satellite bubbles are observed when high emulsifier concentrations are used, for example, 3% wt. SDS and 20% wt. WPI (results are not shown). Satellite bubbles are mainly detected through their sudden appearance in the pores (see the inset of Figure 7.6A). For 3% wt. SDS, the inflow of satellite bubbles can be observed at P_d^* = 1200-1500 mbar. At the lower end of this pressure range, the inflow of satellite bubbles is sensitive to the flow rate of the

continuous phase in the collection channel: a lower continuous phase flow rate allows the satellite bubbles to accumulate in front of the pores and thus flow into the pores. The satellite bubbles can serve as 'tracking particles' to demonstrate the continuous phase inflow (Figure 7.6B). In the pore, the satellite bubbles are repeatedly accelerated and decelerated during the bubble necking stage and the subsequent pore filling stage (Figure 7.6B), corresponding to the back-and-forth movement of the meniscus; as a result, small eddies are created. When the satellite bubbles move along the meniscus towards the neck and finally out of the pore, their velocity can reach a maximum value of approximately 0.1~0.2 m/s (Figure A7.4).

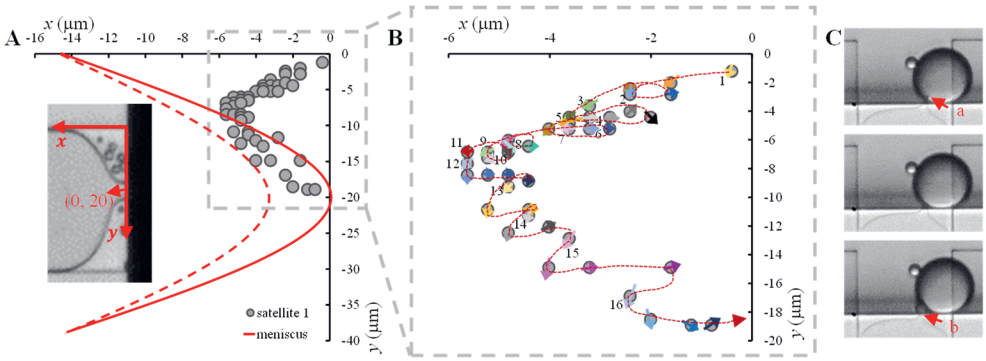

Figure 7.6. *A. The time-dependent positions of one satellite bubble (grey circles) in the pore, observed at* P_d^* *= 1350 mbar for 3% wt. SDS. The positions were analysed every 20 μs. The red solid and dashed lines represent the positions of the meniscus when the neck starts thinning and breaks up, respectively. B. The instantaneous moving directions of the satellite bubble along its trajectory. The numbers (1–16) indicate a sudden change in the moving direction of the satellite bubble; for each number the colour gradient (light to dark) indicates time (not drawn to scale to represent velocity). The dashed line is drawn to guide the eye. C. Illustration of satellite droplet formation in a 0.5% wt. SDS-hexadecane system, for droplet formation in the high-pressure regime. a – represents the connection between the neck and the primary droplet inside the continuous phase; b – represents the connection between the neck and the dispersed phase inside the pore.*

The formation of satellite bubbles, inside the continuous phase channel where bubbles are collected, is not visible due to bubble crowdedness in front of the pores. However, the formation of satellite *droplets* can be studied by direct observation in this device, and the findings could be extended to the formation of satellite bubbles since in both cases the viscosity of the dispersed phase is relatively low [184]. In Figure 7.6C, the neck protrudes into the continuous phase. The end of the neck connecting to the growing droplet (point a) ruptures *inside the continuous phase channel*, releasing the primary droplet. Meanwhile, the remaining dispersed phase in the neck relaxes into a spherical satellite droplet [185], leading to the shrinkage of the neck at the location of the pore edge (point b) and the growth of the

satellite droplet in volume; upon rupture *inside the pore*, a satellite droplet is released into the continuous phase channel.

Satellite bubbles (and droplets) are formed at high emulsifier concentrations upon an effective decrease in dynamic surface tension at the neck region during the neck thinning process, on a time scale of a few microseconds. The change in surface tension can be related either to the Marangoni stress driving surface flow from the expanding bubble surface towards the neck region that is depleted during the neck thinning process [181], or to the movement of the rupture location [182] from inside the pore to into the continuous phase channel, where emulsifier adsorption to replenish the neck region is likely enhanced by the continuous phase flowing in the channel (i.e., convection). Compared with satellite bubbles, we observe satellite droplets (hexadecane-in-water) for an extended range of SDS concentrations above 0.5% wt., which is in agreement with previous observations [186]. This can be ascribed to the higher viscosity of hexadecane that prolongs the neck thinning process and thus allows more SDS molecules to adsorb at the neck region, leading to lower interfacial tension. Lastly, when the emulsifier concentration is low (e.g., 0.1% wt. in comparison to 3% wt.), the neck region is most probably subject to a constant surface tension close to that of the pure air-water interface. The high surface tension leads to rapid rupture of the thinning neck and thus prevents the formation of satellite bubbles [184,187,188].

Dynamic adsorption and bubble formation for various proteins

In this section, the results obtained for 0.1% wt. SDS will be compared with those obtained for 5% wt. proteins, including WPI, β-lac, and BSA. These concentrations are selected since they enable the comparison for a comparable range of applied pressures: stable bubble formation in the dripping regime bounded by a similar P_{cross}.

The bubble necking time as function of the normalised applied pressure is shown in Figure 7.7A. In the low-pressure regime, t_n decreases as function of the normalised applied pressure – as previously shown for low concentrations of SDS and WPI. Compared with those of SDS, t_n values (and thus d_0 values shown in Figure 7.7C) obtained for proteins are higher, which can be ascribed to interfacial viscoelasticity due to intermolecular interactions of adsorbed proteins [61]. Among proteins, the slight difference observed in t_n and thus d_0 may reflect differences in the strength of interfacial network or of interaction between proteins and channel wall (i.e., potentially changed wetting properties of channel wall in the presence of

BSA). In the high-pressure regime at normalised applied pressures below 400 mbar, t_n values are independent of the applied pressure and the type of emulsifiers, indicating that any adsorption occurring during the pore filling stage towards the meniscus can be ignored. At higher normalised applied pressures, t_n starts increasing upon dripping-jetting transition, for first SDS and then BSA, while t_n levels off for WPI and β-lac (Figure 7.7A). As also illustrated for WPI [160] and SDS (Figure 7.4A) at increasing concentrations, the sudden increase in t_n is likely resulting from combined effects of lowered pore filling time (decreasing below t_n) and stronger emulsifier mass transfer towards the surface of the expanding bubble. The latter lowers the dynamic surface tension of the bubble surface and causes a Marangoni flow towards the neck region that delays its final break-up [189].

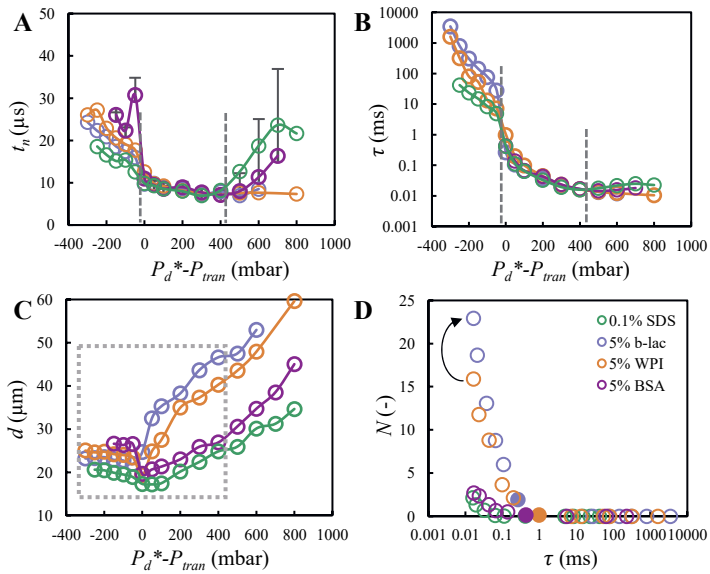

Figure 7.7. *The bubble necking time (A), the bubble formation time (B), and the bubble size (C) as function of the normalised applied pressure for 0.1% wt. SDS (○) and 5% wt. β-lac (○), WPI (○), and BSA (○). The proteins were tested in a chip with a pore height of 0.93 µm, which leads to P_{tran} = 1500 mbar. To fairly compare the results, the normalised applied pressures of (P_d^* - P_{tran}) were calculated. D. The corresponding number of coalescence events as function of the bubble formation time. The transition pressure is marked with filled symbols for SDS and various proteins. In D, the arrow guides the eye: comparison between WPI and β-lac. In the high-pressure regime, bubbles with N < 0.5 are considered stable.*

The bubble formation time is closely set by the initiation of bubble formation in the low-pressure regime and sets the bubble coalescence stability in the high-pressure regime. In the low-pressure regime, τ strongly decreases as function of P_d^*, and SDS adsorption is more efficient than proteins (i.e., WPI followed by β-lac) in lowering the dynamic surface tension (Figure 7.7B) and thus initiating bubble formation. Here, adsorption is likely enhanced due

to continuous phase inflow, which creates a flow field and eddies in the continuous phase inside the pore, and also refreshes the continuous phase timely. The higher efficiency of WPI compared to β-lac was also found during previous emulsification studies; upon emulsification at a comparable applied pressure, WPI yielded many more droplets than β-lac [91]. In the high-pressure regime, at normalised applied pressures below 400 mbar, τ decreases as function of P_d^*, showing again no dependency on the type of emulsifiers. Here, τ is mainly determined by the applied pressure and the (almost constant) hydrodynamic flow resistance of the pore. At higher applied pressures, τ starts increasing mainly for SDS and BSA, which is in line with that seen for t_n (Figure 7.7A).

Bubble coalescence dynamics for various proteins

In the high-pressure regime, initial bubbles (with size d_0) further coalesce, and the coalesced bubble size (d_{coal}) increases as function of the normalised applied pressure (Figure 7.7C). While the d_0 values are independent of the normalised applied pressure and the type of emulsifiers (Figure A7.5), the d_{coal} values are smaller for SDS than for proteins, with the latter showing an order of BSA < WPI < β-lac. To compare the stabilising effects of emulsifier adsorption at the bubble surface, we calculate the number N of coalescence events that a coalesced bubble has undergone. By using the volumes of initial ($V_0 = \frac{\pi}{6} d_0^3$) and coalesced bubbles ($V_{coal} = \frac{\pi}{6} d_{coal}^3$), the number of coalescence events, $N = \frac{V_{coal}}{V_0} - 1$, is plotted for SDS and various proteins versus the bubble formation time. N is studied for normalised applied pressures that produce *initially monodisperse* bubbles (within the dashed box; Figure 7.7C). In Figure 7.7D, as expected, bubbles are formed and immediately stabilised ($N = 0$) in the low-pressure regime at $\tau > 1$ ms for proteins and $\tau > 0.1$ ms for SDS. In the high-pressure regime for τ being as low as 10 μs, the extent of bubble coalescence shows a strong dependence on the type of emulsifiers. N values are relatively identical for SDS and BSA, and they are much lower than those obtained for WPI followed by β-lac. Within the *short-term*, BSA and, to a smaller extent, WPI are more efficient than β-lac in stabilising the initial and coalesced bubbles, and this is in line with their ability to lower the *dynamic surface tension* as discussed above. Hence, it is likely that the better foamability and the short-term foam stability of WPI than β-lac can be ascribed to the presence of BSA (and α-lac [91], which yielded many more droplets than WPI, observed in a previous emulsification study).

The above-mentioned observation is in stark contrast to that observed in a homogeniser. For example, at a constant concentration (2% wt., pH 7), the emulsifying capacity of these proteins is in the order of β-lac > BSA (> α-lac) [174], which is in line with their ability to reach a lower *equilibrium interfacial tension* that is in the order of β-lac (< WPI) < BSA, obtained at a concentration of 0.5% wt. [178]. Moreover, according to Muijlwijk et al. (2017) [27], to stabilise droplets against coalescence, a *higher* concentration and a *longer* adsorption time are needed for WPI (100 ms for 0.01% wt. WPI) than β-lac (31 ms for 0.005% wt. β-lac), which, maybe surprisingly, hints at the poorer performance of WPI in their experiment. On one hand, it is important to realise that in the coalescence chamber used by Muijlwijk and co-authors, 100 ms and 31 ms are relatively long times, during which emulsifiers are allowed to adsorb at the surface of individual and spatially-separated droplets. It is reasonable that droplets can be stabilised with an extremely low emulsifier concentration when the adsorption time is long enough to obtain monolayer surface coverage. On the other hand, to stabilise droplets and bubbles against coalescence on a *long-term*, not only fast adsorption (which results in a fast decrease in dynamic interfacial tension and the *short-term* stabilisation) is important, but alo the interactions between emulsifier molecules at the surface are crucial. Accordingly, more factors are likely playing a role in interface stabilisation For example, the microstructure of the proteins, the formation of a viscoelastic interface, the purity of the proteins adsorbed at the interface [27], and the oxidation level [58] of the proteins, just to name a few.

7.5 Conclusions

An important feature of the *partitioned-EDGE* device is the extreme shallowness of the main plateau and pores, which introduces high Laplace pressures that dominate bubble formation. The Laplace pressure of the bare meniscus marks the transition between low- and high-pressure regimes of bubble formation. Emulsifier adsorption plays a role in the initiation of bubble formation (i.e., bubble formation frequency) in the low-pressure regime, and the bubble coalescence stability in the high-pressure regime. These roles mainly depend on the efficiency of emulsifier adsorption in lowering the dynamic surface tension of the meniscus and the bubble surface, respectively. Next to that, in the low-pressure regime, emulsifier adsorption affects the interfacial properties of the meniscus, which influence the neck thinning process and thus the initial bubble size.

Emulsifiers (i.e., SDS and proteins including WPI, β-lac, and BSA) were tested at various concentrations (i.e., 0.05-3% wt. for SDS and 5% wt. for proteins). As SDS concentration increases, the bubble formation frequency increases in the low-pressure regime due to the faster SDS adsorption and decreases in the high-pressure regime due to the earlier dripping-jetting transition, upon which large initial bubbles are formed at the pores. In addition, we found that SDS adsorption is more efficient than proteins; specifically, BSA and then WPI are more efficient than β-lac, in lowering the dynamic surface tension of the meniscus and the bubble surface. In the order of SDS, BSA, WPI and β-lac, emulsifier adsorption towards the former location leads to an increasingly higher bubble formation frequency in the low-pressure regime, and that towards the latter location, at time scales down to 10 μs (i.e., short-term stabilisation), results in an increasingly lower extent of bubble coalescence in the high-pressure regime.

To summarise, we studied emulsifier adsorption at time scales that are relevant to bubble (and droplet) formation during large-scale production, such as 0.1-30 ms in high-pressure homogenisers and 0.1-100 s in colloid mills [153]. Our insights can be used to understand emulsifier adsorption and its influences on the formation and instant coalescence of bubbles (and droplets) formed during large-scale production; next to that, the partitioned-EDGE device can be used as a tool for the characterisation and selection of emulsifiers for specific applications.

7.6 Appendix

7.6.1 The pore filling time for SDS concentration effects

The pore filling time is dominated by emulsifier adsorption in the low-pressure regime, and it is determined by the applied pressure and the hydrodynamic flow resistance of the pore in the high-pressure regime.

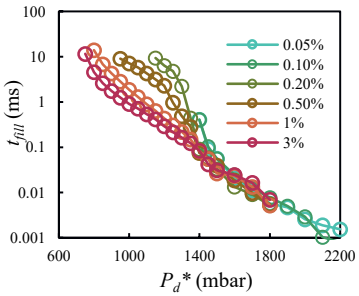

Figure A7.1. *The pore filling time as function of the applied pressure for various SDS concentrations.*

7.6.2 The neck thinning process w_t/w_0

The neck thinning process is monitored for representative pressures in sub-range I and II, for the effects of applied pressure and SDS concentration (0.2 and 3% wt.). It is clear that the neck thinning process is influenced by the applied pressure and SDS concentration; besides, at high SDS concentrations, the neck thinning rate varies over time, which likely indicates a decrease of dynamic surface tension of the neck region at microsecond time scales.

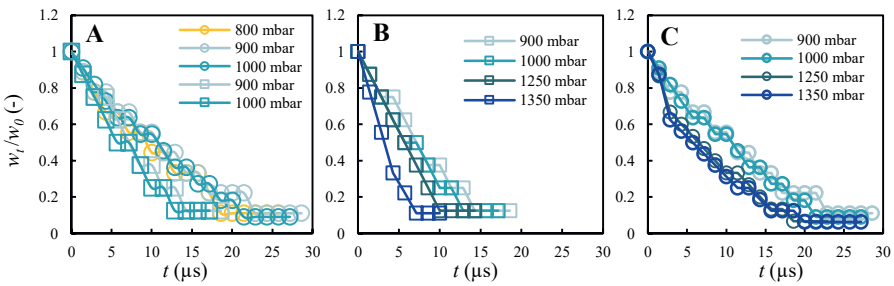

Figure A7.2. *The neck thinning process. Effects of applied pressure and SDS concentration in sub-range I are shown in A. Squares: 0.2% wt.; circles: 3% wt. Comparison among applied pressures in sub-range I and II for relatively low (i.e., 0.2% wt. in B) and high (i.e., 3% wt. in C) SDS concentrations. In A-C, w_0 and w_t are the initial neck width and the neck width varying overtime, respectively; the neck breaks up at t_n.*

7.6.3 The bubble size distribution

The coefficient of variation (CV) is calculated for different applied pressures and SDS concentrations (0.05-3% wt.).

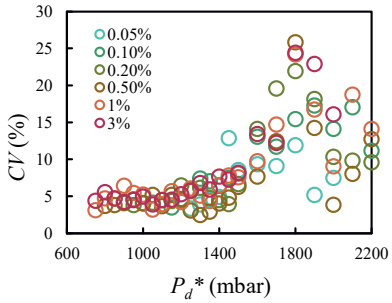

Figure A7.3. *The CV as function of the applied pressure for various SDS concentrations.*

7.6.4 The velocity for satellite bubble inflow

The velocity of satellite bubble reaches a maximum value of about 0.1~0.2 m/s, when the satellite bubble moves along the meniscus towards the neck region and finally out of the pore.

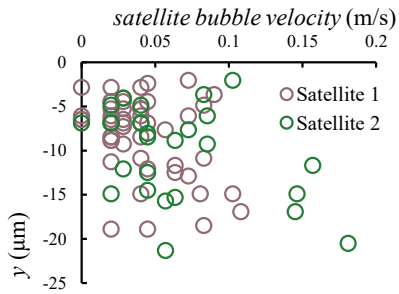

Figure A7.4. *The velocity of the satellite bubble inside the pore.*

7.6.5 The initial bubble size

The initial bubble size is almost constant as function of the normalised applied pressure in the range of 0-400 mbar, independent of the type of emulsifiers (i.e., 0.1% wt. SDS and 5% wt. proteins), and these observations are in line with the necking time shown in Figure 7.7A.

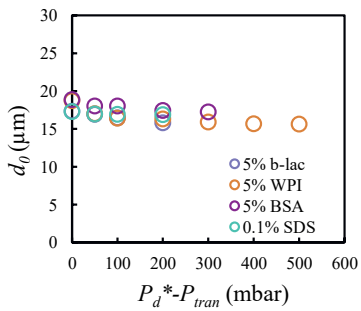

Figure A7.5. *The initial bubble size as function of the normalised applied pressure. The proteins were tested in a chip with a pore height of 0.93 μm, which leads to P_{tran} = 1500 mbar. To fairly compare the results, the normalised applied pressures (P_d^* - P_{tran}) need to be used.*

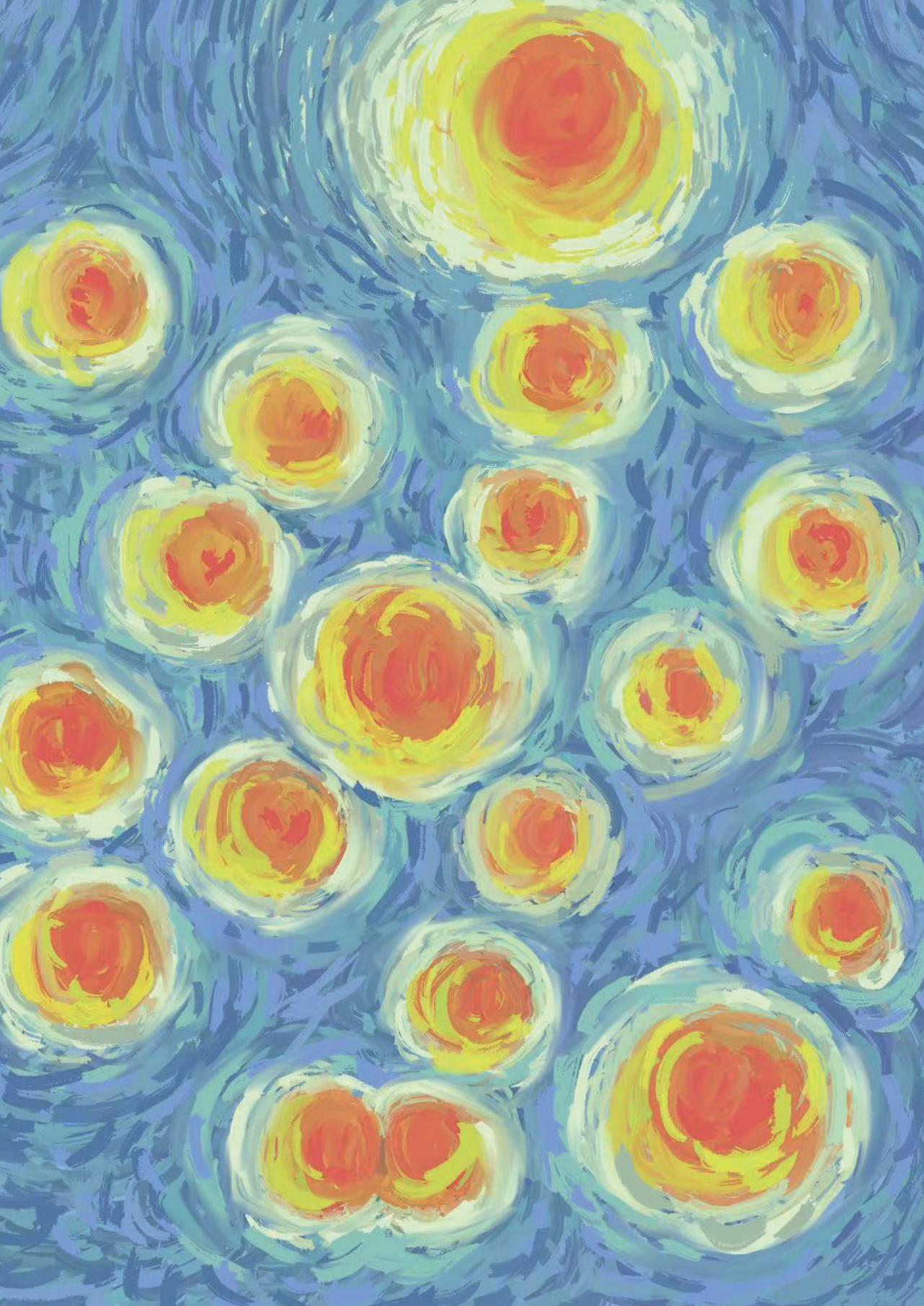

CHAPTER || 8

Mapping bubble formation and coalescence in a tubular cross-flow membrane foaming system

This chapter has been published as Deng, B., Neef, T., Schroën, K., & De Ruiter, J. Mapping bubble formation and coalescence in a tubular cross-flow membrane foaming system. *Membranes*, **2011**, 11(9), 710.

8.1 Abstract

Membrane foaming is a promising alternative to conventional foaming methods to produce uniform bubbles. In this study, we provide a fundamental study of a cross-flow membrane foaming (CFMF) system to understand and control bubble formation for various process conditions and fluid properties. Observations with high spatial and temporal resolution allowed us to study bubble formation and bubble coalescence processes simultaneously. Bubble formation time and the snap-off bubble size (d_0) were primarily controlled by the continuous phase flow rate (Q_c); they decreased as Q_c increased, from 1.64 to 0.13 ms and from 125 to 49 µm, respectively. Coalescence resulted in an increase in bubble size ($d_{coal} > d_0$), which can be strongly reduced by increasing either continuous phase viscosity or protein concentration – factors that only slightly influence d_0. Particularly, in a 2.5% wt. whey protein system, coalescence could be suppressed with a coefficient of variation below 20%. The stabilising effect is ascribed to the convective transport of proteins and the intersection of time scales (i.e., µs to ms) of bubble formation and protein adsorption. Our study provides insights into the membrane foaming process at relevant (micro-) length and time scales and paves the way for its further development and application.

Graphical abstract

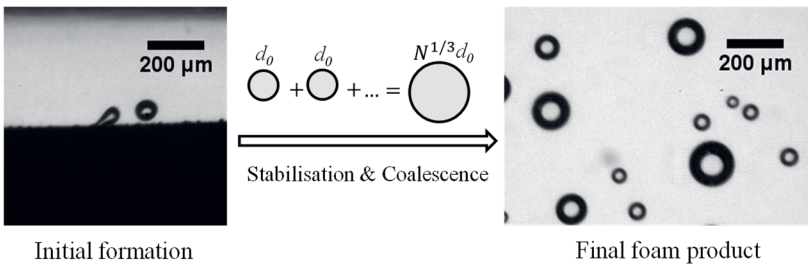

8.2 Introduction

Foams are widely used in our daily life such as in pharmaceuticals, cosmetics and foods. Each application has specific demands for stability and functionality of the foams, and thus targets different bubble properties (i.e., bubble size and bubble size distribution), which are strongly influenced by the foaming techniques. Foams are conventionally produced and studied in high-speed stirrer/mixer [190] and rotor-stator systems [191] that operate based on continuous fragmentation of larger bubbles into small bubbles. These traditional techniques are relatively easy to scale-up, but are also associated with limitations, including high energy input and limited control over the bubble properties. High shear and high emulsifier concentration are needed to obtain a foam with relatively monodisperse and small bubbles. Alternatively, other methods like packed-bed system [192], microfluidic devices [193], and membrane systems [194–197] can directly generate individual bubbles with desired size and improved monodispersity. The packed bed and membrane systems are capable of achieving high throughput, while that is not the case yet for microfluidic devices that are still in need of upscaling.

In a cross-flow membrane foaming (CFMF) system, the dispersed phase is injected into the continuous phase passing through a porous membrane matrix, and bubbles are detached at the membrane surface by the cross-flowing continuous phase. Compared to membrane emulsification, which has been substantially studied and reviewed [78,198–201], only a few studies were conducted on membrane foaming and in most of these cases a high emulsifier concentration (e.g., 10% wt. whey protein) was used and any short-term destabilisation process (in particular, coalescence) was thus not taken into account. The bubble properties and resulting foam stability were evaluated at the outlet of the foaming systems and were then explained in terms of the applied process parameters and/or the membrane properties such as pore size [194,197]. However, these final bubble properties are an equilibrium state following the formation and re-coalescence of bubbles flowing in the continuous phase, with the latter process causing an increased bubble size and higher polydispersity [202]. To make a monodisperse foam, choosing a membrane with uniform pores is not sufficient, as was found with a micro-engineered membrane for emulsification [203]. It is thus crucial to first understand the bubble production process within very short timescales, and thereafter manipulate other factors accordingly, such as the emulsifier concentration to stabilise the freshly-generated

bubbles. To the best of our knowledge, such a fundamental study of bubble formation in a cross-flowing membrane foaming system is still missing.

The goal of this study is to investigate the cross-flow membrane foaming process by in-line high-speed visualisation of bubble formation and mapping of potential bubble coalescence. Whey protein isolate, which is often used in commercial food foams, is used as the emulsifier, and we study the bubble properties such as bubble size (distribution) and formation frequency under the effects of transmembrane pressure, continuous phase flow rate and viscosity, as well as protein concentration. To indicate the occurrence of coalescence (if any), we observe the bubbles at two distinct positions in the foaming system: first, bubbles that are initially formed at the membrane surface, and second, bubbles flowing through an observation chamber at a short distance downstream from the membrane.

8.3 Experimental

8.3.1 Materials

In a cross-flow membrane foaming (CFMF) system, air bubble formation was studied in aqueous (Milli-Q, Merck Millipore) solutions of whey protein isolate (BiPro, 97.5% purity, Agropur, Canada) at various concentrations and viscosities. Viscosity was adapted using glycerol (99.5% purity, VMR International, Leuven, Belgium). The viscosity was measured at 20 °C in triplicate using an Anton Paar Rheometer (MCR301, Anton Paar GmbH, Graz, Austria) which is equipped with a Couette cell (C-DG26).

A tubular-type polypropylene membrane with a macroscopic water contact angle of 120° was used in the CFMF system. The membrane has an outer diameter of 2.7 mm and a length of approximately 20 mm. The outer surface of the membrane shows a partially-interconnected pore network, with pore sizes ranging from a few to tens of micrometres (Figure 8.1).

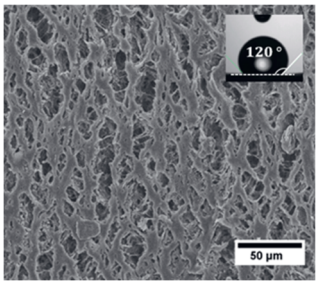

Figure 8.1. *SEM photograph of the outer membrane surface. A snapshot for the macroscopic contact angle measurement is shown on top of the SEM image. The measurement is performed on a piece of unused membrane and the measured contact angle is about 120°.*

8.3.2 Set-up

The set-up for the CFMF experiment is schematically shown in Figure 8.2. The core of the set-up is the membrane module (that holds a membrane) where foaming takes place. The membrane module has two inlets for the air and continuous phases, a tubular chamber of 3.8 mm inner diameter in which foaming takes place, and one joint outlet. The membrane was inserted in the middle of the module, and a pressure controller fed air and continuous phases (via a feed tank) to the module. Between the inner wall of the module and the outer surface of the membrane, there is a gap of 0.55 mm. Bubble formation takes place by the action of the cross-flowing continuous phase that shears off the bubbles from the membrane surface, and next transports them towards the exit.

Bubble formation can be observed along the membrane (Figure 8.2). We chose a position near the continuous phase inlet albeit on the opposite side, marked by a rectangle in Figure 8.2. Additionally, a quartz flow cell (Type 55, Fireflysci, Canada) was connected to observe bubbles at 10 or 100 cm downstream of the membrane module, while keeping the total tubing length (and the flow resistance) constant. The flow cell has a height of about 0.4 mm, which allows us to observe undeformed bubbles in a more-or-less single flow plane. To investigate the bubble properties over time, we analysed bubbles formed upstream across from the continuous phase inlet and compared them with bubbles flowing downstream through the flow cell (see the insets of Figure 8.2).

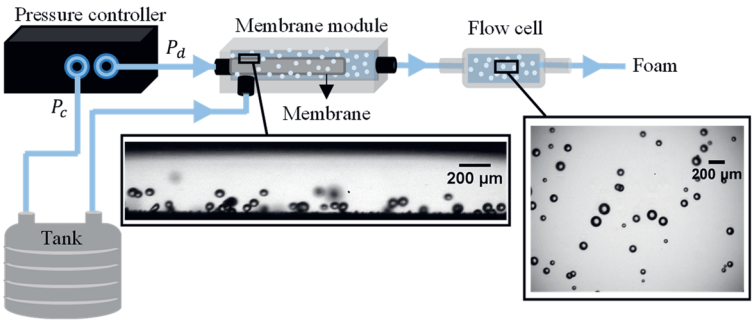

Figure 8.2. *Schematic overview of the experimental set-up. The images show bubble formation at the membrane surface across from the continuous phase inlet and bubbles in the flow cell. The schematic is not drawn to scale.*

8.3.3 Membrane foaming

The flows of the air and continuous phases were both driven by pressure and controlled with the digital pressure controller that is operated with Smart Interface Software (Elveflow®, France). First, the (dispersed) air phase was injected into the system at pressure P_d. The pressure drop over the air phase occurs mainly across the relatively narrow pores of the membrane, such that the air pressure inside the membrane is also P_d. The continuous phase was then fed from the feed tank at pressure P_c, which drops more gradually over the full flow path, from P_c at the flow controller to zero (absolute pressure) at the outlet. We estimated the flow resistance of each system component and found that at the continuous phase inlet of the membrane module, the pressure P_c has dropped by approximately 55%; The effective continuous phase pressure is thus defined as $P_{c,eff}$ that equals $P_{c,eff} = P_c \cdot (1 - 0.55)$. From this, the transmembrane pressure P_{trm} is calculated by $P_{trm} = P_d - P_{c,eff}$. The pressure P_{trm} is the effective pressure drop over the pores, and drives the bubble formation.

The bubble formation was investigated under the effects of process conditions and fluid properties. Firstly, the bubble formation was studied as function of P_{trm} in the range of 100-400 mbar. The corresponding air flow rate (Q_d) was estimated from the volumetric production rate of foam collected at the outlet, with the liquid entrapped within the foam being subtracted. A constant continuous phase flow rate (Q_c) was applied to eliminate potential differences in the convective transport of proteins towards the air-water interface. Secondly, for a given P_{trm}, the bubble formation was evaluated under the effect of Q_c – the volumetric flow rate measured by weighing the outflow of the system. It varies between $6.4 \cdot 10^{-6}$ and $2.1 \cdot 10^{-5}$ m^3/s, which corresponds to a cross-flow velocity of 1.6-5.4 m/s in the membrane module. Our window of operation is determined by pore activation and the possibility of visualisation. Operation at low P_{trm} or high Q_c is limited by low activation of the pores. Operation at high P_{trm} or low Q_c is in principle possible and leads to high bubble productivity, but the bubble fraction is then too high for visualisation. Lastly, to study the effect of continuous phase viscosity (η) and protein concentration (c), process conditions were fixed to P_{trm} = 200 mbar and $Q_c = 1.5 \cdot 10^{-5}$ m^3/s, using either constant c = 1% wt. with η varying as 1.3, 1.5 and 2 mPa·s, or constant η = 1.3 mPa·s with c varying as 0.5, 1.0 and 2.5% wt.

For practical reasons, protein solutions were re-used (up to 10 times) during the experiments. Since the reduction of protein concentration over time was under 20% (Figure A8.1), this effect was ignored. The module and tubing were cleaned with MilliQ-water between different experimental conditions, and the membrane was replaced once the pressure applied to the air phase was switched off and on again (every day). All the experiments were performed at ambient temperature.

8.3.4 Image analysis

A high-speed camera (FASTCAM SA-Z, Photron Limited, Japan) is attached to the inverted microscope (Axiovert 200 MAT, Carl Zeiss B.V., the Netherlands) and used to observe and visualise bubbles in the CFMF system. Videos were recorded at 20,000 frames per second and with a resolution of 0.314 pixels/µm. For each experimental condition, two videos were recorded at two distinct positions in the CFMF system: capturing either bubble formation at the membrane surface across from the continuous phase inlet (Figure 8.2), or bubbles flowing through the flow cell during their transport to the outlet.

A custom-written code in Matlab R2018b was used to calculate the diameters of bubbles that are directly formed at the pore openings (d_0, averaged for up to 100 bubbles) and that are the result of coalescence (d_{coal}, averaged for up to 100 bubbles), respectively. Histogram plots of the bubble diameters were made to visualise the number-averaged bubble size distribution. Moreover, the bubble size distribution was also characterised by the coefficient of variation (CV), defined as CV (%) = $(\delta/d) \cdot 100$ (in which, δ is the standard deviation and d the number-averaged bubble diameter). Average bubble formation frequencies were estimated by $f_0 = Q_d/V_0$ and $f_{coal} = Q_d/V_{coal}$, where V_0 and V_{coal} are the volumes corresponding to d_0 and d_{coal}, respectively. Furthermore, two time scales were estimated during a bubble formation cycle using the videos. The interval time is the lag time between two bubble growing processes at the same pore opening, and the bubble growing time is the time of actual bubble growth at the pore opening. These were measured for each experimental condition, and the values were averaged for up to 30 bubbles.

8.4 Results and Discussions

8.4.1 General bubble behaviour in CFMF

We study bubble formation as function of the transmembrane pressure (P_{trm}). Bubble formation only occurs if the transmembrane pressure exceeds the activation pressure. This activation pressure equals the capillary pressure of the meniscus in the narrow pore, which is defined as $P_{cap} = \frac{4\gamma\cos(\theta)}{d_p}$, where γ is the surface tension between the air and continuous phases, d_p the diameter of the pore (opening), and θ the contact angle between the continuous phase and the membrane surface [78]. At P_{trm} as low as 50 mbar, a few pores form bubbles at an extremely low formation frequency (too low for quantitative analysis of d_0 and the corresponding f_0). The activation pressure for bubble formation is thus assumed to be approximately 50 mbar. For contact angles > 90°, the air phase would flow out of the pores automatically, and the growing bubble would possibly spread out at the (hydrophobic) membrane surface, which would lead to extensive coalescence at the membrane surface [22,200], which is not observed in the present study. Thus the macroscopic contact angle (120° as measured for an unused membrane) is not the actual contact angle in the system. Possible explanations are differences between micro- and macroscopic contact angle, which is known to occur on porous surfaces such as membranes. More probably protein adsorption renders the membrane surface more hydrophilic (< 90°).

We can estimate the effective diameter d_p of (circular) pores that are activated based on P_{cap} = 50 mbar and γ varying between equilibrium value (~50 mN/m) and that of the pure air-water interface (~72 mN/m). For θ we assumed a microscopic contact angle of about 80°. The estimated diameter of the activated pores is of the order of 10 µm, which corresponds to the largest observed pores. This means that at low P_{trm}, only the relatively large surface pores are activated to form bubbles, while the smaller pores need a higher activation pressure. When increasing P_{trm} above 50 mbar, bubbles are increasingly present in the membrane module. This behaviour is ascribed to the increasing number of active pores (Figure 8.3A 1,2, indicated by the arrows) and the increasing frequency of the pores, with smaller pores having a lower frequency.

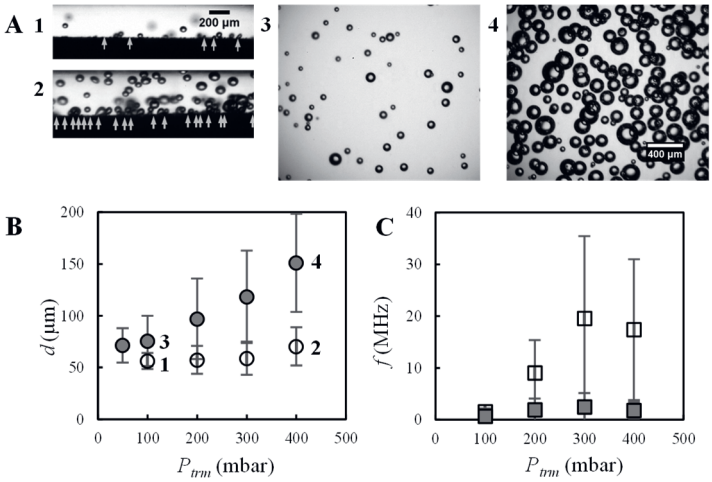

Figure 8.3. *Bubble formation behaviour as function of transmembrane pressure, P_{trm} (at constant Q_c = $1.5 \cdot 10^{-5}$ m^3/s and c = 1% wt.). A. Snapshots of bubble behaviour obtained when using different transmembrane pressures (low – 1,3 and high – 2,4). 1,2 – Visualisation of bubble formation at the membrane surface in the module; 3,4 – Visualisation of bubbles that are flowing through the flow cell (10 cm downstream). It is noted that in 1,2, only pores located at a single tangent line of (part of) the membrane are in our focal plane, while in 3,4 bubbles formed from the whole membrane surface (circumference and length) are present. In 1,2, the arrows roughly indicate the position of active pores. B. Bubble sizes d_0 and d_{coal}, with a typical CV of ~20% and ~40%, respectively. C. Bubble formation frequencies. The large error bars reflect the width of the size distribution, yet they are expected to be much smaller when studying individual pores. The bubble sizes (and the corresponding formation frequencies) are indicated with two different symbols: d_0 (f_0) – unfilled circle (square) and d_{coal} (f_{coal}) – filled circle (square).*

Along the system, going from the membrane module (where d_0 is estimated) to downstream in the flow cell (where d_{coal} is derived), there is more substantial increase in bubble size at higher P_{trm} (compare Figure 8.3A from 2 to 4 versus Figure 8.3A from 1 to 3). The two bubble diameters (estimated in the module and flow cell) and their corresponding formation frequencies are plotted to quantify the effects of P_{trm} on bubble formation and stabilisation (Figure 8.3B,C). The bubble diameter d_0 only slightly increases when P_{trm} is increased to up to 300 mbar, showing a similar trend as that was reported previously [197], and it increases relatively more at P_{trm} = 400 mbar. In contrast to the overall slight variation in d_0, the coalesced bubble diameter d_{coal} significantly increases with P_{trm}. The difference indicates the co-existence of bubble formation and bubble coalescence in the 1% wt. whey protein system. The d_{coal} increases much more strongly than the rather constant d_0 for increasing P_{trm} (Figure 8.3B), which is indicative of an increasing extent of bubble coalescence. Last but not least, with increasing P_{trm} the formation frequency of coalesced bubbles was increasingly lower than the corresponding f_0 (Figure 8.3C). For a given continuous phase flow rate, bubble

formation frequency is determined by both the P_{trm} and the bubble size, which has opposite effects [204]. As shown in Figure 8.3C, f_0 first increases and then decreases with increasing P_{trm}. The decrease may be explained by the increased size of the bubbles (i.e., d_0) and a higher extent of bubble coalescence (at high P_{trm}), leading to the overall much lower.

To confirm whether coalescence mainly occurs in the membrane module or continues downstream, we measured d_{coal} at two distinct positions along the flow path, namely at a distance of 10 cm and further of 100 cm downstream the membrane module (Figure A8.2). The obtained d_{coal} values are similar, which proves that bubbles coalesce mostly in the membrane module during or shortly after their formation, reaching a stable situation within a short-term. This finding allows us to limit ourselves to a flow cell position of 10 cm downstream for all the remaining experiments.

8.4.2 Bubble formation at the membrane surface

We first introduce the forces which dictate bubble formation. As was reported for cross-flow membrane emulsification systems, the bubble is subjected to four forces while growing at the membrane surface, which are the shear force imposed by the continuous phase flow rate and viscosity, the buoyancy force, the inertia force and the interfacial tension force [199,204]. For bubble formation in the present system, the interfacial tension force is the holding force, and scales as either $\frac{\gamma R_p^2}{R_0}$ or γR_p, depending on the applicability of a force or a torque balance (R_p is the radius of the pore and R_0 the in-line radius of the bubble which grows towards d_0) [205]. The shear force, which scales as $v_c \eta R_0$, is considered to be the only driving force among the rest of the forces since the other two forces are at least two orders of magnitude smaller. The bubble stays attached to the pore opening and snaps off when, for a certain bubble size, the shear force exceeds the surface tension force [132,206]. The force or torque balance leads to $d_0 \sim \mathrm{Ca}^{-n}$, with $\mathrm{Ca} = \frac{\eta v_c}{\gamma}$ the Capillary number of the continuous phase flow and n the power-law exponent whose value is between 0.5 and 1.

In our experiments, the continuous phase flow rate (Q_c), protein concentration (c) and continuous phase viscosity (η) are varied, and bubble formation at the membrane surface is studied. In accordance with the definition of forces, our experimental parameters can influence this force or torque balance: by increasing either the flow rate or the viscosity of the continuous phase, the shear force increases; by increasing the protein concentration, faster

protein adsorption can lower the (dynamic) surface tension faster and thus rapidly reduce the holding force (in the case that protein adsorption can appreciably take place within the very short time scales for bubble formation). In both cases, bubbles can be detached earlier from the pore openings [179,207].

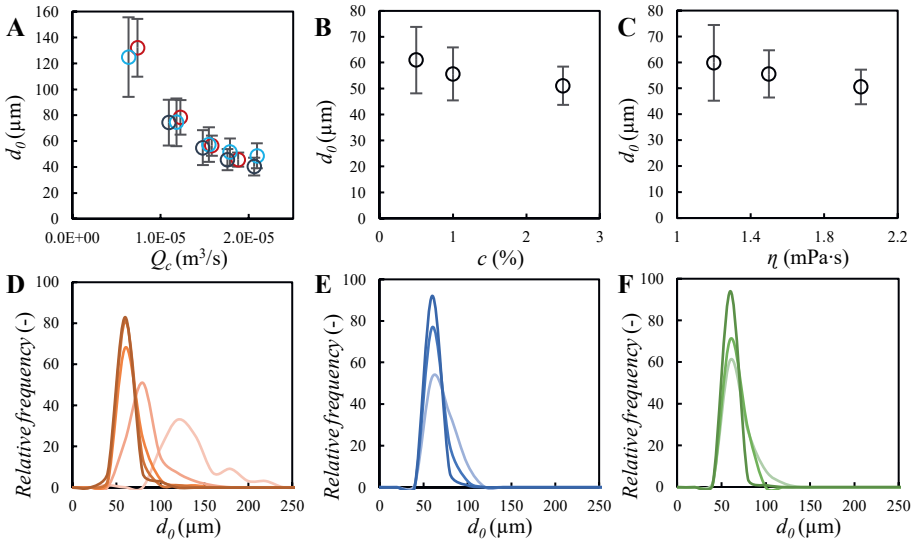

Figure 8.4. *Properties of bubbles (with d_0) formed at the membrane surface. A. Shear effect investigated for P_{trm} equal to 100 (○), 200 (○) and 300 (○) mbar. Results at P_{trm} = 400 mbar are not included because bubbles that are initially formed at the pores cannot be measured due to bubble crowdedness. B. Protein concentration effect. C. Continuous phase viscosity effect. In B and C, the process conditions are P_{trm} = 200 mbar and $Q_c = 1.5 \cdot 10^{-5}$ m³/s. Corresponding to d_0 values shown in A-C, the size distribution (obtained at P_{trm} = 200 mbar for A) is given in D-F. Darker colours indicate an increase in the evaluated parameter .*

The bubble size is firstly investigated as function of continuous phase flow rate. Please note that bubbles growing at the membrane surface tend to be deformed by the flow of the continuous phase, particularly when a high continuous phase flow rate (Q_c) is applied. d_0 significantly decreases as Q_c increases (Figure 8.4A), which is in line with what was reported for other membrane foaming systems [197,206] or membrane emulsification [208,209]. At lower Q_c, the bubble stays attached to the pore opening for a longer time, thus obtaining a larger size, while at higher Q_c, d_0 reduces to about 50 µm for the highest Q_c's measured. The results agree with the proposed scaling with Ca, with a fitted power-law exponent $n = 0.8 \pm 0.1$.

The d_0 almost shows no dependency on the transmembrane pressure for P_{trm} = 100-300 mbar for any given Q_c (Figure 8.4A). At P_{trm} = 400 mbar, the small increase in d_0 represents the volume of air added during the final detachment process of the bubble due to a higher air

flow rate [209]. The strong dependency of d_0 on Q_c indicates that the high shear flow dominates overall behaviour; the effects of transmembrane pressure and fluid properties on bubble formation at the membrane surface can be neglected.

Additionally, only a minor decrease can be observed in d_0 as function of protein concentration and continuous phase viscosity (Figure 8.4B, C), which are both evaluated at P_{trm} = 200 mbar and Q_c = $1.5 \cdot 10^{-5}$ m^3/s (Figure 8.4A). By raising the continuous phase viscosity, the average bubble size d_0 is reduced to about 50 µm due to its effects on increasing the shear force and potentially also the (dynamic) surface tension force. The decreasing trend with viscosity collapses onto the same $Ca^{-0.8}$ behaviour (assuming a constant surface tension, Figure A8.3). For these experiments taken at larger Ca, the rather constant d_0 can be ascribed to the fast bubble detachment process induced by shear force exerted by the continuous phase [209]. When the protein concentration increases to 2.5% wt., the d_0 decreases also just slightly to approximately 51 µm. The decrease is ascribed to faster protein adsorption which further lowers the (dynamic) surface tension and advances the force balance for bubble snap-off. Moreover, because the surface tension only can be decreased to a limited extent, bounded by the equilibrium surface tension of the air-water interface stabilised by whey proteins, the influence of protein adsorption on bubble size is moderate. Hence, bubble formation at the membrane surface falls into a regime where bubble snap-off is dominated by shear force, and under the conditions studied here, mainly controlled by the continuous phase flow rate [199].

The bubble size distribution varies with bubble size. The histogram plot indicates that bubbles with higher monodispersity are formed as Q_c increases, with the main peak in the plot shifting from right to left (Figure 8.4D). In addition to the effects of Q_c, the bubble size distribution can further be narrowed by increasing the protein concentration and/or the continuous phase viscosity (Figure 8.4E, F). Bubbles with diameters in the range of 40-60 µm account for more than 90% of the size distributions (Figure 8.4E, F). The corresponding coefficient of variation (CV) is below 15% when the highest protein concentration and/or viscosity is used (Figure 8.4E, F). However, the average d_0 can be decreased only to a limited extent (to approximately 50 µm), with the smallest bubbles having a diameter of approximately 40 µm (corresponding to the left side of the histogram plot), which is independent of the experimental conditions, and the bubble size distribution cannot be infinitely narrowed. This can be ascribed to the characteristics of protein adsorption and the

properties of the used membrane – the pore size and the pore size distribution. Specifically, when bubble formation is much faster than protein adsorption, the surface tension keeps constant as that of the pure interface, limited by the efficiency of protein adsorption; moreover, the smallest pores that have a lower holding force, produce smaller bubbles, thus widening the bubble size distribution [204], and determine the lower boundary of the bubble size distribution. In addition, the interactions between bubbles can influence the bubble size distribution by detaching the bubbles early on [210].

8.4.3 Bubble coalescence

To thoroughly understand the CFMF system, the bubble coalescence is also evaluated as function of the same experimental parameters. Firstly, within the resolution of our experimental results, coalescence of bubbles growing at adjacent active pores is rarely visually observed. Instead, coalescence often happens upon collision amongst flowing bubbles or a collision between a flowing bubble and a forming bubble. To demonstrate the extent of bubble coalescence, we report here the bubble size measured in the flow cell (d_{coal}). In addition, we compare the volumes (V_0 and V_{coal}) of single and coalesced bubbles to estimate the number N of coalescence events a bubble has undergone: $N = V_{coal}/V_0 - 1$. Because V_0 may show variations across different positions at the membrane surface (Figure A8.4), due to the pressure drop in the continuous phase and the presence of bubbles (which further influences the local flow rate and viscosity of the continuous phase), the absolute values of the estimates for N are shown in Figure A8.5, yet general conclusions can be drawn and will be discussed below.

For a given transmembrane pressure, d_{coal} decreases as Q_c increases (Figure 8.5A), and is always larger than its corresponding d_0. Yet, N increases as function of Q_c, which is possibly resulted from faster bubble formation (i.e., less protein adsorption) (Figure A8.5). At any fixed Q_c, d_{coal} as well as N increase with P_{trm} due to increasing bubble crowdedness (Figure A8.5), and thus the higher propensity to coalescence. Furthermore, as function of the protein concentration, the d_{coal} decreases strongly, much more than d_0 (Figure 8.5B). With the highest protein concentration tested (2.5% wt.), d_{coal} is very similar to d_0, and bubble coalescence is effectively suppressed with $N \approx 0$ (Figure A8.5 and Figure A8.6). When a sufficiently high protein concentration is used, more proteins are able to adsorb to the bubble surface before bubble-bubble interactions take place, thus preventing bubble coalescence

[128,211]. Lastly, the d_{coal} also decreases and converges to d_0 when a higher continuous phase viscosity is used (Figure 8.5C), which can be explained by the slower movement of bubbles [194] and the slower drainage process of the liquid thin film (between bubbles) [3], delaying (or diminishing) bubble coalescence. To summarise, the continuous phase properties (namely, protein concentration and viscosity) show vastly different influences on either bubble formation or bubble coalescence: 1) they can control the size at bubble formation (d_0) only to a very limited extent, with Q_c being the dominating factor; 2) they significantly suppress coalescence and thus the formation of larger bubbles (d_{coal}).

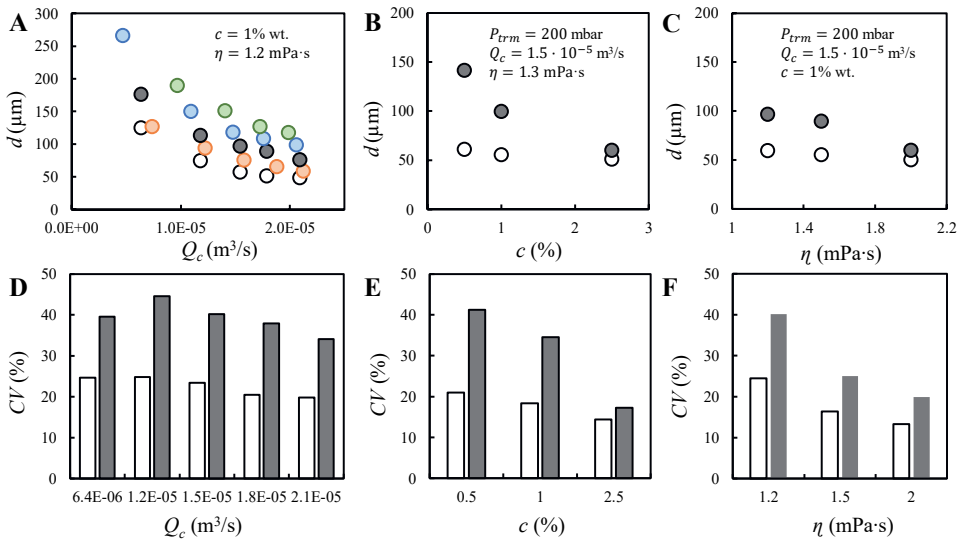

Figure 8.5. *The size and size distribution of coalesced, stabilised bubbles. The bubble size (d_{coal}, presented with filled circles) under the effects of A. shear flow, B. protein concentration, and C. continuous phase viscosity. In A, the effect of shear flow on d_{coal} is investigated for P_{trm} equal to 100 (●), 200 (●), 300 (●) and 400 (●) mbar. In A-C, the size of initial bubbles (d_0) measured at P_{trm} = 200 mbar is plotted for comparison and is presented with unfilled circle (○). Coefficient of variation (CV) corresponding to d_0 and d_{coal} measured at P_{trm} = 200 mbar shown in A-C is presented in D-F. The unfilled and filled bars represent the CV of initially formed and coalesced bubbles, respectively.*

The coefficient of variation (CV) is used to characterise the bubble size distribution (Figure 8.5D-F). The CV is always higher for the coalesced bubbles than for the initially formed bubbles. The CV only can be reduced to a limited extent when we increase the continuous phase flow rate, and we obtain a minimum CV of 20 and 34% for d_0 and d_{coal}, respectively. The CV does decrease strongly down to 14 and 17%, respectively, when measures are taken to enhance stabilisation of the freshly-created interfaces, namely by raising the protein concentration or increasing the continuous phase viscosity. In both cases, a smaller average

bubble size is accompanied by a smaller CV as the bubble size distribution is narrowed on the upper end. These results indicate that to tightly control the properties of bubbles in the end product, irrespective of the membrane properties, it is crucial to manipulate the operation conditions and the fluid properties to control bubble formation and, especially, to prevent bubble coalescence by sufficiently fast stabilisation of the freshly-created interface and by slowing down the approaching bubbles, and thus the film drainage process.

8.4.4 Bubble formation dynamics – Time scales

Within our experimental resolution, we observe that bubble formation can be separated into two stages: a bubble growing stage and an interval stage. The latter stage corresponds to a period of time between the moment that one bubble detaches and that the next bubble appears. The two corresponding time scales are the bubble growing time (red symbols in Figure 8.6A) and the interval time (grey symbols in Figure 8.6A). For a given transmembrane pressure, the bubble growing time significantly decreases from 1.64 to 0.13 ms as Q_c increases (Figure 8.6A). This is because with increasing Q_c the shear force increases and the bubble is sheared off faster. The corresponding interval time only slightly decreases and converges towards the bubble growing time for $Q_c > 1.5 \cdot 10^{-5}$ m^3/s. We highlight that both time scales can decrease to hundreds of microseconds. Muijlwijk and co-authors (2017) [111] reported that in a 1% wt. β-lactoglobulin system, which is the main component of whey protein, bubbles are stable against coalescence only if a 100 milliseconds (within the experimental resolution) is allowed for protein adsorption before bubble-bubble interactions occur. Additionally, in a 5% wt. whey protein system, we recently demonstrated that micrometre-sized bubbles can be sufficiently stabilised at a time scale larger than 1 millisecond; and at a time scale of ~0.01-1 milliseconds, bubble formation co-exists with finite bubble coalescence [148]. Therefore, the similar observations of bubble formation and controllable bubble coalescence in the current CFMF system can be explained by the intersecting time scales of bubble formation and protein adsorption [148].

The final bubble size reflects a balance between bubble formation and bubble coalescence. The probability of bubble coalescence is steeply decreasing when a monolayer surface coverage is achieved. When the protein concentration or the continuous phase viscosity is manipulated, and both Q_c and P_{trm} are fixed, bubbles are likely to grow at a fixed surface expansion rate within a fixed period of time, ranging mostly from 0.13 up to 0.23 ms (Figure

8.6B). To explain the bubble stabilisation in the 2.5% wt. whey protein system, we introduce a dimensionless *Péclet* number (Pé, defined as Pé = $\frac{Lv_c}{D}$, where D is the diffusion coefficient and L is a characteristic length), which describes the relative importance of convection and diffusion during the transport of proteins. We first calculate the diffusion coefficient of β-lactoglobulin (as the representative component of whey protein) using the Stoke-Einstein equation and then obtain Pé ≫ 1 (Appendix 8.6.7). Therefore, the above-mentioned surprisingly high bubble stability can be ascribed to high bulk concentration and bulk convection (enhanced mass transport of proteins). Additionally, given the bubble size encountered in this study, the highly curved surface can also accelerate the protein adsorption process and thus contribute to the high bubble stability [13].

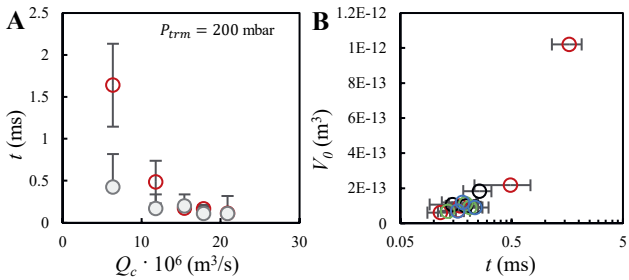

Figure 8.6. *Two time scales for bubble formation at the membrane surface. A. Bubble growing time (○) and the interval time (○) as function of the continuous phase flow rate. B. The average volume of initial bubbles as function of the bubble growing time for the effects of Q_c (○), P_{trm} (○), c (○) and η (○). The bubble volumes correspond to that presented in Figure 8.4A-C. The two time scales were derived based on 30 bubble formation events, focusing on bubble formation from three positions in the field of view of the membrane in the video recorded at a frame rate of 20,000 frames per second.*

8.5 Conclusions

In the cross-flow membrane foaming (CFMF) system, bubble formation is studied using whey protein as the emulsifier. At a (sub)millisecond time scale, bubbles continuously grow at the pores and snap off based on a force balance mechanism. The snap-off bubble size () is dominated by the continuous phase shear force; there is almost no dependency on the transmembrane pressure. The final bubble size (d_{coal}) is also determined by bubble coalescence, and it is greatly reduced at higher protein concentration and/or higher continuous phase viscosity. The d_{coal} can be almost equal to d_0, and the coefficient of variation (CV) can be well controlled below 20%. This means that in an ideal CFMF system where bubbles can be directly stabilised, a foam product composed of monodisperse bubbles with targeted size can be produced.

To further understand and optimise the CFMF system, several aspects such as membrane properties and dimensionless analysis of membrane foaming systems, etc. can be investigated in-depth in future work. For example, as was reported for membrane emulsification, specifically, small membrane pores allow for the formation of monodisperse and small droplets, which have higher storage stability; meanwhile, the small pore size may screen out the effects of other tested parameters during emulsification [200]. Hence, it is also interesting to explore the effect of the small pore size and unravel the potential competitive effects of small pore size and continuous phase shear on the formation mechanism and the probability of coalescence of bubbles. This could be studied for a range of membranes with well-defined pore size distribution, and to gain insights on the individual pore level, using microfluidic devices operating under similar shear conditions.

In general, our study provides insights into what is happening during the production of (food) foams at a (sub)millisecond time scale, and the insights generated can also be used to understand and steer large-scale processes better.

8.6 Appendix

8.6.1 Protein concentration loss over time

Due to the high continuous phase flow rate, a 4 L protein solution can run out within 3 minutes in the current experimental set-up. Hence, the re-use of the protein solutions is considered to be more practically efficient and sustainable. Before doing that, to figure out whether the potential decrease in protein concentration may influence the experimental results, the concentration of the protein solutions taken from the feed tank (for the continuous phase) after re-use of 0, 1, 3, 5, 7 and 9 times, was measured in triplicate using the Dumas method. The results indicate that after 9 times of re-use, the protein concentration only decreases by approximately 20%, which can be ignored (Figure A8.1). Hence, the protein solution was re-used up to 10 times.

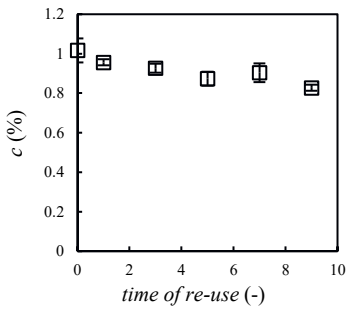

Figure A8.1. *Protein concentration as function of times of the re-use. The initial concentration is 1% wt.*

8.6.2 Comparison of coalescence at two distinct positions downstream the module

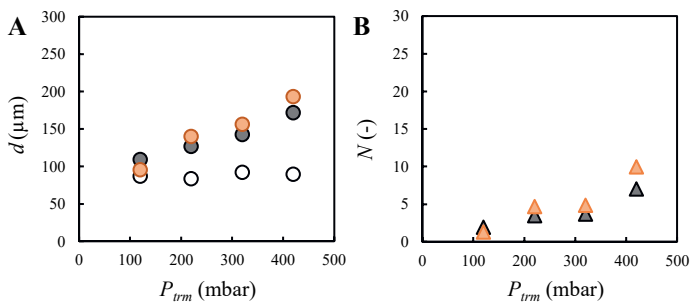

Figure A8.2. *Bubble coalescence observed at two distinct positions in the CFMF system. A. Bubble diameter as function of the transmembrane pressure, for Q_c = 1.1·10^{-5} m^3/s in a 1% wt. whey protein system. B. The number of coalescence events. In A, the bubble size d_0 measured in the membrane module is represented by unfilled circles (○). In A and B, the bubble size d_{coal} is indicated by filled circles and the number of coalescence events is indicated by filled triangles, obtained at 10 cm (●, ▲) and 100 cm (●, ▲) downstream the module. The CV for d_{coal} measured at the two distinct positions varies in the range of 26~35%.*

The flow cell is attached to the module downstream at a distance of either 10 or 100 cm. The d_{coal} values obtained for these two scenarios are compared to confirm whether coalescence mainly occurs in the membrane module during or shortly after bubble formation (10 cm), or the bubbles continue to coalesce along the flow path (100 cm). In Figure A8.2, similar d_{coal} values (and thus similar N values) show that coalescence mainly happens in the membrane module in the current system.

8.6.3 Fitting of the scaling ~Ca^{-n}

Based on the bubble formation mechanism in the CFMF system, we proposed a scaling with Ca^{-n}, where $Ca = \frac{v_c \eta}{\gamma}$ is the dimensionless capillary number, to describe the bubble size (d_0) for the effects of continuous phase velocity and viscosity. Assuming a constant surface tension, we fitted the proposed scaling (which is simplified as $(v_c \cdot \eta)^{-n}$) to the experimental data and obtained the power-law exponent $n = 0.8 \pm 0.1$. Both the experimental data and the fitted scaling are shown in Figure A8.3.

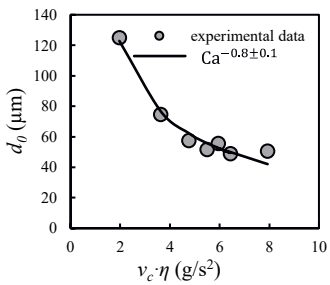

Figure A8.3. *The bubble size versus the shear force ($v_c \cdot \eta$). These data are shown in the manuscript in Figure 8.4A (for P_{trm} = 200 mbar) and C. The fitting was performed by non-linear least square regression.*

8.6.4 General bubble behaviour in the CFMF system – Pressure analysis

Ideally, bubbles growing at the membrane surface should be subjected to the same experimental conditions (once a certain series of experimental conditions are applied), and should show no dependency on the position of the membrane (e.g., positioning upstream or downstream inside the module).

However, the continuous phase pressure may drop along the length of the membrane in the direction of flow. Consequently, for certain applied pressure conditions (P_d, P_c), an increasing transmembrane pressure can be expected to act across the pores along the length of the membrane: P_{trm} at the beginning of the module and P_{trm}' at the outlet of the module (see the sketch in Figure A8.4-1, $P_{trm} < P_{trm}'$). The variation of d_0 with P_{trm} is relatively

minor for P_{trm} = 100-300 mbar (Figure 8.3B); yet, if the P_{trm} increases towards 400 mbar (or even higher) along the membrane, slightly larger bubbles could form directly from the pores.

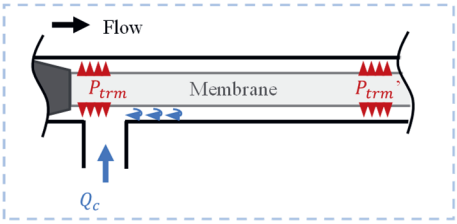

Figure A8.4-1. *Schematic overview of potential variation in transmembrane pressure along the length of the membrane inside the module. The schematic is not drawn to scale.*

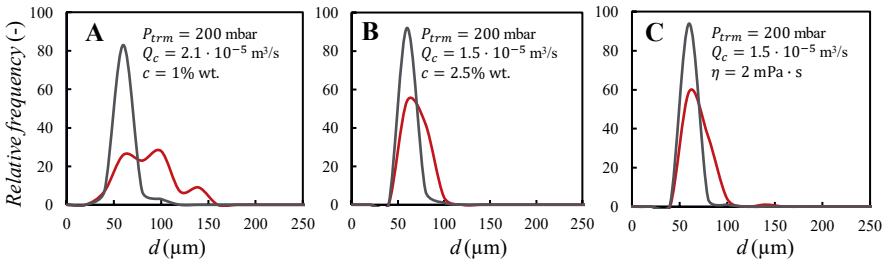

Figure A8.4-2. *Histogram plots for bubbles with d_0 (grey line) and d_{coal} (red line). The corresponding experimental conditions for A-C are marked in the figures.*

The observations in the membrane module can be made with only two narrow strips along the membrane in the focal plane (Figure A8.4-1). For the analysis we chose bubbles formed upstream of the membrane across from the continuous phase inlet, which experiences laminar flow conditions. In contrast, we have observed that near the continuous phase inlet bubbles are formed in a less-predictable fashion (in terms of bubble size, formation frequency and coalescence), due to the presence of circulating flows (indicated by blue eddies, Figure A8.4-1). Specifically, relatively larger bubbles have been observed to form directly at the membrane surface. The presence of these bubbles in the module means that the reported d_0 (from exclusively the strip located across from the continuous phase inlet) may be a slight underestimation of the bubble diameter averaged over the full membrane, and thus the number of coalescence events will be overestimated. In addition, bubbles that flow near the continuous phase inlet are stretched (and deformed) within the circulating flow and are occasionally observed to break up into (two) smaller bubbles.

Even if we measure d_0 *locally* directly upstream of the membrane across the continuous phase inlet, the measurement seems to be still representative of the full membrane. The size

distribution of d_0 (grey line in Figure A8.4-2) shows good similarity with that of d_{coal} that includes bubbles formed *anywhere* along the membrane (red line); that is, for conditions (namely, at high protein concentration or high continuous phase viscosity, Figure A8.4-2B, C) under which coalescence would be largely limited. The larger difference observed between d_0 and d_{coal} as shown in Figure A8.4-2A can then be largely ascribed to the high extent of bubble coalescence.

8.6.5 The number of coalescence events, N

To illustrate the extent of coalescence, the number ($N = \frac{V_{coal}}{V_0}$ - 1) of coalescence events is estimated. The V_0 and V_{coal} are the volumes of bubbles with d_0 and d_{coal}, which are shown in Figures 8.4 and 8.5, respectively. Generally, bubbles coalesce to a higher extent as Q_c and P_{trm} increase, while the coalescence can be suppressed with increasing protein concentration and continuous phase viscosity.

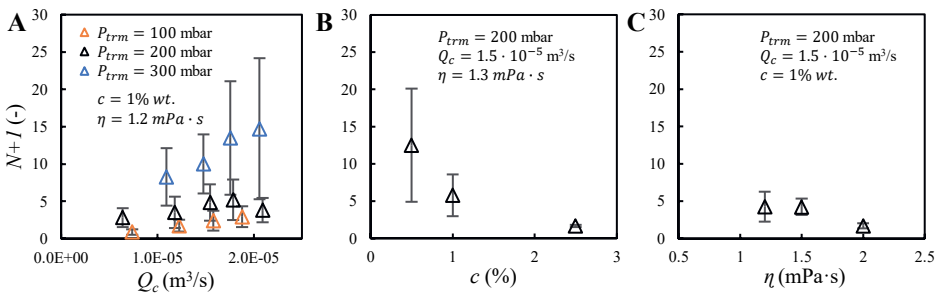

Figure A8.5. *The number of coalesced bubbles (N+1). In the order of A-C, the effects of the continuous phase flow rate (for a series of transmembrane pressures), the protein concentration, and the continuous phase viscosity are presented.*

8.6.6 Bubble coalescence can be suppressed with 2.5% wt. whey protein

To demonstrate the stabilising effect of 2.5% wt. whey protein on the d_0, the d_{coal} is evaluated as function of P_{trm} and compared with the 1% wt. whey protein system. For the 2.5% wt. whey protein system, similar d_0 and d_{coal} can be obtained, showing no dependency on P_{trm} and thus that coalescence is effectively suppressed.

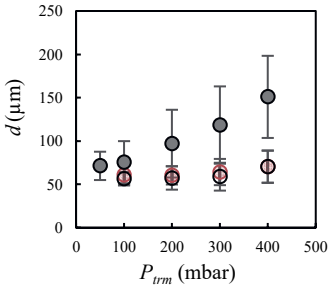

Figure A8.6. *Bubble diameters as function of transmembrane pressure. The continuous phase flow rate is fixed at Q_c = 1.5·10^{-5} m^3/s. For comparison, the initial bubbles with d_0 are only shown for 1% wt. whey protein (○), and the d_{coal} is evaluated for both 1% wt. (●) and 2.5% wt. (●) whey protein solutions.*

8.6.7 Calculation of D and Pé

The diffusion coefficient is calculated using the Stokes-Einstein equation $D = \frac{kT}{6\pi\eta r}$ with k = 1.38·10^{-23} J/K, T = 293 K, η = 1.3·10^{-3} kg/(m·s) and $r = 0.066M^{1/3} \cdot 10^{-9}$ [212]. The last item is the minimum molecule radius (in meter, m), which is expressed as function of the molecular weight (M, in Daltons) with M for β-lactoglobulin being 18000 Da.

The *Péclet* number is calculated as Pé = $\frac{v_c L}{D}$. The characteristic length scale (L) in the CFMF system is set as 5.5·10^{-4} m which represents the gap distance between the membrane surface and the inner wall of the membrane module. The velocity (v_c) of the continuous phase flowing through the gap is estimated as 4 m/s. The estimate for the *Péclet* number based on the diffusion coefficient of β-lactoglobulin is 2·10^7 ≫ 1, indicating the dominance of bulk convection (over bulk diffusion) and thus the enhanced mass transport of proteins, leading to improved coalescence stability of the bubbles.

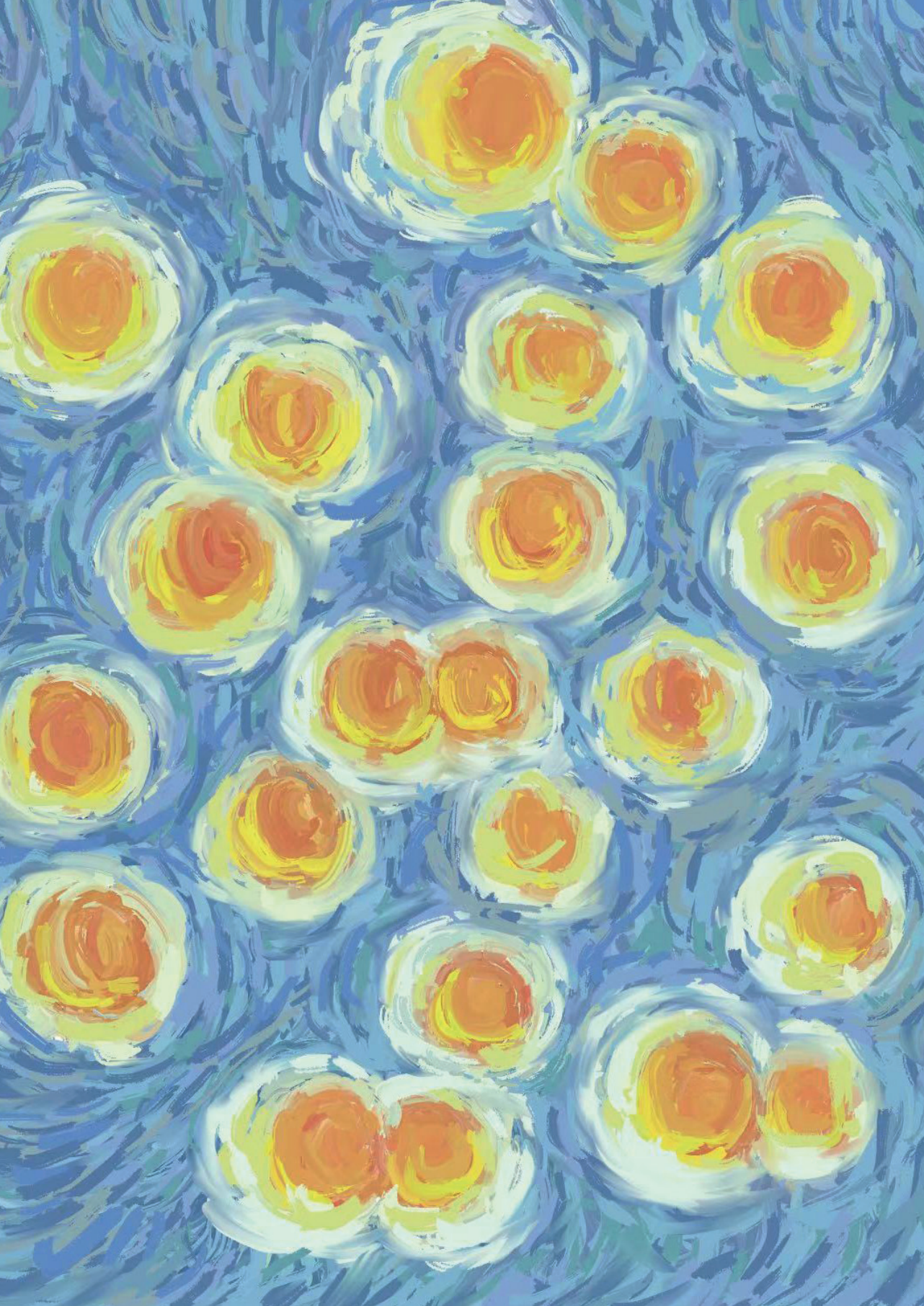

CHAPTER || 9

General discussion

9.1 Introduction

This thesis focuses on two aspects of bubbles: 1) making monodisperse bubbles, and identifying the underlying mechanism, and 2) using spontaneous microfluidic devices as analytical tools to monitor various sub-mechanisms that ultimately need to be brought together to get stable foam (and to some extent also emulsion) food products.

Chapter 2 provides an overview of microfluidic studies performed for bubbles and droplets. From the available designs, a spontaneous partitioned-EDGE device is selected to be used in this thesis because it is relatively easy to control over bubble/droplet formation. **Chapter 3** is dedicated to the characterisation of the general behaviour of bubble formation and stabilisation in the selected microfluidic partitioned-EDGE device, ranging from monodisperse bubbles formed and stabilised directly at low pressures, to less monodisperse, larger bubbles formed at higher pressures through coalescence. **Chapter 4** explores the process conditions (e.g., applied pressures and liquid phase properties) that govern the production of monodisperse bubbles; also in this chapter, a unifying discussion of the 'dripping-jetting' transition in spontaneous microfluidic devices is given. In **Chapter 5**, the partitioned-EDGE device is used as a microfluidic tensiometer to monitor dynamic surface and interfacial tension for bubble and droplet surfaces, respectively, at (sub)millisecond time scales. This tensiometer allows straightforward interpretation using the bubble and droplet formation frequency. In **Chapter 6**, the partitioned-EDGE device is used to study the *instant* coalescence of bubbles formed within short time scales, e.g., down to tens of microseconds. In **Chapter 7**, dynamic adsorption is studied via monitoring the bubble formation process and the resulting bubble properties, and it is studied for the effects of the type (i.e., SDS and proteins) and concentration of emulsifiers. In **Chapter 8**, bubble formation and stabilisation are investigated in an application-relevant system – a cross-flow membrane foaming system. In the current chapter, we first discuss the main findings and then share insights related to application in practice.

9.2 Main findings and conclusions

The literature review in **Chapter 2** follows that although the majority of studies are dedicated to droplets, the few studies on bubbles indicate that microfluidics can be used to make bubbles, and create in-depth understanding of the bubble formation process. Amongst the available designs, the so-called EDGE devices are less sensitive to perturbations in pressures

and flows; moreover, with the so-called partitioned-EDGE device, the pressure stability and thus the productivity of droplets was found to further increase. The partitioned-EDGE device was successively used to make monodisperse droplets, even within two distinct regimes [42], and this rich behaviour made it an ideal starting point for the work shown in this thesis that mostly revolves around bubbles, and in some chapters is extended to droplets. The overall behaviour of bubble formation in the partitioned-EDGE device is described in Chapter 3, and specific parts thereof are described in Chapters 4-6.

In **Chapter 3**, whey protein isolate (WPI) was chosen as the emulsifier, and we used the partitioned-EDGE device to study bubble formation as function of applied pressure. It was found that bubble formation shows two pressure regimes, delineated by the Laplace pressure of the pure air-water interface. At applied pressures below this transition pressure, dynamic adsorption reduces the Laplace pressure of the meniscus to the pre-set applied pressure (i.e., by lowering the surface tension, indicated by the downward arrows in Figure 9.1); at higher applied pressures, bubble formation takes place immediately upon applying pressure. This finding together with other findings obtained from Chapters 3 and 4, provide a solid basis for the experimental designs in Chapters 5 and 6.

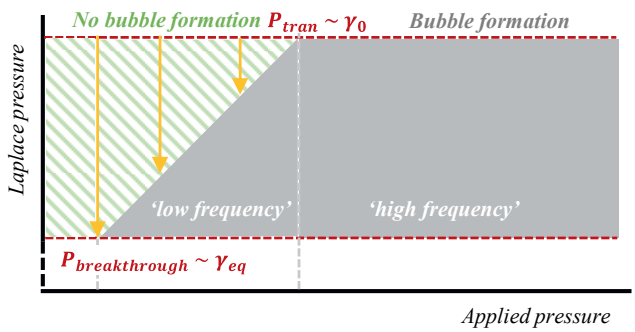

Figure 9.1. *Schematic illustration of the pattern for applied pressures in the partitioned-EDGE device. Yellow arrows indicate a lowering of the Laplace pressure by adsorption of emulsifier.*

To continue to summarise **Chapter 3**, emulsifier adsorption plays distinct roles in the two pressure regimes as shown in Figure 9.1. In the low-pressure regime, which is also called the 'dynamic regime', dynamic adsorption plays a role in the initiation of bubble formation; monodisperse bubbles are formed and stabilised (i.e., no coalescence occurred), with bubble formation frequency increasing with applied pressure. In the high-pressure regime, bubbles are immediately formed because the applied pressure exceeds the transition pressure. This regime is also called the 'static regime' since dynamic adsorption is only responsible for

reducing bubble coalescence, with the extent of bubble coalescence increasing at higher bubble formation frequency.

When zooming in on one bubble formation cycle, in **Chapter 3** we distinguished two consecutive sub-processes: one for pore filling and one for necking, both with their typical time scales that together form the bubble formation time, and that are applied in later chapters. In the low-pressure regime, the bubble formation time is dominated by protein adsorption occurring during the pore filling stage, varying in the range of 0.001~1 s; in the high-pressure regime, the bubble formation time varies in the range of 0.01~1 ms.

In **Chapter 4**, we studied bubble size and bubble formation frequency (which is one over the bubble formation time) as function of applied pressure for various liquid phase properties (e.g., protein concentration and continuous phase viscosity), by characterising the two sub-processes (pore filling and necking). It is clear that in the low-pressure regime, the bubble formation frequency increases with increasing protein concentration, due to faster protein adsorption at increasing concentrations; in the high-pressure regime, bubble coalescence can be largely suppressed using a combination of *moderate* protein concentration and continuous phase viscosity. At high protein concentration (e.g., 10% wt. WPI) and continuous phase viscosity (e.g., 6 mPa·s), increased bubble size and polydispersity was found. Also in this chapter, we demonstrated that the 'dripping-jetting' transition, which is typically marked by increased size and polydispersity of bubbles/droplets in spontaneous devices, can be explained by the relative magnitude of the aforementioned two time scales. Furthermore, we could pinpoint the rich bubble formation behaviour (and stabilisation), and ascribe it to one of the crucial features of the partitioned-EDGE device, namely the extreme shallowness of the main plateau and pores.

In **Chapter 5**, we used the partitioned-EDGE device as a microfluidic tensiometry (i.e., the 'EDGE tensiometer') based on bubble (and droplet) formation in the low-pressure regime. From Chapters 3 and 4, it is clear that the low-pressure regime is bounded by two Laplace pressures: the Laplace pressure of the saturated air-water interface sets the minimum applied pressure, and that of the clean air-water interface sets the maximum applied pressure (i.e., the transition pressure; as sketched in Figure 9.1). The EDGE tensiometer intrinsically allows to assess nearly the full range of dynamic interfacial tension at time scales that are determined by dynamic adsorption. The dynamic surface and interfacial tension were measured as function of the formation time of bubbles and droplets. For 0.05-1% wt. SDS, the dynamic

surface and interfacial tension can be measured at time scales down to ~0.1 ms and ~1 ms for bubble and droplet surfaces, respectively.

In **Chapter 6**, the rich behaviour of bubble formation and coalescence reported for the high-pressure regime in Chapter 3, was revisited, and we used the partitioned-EDGE device to study the *instant* coalescence of bubbles formed at high frequency. We used different device geometries and liquid phase properties, and evaluated the extent of bubble coalescence as function of the bubble formation time, which coincides with the time available for protein adsorption. We found that bubble coalescence increases with decreasing bubble formation time, and can be suppressed by using higher protein concentration and continuous phase viscosity within certain boundaries as mentioned in Chapter 4. The relationship between the extent of bubble coalescence and the bubble formation time was captured in a semi-empirical model. Through fitting the model to the series of experimental results obtained for a range of WPI concentrations, a crucial fitting parameter t_1 could be identified, which is the minimum time required for a certain protein concentration to stabilise a foam. The t_1 decreases from 0.5 to 0.1 ms as the protein concentration increases from 2.5 to 7.5% wt. Besides, we found that by decreasing the pore and partition width in the partitioned-EDGE device, we can promote bubble crowdedness in the collection channel and interactions between bubbles growing at adjacent pores, both of which lead to a higher extent of bubble coalescence.

Based on findings from Chapters 3-6, in **Chapter 7**, we systematically studied emulsifier adsorption with respect to bubble formation and coalescence stability. We focused on SDS and compared the results with those obtained for various proteins, including WPI (Chapters 4 and 6), BSA and β-lac. The general behaviour of bubble formation and coalescence is not influenced by the type of emulsifiers. Yet, compared with a high concentration of WPI, a high concentration of SDS initiates the 'dripping-jetting' transition even earlier. The bubble dynamics in the presence of SDS show richer behaviours, which is likely due to the faster adsorption of SDS molecules. At very short time scales down to 10 μs, SDS followed by BSA and then WPI are more efficient than β-lac in suppressing bubble coalescence. The aforementioned observations are linked to the effect of dynamic surface tension.

In **Chapter 8**, we left the highly-defined world of microfluidic systems, and instead, studied bubble formation and coalescence in a cross-flow membrane foaming system, for varied protein concentrations (0.5-2.5% wt. WPI), continuous phase viscosities, as well as dispersed and continuous phase flow rates. In this shear-based system, bubbles are formed based on a

force balance between the viscous drag force and the surface tension force. For bubbles formed at a time scale of about 0.1 ms, bubble coalescence can be suppressed by 2.5% wt. WPI in the CFMF system, while in the partitioned-EDGE system (Chapter 6) this was 10% wt. WPI at the same formation time. The difference most probably stems from differences in bubble crowdedness as a result of the differences in the geometry of bubble formation units, and in the flow conditions that influence the emulsifier mass transfer.

9.3 Putting our findings in a broader perspective

9.3.1. Emulsifier adsorption

Emulsifier adsorption plays a crucial role in the formation as well as stabilisation of bubbles (and droplets), which is a well-established fact, but how these effects interrelate is not that well known. In this thesis, we used partitioned-EDGE devices to monitor very precisely their relative importance, and did so within very short timescales, which generated many new insights. In **Chapters 4-5** and **7**, relying on the characteristics of bubble formation in the low-pressure regime, we quantified how fast dynamic surface tension is lowered at increasing emulsifier concentration. The emulsifier properties (i.e., the type and concentration) determine the magnitude of time scales at which the dynamic surface tension decreases with time. As an illustration, for our extreme cases of high concentrations of WPI (i.e., 10% wt.) and SDS (i.e., 1% wt.), the dynamic surface tension varies between two equilibrium values, namely those of the *clean* and the nearly *saturated* interfaces, at time scales of approximately 1.5-1000 ms and 0.15-15 ms, respectively. Besides, emulsifier adsorption is also significantly influenced by the flow conditions (i.e., of the continuous phase). In **Chapter 6**, where we focused on bubble formation and coalescence in the high-pressure regime, we found that to stabilise a foam (i.e., to prevent bubbles from coalescing), the minimum time required for whey protein adsorption decreases with increasing protein concentration; from our semi-empirical model, the minimum time decreases from 0.5 to 0.1 ms as the protein concentration increases from 2.5 to 7.5% wt. Moreover, in **Chapter 7**, we found that bubble coalescence can be suppressed (at time scales down to 0.02 ms) with SDS concentrations below 0.2% wt. In comparison to the meniscus that is constricted inside the pore in the low-pressure regime, in the high-pressure regime emulsifier adsorption occurs at the bubble surfaces that are directly exposed to the flowing continuous phase that enhances mass transfer.

Up till now, in general an equilibrium interfacial tension would be used in microfluidic studies [33,38,47,92], and the effects of interfacial tension are to some extent related to the composition of the phases (e.g., through varying the dispersed phase) [48]. Some even mention the crucial role of dynamic interfacial surface [41,45,77,126,183], and take it into consideration [12], although often equilibrium values are used. In this sense, this thesis provides crucial insights on emulsifier adsorption at short time scales, from various aspects of dynamic interfacial tension decay and interface stabilisation, and adds to the current knowledge base a piece that was mostly missing.

9.3.2. Bubble formation in partitioned-EDGE device and its use as analysis tools

In this thesis, the partitioned-EDGE device was used to make bubbles (**Chapters 3** and **4**). This allowed us to distinguish two pressure regimes that are termed the low- and high-pressure regimes. The two pressure regimes are delineated by the Laplace pressure corresponding to that of the clean air-water surface. The typical bubble sizes for the two pressure regimes are approximately 24 and 16 µm, respectively, unlike the increase (from 9 to 28 µm) observed during droplet formation. Besides, in the high-pressure regime, bubble formation co-exists with bubble coalescence, and the coalesced bubble size increases with the applied pressure (i.e., due to the shorter bubble formation time that sets a shorter time available for emulsifier adsorption before bubble-bubble interactions take place). Compared with droplet formation, richer behaviours are found in the bubble formation system, although it is essentially ***'opportunistic'***. The co-existence of bubble formation and coalescence can be ascribed to the physiochemical characteristics of the air phase, namely its extremely low viscosity, which results in the much faster surface expansion for bubbles than droplets, and the properties of the emulsifier. When using the slow-adsorbing whey protein, coalescence was observed (**Chapters 3** and **6**), while in **Chapter 7**, the fast-adsorbing SDS prevents bubble coalescence that is unless the SDS concentration is below 0.2% wt.

Relying on the characteristics of bubble formation in the low- and high-pressure regimes, the partitioned-EDGE device is further developed into a microfluidic tensiometer (**Chapter 5**) and a coalescence detector (**Chapter 6**), respectively. The microfluidic tensiometer can be used for the measurement of dynamic surface and interfacial tension for both bubble and droplet surfaces, respectively. To apply the partitioned-EGDE device as a coalescence detector in the *droplet* system, we suggest using a relatively *low* emulsifier concentration, which allows the intersection of time scales of emulsifier adsorption and (slow) droplet

formation. To be complete, the features of the partitioned-EDGE device provide routes to study emulsifier adsorption at very short time scales (see section 9.3.4). Besides, it is good to point out that although bubbles and droplets can be studied in the same devices, findings are not always translatable, unless the underlying sub-processes are well understood.

9.3.3. Unifying 'dripping-jetting' transition in microfluidics

The 'dripping-jetting' transition is observed in both shear-based and spontaneous devices but is defined differently. In shear-based devices, the droplet formation mechanisms transit from squeezing all the way to parallel flow (no droplet formation) upon increasing the capillary number of the *continuous phase* [17]. In between squeezing and parallel flow, dripping and jetting regimes have been distinguished. As droplet formation transits from dripping to jetting regime at a critical capillary number, the neck that connects the expanding droplet to the side channel (i.e., the supplying channel of the dispersed phase) becomes longer and moves further into the main channel. Generally, the droplet size decreases as function of the capillary number and increases with the increasing flow rate ratio in the dripping regime, while it decreases with both the capillary number and the increasing flow rate ratio in the jetting regime. The droplet formation frequency increases with both the capillary number and the flow rate ratio in these two regimes.

In spontaneous devices, the dripping-jetting transition is typically considered and gives rise to an increase in droplet size and polydispersity [39,48,139,141,183,213], occurring at a critical flow rate of the *dispersed phase* or its capillary number. Upon the transition, the droplet formation frequency decreases due to the formation of large droplets [39]. In the current thesis, the dripping-jetting transition occurs in the high-pressure regime (Figure 9.2). As mentioned in **Chapter 4**, the dripping-jetting transition mostly takes place at the pressure where the two time scales for pore filling and necking intersect (i.e., at the cross-over pressure, P_{cross}). Although not mentioned as such by the authors, similar observations have been obtained e.g., in a terrace-based microchannel system; in the presence of 1% wt. SDS, a sudden increase in droplet size is observed at the dispersed phase flow velocity that allows the time for inflation on the terrace to intersect with that for droplet detachment in the well [183].

Factors that influence either the pore filling time or the bubble necking time, and thus their intersection, influence the dripping-jetting transition. It is good to mention that the dripping-jetting transition is strongly influenced by the emulsifier properties. In the device with narrow

pores, or with wide pores while at low emulsifier concentration, the transition occurs an applied pressure above the P_{cross}. At relatively high emulsifier concentration, the transition occurs at P_{cross}, which advances at increasing concentration as mentioned in the previous section. Lastly, the Marangoni stress that drives the emulsifier from the expanding bubble surface towards the location of the thinning neck, which is very likely playing a role in the presence of high concentration of emulsifiers, is expected to be partially responsible for the extension of the neck thinning process [28,180] and subsequently the dripping-jetting transition (**Chapter 7**). In this sense, we should consider the flow field, which plays an important role in emulsifier adsorption towards the expanding bubble surface. We expect that our unifying discussion and characterisation of the 'dripping-jetting' transition in spontaneous devices, will help to compare results obtained for different geometries.

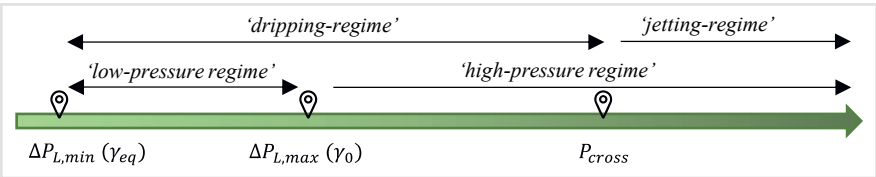

Figure 9.2. *The crucial pressures encountered in spontaneous devices, in the presence of WPI.*

9.3.4. Crucial features of the partitioned-EDGE device

The distribution of the hydrodynamic flow resistance

In the partitioned-EDGE device, the hydrodynamic flow resistance increases along the flow path, from the shallow plateau to the shallow and narrow pores (Figure 9.3, left); yet, in other spontaneous devices like a terrace-based microchannel, it is the other way around (Figure 9.3, right). This feature is of great relevance, and its importance manifests in a few aspects. First, it is responsible for the complete filling of the shallow plateau before bubble formation at any of the pores, which resists fluctuations in pressures as well as flows, and prevents any preferential flow through certain pores, and thus warrants stable operation of the device within a wide range of applied pressures [42]. Indeed, we observed that all the pores can be activated throughout the full range of applied pressures, although the pores form bubbles in an alternating way in the low-pressure regime. Second, the high hydrodynamic flow resistance of the pore ($\mathcal{R}_{pore}$) also guarantees its dominance over the air flow rate into the growing bubble (Q'_{bub}), which is then less affected by fluctuations in pressures and flows. In **Chapter 3**, we defined $V_0 = Q'_{bub} \cdot t_n$, with t_n being the bubble necking time, during which

the bubble grows in volume and finally snaps off. Q'_{bub} is determined by the Laplace pressure of the constricted meniscus and the hydrodynamic flow resistance of the pore ($\mathcal{R}_{pore}$). In the situations where emulsifier adsorption towards the constricted meniscus is neglected, the Laplace pressure corresponds to that of the pure meniscus and is thus constant in the high-pressure regime (as explained in **Chapter 6**). In **Chapters 3** and **4**, this leads to the formation of monodisperse bubbles in the high-pressure regime, and the bubble size is independent of the applied pressures and flow field (i.e., continuous phase flow velocity). In **Chapter 6**, this provides a solid platform for our investigation of the coalescence behaviour of monodisperse bubbles at short time scales. It is interesting to mention that (as will be discussed in section 9.4.1), we do observe preferential flow in the low-pressure regime when pores with non-uniform hydrodynamic flow resistance are assembled on the same shallow plateau.

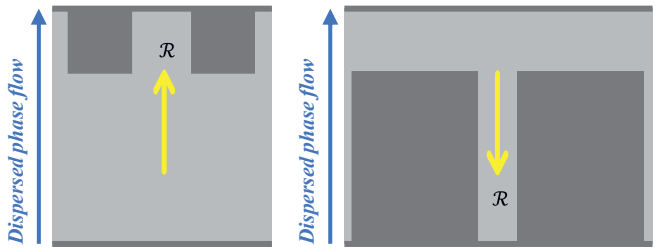

Figure 9.3. *Schematic illustration of the distribution of hydrodynamic flow resistance. Left: in the partitioned-EDGE device; right: in a terrace-based microchannel. The yellow arrows indicate the increase in resistance. Not drawn to scale.*

Apart from the overall hydrodynamic flow resistance, it is also crucial to realise that the geometrical properties of the device can be further designed specifically, to tune bubble formation and thus bubble properties.

- *The pore height (h)*. The pore height is the most crucial geometry property of spontaneous devices, that sets the droplet and bubble sizes [86,92,139,141]. Besides, the pore height (together with the pore width) determines the relative magnitude of the Laplace pressure (as will be discussed below).
- *The pore width (w), aspect ratio (w/h), and partition width*. The Laplace pressure also scales with the pore width – the pore widths in the same range as the pore height. Besides, as discussed in **Chapter 6**, the 'dripping-jetting' transition occurs at higher applied pressures for narrow pores (within boundaries). Yet, it is important to keep in mind that the aspect ratio should be larger than a certain value, for instance $w/h >$

2.5 [90,126], to enable droplet formation in spontaneous devices. Lastly, in **Chapter 6**, we found that through the pore width (as well as the partition width) (i.e., the distance between the centre of two pores) we can tune interactions between bubbles growing at adjacent pores, and thus bubble coalescence.

- *The plateau length (l/L)*. We can vary the plateau length to adjust the hydrodynamic flow resistance of the pore, and thus the 'dripping-jetting' transition by adjusting the pore filling time. While a longer plateau length leads to delayed dripping-jetting transition and thus extends the operation window for making monodisperse bubbles in a controllable manner, it is important to keep in mind that the bubble formation frequency is reduced.

The extremely shallow bubble formation units

The *extreme shallowness* of the partitioned-EDGE device leads to a sufficiently large gap (ΔP) between the two critical Laplace pressures, namely those of the pure and the (nearly) saturated interfaces, and thus the division of low- and high-pressure regimes. As shown in Figure 9.4 (square), these two Laplace pressures become closer as the pore height increases, and are relatively independent of the aspect ratio (*w/h*). In principle, the low-pressure regime diminishes as the pore height increases. Besides, the fact that the *slow-adsorbing whey protein* is used to stabilise *bubbles* guarantees the existence of a high-pressure regime; whey protein adsorption and the fast bubble formation (as a result of the extremely low viscosity of the air phase) compete at time scales down to tens of microseconds, leading to the finite extent of bubble coalescence.

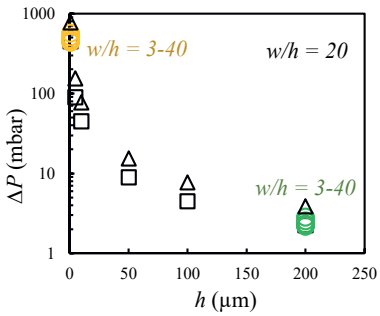

Figure 9.4. *The effective range of applied pressures for varied pore height (□, Δ) and aspect ratio (○○). ΔP represents the difference between the Laplace pressure of the clean interface and that of the saturated interface. Two examples are shown for whey protein-stabilised air-water interface (□) and SDS-stabilised hexadecane-water interface (Δ).*

As mentioned previously, the typical co-existence of bubble formation and coalescence does not occur for fast-adsorbing emulsifiers such as SDS when used at a high enough concentration (**Chapter 7**). Therefore, when sufficiently high pore height and/or SDS concentration (> 0.2% wt. in this thesis) are used, bubble and droplet formation are only regulated by the 'dripping-jetting' transition, as is usually observed in the literature [47,48,126,127]. Specifically in terms of droplets, even with relatively low concentrations of SDS, SDS adsorption mostly exceeds droplet formation, namely, coalescence is suppressed. But still, a wide range of applied pressures bounded by the two critical Laplace pressures provides a platform for studying the dynamics of emulsifier adsorption at bubble surfaces (e.g., as demonstrated for pore height 1 μm, **Chapter 5**).

Our study expands the operation window of spontaneous devices, which can be used not only for up-scaling (and thus for practical application) but also for the investigation of highly dynamic processes such as surface tension (**Chapter 5**) and coalescence (**Chapter 6**). In principle, any spontaneous or shear-based micro-structured devices (e.g., cross-flow membrane emulsification system [132]), can be developed into a tool like the microfluidic tensiometer (explained in **Chapter 5**), although an increasingly higher resolution of the pressure system is required as the pore height increases. In that sense, the shallow height of the current device makes it easier to use.

Pore and main plateau (width)

The standard pore width of the partitioned-EDGE device used in this thesis is 40 μm, but a wider operation window (or dripping regime) can be obtained for narrower pores, for instance 5 or 10 μm. Besides, for a pore width of 40 μm, two necks have been observed from the same pore at applied pressures that exceed the cross-over pressure (**Chapter 3**). Moreover, when the pore width is 80 μm, each pore behaves like a regular EDGE device, marked by the formation of more than two necks from the same pore (Figure 9.5). In a regular EDGE device, the distance between two droplet detachment positions scales with the plateau height; as the plateau height decreases from 2.6 to 1.2 μm, the distance between droplet formation points decreases from 65~70 μm (and 40~50 μm for bubble formation) to about 29 μm, which can be even less for bubble formation [92], which is in line with our observation of more necks forming from wider pores.

To scale up the partitioned-EDGE device for large-scale production of monodisperse bubbles and droplets, we suggest optimising the device design first by using a regular EDGE device with the desired plateau (and pore) height to determine the bubble (or droplet) size as function of the plateau height [42] and the efficient distance between two detachment positions. Based on this, the pores in the partitioned-EDGE device can be designed rationally and up-scaled.

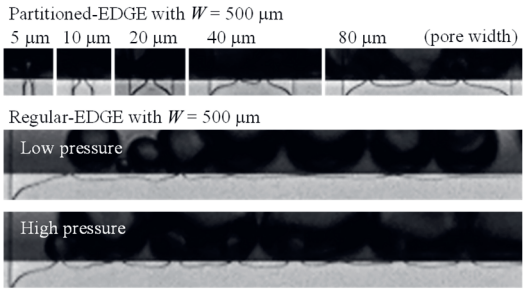

Figure 9.5. *Snapshots of bubble formation in the partitioned-EDGE with various pore widths, and the regular EDGE. W represents the total width of the main plateau. For the regular-EDGE, only part of the main plateau (along the width) is shown.*

9.3.5. Microfluidic tensiometry

As a proof of concept, we used the EDGE tensiometer (introduced in **Chapter 5**) to measure the dynamic surface tension behaviour for surfactants (SDS, Tween 20) and various proteins (Figure 9.6**)**. As expected, the dynamic surface tension decreases with the bubble formation time and the emulsifier concentration. Varying the type of the emulsifiers leads to large shifts in the plots of dynamic surface tension versus the bubble formation time. With 1% wt. SDS, the dynamic surface tension decreases faster than with 1% wt. Tween 20, which is likely caused by the faster disaggregation of SDS micelles [54]. Among proteins, sodium caseinate (SC) and then WPI are more efficient than β-lac in lowering the dynamic surface tension, although it is good to point out that for SC (and BSA), wetting issues can be expected, leading to bubble formation taking place at more than two locations from the same pore (the bottom snapshot in Figure 9.6) and an underestimated bubble formation time. As explained in **Chapter 5**, a small variation in contact angle around 15º by 5º or 10º only leads to small variation in dynamic surface tension (of 1.2-2.8 mN/m); however, for a contact angle of around 50º, such variation in contact angle leads to a variation of 9.6-19.6 mN/m, which makes the measurement not reliable anymore.

To use the microfluidic tensiometer effectively, a few recommendations are**:** 1) to carry out the measurements with narrow pores, with which we expect the inflow of the continuous

phase and thus the wetting issues to dampen to some extent; 2) to modify the channel surface to prevent wettability changes [150]. We expect the EDGE tensiometer to find a wide range of applications, e.g., as high-throughput screening tools for emulsifiers that can be evaluated at time scales as emulsifier adsorption would occur during large-scale processing, and under similar conditions. Thus the kinetics of emulsifier adsorption can be understood in great detail, as that has been touched upon through analysis of dynamic interfacial tension [23,55,155] and droplet coalescence [24]. Next to that, the relationship between the dynamic surface tension and the bubble formation time can be used to estimate the diffusion coefficient of SDS towards a nearly clean interface (i.e., based on the short-term estimation) [157,214]. To bring these measurements closer to practice, the devices can be extended to include mixing (e.g., to induce transverse flow, which stretches and folds the fluid over the cross-section of the channel) [215] and elevated temperature [4,216], both of which can enhance mass transfer, as well as longer residence channel, which can be used to produce insights about the long-term behaviours (in the downstream channel) [217].

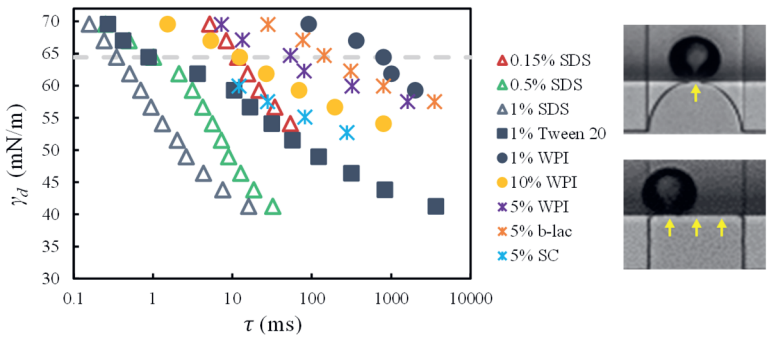

***Figure 9.6**. The dynamic surface tension versus the bubble formation time. These data sets were used in the form of bubble formation time (i.e., pore filling time) as function of applied pressure in **Chapters 4** and **7**. The snapshots were recorded for WPI (up) and BSA (bottom) in the low-pressure regime, with arrows pointing to the location where bubble formation was observed.*

9.4 Practical aspects related to large-scale production

9.4.1 Microfluidic model membranes to check insights obtained earlier

The currently used highly-defined partitioned-EDGE device is the ultimate model system to generate insights into bubble formation and stabilisation in membrane systems. In membrane systems, the pore size would be less ideal, and that is why we now used a partitioned-EDGE device with *pore size distributions*. In this microfluidic 'membrane' device, two pore widths (5 and 40 µm) are randomly placed and separated by three different partition widths (5, 40 and 80 µm). The pore height is fixed, and the transition pressure is approximately 1750 and

1500 mbar for pore widths of 5 and 40 µm, respectively. For 5% wt. WPI, the breakthrough pressures are 1350 and 1200 mbar, respectively. In this trial experiment, the pore frequency is measured as function of the applied pressure, for which three sub-ranges can be distinguished. I. 1300-1400 mbar with both pores in the low-pressure regime; II. 1500-1700 mbar with only the wider pores in the high-pressure regime; III. 1700-1900 mbar with both pores in the high-pressure regime. For sub-range I, bubble formation is only observed from the wider pores, and the bubble formation frequency increases with the applied pressure, which is similar to that observed for 'standard' partitioned-EDGE (Figure 9.7A). For sub-range II (Figure 9.7B), again, bubbles are only formed from the wider pores due to the competition for air flow among pores, which is won by the wider pores that have lower hydrodynamic flow resistance. Finally, at applied pressures higher than the transition pressure for both pores, almost all the pores actively form bubbles (Figure 9.7C). In line with observations for standard partitioned-EDGE, as the bubble formation frequency increases with applied pressure for narrow pores, both the bubble size that leads to a decrease in the bubble formation frequency (Figure 9.7C), and the polydispersity increase for the wider pores because dripping-jetting transition occurs above the cross-over pressure (~1950 mbar for wide pores and 2050 mbar for narrow pores).

It is good to point out that not all narrow pores are activated at the same time; narrow pores separated by wide partitions and away from the wide pores, are activated first and form bubbles at a higher frequency (red box 1 and 3). The narrow pores that are separated by narrow partitions and positioned in between two wide pores (indicated by box 2, and two circles) might be activated at higher applied pressures (not further discussed), accompanied by two down-sides that are: 1) increasingly larger bubbles are formed from the wide pores, and 2) dripping-jetting transition occurs for the narrow pores. In an actual membrane foaming system, it can be expected that the dispersed phase flows preferentially through the large pores, and to controllably produce monodisperse bubbles, the highest applied pressure is limited by the 'blow-up' pressure (i.e., at which instability occurs) of these large pores.

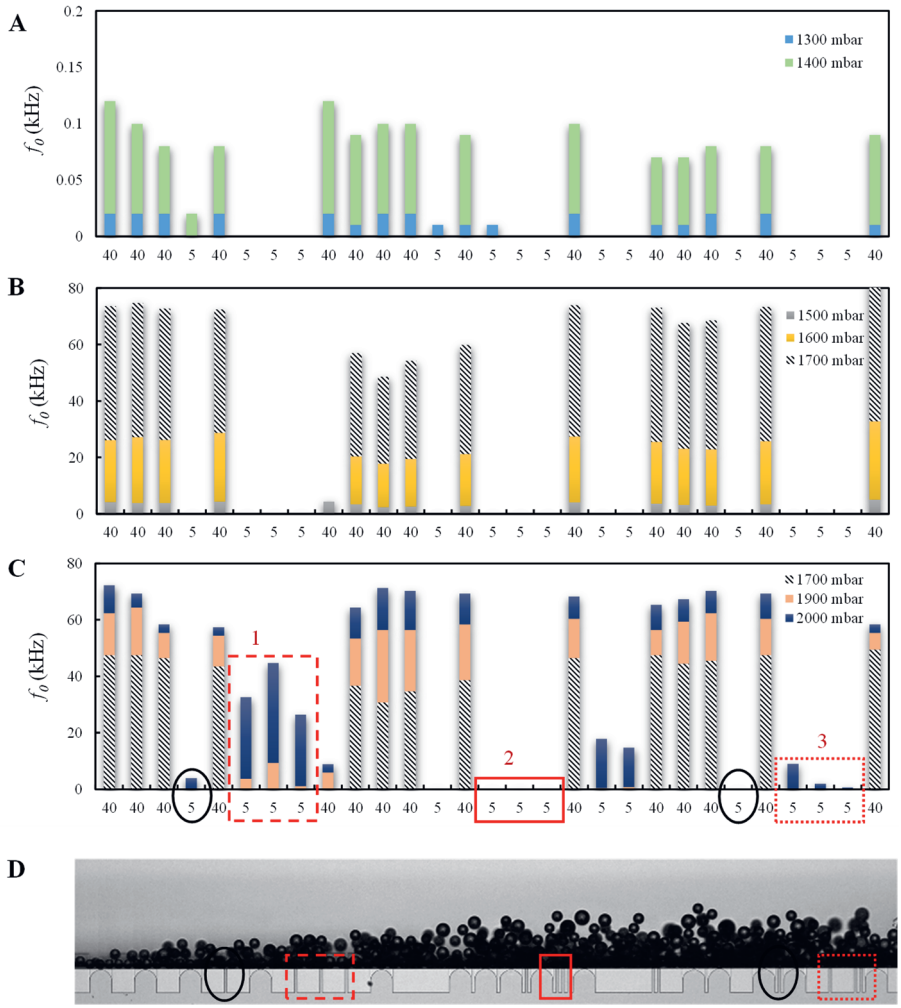

***Figure 9.7**. Bubble formation frequency for each pore in the membrane chip. In this membrane chip, the width of the main plateau is 1500 µm, including 28 pores with s = 5 or 40 µm and w = 5, 40 or 80 µm. The plateau and pore height is approximately 0.93 µm. The 5% wt. WPI solution has 2 mPa·s.*

From **Chapters 3**, **4** and **6** follows that the partitioned-EDGE device can produce monodisperse bubbles within a wide range of applied pressures, and the bubble properties can be tuned through device geometry and liquid phase properties. Besides, via tailoring the device geometry, the operation window of the dripping regime can be extended, and bubble crowding in the collection channel and bubble-bubble interactions at adjacent pores can be promoted, both of which may promote bubble coalescence, leading to increased bubble size. Accordingly, as discussed in section 9.3.1, emulsifiers and their concentrations need to be chosen wisely, ideally in such a way that they can stabilise the bubbles timely [128]. The features

of the partitioned-EDGE device make it an interesting candidate for up-scaling and thus making monodisperse bubbles for practical applications. Parallelisation is the typical way of up-scaling microfluidic devices [18,21,43,78,95,141,143]. From the membrane trial, it is clear that to up-scale the partitioned-EDGE device, it is preferable to create parallel, identical pores on the same main plateau, using relatively narrow pores showing delayed 'dripping-jetting' transition, and to parallelise main plateaus with similar pore sizes. Besides, it is also good to mention that coalescence is not always bad; in the device with the distance between the centre of two pores being smaller than the (initial) bubble size, a finite extent of coalescence leads to the formation of relatively monodisperse coalesced bubbles and the bubble size is almost independent of the applied pressure. Although making and letting an up-scaled system work will again bring challenges, we believed that these insights provide a solid theoretical and experimental background for the up-scaling of the partitioned-EDGE device to an industry-relevant level, which may be the next step.

9.4.2 Cross-flow membrane foaming

When comparing the partitioned-EDGE system to the cross-flow membrane foaming (CFMF) system as described in **Chapter 8**, we observed that in the presence of 2.5% wt. WPI, the coalescence of bubbles formed at 0.1 ms only occurs in partitioned-EDGE system, which is most likely due to the more widely spaced pores in the membrane system. Also with skimmed milk (which has a protein content of about 3.7% wt., yet with higher viscosity), the CFMF system makes a very stable foam (Figure 9.8). These observations indicate that microfluidic investigations might overestimate the amount of emulsifier needed to make stable foams in practice [59]. In conventional systems with vigorous mixing, mass transfer is expectedly even more intense [14,61,174], which may explain this. It would be good to also incorporate these effects in future microfluidic devices for large-scale production, or analysis purposes. To fully understand a certain process (e.g., foaming or emulsification), both the *short-term behaviours*, which can be probed with microfluidic devices, and the *long-term behaviours* that are most relevant to end products, which can be studied with both conventional methods and novel microfluidic methods, should be considered.

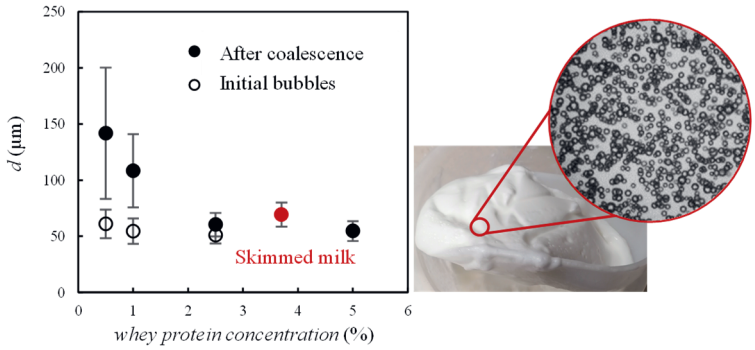

***Figure 9.8**. Bubble formation and coalescence observed in the CFMF system The experimental conditions are described in **Chapter 8**. The red dot represents the result obtained for skimmed milk.*

9.5 Concluding remarks

At the end of this thesis we celebrate the versatility of partitioned-EDGE that hosts many advantages in one little device; it can be used as: 1) a bubble (droplet) generator; 2) a microfluidic tensiometer for the measurement of the kinetics of emulsifier adsorption (which will be the next step) and the resulting dynamic surface and interfacial tension; 3) a tool with which bubble coalescence can be monitored at *microsecond* time scales. The overall system can be used for high throughput screening of emulsifier materials and other process conditions. The adsorption time, which is typically the bubble formation time in microfluidics, varies in the range of 10^{-5}-10^{0} s in the partitioned-EDGE device; these time scales cover those present in most of the foaming and emulsification systems used in practice [15,152]. Therefore, the findings shown in this thesis improve the understanding of significant factors that influence the formation and stabilisation of (food) foams at relevant length and time scales. The unifying discussion of e.g., dripping-jetting transition, will help the design of microfluidic devices (in particular, spontaneous devices, or those utilise capillary action) for controllable production of monodisperse foams with desired properties, and help extend the operation window of spontaneous microfluidic devices.

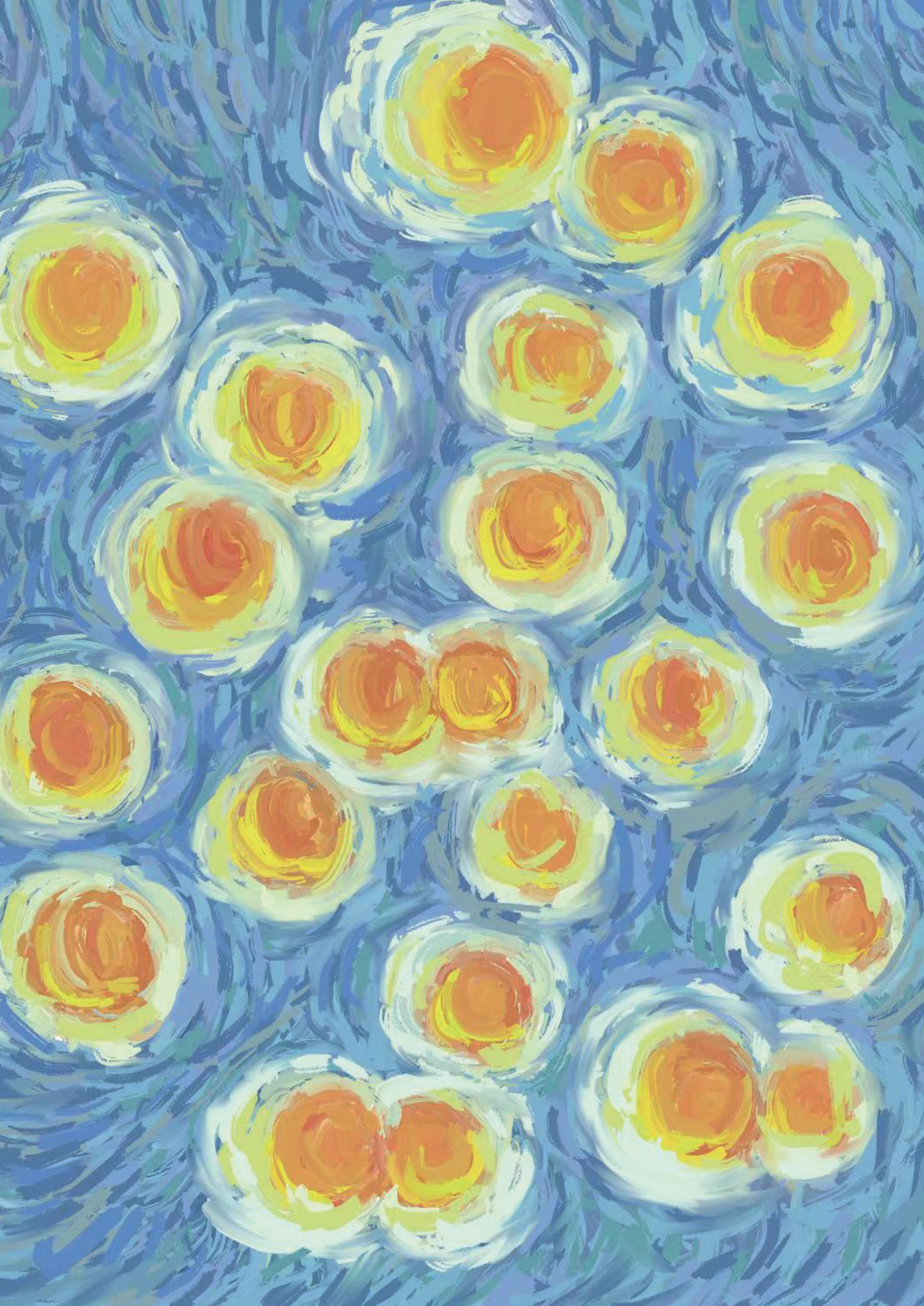

R

References

1. Walstra, P., J. T. M. Wouters & T. J. Geurts. *Dairy science and technology*. *CRC* (2005). doi:https://doi.org/10.1201/9781420028010.

2. Klaseboer, E., Chevaillier, J. P., Gourdon, C. & Masbernat, O. Film drainage between colliding drops at constant approach velocity: Experiments and modeling. *J. Colloid Interface Sci.* **229**, 274–285 (2000).

3. Damodaran, S. Protein stabilization of emulsions and foams. *J. Food Sci.* **70**, 54–66 (2005).

4. Dudek, M., Fernandes, D., Helno Herø, E. & Øye, G. Microfluidic method for determining drop-drop coalescence and contact times in flow. *Colloids Surfaces A Physicochem. Eng. Asp.* **586**, 124265 (2020).

5. McClements, D. J. *Principles, practicies, and techniques*. *Food Emulsions* vol. 2 (2005).

6. Drenckhan, W. & Langevin, D. Monodisperse foams in one to three dimensions. *Curr. Opin. Colloid Interface Sci.* **15**, 341–358 (2010).

7. Stang, M., Karbstein, H. & Schubert, H. Adsorption kinetics of emulsifiers at oil-water interfaces and their effect on mechanical emulsification. *Chem. Eng. Process.* **33**, 307–311 (1994).

8. Brösel, S. & Schubert, H. Investigations on the role of surfactants in mechanical emulsification using a high-pressure homogenizer with an orifice valve. *Chem. Eng. Process. Process Intensif.* **38**, 533–540 (1999).

9. Eastoe, J. & Dalton, J. S. Dynamic surface tension and adsorption mechanisms of surfactants at the air-water interface. *Adv. Colloid Interface Sci.* **85**, 103–144 (2000).

10. Alvarez, N. J., Vogus, D. R., Walker, L. M. & Anna, S. L. Using bulk convection in a microtensiometer to approach kinetic-limited surfactant dynamics at fluid-fluid interfaces. *J. Colloid Interface Sci.* **372**, 183–191 (2012).

11. Wang, K., Zhang, L., Zhang, W. & Luo, G. Mass-transfer-controlled dynamic interfacial tension in microfluidic emulsification processes. *Langmuir* **32**, 3174–3185 (2016).

12. Kiratzis, I., Kovalchuk, N. M., Simmons, M. J. H. & Vigolo, D. Effect of surfactant addition and viscosity of the continuous phase on flow fields and kinetics of drop formation in a flow-focusing microfluidic device. *Chem. Eng. Sci.* **248**, 117183 (2022).

13. Chen, Y., Narayan, S. & Dutcher, C. S. Phase-dependent surfactant transport on the microscale: interfacial tension and droplet coalescence. *Langmuir* **36**, 14904–14923 (2020).

14. Walstra, P. *Physical chemistry of foods*. *Physical Chemistry of Foods* (2003). doi:10.1201/9780203910436.

15. Drenckhan, W. & Saint-Jalmes, A. The science of foaming. *Adv. Colloid Interface Sci.* **222**, 228–259 (2015).

16. Garstecki, P., Fuerstman, M. J., Stone, H. A. & Whitesides, G. M. Formation of droplets and bubbles in a microfluidic T-junction - Scaling and mechanism of break-up. *Lab Chip* **6**, 437–446 (2006).

17. Muijlwijk, K., Berton-carabin, C. & Schroën, K. Cross- flow microfluidic emulsification from a food perspective. *Trends Food Sci. Technol.* **49**, 51–63 (2016).

18. Van Dijke, K., Veldhuis, G., Schroën, K. & Boom, R. Parallelized edge-based droplet generation (EDGE) devices. *Lab Chip* **9**, 2824–2830 (2009).

19. Kobayashi, I., Wada, Y., Uemura, K. & Nakajima, M. Microchannel emulsification for mass production of uniform fine droplets: Integration of microchannel arrays on a chip. *Microfluid. Nanofluidics* **8**, 255–262 (2010).

20. Amstad, E. *et al.* Robust scalable high throughput production of monodisperse drops. *Lab Chip* **16**, 4163–4172 (2016).

21. Vladisavljević, G. T. *et al.* Long-term stability of droplet production by microchannel (step) emulsification in microfluidic silicon chips with large number of terraced microchannels. *Chem. Eng. J.* **333**, 380–391 (2018).

22. Van Der Graaf, S., Steegmans, M. L. J., Van Der Sman, R. G. M., Schroën, C. G. P. H. & Boom, R. M. Droplet formation in a T-shaped microchannel junction: A model system for membrane emulsification. *Colloids Surfaces A Physicochem. Eng. Asp.* **266**, 106–116 (2005).

23. Brosseau, Q., Vrignon, J. & Baret, J. C. Microfluidic dynamic interfacial tensiometry (μDIT). *Soft Matter* **10**, 3066–3076 (2014).

24. Riechers, B. *et al.* Surfactant adsorption kinetics in microfluidics. *Proc. Natl. Acad. Sci.* **113**, 11465–11470 (2016).

25. Baret, J. C., Kleinschmidt, F., Harrak, A. El & Griffiths, A. D. Kinetic aspects of emulsion stabilization by surfactants: A microfluidic analysis. *Langmuir* **25**, 6088–6093 (2009).

26. Krebs, T., Schroën, K. & Boom, R. Coalescence dynamics of surfactant-stabilized emulsions studied with microfluidics. *Soft Matter* **8**, 10650–10657 (2012).

27. Muijlwijk, K., Colijn, I., Harsono, H., Krebs, T. & Berton-Carabin, C. Coalescence of protein-stabilised emulsions studied with microfluidic. *Food Hydrocoll.* **70**, 94–104 (2017).

28. Shelley L., A. Droplets and bubbles in microfluidic devices. *Annu. Rev. Fluid Mech.* **48**, 285–309 (2016).

29. Xu, J. H., Li, S. W., Tan, J., Wang, Y. J. & Luo, G. S. Preparation of highly monodisperse droplet in a T-junction microfluidic device. *AIChE J.* **52**, 3005–3010 (2006).

30. Wehking, J. D., Gabany, M., Chew, L. & Kumar, R. Effects of viscosity, interfacial tension, and flow geometry on droplet formation in a microfluidic T-junction. *Microfluid. Nanofluidics* **16**, 441–453 (2014).

31. Sivasamy, J., Wong, T. N., Nguyen, N. T. & Kao, L. T. H. An investigation on the mechanism of droplet formation in a microfluidic T-junction. *Microfluid. Nanofluidics* **11**, 1–10 (2011).

32. Van Steijn, V., Kleijn, C. R. & Kreutzer, M. T. Predictive model for the size of bubbles and droplets created in microfluidic T-junctions. *Lab Chip* **10**, 2513–2518 (2010).

33. Garstecki, P. *et al.* Formation of monodisperse bubbles in a microfluidic flow-focusing device. *Appl. Phys. Lett.* **85**, 2649–2651 (2004).

34. Lorenceau, E., Sang, Y. Y. C., Höhler, R. & Cohen-Addad, S. A high rate flow-focusing foam generator. *Phys. Fluids* **18**, 097103 (2006).

35. Sullivan, M. T. & Stone, H. A. The role of feedback in microfluidic flow-focusing devices. *Philos. Trans. R. Soc. A Math. Phys. Eng. Sci.* **366**, 2131–2143 (2008).

36. Lu, Y., Fu, T., Zhu, C., Ma, Y. & Li, H. Z. Scaling of the bubble formation in a flow-focusing device: Role of the liquid viscosity. *Chem. Eng. Sci.* **105**, 213–219 (2014).

37. Wang, K., Lu, Y. C., Xu, J. H. & Luo, G. S. Determination of dynamic interfacial tension and its effect on droplet formation in the T-shaped microdispersion process. *Langmuir* **25**, 2153–2158 (2009).

38. Sugiura, S., Nakajima, M., Iwamoto, S. & Seki, M. Interfacial tension driven monodispersed droplet formation from microfabricated channel array. *Langmuir* **17**, 5562–5566 (2001).

39. Sugiura, S., Nakajima, M. & Seki, M. Preparation of monodispersed emulsion with large droplets using microchannel emulsification. *J. Am. Oil Chem. Soc.* **79**, 515–519 (2002).

40. Van Dijke, K. *et al.* Effect of viscosities of dispersed and continuous phases in microchannel oil-in-water emulsification. *Microfluid. Nanofluidics* **9**, 77–85 (2010).

41. Stoffel, M. *et al.* Bubble production mechanism in a microfluidic foam generator. *Phys. Rev. Lett.* **108**, 198302 (2012).

42. Sahin, S. & Schroën, K. Partitioned EDGE devices for high throughput production of monodisperse emulsion droplets with two distinct sizes. *Lab Chip* **15**, 2486–2495 (2015).

43. Schroën, K., Bliznyuk, O., Muijlwijk, K., Sahin, S. & Berton-Carabin, C. C. Microfluidic emulsification devices: from micrometer insights to large-scale food emulsion production. *Curr. Opin. Food Sci.* **3**, 33–40 (2015).

44. Maan, A. A., Schroën, K. & Boom, R. Spontaneous droplet formation techniques for monodisperse emulsions preparation - Perspectives for food applications. *J. Food Eng.* **107**, 334–346 (2011).

45. Van Dijke, K. C., Schroën, K., van der Padt, A. & Boom, R. EDGE emulsification for food-grade dispersions. *J. Food Eng.* **97**, 348–354 (2010).

46. ten Klooster, S., Sahin, S. & Schroën, K. Monodisperse droplet formation by spontaneous and interaction based mechanisms in partitioned EDGE microfluidic device. *Sci. Rep.* **9**, 7820 (2019).

47. Mi, S., Fu, T., Zhu, C., Jiang, S. & Ma, Y. Mechanism of bubble formation in step-emulsification devices. *AIChE J.* **66**, 16777 (2019).

48. Mittal, N., Cohen, C., Bibette, J. & Bremond, N. Dynamics of step-emulsification: From a single to a collection of emulsion droplet generators. *Phys. Fluids* **26**, 082109 (2014).

49. Huston, S. D., Cabral, J. T., William J. Goodrum, J., Beers, K. L. & Eric J. Amis. Microfluidic interfacial tensiometry. *Appl. Phys. Lett.* **87**, 081905 1–2 (2005).

50. Chen, Y. & Dutcher, C. S. Size dependent droplet interfacial tension and surfactant transport in liquid-liquid systems, with applications in shipboard oily bilgewater emulsions. *Soft Matter* **16**, 2994–3004 (2020).

51. Steegmans, M. L. J., Warmerdam, A., Schroen, K. G. P. H. & Boom, R. M. Dynamic interfacial tension measurements with microfluidic Y-junctions. *Langmuir* **25**, 9751–9758 (2009).

52. Xu, J. H., Dong, P. F., Zhao, H., Tostado, C. P. & Luo, G. S. The dynamic effects of surfactants on droplet formation in coaxial microfluidic devices. *Langmuir* **28**, 9250–9258 (2012).

53. Muijlwijk, K., Hinderink, E., Ershov, D., Berton-Carabin, C. & Schroën, K. Interfacial tension measured at high expansion rates and within milliseconds using microfluidics. *J. Colloid Interface Sci.* **470**, 71–79 (2016).

54. Wang, X., Riaud, A., Wang, K. & Luo, G. Pressure drop-based determination of dynamic interfacial tension of droplet generation process in T-junction microchannel. *Microfluid. Nanofluidics* **18**, 503–512 (2015).

55. Liang, X., Li, M., Wang, K. & Luo, G. Determination of time-evolving interfacial tension and ionic surfactant adsorption kinetics in microfluidic droplet formation process. *J. Colloid Interface Sci.* **617**, 106–117 (2022).

56. Gu, H., Duits, M. H. G. & Mugele, F. Interfacial tension measurements with microfluidic tapered channels. *Colloids Surfaces A Physicochem. Eng. Asp.* **389**, 38–42 (2011).

57. Liu, S. & Dutcher, C. S. Measurements of static and dynamic bubble surface tension using a deformation-based microfluidic tensiometer. *J. Phys. Chemisry B* **125**, 13916–13927 (2021).

58. Hinderink, E. B. A., Kaade, W., Sagis, L., Schroën, K. & Berton-Carabin, C. C. Microfluidic investigation of the coalescence susceptibility of pea protein-stabilised emulsions: Effect of protein oxidation level. *Food Hydrocoll.* **102**, (2020).

59. Berton-Carabin, C. C., Sagis, L. & Schroën, K. Formation, structure, and functionality of interfacial layers in food emulsions. *Annu. Rev. Food Sci. Technol.* **9**, 551–87 (2018).

60. Wilson, A. J. *Foams: Physics, chemistry and structure*. (Springer Series in Applied Biology, 1989).

61. Narsimhan, G. & Xiang, N. Role of proteins on formation, drainage, and stability of liquid food foams. *Annu. Rev. Food Sci. Technol.* **9**, 45–63 (2018).

62. Taccoen, N., Lequeux, F., Gunes, D. Z. & Baroud, C. N. Probing the mechanical strength of an armored bubble and its implication to particle-stabilized foams. *Phys. Rev. X* **6**, 1–11 (2016).

63. Lam, S., Velikov, K. P. & Velev, O. D. Pickering stabilization of foams and emulsions with particles of biological origin. *Curr. Opin. Colloid Interface Sci.* **19**, 490–500 (2014).

64. Murray, B. S., Durga, K., Yusoff, A. & Stoyanov, S. D. Stabilization of foams and emulsions by mixtures of surface active food-grade particles and proteins. *Food Hydrocoll.* **25**, 627–638 (2011).

65. Saari, H., Fuentes, C., Sjöö, M., Rayner, M. & Wahlgren, M. Production of starch nanoparticles by dissolution and non-solvent precipitation for use in food-grade Pickering emulsions. *Carbohydr. Polym.* **157**, 558–566 (2017).

66. Schröder, A., Sprakel, J., Schroën, K. & Berton-Carabin, C. C. Tailored microstructure of colloidal lipid particles for Pickering emulsions with tunable properties. *Soft Matter* **13**, 3190–3198 (2017).

67. Muijlwijk, K., Berton-Carabin, C. & Schroën, K. How microfluidic methods can lead to better emulsion products. *Lipid Technol.* **27**, 234–236 (2015).

68. Güell, C., Ferrando, M., Trentin, A. & Schroën, K. Apparent interfacial tension effects in protein stabilized emulsions prepared with microstructured systems. *Membranes (Basel).* **7**, 1–12 (2017).

69. Gunes, D. Z. Microfluidics for food science and engineering. *Curr. Opin. Food Sci.* **21**, 57–65 (2018).

70. Wang, K., Lu, Y. C., Xu, J. H., Tan, J. & Luo, G. S. Generation of micromonodispersed droplets and bubbles in the capillary embedded T-junction microfluidic devices. *AIChE J.* **57**, 299–306 (2011).

71. Xu, J. H., Li, S. W., Chen, G. G. & Luo, G. S. Formation of monodisperse microbubbles in a microfluidic device. *AIChE J.* **52**, 2254–2259 (2006).

72. Chen, C., Zhu, Y., Leech, P. W. & Manasseh, R. Production of monodispersed micron-sized bubbles at high rates in a microfluidic device. *Appl. Phys. Lett.* **95**, 1–4 (2009).

73. Wang, X., Zhu, C., Fu, T., Qiu, T. & Ma, Y. Critical condition for bubble breakup in a microfluidic flow-focusing junction. *Chem. Eng. Sci.* **164**, 178–187 (2017).

74. Zhang, C. *et al.* Dynamics of bubble formation in highly viscous liquids in a flow-focusing device. *Chem. Eng. Sci.* **172**, 278–285 (2017).

75. Fu, T., Funfschiling, D., Ma, Y. & Li, H. Z. Scaling the formation of slug bubbles in microfluidic flow-focusing devices. *Microfluid Nanofluid* **8**, 467–475 (2010).

76. Wang, K., Xie, L., Lu, Y. & Luo, G. Generating microbubbles in a co-flowing microfluidic device. *Chem. Eng. Sci.* **100**, 486–495 (2013).

77. Yasuno, M. *et al.* Monodispersed microbubble formation using microchannel technique. *AIChE J.* **50**, 3227–3233 (2004).

78. Vladisavljević, G. T., Kobayashi, I. & Nakajima, M. Production of uniform droplets using membrane, microchannel and microfluidic emulsification devices. *Microfluid. Nanofluidics* **13**, 151–178 (2012).

79. Maan, A. A., Nazir, A., Khan, M. K. I., Boom, R. & Schroën, K. Microfluidic emulsification in food processing. *J. Food Eng.* **147**, 1–7 (2014).

80. Gañán-Calvo, A. M. Perfectly monodisperse microbubbling by capillary flow focusing: An alternate physical description and universal scaling. *Phys. Rev. E* **69**, (2004).

81. Cubaud, T. & Mason, T. G. Capillary threads and viscous droplets in square microchannels. *Phys. Fluids* **20**, 1–11 (2008).

82. Fu, T. & Ma, Y. Bubble formation and breakup dynamics in microfluidic devices: A review. *Chem. Eng. Sci.* **135**, 343–372 (2014).

83. Dang, M., Yue, J. & Chen, G. Numerical simulation of Taylor bubble formation in a microchannel with a converging shape mixing junction. *Chem. Eng. J.* **262**, 616–627 (2015).

84. Wörner, M. Numerical modeling of multiphase flows in microfluidics and micro process engineering: A review of methods and applications. *Microfluid. Nanofluidics* **12**, 841–886 (2012).

85. Van Dijke, K. C., Veldhuis, G., Schroën, K. & Boom, R. M. Simultaneous formation of many droplets in a single microfluidic droplet formation unit. *AIChE J.* **56**, 833–836 (2010).

86. Sugiura, S., Nakajima, M., Kumazawa, N., Iwamoto, S. & Seki, M. Characterization of spontaneous transformation-based droplet formation during microchannel emulsification. *J. Phys. Chem. B* **106**, 9405–9409 (2002).

87. Rayner, M., Trägårdh, G., Trägårdh, C. & Dejmek, P. Using the Surface Evolver to model droplet formation processes in membrane emulsification. *J. Colloid Interface Sci.* **279**, 175–185 (2004).

88. Van Dijke, K. C., Schroën, K. C. P. G. H. & Boom, R. M. Microchannel emulsification: From computational fluid dynamics to predictive analytical model. *Langmuir* **24**, 10107–10115 (2008).

89. Kobayashi, I., Mukataka, S. & Nakajima, M. CFD simulation and analysis of emulsion droplet formation from straight-through microchannels. *Langmuir* **20**, 9868–9877 (2004).

90. Montessori, A., Lauricella, M., Stolovicki, E., Weitz, D. A. & Succi, S. Jetting to dripping transition: Critical aspect ratio in step emulsifiers. *Phys. Fluids* **31**, (2019).

91. Sahin, S., Bliznyuk, O., Rovalino Cordova, A. & Schroën, K. Microfluidic EDGE emulsification: The importance of interface interactions on droplet formation and pressure stability. *Sci. Rep.* **6**, (2016).

92. Van Dijke, K., De Ruiter, R., Schroën, K. & Boom, R. The mechanism of droplet formation in microfluidic EDGE systems. *Soft Matter* **6**, 321–330 (2010).

93. Eggersdorfer, M. L., Seybold, H., Ofner, A., Weitz, D. A. & Studart, A. R. Wetting controls of droplet formation in step emulsification. *PNAS* **115**, 9479–9484 (2018).

94. Nisisako, T. & Torii, T. Microfluidic large-scale integration on a chip for mass production of monodisperse droplets and particles. *Lab Chip* **8**, 287–293 (2008).

95. Hashimoto, M. *et al.* Formation of bubbles and droplets in parallel, coupled flow-focusing geometries. *Small* **4**, 1795–1805 (2008).

96. Barbier, V., Willaime, H., Tabeling, P. & Jousse, F. Producing droplets in parallel microfluidic systems. *Phys. Rev. E* **74**, (2006).

97. Sugiura, S., Nakajima, M. & Seki, M. Effect of channel structure on microchannel emulsification. *Langmuir* **18**, 5708–5712 (2002).

98. Opalski, A. S., Makuch, K., Lai, Y. K., Derzsi, L. & Garstecki, P. Grooved step emulsification systems optimize the throughput of passive generation of monodisperse emulsions. *Lab Chip* **19**, 1183–1192 (2019).

99. Hoang, D. A. *et al.* Design and characterization of bubble-splitting distributor for scaled-out multiphase microreactors. *Chem. Eng. J.* **236**, 545–554 (2014).

100. Rayner, M. & Dejmek, P. *Engineering aspects of food emulsification and homogenization*. (CRC Press, 2015).

101. Muijlwijk, K., Huang, W., Vuist, J. E., Berton-Carabin, C. & Schroën, K. Convective mass transport dominates surfactant adsorption in a microfluidic Y-junction. *Soft Matter* **12**, 9025–9029 (2016).

102. Morini, G. L. Laminar-to-turbulent flow transition in microchannels. *Microscale Thermophys. Eng.* **8**, 15–30 (2004).

103. Walstra, P., Förster, T., Walstra, P. & Förster, T. Principles of emulsion formation. *Chem. Eng. Sci.* **48**, 333–349 (1993).

104. Walstra, P. & Smulders, P. E. A. Emulsion formation. in *Modern Aspects of Emulsion Science* (ed. Bernard P Binks) 56–99 (1998).

105. Muijlwijk, K., Li, X., Berton-Carabin, C. & Schroën, K. Dynamic fluid interface formation in microfluidics: Effect of emulsifier structure and oil viscosity. *Innov. Food Sci. Emerg. Technol.* **45**, 215–219 (2018).

106. Yang, L., Wang, K., Tan, J., Lu, Y. & Luo, G. Experimental study of microbubble coalescence in a T-junction microfluidic device. *Microfluid. Nanofluidics* **12**, 715–722 (2012).

107. Fu, T., Ma, Y. & Li, H. Z. Bubble coalescence in non-Newtonian fluids in a microfluidic expansion device. *Chem. Eng. Process. Process Intensif.* **97**, 38–44 (2015).

108. Mazutis, L., Baret, J. C. & Griffiths, A. D. A fast and efficient microfluidic system for highly selective one-to-one droplet fusion. *Lab Chip* **9**, 2665–2672 (2009).

109. Mazutis, L. & Griffiths, A. D. Selective droplet coalescence using microfluidic systems. *Lab Chip* **12**, 1800–1806 (2012).

110. Krebs, T., Schroen, K. & Boom, R. M. A microfluidic method to study demulsification kinetics. *Lab Chip* **12**, 1060–1070 (2012).

111. Muijlwijk, K. Microfluidic methods to study emulsion formation. (Wageningen University & Research, 2017). doi:10.18174/403476.

112. Berton-Carabin, C. C., Schröder, A., Rovalino-Cordova, A., Schroën, K. & Sagis, L. Protein and lipid oxidation affect the viscoelasticity of whey protein layers at the oil–water interface. *Eur. J. Lipid Sci. Technol.* **118**, 1630–1643 (2016).

113. Saint-Jalmes, A. Physical chemistry in foam drainage and coarsening. *Soft Matter* **2**, 836–849 (2006).

114. Laporte, M., Montillet, A., Della Valle, D., Loisel, C. & Riaublanc, A. Characteristics of foams produced with viscous shear thinning fluids using microchannels at high throughput. *J. Food Eng.* **173**, 25–33 (2016).

115. Krebs, T., Ershov, D., Schroen, C. G. P. H. & Boom, R. M. Coalescence and compression in centrifuged emulsions studied with in situ optical microscopy. *Soft Matter* **9**, 4026–4035 (2013).

116. Feng, H. *et al.* Manipulating and quantifying temperature-triggered coalescence with microcentrifugation. *Lab Chip* **15**, 188–194 (2015).

117. Skurtys, O. & Aguilera, J. M. Applications of microfluidic devices in food engineering. *Food Biophys.* **3**, 1–15 (2008).

118. Deosarkar, S. S., Khedkar, C. D., Kalyankar, S. D. & Sarode, A. R. Ice cream: Uses and method of manufacture. *Encycl. Food Heal.* 391–397 (2015) doi:10.1016/B978-0-12-384947-2.00384-6.

119. Zúñiga, R. N. & Aguilera, J. M. Aerated food gels: fabrication and potential applications. *Trends Food Sci. Technol.* **19**, 176–187 (2008).

120. Lazidis, A., de Almeida Parizotto, L., Spyropoulos, F. & Norton, I. T. Reprint of: Microstructural design of aerated food systems by soft-solid materials. *Food Hydrocoll.* **73**, 110–119 (2017).

121. Berton, C., Genot, C. & Ropers, M. H. Quantification of unadsorbed protein and surfactant emulsifiers in oil-in-water emulsions. *J. Colloid Interface Sci.* **354**, 739–748 (2011).

122. Garstecki, P., Stone, H. A. & Whitesides, G. M. Mechanism for flow-rate controlled breakup in confined geometries: A route to monodisperse emulsions. *Phys. Rev. Lett.* **94**, 164501 (2005).

123. Kawakatsu, T., Kikuchi, Y. & Nakajima, M. Regular-sized cell creation in microchannel emulsification by visual microprocessing method. *J. Am. Oil Chem. Soc.* **74**, 317–321 (1997).

124. Kobayashi, I. *et al.* Straight-through microchannel devices for generating monodisperse emulsion droplets several microns in size. *Microfluid. Nanofluidics* **4**, 167–177 (2008).

125. Zhang, Z., Jiang, S., Zhu, C., Ma, Y. & Fu, T. Bubble formation in a step-emulsification microdevice with parallel microchannels. *Chem. Eng. Sci.* **224**, 115815 (2020).

126. Crestel, E., Derzsi, L., Bartolomei, H., Bibette, J. & Bremond, N. Emulsification with rectangular tubes. *Phys. Rev. Fluids* **4**, 073602 (2019).

127. Montessori, A., Lauricella, M., Succi, S., Stolovicki, E. & Weitz, D. Elucidating the mechanism of step emulsification. *Phys. Rev. Fluids* **7**, 072202 (2018).

128. Jafari, S. M., Assadpoor, E., He, Y. & Bhandari, B. Re-coalescence of emulsion droplets during high-energy emulsification. *Food Hydrocoll.* **22**, 1191–1202 (2008).

129. Hinderink, E. B. A. *et al.* Early film formation in protein-stabilised emulsions : Insights from a microfluidic approach. *Food Hydrocoll.* **118**, (2021).

130. Bruus, H. *Theoretical microfluidics*. *Oxford University Press Inc.* vol. 45 (Oxford University Press Inc., 2008).

131. Dangla, R., Fradet, E., Lopez, Y. & Baroud, C. N. The physical mechanisms of step emulsification. *J. Phys. D. Appl. Phys.* **46**, 114003 (2013).

132. Geerken, M. J., Lammertink, R. G. H. & Wessling, M. Interfacial aspects of water drop formation at micro-engineered orifices. *J. Colloid Interface Sci.* **312**, 460–469 (2007).

133. Tcholakova, S., Denkov, N. D., Ivanov, I. B. & Campbell, B. Coalescence in β−lactoglobulin−stabilized emulsions: Effects of protein adsorption and drop size. *Langmuir* **18**, 8960−8971 (2002).

134. De Jongh, H. H. J. *et al.* Protein adsorption at air-water interfaces: A combination of details. *Biopolymers* **74**, 131–135 (2004).

135. Alvarez, N. J., Walker, L. M. & Anna, S. L. A microtensiometer to probe the effect of radius of curvature on surfactant transport to a spherical interface. *Langmuir* **26**, 13310–13319 (2010).

136. Zhou, H., Yao, Y., Chen, Q., Li, G. & Yao, S. A facile microfluidic strategy for measuring interfacial tension. *Appl. Phys. Lett.* **103**, (2013).

137. Segers, T., Lohse, D., Versluis, M. & Frinking, P. Universal equations for the coalescence probability and long-term size stability of phospholipid-coated monodisperse microbubbles formed by flow focusing. *Langmuir* **33**, 10329–10339 (2017).

138. Ofner, A. *et al.* High-throughput step emulsification for the production of functional materials using a glass microfluidic device. *Macromol. Chem. Phys.* **218**, 1–10 (2017).

139. Ofner, A. *et al.* Controlled massive encapsulation via tandem step emulsification in glass. *Adv. Funct. Mater.* **29**, 1–9 (2019).

140. Kobayashi, I., Nakajima, M., Chun, K., Kikuchi, Y. & Fujita, H. Silicon array of elongated through-holes for monodisperse emulsion droplets. *AIChE J.* **48**, 1639–1644 (2002).

141. Stolovicki, E., Ziblat, R. & Weitz, D. A. Throughput enhancement of parallel step emulsifier devices by shear-free and efficient nozzle clearance. *Lab Chip* **18**, 132–138 (2017).

142. Tong, J., Nakajima, M., Nabetani, H. & Kikuchi, Y. Surfactant effect on production of monodispersed microspheres by microchannel emulsification method. *J. Surfactants Deterg.* **3**, (2000).

143. Håti, A. G., Szymborski, T. R., Steinacher, M. & Amstad, E. Production of monodisperse drops from viscous fluids. *Lab Chip* **18**, 648–654 (2018).

144. Shui, L., Van Den Berg, A. & Eijkel, J. C. T. Scalable attoliter monodisperse droplet formation using multiphase nano-microfluidics. *Microfluid. Nanofluidics* **11**, 87–92 (2011).

145. Hein, M., Afkhami, S., Seemann, R. & Kondic, L. Capillary focusing close to a topographic step: shape and instability of confined liquid filaments. *Microfluid. Nanofluidics* **18**, 911–917 (2015).

146. Zhang, Z. *et al.* Bubble formation in a step-emulsification microdevice: Hydrodynamic effects in the cavity. *J. Ind. Eng. Chem.* **94**, 127–133 (2021).

147. Schroën, K. *et al.* Droplet microfluidics for food and nutrition applications. *micromachines* **12**, 1–27 (2021).

148. Deng, B., Schroën, K. & De Ruiter, J. Effects of dynamic adsorption on bubble formation and coalescence in partitioned-EDGE devices. *J. Colloid Interface Sci.* **602**, 316–324 (2021).

149. Jin, F., Balasubramaniam, R. & Stebe, K. J. Surfactant adsorption to spherical particles: The intrinsic length scale governing the shift from diffusion to kinetic-controlled mass transfer. *J. Adhes.* **80**, 773–796 (2004).

150. Schroën, K., Ferrando, M., de Lamo-Castellví, S., Sahin, S. & Güell, C. Linking findings in microfluidics to membrane emulsification process design: The importance of wettability and component interactions with interfaces. *Membranes (Basel).* **6**, (2016).

151. Abedi, S., Suteria, N. S., Chen, C. C. & Vanapalli, S. A. Microfluidic production of size-tunable hexadecane-in-water emulsions: Effect of droplet size on destabilization of two-dimensional emulsions due to partial coalescence. *J. Colloid Interface Sci.* **533**, 59–70 (2019).

152. Schroën, K., de Ruiter, J. & Berton-Carabin, C. The importance of interfacial tension in emulsification: Connecting scaling relations used in large scale preparation with microfluidic measurement methods. *ChemEngineering* **4**, 1–22 (2020).

153. Schultz, S., Wagner, G., Urban, K. & Ulrich, J. High-pressure homogenization as a process for emulsion formation. *Chem. Eng. Technol.* **27**, 361–368 (2004).

154. Apolito, R. D. *et al.* Measuring interfacial tension of emulsions in situ by microfluidic. *Langmuir* **34**, 4991–4997 (2018).

155. Kalli, M., Chagot, L. & Angeli, P. Comparison of surfactant mass transfer with drop formation times from dynamic interfacial tension measurements in microchannels. *J. Colloid Interface Sci.* **605**, 204–213 (2022).

156. Pawliszak, P. *et al.* Interfacial tension sensor for low dosage surfactant detection. *colloids and interfaces* **5**, 1–12 (2021).

157. Kinoshita, K., Parra, E. & Needham, D. Adsorption of ionic surfactants at microscopic air-water interfaces using the micropipette interfacial area-expansion method : Measurement of the diffusion coefficient and renormalization of the mean ionic activity for SDS. *J. Colloid Interface Sci.* **504**, 765–779 (2017).

158. Ho, T. M., Razzaghi, A., Ramachandran, A. & Mikkonen, K. S. Emulsion characterization via microfluidic devices: A review on interfacial tension and stability to coalescence. *Adv. Colloid Interface Sci.* **299**, 102541 (2022).

159. Nguyen, N. *et al.* Interfacial tension measurement with an optofluidic sensor. *IEEE Sens. J.* **7**, 692–697 (2007).

160. Deng, B., Schroën, K. & De Ruiter, J. Dynamics of bubble formation in spontaneous microfluidic devices: Controlling dynamic adsorption via liquid phase properties. *J. Colloid Interface Sci.* **622**, 218–227 (2022).

161. Hiemenz, P. C. & Raj Rajagopaplan. *Principles of colloid and surface chemistry*. (1997).

162. Pratap, V., Moumen, N. & Subramanian, R. S. Thermocapillary motion of a liquid drop on a horizontal solid surface. *Langmuir* **91**, 5185–5193 (2008).

163. Alvarez, N. J., Walker, L. M. & Anna, S. L. Diffusion-limited adsorption to a spherical geometry: The impact of curvature and competitive time scales. *Phys. Rev. E* **82**, (2010).

164. Jiang, Y., Geng, T., Li, Q., Li, G. & Ju, H. Equilibrium and dynamic surface tension properties of salt-free catanionic surfactants with different hydrocarbon chain lengths. *J. Mol. Liq.* **204**, 126–131 (2015).

165. Hinderink, E. B. A. *et al.* Interfacial protein-protein displacement at fluid interfaces. *Adv. Colloid Interface Sci.* **305**, (2022).

166. Won, J. Y. *et al.* Mixed adsorption mechanism for the kinetics of BLG interfacial layer formation at the solution/tetradecane interface. *Colloids Surfaces A Physicochem. Eng. Asp.* **519**, 146–152 (2017).

167. Hunt, J. A. & Dalgleish, D. G. Adsorption behaviour of whey protein isolate and caseinate in soya oil-in-water emulsions. *Food Hydrocoll.* **8**, 175–187 (1994).

168. Delahaije, R. J. B. M., Gruppen, H., Giuseppin, M. L. F. & Wierenga, P. A. Quantitative description of the parameters affecting the adsorption behaviour of globular proteins. *Colloids Surfaces B Biointerfaces* **123**, 199–206 (2014).

169. Gomez, J. M. A. & Rodríguez Patino, J. M. Formulation engineering of food model foams containing diglycerol esters and β-Lactoglobulin. *Ind. Eng. Chem. Res.* **45**, 7510–7519 (2006).

170. Fainerman, V. B., Aksenenko, E. V, Lylyk, S. V, Tarasevich, Y. I. & Miller, R. Adsorption of surfactants and proteins at the interface between their aqueous solution drop and air saturated by hexane vapour. *Colloids Surfaces A Physicochem. Eng. Asp.* **521**, 211–220 (2017).

171. Martinez, M. J., Carrera, C., Rodríguez, J. M. & Pilosof, A. M. R. Interactions in the aqueous phase and adsorption at the air – water interface of caseinoglycomacropeptide (GMP) and b-lactoglobulin mixed systems. *Colloid Surfaces B Biointerfaces* **68**, 39–47 (2009).

172. Thaís do Prado Silva, J., Nicoletti, V. R., Schroën, K. & Ruiter, J. De. Enhanced coalescence stability of droplets through multi-faceted microgel adsorption behaviour. *J. Food Eng.* **317**, 110850 (2022).

173. Tadros, T. F. *Emulsion formation, stability, and rheology*. *Emulsion Formation and Stability* (Wiley-VCH Verlag GmbH & Co. KGaA, 2013). doi:10.1002/9783527647941.

174. Joseph F., Z. *Functionality of proteins in food*. *Springer science & business media* (1997).

175. Zhu, P. & Wang, L. Passive and active droplet generation with microfluidics : A review. *Lab Chip* **17**, 34–75 (2017).

176. Berry, J. D., Neeson, M. J., Dagastine, R. R., Chan, D. Y. C. & Tabor, R. F. Measurement of surface and interfacial tension using pendant drop tensiometry. *J. Colloid Interface Sci.* **454**, 226–237 (2015).

177. Dabestani, M., Yeganehzad, S., Krzan, M. & Miller, R. Characterisation of egg white adsorption layers under equilibrium and dynamic conditions. *Colloids Surfaces A Physicochem. Eng. Asp.* **568**, 29–35 (2019).

178. Saito, M., Yin, L. J., Kobayashi, I. & Nakajima, M. Preparation characteristics of monodispersed oil-in-water emulsions with large particles stabilized by proteins in straight-through microchannel emulsification. *Food Hydrocoll.* **19**, 745–751 (2005).

179. Tcholakova, S., Denkov, N. D. & Lips, A. Comparison of solid particles, globular proteins and surfactants as emulsifier. *Phys. Chem. Chem. Phys.* **10**, 1608–1627 (2008).

180. Kovalchuk, N. M., Nowak, E. & Simmons, M. J. H. Effect of soluble surfactants on the kinetics of thinning of liquid bridges during drops formation and on size of satellite droplets. *Langmuir* **32**, 5069–5077 (2016).

181. Kovalchuk, N. M., Nowak, E. & Simmons, M. J. H. Kinetics of liquid bridges and formation of satellite droplets: Difference between micellar and bi-layer forming solutions. *Colloids Surfaces A Physicochem. Eng. Asp.* **521**, 193–203 (2017).

182. Roché, M., Aytouna, M., Bonn, D. & Kellay, H. Effect of surface tension variations on the pinch-Off behavior of small fluid drops in the presence of surfactants. *Phys. Rev. Lett.* **103**, 1–4 (2009).

183. Sugiura, S., Nakajima, M., Oda, T., Satake, M. & Seki, M. Effect of interfacial tension on the dynamic behavior of droplet formation during microchannel emulsification. *J. Colloid Interface Sci.* **269**, 178–185 (2004).

184. Liu, Z. *et al.* Effects on droplet generation in step-emulsification microfluidic devices. *Chem. Eng. Sci.* **246**, 116959 (2021).

185. Sun, X., Zhu, C., Fu, T., Ma, Y. & Li, H. Z. Dynamics of droplet breakup and formation of satellite droplets in a microfluidic T-junction. *Chem. Eng. Sci.* **188**, 158–169 (2018).

186. Vladisavljevi, G. T., Kobayashi, I. & Nakajima, M. Generation of highly uniform droplets using asymmetric microchannels fabricated on a single crystal silicon plate : Effect of emulsifier and oil types. *Powder Technol.* **183**, 37–45 (2008).

187. Wang, K., Xu, J., Liu, G. & Luo, G. *Role of interfacial force on multiphase microflow — An important meso-scientific issue*. *Advances in Chemical Engineering* vol. 47 (Elsevier Inc., 2015).

188. Chaurasia, A. S., Josephides, D. N. & Sajjadi, S. Buoyancy-driven drop generation via microchannel revisited. *Microfluid. Nanofluidics* **18**, 943–953 (2015).

189. Giménez-Ribes, G., Sagis, L. M. C. & Habibi, M. Interfacial viscoelasticity and aging effect on droplet formation and breakup. *Food Hydrocoll.* **103**, (2020).

190. Yang, X., Berry, T. K. & Foegeding, E. A. Foams prepared from whey protein isolate and egg white protein: 1. physical, microstructural, and interfacialproperties. *J. Food Sci.* **74**, 259–268 (2009).

191. Narchi, I., Vial, C. & Djelveh, G. Effect of protein-polysaccharide mixtures on the continuous manufacturing of foamed food products. *Food Hydrocoll.* **23**, 188–201 (2009).

192. Nazir, A., Maan, A. A., Sahin, S., Boom, R. M. & Schroën, K. Foam preparation at high-throughput using a novel packed bed system. *Food Bioprod. Process.* **94**, 561–564 (2015).

193. Deng, B., De Ruiter, J. & Schroën, K. Application of microfluidics in the production and analysis of food foams. *Foods* **8**, (2019).

194. Bals, A. & Kulozik, U. The influence of the pore size, the foaming temperature and the viscosity of the continuous phase on the properties of foams produced by membrane foaming. *J. Memb. Sci.* **220**, 5–11 (2003).

195. Bals, A. & Kulozik, U. Effect of pre-heating on the foaming properties of whey protein isolate using a membrane foaming apparatus. *Int. Dairy J.* **13**, 903–908 (2003).

196. Müller-Fischer, N., Bleuler, H. & Windhab, E. J. Dynamically enhanced membrane foaming. *Chem. Eng. Sci.* **62**, 4409–4419 (2007).

197. Carballido, L., Dabrowski, M. L., Dehli, F., Koch, L. & Stubenrauch, C. Monodisperse liquid foams via membrane foaming. *J. Colloid Interface Sci.* **568**, 46–53 (2020).

198. Gijsbertsen-Abrahamse, A. J., Van Der Padt, A. & Boom, R. M. Status of cross-flow membrane emulsification and outlook for industrial application. *J. Memb. Sci.* **230**, 149–159 (2004).

199. Hancocks, R. D., Spyropoulos, F. & Norton, I. T. Comparisons between membranes for use in cross flow membrane emulsification. *J. Food Eng.* **116**, 382–389 (2013).

200. Zanatta, V. *et al.* Stability of oil-in-water emulsions produced by membrane emulsification with microporous ceramic membranes. *J. Food Eng.* **195**, 73–84 (2017).

201. Piacentini, E., Imbrogno, A., Drioli, E. & Giorno, L. Membranes with tailored wettability properties for the generation of uniform emulsion droplets with high efficiency. *J. Memb. Sci.* **459**, 96–103 (2014).

202. Schröder, V. & Schubert, H. Production of emulsions using microporous, ceramic membranes. *Colloids Surfaces A Physicochem. Eng. Asp.* **152**, 103–109 (1999).

203. Abrahamse, A. J., Van Lierop, R., Van der Sman, R. G. M., Van der Padt, A. & Boom, R. M. Analysis of droplet formation and interactions during cross-flow membrane emulsification. *J. Memb. Sci.* **204**, 125–137 (2002).

204. Peng, S. J. & Williams, R. A. Controlled production of emulsions using a crossflow membrane. Part I: Droplet formation from a single pore. *Chem. Eng. Res. Des.* **76**, 894–901 (1998).

205. De Luca, G., Di Maio, F. P., Di Renzo, A. & Drioli, E. Droplet detachment in cross-flow membrane emulsification: Comparison among torque- and force-based models. *Chem. Eng. Process. Process Intensif.* **47**, 1150–1158 (2008).

206. Mirsandi, H. *et al.* Bubble formation from an orifice in liquid cross-flow. *Chem. Eng. J.* **386**, 120902 (2020).

207. Van Der Graaf, S., Schroën, C. G. P. H., Van Der Sman, R. G. M. & Boom, R. M. Influence of dynamic interfacial tension on droplet formation during membrane emulsification. *J. Colloid Interface Sci.* **277**, 456–463 (2004).

208. Vladisavljević, G. T. & Schubert, H. Preparation of emulsions with a narrow particle size distribution using microporous α-alumina membranes. *J. Dispers. Sci. Technol.* **24**, 811–819 (2003).

209. Van Der Graaf, S., Nisisako, T., Schroën, C. G. P. H., Van Der Sman, R. G. M. & Boom, R. M. Lattice Boltzmann simulations of droplet formation in a T-shaped microchannel. *Langmuir* **22**, 4144–4152 (2006).

210. Kobayashi, I., Yasuno, M., Iwamoto, S. & Shono, A. Microscopic observation of emulsion droplet formation from a polycarbonate membrane. *Colloids Surfaces A Physicochem. Eng. Asp.* **207**, 185–196 (2002).

211. Christov, N. C. *et al.* Capillary mechanisms in membrane emulsification : Oil-in-water emulsions stabilized by Tween 20 and milk proteins. *Colloids Surfaces A Physicochem. Eng. Asp.* **209**, 83–104 (2002).

212. Erickson, H. P. Size and shape of protein molecules at the nanometer level determined by sedimentation, gel filtration, and electron microscopy. *Biol. Proced. Online* **11**, 32–51 (2009).

213. Li, Z., Leshansky, A. M., Pismen, L. M. & Tabeling, P. Step-emulsification in a microfluidic device. *Lab Chip* **15**, 1023–1031 (2015).

214. Fainermap, V. B., Makievski, A. V & Millerb, R. The analysis of dynamic surface tension of sodium alkyl sulphate solutions, based on asymptotic equations of adsorption kinetic theory. *Colloids Surfaces A Physicochem. Eng. Asp.* **87**, 61–75 (1994).

215. Stroock, A. D. *et al.* Chaotic mixer for microchannels. *Science (80-.).* **295**, 647–651 (2002).

216. Bera, B., Khazal, R. & Schroën, K. Coalescence dynamics in oil-in-water emulsions at elevated temperatures. *Sci. Rep.* **11**, 1–11 (2021).

217. Dudek, M., Chicault, J. & Øye, G. Microfluidic investigation of crude oil droplet coalescence : Effect of oil/water composition and droplet aging. *Energy & Fuels* **34**, 5110–5120 (2020).

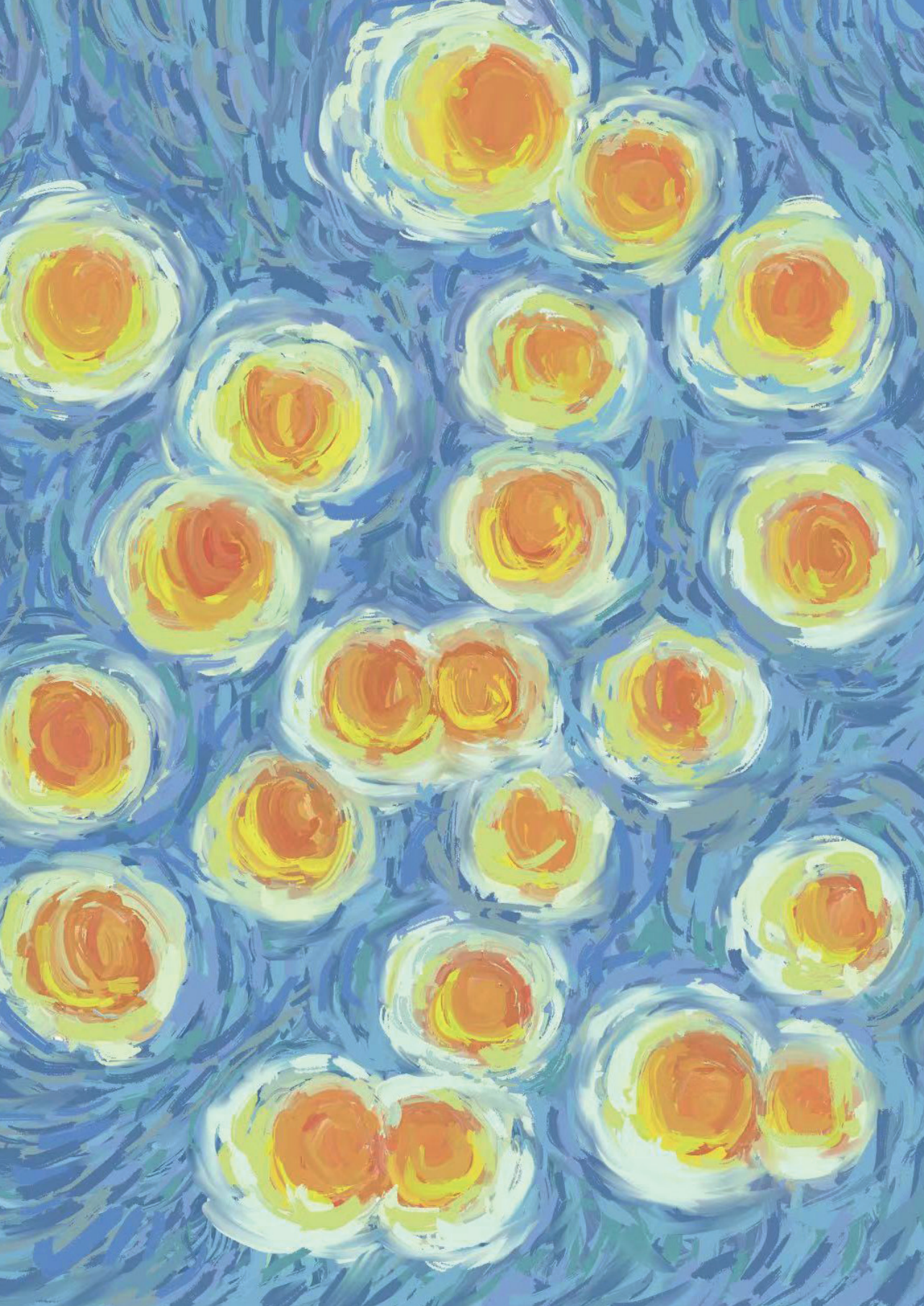

S

Summary

Foams are dispersions of gas in an aqueous or a solid phase, in the form of bubbles. During or after formation, the bubbles can be destabilised via creaming, disproportionation, and coalescence. Typically, coalescence is most relevant at (sub)millisecond time scales, and to prevent bubble coalescence, bubbles need to be covered by emulsifiers. Yet, compared to the minimum amount of emulsifier needed for surface stabilisation (i.e., monolayer surface coverage), the concentration used in practice is much higher. To utilise emulsifiers efficiently, it is crucial to understand the efficiency of emulsifier adsorption in suppressing bubble coalescence at relevant length and time scales.

The characterisation of emulsifier adsorption and its roles in bubble stabilisation at (sub)millisecond time scales is largely limited by technological challenges, e.g., inaccessibility of the production lines and the much longer time scales needed for conventional techniques. In the present work, we aim to characterise emulsifier adsorption and its roles in bubble formation and stabilisation (i.e., against coalescence) at very short scales. To do so, we introduced new microfluidic techniques that allow highly reproducible fast bubble formation, and studied emulsifier adsorption by monitoring the dynamic surface tension and the increase in bubble size (due to bubble coalescence) as function of the bubble formation time.

The literature review in **Chapter 2** follows that microfluidics can be used to create in-depth understanding of the bubble formation process, although the majority of studies has been dedicated to droplets. From the available designs, the partitioned-EDGE device stands out due to its crucial features of making multiple droplets simultaneously and stably within two distinct regimes, over a wide range of applied pressures. As such rich behaviours are also expected to hold for bubble formation, the partitioned-EDGE was the starting point for the present work.

In **Chapter 3**, we studied bubble formation as function of applied pressure and focused on the general behaviour in partitioned-EDGE devices. We found that bubble formation shows two pressure regimes, divided by the Laplace pressure of the clean air-water interface. Emulsifier adsorption (i.e., whey protein in this chapter) plays distinct roles; in the low-pressure regime, dynamic adsorption lowers the surface tension of the meniscus and plays a role in the initiation of bubble formation; in the high-pressure regime, dynamic adsorption at the surface of expanding and coalescing bubbles is responsible for limiting bubble coalescence. We have related the extent of bubble coalescence to the bubble formation time,

which is the time available for protein adsorption, and found that the extent of bubble coalescence increases as bubbles are formed at an increasing frequency. We have successfully captured this relationship in a semi-empirical coalescence model, based on a conceptual understanding of the stabilisation process and a mass balance of the proteins adsorbed at the bubble surface. Furthermore, we zoomed in on one bubble formation cycle, which can be sub-divided into two sub-processes: pore filling and necking. Each sub-process corresponds to a typical time scale that varies distinctly in the two pressure regimes; the pore filling time is dominated by protein adsorption in the low-pressure regime and by the applied pressure in the high-pressure regime; the necking time decreases with the applied pressure in the low-pressure regime, and levels off in the high-pressure regime. Based on these findings, it is clear that partitioned-EDGE devices can be used to make monodisperse bubbles within a wide range of conditions, with bubbles showing even richer behaviour than previously demonstrated for droplets.

As a next step, in **Chapter 4**, we studied bubble formation and the resulting bubble properties for various liquid phase compositions. We found that the bubble size mainly scales with the bubble necking time, which scales with the continuous phase viscosity. Next to that, the bubble formation frequency scales inversely with the bubble formation time, which decreases with increasing protein concentration in the low-pressure regime and increases with increasing continuous phase viscosity in the high-pressure regime, due to faster protein adsorption and slower neck thinning, respectively. Characterisation of these sub-processes provides crucial insights into the effects of the liquid phase properties on bubble formation, and thus on the corresponding bubble properties. Furthermore, we found that at moderate protein concentration and continuous phase viscosity, monodisperse bubbles are formed and maintained to certain extent, while at high protein concentration (e.g., 10% wt. WPI) and continuous phase viscosity (e.g., 6 mPa·s), larger and polydispersed bubbles are formed. The latter is mainly due to the promoted dripping-jetting transition, while bubble coalescence can be suppressed to a higher extent. From this follows that the liquid phase properties should be adjusted within certain boundaries to both control bubble formation (in the dripping regime) and suppress coalescence. In **Chapters 5** and **6**, we used the partitioned-EDGE device as an analytical tool to study dynamic processes occurring during bubble formation and stabilisation at relevant time scales. In **Chapter 5**, we used the partitioned-EDGE device as a microfluidic tensiometer to measure the dynamic surface and interfacial tension of bubble

and droplet surfaces, respectively. We showed that in the presence of 0.05-1% wt. SDS, the dynamic surface and interfacial tension can be measured at time scales in the range of 0.1-90 ms and 1-1500 ms for bubble and droplet surfaces, respectively. It is also good to mention that our microfluidic tensiometer allows to access nearly the full range of dynamic surface (and interfacial) tension, varying between that of a clean and saturated surface.

In **Chapter 6**, we used the partitioned-EDGE device to study instant coalescence occurring during or after bubble formation. The extent of bubble coalescence was investigated as function of the bubble formation time (> 0.01 ms) for various liquid phase properties and device geometries. Bubble coalescence increases with decreasing bubble formation time, and can be suppressed by increasing protein concentration and continuous phase viscosity within certain boundaries as mentioned in Chapter 4. Next to that, bubble coalescence was promoted by bubble crowdedness in the collection channel and interactions between growing bubbles. Furthermore, we have revisited the semi-empirical coalescence model introduced in Chapter 3, and incorporated an assumption that protein adsorption (towards the surface of coalescing bubbles) follows a Langmuir isotherm. The model fits the data well and yields a realistic estimate of the minimum time scale required for a certain protein concentration to stabilise a foam; this minimum time scale decreases with increasing protein concentration.

From the above, it is clear that our partitioned-EDGE device is a versatile system that can be used as both bubble generator (Chapters 3 and 4) and analytical tool (Chapters 5 and 6). In **Chapter 7**, as a proof of concept, we systematically studied emulsifier adsorption for various emulsifiers: SDS adsorption is compared to proteins, including WPI (as in Chapters 4 and 6), β-lactoglobulin (β-lac), and bovine serum albumin (BSA). In line with the literature, SDS is much more efficient than proteins in lowering the dynamic surface tension and stabilising bubbles against coalescence. In addition, we found that on a short-term, the dynamic surface tension better describes bubble coalescence stability than the corresponding equilibrium surface tension. For example, at time scales as low as 10 μs, BSA and then WPI are more efficient than β-lac in lowering the dynamic surface tension and suppressing the *instant* coalescence of bubbles, while the corresponding equilibrium surface tension shows an increasing trend for β-lac followed by WPI and then BSA.

In **Chapter 8**, we stepped away from the highly idealised world of microfluidics, and studied bubble formation and coalescence in a cross-flow membrane foaming system, for varied protein concentrations (0.5-2.5% wt. WPI), continuous phase viscosities, as well as dispersed

and continuous phase flow rates. We found that for bubbles formed at a time scale of about 0.1 ms, bubble coalescence can be suppressed by 2.5% wt. WPI in the membrane system, while it is 10% wt. WPI in the partitioned-EDGE system (Chapter 6). The difference most probably stems from differences in bubble crowdedness as a result of the differences in spacing and geometry of the bubble formation units, and in the flow conditions that influence emulsifier mass transfer.

Finally, in **Chapter 9**, we extensively reviewed the findings obtained in this thesis and the crucial features of the partitioned-EDGE that guarantee the rich behaviour during bubble formation and coalescence. We found that it is only possible to translate findings obtained for droplets to bubbles (or the other way around), when the sub-processes occurring during the formation and coalescence, of droplets and bubbles, are well understood (e.g., as done within this thesis for the analysis of 'dripping-jetting' transition). Besides, to evaluate emulsifier adsorption and its roles in bubble formation and coalescence stability, it is crucial to do so at relevant *length* and *time* sales, and to warrant practical application of these insights, also under *process conditions* close to those used in practice. To conclude, we show that our partitioned-EDGE is a versatile (model) system, which can be (up-scaled and) used to make monodisperse bubbles, as well as to follow emulsifier adsorption via monitoring dynamic surface (and interfacial) tension and bubble coalescence, which are necessary albeit rather underexplored insights that are needed to obtain stable foam (and emulsion) products.

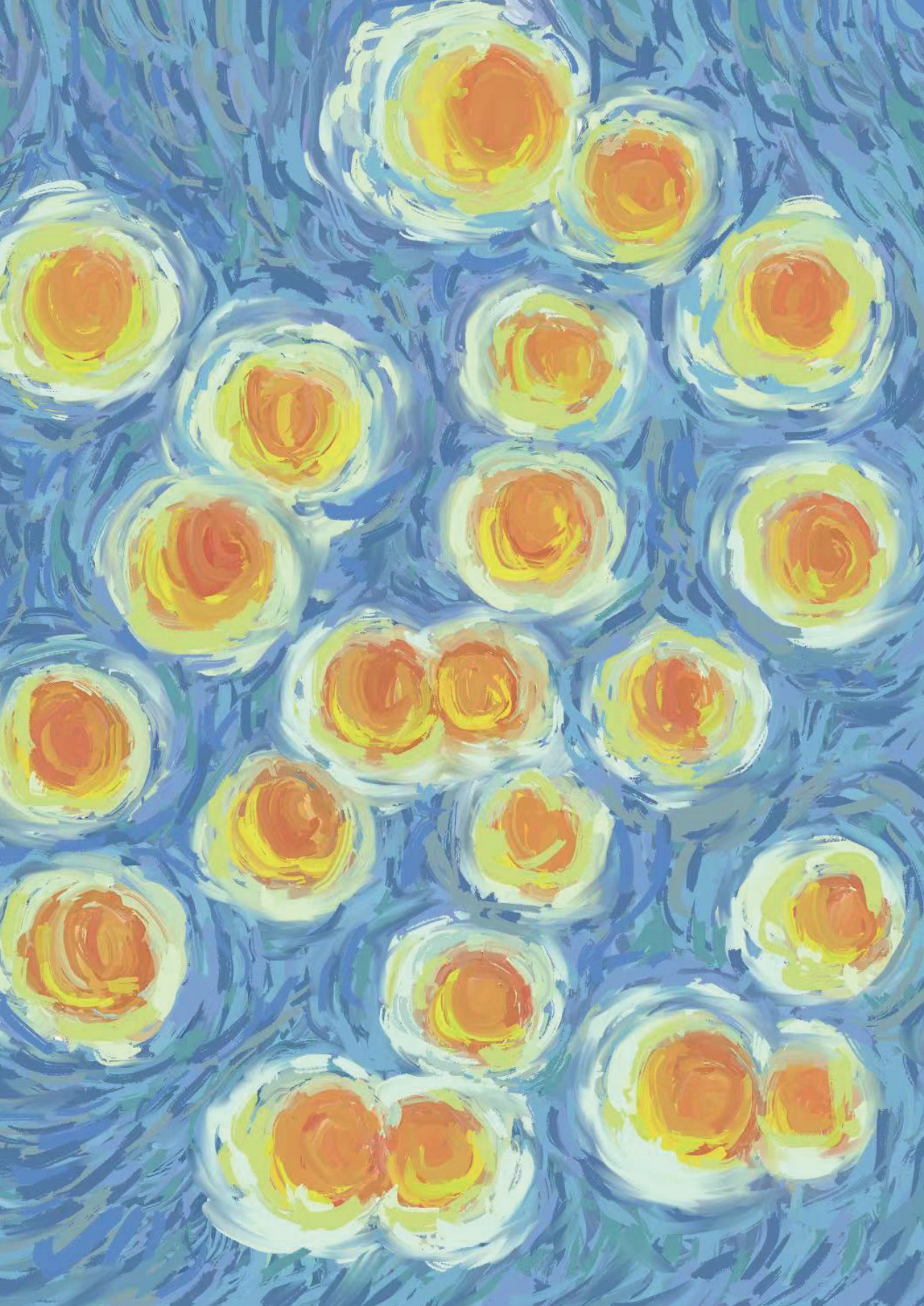

Appendices

Acknowledgments

About the author

Publications

Overview of completed training activities

Acknowledgments

After ‘countless’ months, my PhD journey comes to an end. The last four years are not easy, yet worthy. With this thesis, I would like to express my gratitude to all those who have contributed to this thesis and accompanied me throughout.

To start, I would like to thank my supervisors *Karin* and *Jolet*. *Karin*, thank you for having me on board four years ago. With that decision, my story in the Netherlands started. During the past four years, your unconditional support are indispensable for my ‘smooth’ progress and transition; your dedication to work always motivates me to learn and grow. I am extremely grateful for your guidance on the project, your *asap* feedback on the manuscript, your encouragement, and much more. *Jolet*, you became my daily supervisor one year later. I am truly grateful for your knowledge transfer, your advice on both science and life, and especially, our ‘17:00 o’clock’ meetings in the last year. Thanks for all the inspiring discussions and in-depth talks we had. I have learned loads from you.

Looking back, I received a lot of support and assistance from many people. Without you, the beginning, the process, and the ending of my PhD journey would not proceed smoothly. *Marjan, Ilona, Chantal*, and *Evelyn*, thank you for the administrative support. *Martin*, thanks for your help with the expense declaration. *Maurice*, thanks for getting me started with microfluidic experiments, for all the technical support, and also for answering many of my questions proposed in the late afternoons on Friday. *Jos* and *Wouter*, thank you for the introduction for the lab facilities.

Thanks to my project members *Erix, Chris,* and *Maartje* for the fruitful discussions and the useful suggestions. Especially, *Erix*, thank you for every time clearing my documents; and *Maartje*, I appreciate our collaboration on the tensiometer work.

To my MSc and BSc students *Manon, Min, Elske, Tessa, Jin-Li,* and *Dirk,* thank you for exploring this thesis together with me in the lab, and your contributions are really appreciated.

I would like to thank all my FPE colleagues and friends for creating such a cheerful and harmonious working atmosphere. I truly enjoyed our daily life in Axis, our group activities, and our trip to Singapore. To my office mates *Juliana*, *Katharina*, *Regina*, *Patrick*, *Quinten,* and *Hilda*, thanks for your accompanies and your help with my instantaneous questions! *Juliana*, thank you for all the laughs, coffees, lunches and dinners. *Katharina*, we started our

PhD together and it was you who helped me get used to studying abroad. During these four years, I am glad we can share both work-related and private issues, including both toughness and happiness. Together, we had so much fun and also adventure – in De Hoge Veluwe national park. *Regina*, you are always ready to help. I really enjoyed the time we spent together; we had chitchats as well as in-depth discussions. Thank you for sharing with me your project progress and achievements. Of course, I really enjoyed the time we six (with *Martijn*, *Jasper*, and *Chao*) spent together; thank you for your accompanies on this journey. *Ivanna*, it is a great thing to know you and to work with you. I truly enjoyed our talks and dinners. Thank you for the compliment on my little achievements, and thank you for joining me on this journey. *Bijoy*, thanks for getting me started with microfluidic experiments and helping me at the beginning of my PhD. *Wanqing*, I appreciate the talks and discussions we had. Thanks for all your tips and tricks. *Joanne*, thanks for sharing with me your real-time progress and tips with thesis printing. *Yifeng*, my previous neighbour; thanks for your invitations for dinner and your help with our moving. Thank you *Jiarui* and *Lingfeng* for the chats and dinner. Last but not least, *Sicong*, *Qinhui*, *Yu*, *Ruoxuan, Qimeng*, *Jilu*, *Lu, Emma*, *Anna, Andrea, Anouk, Herehau, Sten, Eric, Luc, Yafei, Laurens, Yizhou, Murat, Loes, Yhan, Kieke, Melanie, Julia, Lina, Sirinan, and Koen,* I really appreciate the talks we had. Many thanks to all of you for making my time at FPE so enjoyable and unforgettable.

Lastly, I would like to thank my family. Although you were not directly helping me in the lab, this thesis would not be here without your unconditional support.

亲爱的公婆，感谢你们长期以来的关心、理解和支持。

亲爱的家人们，感谢你们这么多年来对我的鼓励和支持，以及对我爸、妈的陪伴。

最爱的爸、妈，感谢你们对我无条件的爱护和一直以来的理解和信任，以及一直鼓励和支持我做自己想做的事。

邹先生，感谢你的理解、包容和开导，还有无微不至的照顾。十年的时光，很长又很短，感谢陪伴。

邓博心
Boxin Deng

Wageningen, 11/25/2022

About the author

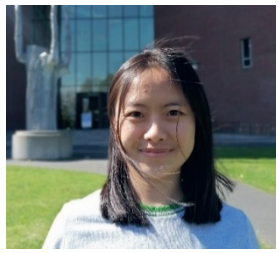

Boxin Deng was born on 30th September 1992 in Heilongjiang Province, China. In 2011, she started her bachelor in Jiangnan University. In the first two and half years, she followed courses, ranging from food engineering to food microbiology. After that, she conducted her bachelor thesis in the Food Quality and Safety faculty, and obtained her bachelor degree in 2015. In the same year, she continued her master study in Jiangnan University, in the Food Science and Technology faculty, and obtained her master degree in 2018.

Also in 2018, Boxin moved to the Netherlands and continued working as a PhD candidate at the Laboratory of Food Process Engineering group of Wageningen University & Research. She worked on the project entitled *Microfluidic analysis of dynamic processes occurring during bubble formation and stabilisation*. The results of her PhD project are presented in this thesis.

Publications

This thesis

Deng, B., De Ruiter, J., & Schroën, K. (2019). Application of Microfluidics in the Production and analysis of food foams. *Foods*, *8*(10), 476. https://doi.org/10.3390/foods8100476

Deng, B., Schroën, K., & De Ruiter, J. (2021). Effects of dynamic adsorption on bubble formation and coalescence in partitioned-EDGE devices. *Journal of Colloid and Interface Science*, *602*, 316-324. https://doi.org/10.1016/j.jcis.2021.06.014

Deng, B., Neef, T., Schroën, K., & De Ruiter, J. (2021). Mapping bubble formation and coalescence in a tubular cross-flow membrane foaming system. *Membranes*, *11*(9), 710. https://doi.org/10.3390/membranes11090710

Deng, B., Schroën, K., & De Ruiter, J. (2022). Dynamics of bubble formation in spontaneous microfluidic devices: Controlling dynamic adsorption via liquid phase properties. *Journal of Colloid and Interface Science*, *622*, 218-227. https://doi.org/10.1016/j.jcis.2022.04.115

Deng, B., Steegmans, M., Schroën, K. & De Ruiter, J. (2022), Capillary pressure-based measurement of dynamic interfacial tension in a spontaneous microfluidic sensor, *Lab on a Chip*, 22, 3860-3868. https://doi.org/10.1039/D2LC00545J

Deng, B., Wijnen, D., Schroën, K. & De Ruiter, J., Onsite coalescence behaviour of whey protein-stabilised bubbles generated at parallel microscale pores: role of pore geometry and liquid phase properties, *submitted*.

Deng, B., Schroën, K., & De Ruiter, J., A microfluidic study of bubble formation and coalescence tuned by dynamic adsorption of SDS and proteins, *submitted*.

Other publications

Schroën, K., **Deng, B.**, Berton-Carabin, C., Marze, S., Corstens, M., Hinderink, E., Microfluidics-based observations to monitor dynamic processes occurring in food emulsions and foams, *submitted*

Deng, B., Li, B., Li, X., Zaaboul, F., Jiang, J., Li, J., ... & Liu, Y. (2018). Using short-wave infrared radiation to improve aqueous enzymatic extraction of peanut oil: Evaluation of peanut cotyledon microstructure and oil quality. *European Journal of Lipid Science and Technology*, *120*(2), 1700285. https://doi.org/10.1002/ejlt.201700285

Overview of completed training activities

Discipline specific activities

Courses

Advanced Food Analysis (VLAG, NL)	2019
Training course: Microfluidics (KU Leuven, Belgium)	2019
Nano- and Microfluidics (JM burgercentrum, NL)	2021
Reaction Kinetics in Food Science (VLAG, NL)	2021
Experimental techniques in fluid mechanics (JM burgercentrum, NL)	2021

Conferences

8th Bubbles & droplets conference (Sofia, Bulgaria)	2019
35th European Colloid & Interface Science (Online) [a]	2021
4th Food structure and Functionality Symposium (Online) [b]	2021
Burgers symposium 2021 (Online)	2021
2nd Edible Soft Matter (Wageningen, NL) [a]	2022

General courses

PhD week (VLAG, NL)	2018
Competence Assessment (WGS, NL)	2018
Searching and Organizing Literature	2020
Presenting with impact (In'to languages, NL)	2019
Effective behaviour in your professional surroundings (WGS,NL)	2019
Philosophy and Ethics of Food Science & Technology (WGS,NL)	2019
Introduction to R	2021
Scientific writing (WGS, NL)	2021
PhD Workshop Carousel (WGS,NL)	2021
Career Perspective (WGS, NL)	2022

Other activities

Preparation of research proposal	2018
PhD study tour to Singapore [a, b]	2022
FPE weekly group meetings	2018-2022
Project meetings with FrieslandCampina	2019-2022
Supervising MSc and BSc students	2019-2022

[a] *Oral* & [b] *Poster*

This research is financially supported by the China Scholarship Council (grant number 201806790006) and FrieslandCampina.

Cover design by Boxin Deng

Printed by ProefschriftMaken ‖ www.proefschriftmaken.nl